

School of Earth and Planetary Sciences

**LINKING ATMOSPHERIC
OXYGENATION TO THE DEEP
EARTH**

Janne Liebmann

0000-0002-0739-3148

This thesis is presented for the Degree of

Doctor of Philosophy

Of

Curtin University

October, 2020

DECLARATION

I, Janne Liebmann, certify that this work contains no material which has been accepted for the award of any other degree or diploma in my name, in any university or other tertiary institution and, to the best of knowledge, contains no material previously published or written by any other person, except where due reference has been made in the text. The author acknowledges that the copyright of published works contained within this thesis resides with the copyright holder(s) of those works. Every reasonable effort has been made to acknowledge the owners of copyright material. I would be pleased to hear from any copyright owner who has been omitted or incorrectly acknowledged.

Signature:.....

(Janne Liebmann)

Date:.....
09 October 2020

PUBLICATIONS DURING THE COURSE OF THIS THESIS

Peer-reviewed journal articles

Liebmann, J., Spencer, C.J., Kirkland, C.K., Bucholz, C.E., He, X., Santosh, M., Xia, X.P., Martin, L., Evans, N. J. Emergence of continents above sea-level influences composition of sediment melts. *Submitted to Terra Nova*.

Liebmann, J., Spencer, C.J., Kirkland, C.K., Bucholz, C.E., Xia, X.P., Martin, L., Kitchen, N. and Shumlyanskyy, L. Coupling of the atmosphere and sediment melts across the Archean-Proterozoic transition. *Submitted to Geochimica et Cosmochimica Acta*.

Liebmann, J., Spencer, C.J., Kirkland, C.K., Ernst, R. E. Large igneous provinces track 2.4 Ga subaerial emergence of continents. *Submitted to Geophysical Research Letters*.

Liebmann, J., Spencer, C.J., Kirkland, C.K., Xia, X.P., and Bourdet, J. Effect of water on $\delta^{18}\text{O}$ in zircon. *Submitted to Chemical Geology*.

Conference presentations

Liebmann, J. Spencer C.J., Bucholz, C.E., Kirkland C.L., Martin, L., Xia, X.P., Kitchen, N., 2020. Coupling atmosphere and sediment melts across the Archean-Proterozoic transition. The Geological Society of America Connects Online, 2020.

Liebmann, J. Spencer C.J., Bucholz, C.E., Kirkland C.L., Martin, L., Xia, X.P., Kitchen, N., 2020. Is Paleoproterozoic atmospheric oxygenation linked to the emergence of continents above sea-level? Evidence from sulfur and oxygen isotopic signatures in Archean to Proterozoic sediment-derived granitoids. Abstract with Programs. Goldschmidt conference, 2020.

Liebmann, J. Spencer C.J., Kirkland C.L., Bucholz, C.E., He, X.F., Tang, L., Santosh, M., Xia, X.P., Martin, L., Evans, N.J., 2019. Emergence of continents above sea-level influences composition of sediment melts. Abstract with Programs. Goldschmidt conference, 2019.

Liebmann, J. and Spencer C.J., 2018. Linking atmospheric oxygenation to the deep Earth. Abstract with Programs. International Association of Gondwana Research Convention 2018.

Other relevant co-authored publications

Spencer, C.J., Partin, C.A., Kirkland, C.L., Raub, T.D., **Liebmann, J.** and Stern, R.A., 2019. Paleoproterozoic increase in zircon $\delta^{18}\text{O}$ driven by rapid emergence of continental crust. *Geochimica et Cosmochimica Acta*, 257, pp.16-25.

Spencer, C.J., Kirkland, C.L., Roberts, N.M.W., Evans, N.J. and **Liebmann, J.**, 2019. Strategies towards robust interpretations of in situ zircon Lu–Hf isotope analyses. *Geoscience Frontiers*.

AUTHORSHIP AGREEMENT FORM



Curtin University

Authorship Agreement Form

The Curtin University [Authorship, Peer Review and Publication of Research Findings Policy and Procedures](#)¹ which references the [Australian Code for the Responsible Conduct of Research](#)², provides clear guidelines regarding attribution of authorship. This form is to assist researchers in capturing discussions around intended publications arising from joint work. It does not replace copyright or certification forms required by publishers.

1. Research

Project Title:	Linking atmospheric oxygenation to the deep Earth		
Project identifier (if applicable)	n/a		
Principal Investigator	Christopher J. Spencer		
Other named investigator/s*	Janne Liebmann	Role	PhD student
Other researcher/s*	Christopher L. Kirkland	Role	Investigator

* Insert additional rows if required

2. Publications/Outputs – the intended outputs from the above research are identified below

Pub*	Description (e.g. method paper)	Publication Type (Conference, journal article etc)
1	Liebmann, J., Spencer, C.J., Kirkland, C.K., Bucholz, C.E., He, X., Santosh, M., Xia, X.P., Martin, L., Evans, N. J. Emergence of continents above sea-level influences composition of sediment melts. Submitted to Terra Nova.	Journal article (submitted)
2	Liebmann, J., Spencer, C.J., Kirkland, C.K., Bucholz, C.E., Xia, X.P., Martin, L., Kitchen, N. and Shumlyansky, L. Coupling of the atmosphere and sediment melts across the Archean-Proterozoic transition. Submitted to Geochimica et Cosmochimica Acta.	Journal article (submitted)
3	Liebmann, J., Spencer, C.J., Kirkland, C.K., Ernst, R. E. Large igneous provinces track 2.4 Ga subaerial emergence of continents. Submitted to Geophysical Research Letters.	Journal article (submitted)
4	Liebmann, J., Spencer, C.J., Kirkland, C.K., Xia, X.P., Bourdet, J. Effect of water in natural zircon on $\delta^{18}\text{O}$. Submitted to Chemical Geology.	Journal article (submitted)

* Insert additional rows if required

3. Proposed order of authors

(add rows as required for additional authors and/or if authorship will differ between multiple outputs)

Pub**	Author**	Corresponding? Y/N
1	1. Janne Liebmann	Y
1	2. Christopher J. Spencer	N
1	3. Christopher L. Kirkland	N
1	4. Claire E. Bucholz	N
1	5. Xiaofang He	N
1	6. M. Santosh	N
1	7. Xiao-Ping Xia	N
1	8. Laure Martin	N
1	9. Noreen J. Evans	N
2	1. Janne Liebmann	Y
2	2. Christopher J. Spencer	N
2	3. Christopher L. Kirkland	N
2	4. Claire E. Bucholz	N
2	5. Xiao-Ping Xia	N
2	6. Laure Martin	N
2	7. Nam Kitchen	N
2	8. Leonid Shumlyansky	N
3	1. Janne Liebmann	Y
3	2. Christopher J. Spencer	N

¹ <http://policies.curtin.edu.au/findapolicy/#A>

² <https://www.nhmrc.gov.au/guidelines-publications/r39>



3	3. Christopher L. Kirkland	N
3	4. Richard E. Ernst	N
4	1. Janne Liebmann	Y
4	2. Christopher J. Spencer	N
4	3. Christopher L. Kirkland	N
4	4. Xiao-Ping Xia	N
4	5. Julien Bourdet	N

* If multiple publications are intended under table 2, and author inclusion and order is the same, then insert "All"

** Attribution of authorship, and role of corresponding author, may have some discipline differences, however, in all cases, inclusion must be based upon substantive intellectual contribution as defined under the Policy. Acceptance should also be sought where intending to name an individual in the acknowledgements.

4. Confirmation of agreement

(add rows as required)

Author Name and Affiliation (if other than Curtin)	Author Signature	Date
1. Christopher J. Spencer, Queen's University, Canada		27 August 2020
2. Christopher L. Kirkland		28 August 2020
3. Claire E. Bucholz, California Institute of Technology, USA		27 August 2020
4. Xiaofang He, China University of Mining & Technology Beijing, China		28 August 2020
5. M. Santosh, China University of Geosciences, Beijing, China.		28 August 2020
6. Xiao-Ping Xia, Guangzhou Institute of Geochemistry, Chinese Academy of Sciences, China		28 August 2020
7. Laure Martin, The University of Western Australia, Australia		4 September 2020
8. Noreen J. Evans		27 August 2020
9. Nami Kitchen, California Institute of Technology, USA		28 August 2020
10. Leonid Shumlyansky		28 August 2020
11. Richard E. Ernst, Carleton University, Canada		27 August 2020
12. Julien Bourdet, CSIRO Kensington, Australia		27 August 2020

All authors should maintain a copy of this completed form for their reference.

ABSTRACT

The Archean-Proterozoic transition marks a time of fundamental geologic, biologic, and atmospheric changes to the Earth system, including oxygenation of the atmosphere (termed the ‘Great Oxygenation Event’), an increase in subaerial continental land area, and widespread, potentially global glaciations. These changes left imprints on the geologic record; for instance 1) the attenuation of mass-independent fractionation of sulfur isotopes associated with the rise of atmospheric oxygen, 2) a shift in the oxygen isotope composition of siliciclastic sediments, and sediment-derived melts concomitant with continental emergence above sea-level, and associated changes in subaerial weathering pattern and erosion, and 3) an increase of subaerial volcanism.

Previous studies have proposed a causal relationship between geodynamic, atmospheric, and biologic processes at the Archean-Proterozoic boundary. However, these models often rely on the correlation of independent records (e.g. the sedimentary and the igneous rocks record) or numerical modelling, and hence involve some ambiguity owing to imprecise age constraints, fragmented records, or poorly constrained variables. In contrast, this thesis is based on a global sample set of sediment-derived granitoids, which allows for direct comparison of a variety of geochemical proxies that track atmospheric oxygen level, crustal recycling, and freeboard (the average elevation of continental crust above sea level). The research presented in this thesis utilizes a range of geochemical tools (i.e. oxygen, sulfur, and hafnium isotope geochemistry of zircon, garnet, and pyrite, respectively, and whole rock major and trace element concentrations), U-Pb zircon geochronology, and petrological evidence to investigate the interplay of lithosphere, atmosphere, and biosphere at the Archean-Proterozoic transition. The results are interpreted in combination with large data compilations; namely, the large igneous province record, oxygen isotopic signatures in detrital zircon and siliciclastic sediments, and whole rock trace element compositions of a global set of Archean and Proterozoic sediments and sediment-derived granites.

The results presented in this thesis demonstrate a ~2.35 Ga increase in $^{18}\text{O}/^{16}\text{O}$ isotope ratio in sediment-derived melts. This increase in oxygen isotope ratio is decoupled from hafnium isotopic signatures, excluding enhanced supracrustal recycling (e.g. through a change in geodynamic regime and the onset of collisional tectonics) as the dominant driver for the increase in $^{18}\text{O}/^{16}\text{O}$ ratio in sediment melts. Instead the change in oxygen isotope ratio is temporally correlated with a ~2.4 Ga increase in subaerial continental large igneous province volcanism, and a 2.43-2.32 Ga shift in the triple oxygen isotope composition of shales, both of which can be reasonably explained through the widespread subaerial emergence of continents. The results of this thesis imply that the observed shift in $^{18}\text{O}/^{16}\text{O}$ ratio in sediment melts may be caused by a compositional change in recycled sediments driven by an increase in freeboard and associated enhanced continental erosion, and subaerial weathering.

Importantly, the change in oxygen isotopic signatures appears to be coeval with the disappearance of mass-independent fractionation signatures of sulfur isotopes in the sediment-derived granitoids of this study. Triple sulfur isotopic signatures are a proxy for atmospheric oxygen level, as large mass-independent fractionation signatures can only be generated under anoxic atmospheric conditions. The coupled behavior of oxygen and sulfur isotopic signatures suggests that atmospheric oxygenation is temporally correlated with continental emergence. The implication of this thesis is that the widespread emergence of continents constitutes a potential driver for ecologic and geologic changes that ultimately led to the oxygenation of the atmosphere – perhaps linked to the removal of CO₂ from the atmosphere through subaerial weathering, a shift towards less reducing volcanic gases associated with diminishing submarine volcanism, or an increased supply of nutrients for photosynthetic microbes in the ocean through enhanced erosion of the emergent continents.

ACKNOWLEDGEMENTS

I owe my gratitude to the support, patience, and advice of many people, without whom the completion of this thesis would have not been possible.

First off, I would like thank my supervisors Chris Spencer, and Chris Kirkland for their excellent support, and guidance throughout this PhD. Countless drafts of the various chapters of this thesis came across their desk. Their constructive feedback, and scientific discussion have contributed immeasurably to the completion and quality of this thesis. Chris Spencer is also thanked for providing me with the opportunity to conduct many exciting, and adventurous field sessions throughout this project (on four different continents!).

I am grateful for the scientific interchange with the researchers I collaborated with during the course of this project. A special thanks goes out to Claire Bucholz for providing samples, and helpful, and critical feedback for chapters 2 and 4 of this thesis. She was an excellent host and instructor during my visit at Caltech. Richard Ernst is thanked for his help and provision of an extensive database for the large igneous provinces project presented in chapter 3. I am thankful for the support of Xiaofang He, and M. Santosh during the field session in Inner Mongolia. Xiaofang He is also thanked for being a great host during my visit at the China University of Geosciences, and for introducing me to the excellent local cuisine. I thank Andreas Petersson, Helen McFarlane, and Leonid Shumlyanskyy for providing samples for this project. Furthermore, I thank Xiao-Ping Xia, Laure Martin, Noreen Evans, Brad McDonald, Hao Gao, Allen Kennedy, Nami Kitchen, Julien Bourdet, Katy Evans, Anusha Shanta, Elaine Miller, and Zakaria Quadir for their help with sample analysis and preparation.

I am grateful for the funding I received from The Institute for Geoscience Research (TIGeR) that enabled me to attend two international conferences.

Finally, I would like to thank all my wonderful friends, new and old, from back home and from what has become my new home over the last years. You turned this journey into an

unforgettable and delightful experience. I thank Christine and Mark, and everyone else from my Australian family, for welcoming me with open arms, and for the uncountable pre-work coffees, beach days, and dinner get-togethers that sweetened so many of my days. An meine Familie und erweiterte Familie zu Hause: Danke, dass ihr immer für mich da seid. Zu wissen, dass ich mich jederzeit auf eure Unterstützung, euren Rat und lustige Anekdoten aus der Mutterstadt und Kiel verlassen kann, bedeutet mir unendlich viel. Vielen Dank für die unzählbaren FaceTime-Anrufe und dafür, dass ihr den weiten Weg in die südliche Hemisphäre auf euch genommen habt, um mich zu besuchen. Ich freue mich riesig darauf, euch endlich wieder persönlich in die Arme zu nehmen. And finally, Bryant, thank you so much for your constant love, encouragement, advice, and support. I would not have got far without it.

TABLE OF CONTENTS

<i>Declaration</i>	<i>i</i>
<i>Publications During the Course of This Thesis</i>	<i>ii</i>
<i>Authorship Agreement Form</i>	<i>iv</i>
<i>Abstract</i>	<i>vi</i>
<i>Acknowledgements</i>	<i>viii</i>
<i>Table of Contents</i>	<i>x</i>
<i>List of Figures</i>	<i>xiv</i>
<i>List of Tables</i>	<i>xvii</i>
<i>List of Abbreviations and Definitions</i>	<i>xix</i>
Chapter 1: Introduction.....	1
1.1 What makes a planet habitable?.....	1
1.2 The Archean Proterozoic Transition.....	3
1.3 Research Objectives & Sample Context	7
1.4 Thesis structure.....	9
1.5 References	11
Chapter 2: Emergence of Continents Above Sea-Level Influences Composition of Sediment Melts.....	16
Abstract	16
2.1 Introduction	17
2.2 Methods	18
2.3 Results	22
2.4. Discussion	25
2.4.1 A Paleoproterozoic increase in zircon $\delta^{18}\text{O}$ in sediment-derived melts	25
2.4.2 Decoupled oxygen and hafnium isotopic signatures.....	25
2.4.3 Changes in sediment composition as a driver for the zircon $\delta^{18}\text{O}$ increase	28
2.4.4. The emergence of continents and its repercussion on sediment $\delta^{18}\text{O}$	29
2.5 Concluding remarks.....	30

2.6 References	30
2.7 Author contributions.....	35
Appendix A.....	35
Appendix B.....	65
Appendix C.....	69
Chapter 3: Large Igneous Provinces Track 2.4 Ga Subaerial Emergence of Continents	74
Abstract	74
3.1 Introduction	75
3.2 Data Source and Eruptive Loci Criteria.....	76
3.3 Subaerial Emergence of Continents Tracked by Continental LIP Record	78
3.4 Repercussion of Continental Emergence on Climate, Atmosphere, and Biosphere.....	82
3.5 References	84
3.6 Author contributions.....	88
Appendix A.....	89
Appendix B	92
Chapter 4: Coupling of the Atmosphere and Sediment Melts Across the Archean Proterozoic Transition.....	114
Abstract	114
4.1 Introduction	115
4.2 Materials and Methods	117
4.2.1 Sample context	117
4.2.2 Methodology.....	119
4.3 Results	126
4.3.1 Bulk-rock geochemistry and mineralogy	126
4.3.2 Geochronology.....	126
4.3.3 Zircon and garnet oxygen isotope geochemistry	126
4.3.4 Sulfur isotope geochemistry.....	129
4.4 Discussion and conclusion	132

4.5 References	136
4.6 Author contributions.....	144
Appendix A.....	144
Appendix B.....	160
Appendix C.....	163
Appendix D	171
Chapter 5: Effect of Water on $\delta^{18}\text{O}$ in zircon	178
Abstract	178
5.1. Introduction	179
5.2. Materials & Methods	180
5.2.1 Sample context	180
5.2.2 Methods	180
5.3. Results	184
5.3.1 Zircon $\delta^{18}\text{O}$ and $^{16}\text{O}^{1\text{H}}/^{16}\text{O}$	184
5.3.2 Raman spectra	185
5.3.3 Zircon trace element concentrations.....	185
5.3.4 Alpha dose.....	187
5.4. Discussion	190
5.4.1. Water uptake in zircon through primary and secondary processes	190
5.4.2. The effect of water uptake on zircon $\delta^{18}\text{O}$	194
5.4.3. Assessing disturbance of the zircon O isotopic system.....	196
5.5. Concluding remarks.....	198
5.6 References	199
5.7 Author contributions.....	203
Appendix A.....	204
Chapter 6: Conclusions	226
6.1 Widespread emergence of continents above sea-level at ~ 2.4 Ga	226
6.1.1 Validity of geochemical signatures used to constrain continental emergence ..	227
6.2 A coevolution of atmosphere and lithosphere?.....	227
6.3 Continental emergence as a potential driver of atmospheric oxygenation.....	228

6.4 Limitations and avenues for future work	230
6.5 Epilogue: Implications for the search of inhabited worlds	230
6.6 References	233

LIST OF FIGURES

Figure 1.1. Characteristic features of habitable and non-habitable planets.....	2
Figure 1.2. Artist's impression of the early and the Earth today.....	3
Figure 1.3. Schematic illustration of two contrasting models proposed to explain oxygen isotopic changes in felsic magmas (recorded by zircon $\delta^{18}\text{O}$) at the Archean-Proterozoic transition.....	6
Figure 1.4. Temporal correlation of continental emergence, a rise of atmospheric oxygen, changes in geochemical proxies, and other secular changes at the Archean Proterozoic transition.....	7
Figure 1.5. Map showing sample locations.....	9
Figure 2.1. Simplified map of the North China Craton.....	19
Figure 2.2. Thin section photomicrographs, CL images of representative zircon grains, concordia diagrams, and oxygen isotope data of representative samples.....	21
Figure 2.3. Rb/Ba vs. Rb/Sr ratios of sediment-derived granitoids.....	24
Figure 2.4. Variation in zircon $\delta^{18}\text{O}$ with >1.5 Ga crystallization.....	26
Figure 2.5. Depleted mantle model age (TDM_{Hf}) vs $\delta^{18}\text{O}$ of single grain analyses of igneous zircon from sediment-derived granitoids.....	27
Figure A1. Thin section photomicrographs, CL images of representative zircon grains, concordia diagrams, and oxygen isotope violin plots of representative samples.....	53
Figure A2. Continuation.....	54
Figure A3. Continuation.....	55
Figure A4. Measured vs. time-integrated Th/U ratios of zircon.....	55
Figure A5. Oxygen isotope data of standards and unknowns.....	56
Figure A6. Hf isotope data of standards and unknowns.....	57
Figure A7. Map with sample locations.....	58
Figure A8. Bulk rock Zr concentration (ppm) vs. ϵ_{Hf}	58
Figure 3.1. Location and locus of emplacement of continental LIP events from 2.7 to 2.0 Ga.....	76

Figure 3.2. Temporal distribution of oceanic and continental LIPs from 2.7 to 2.0 Ga	78
Figure 3.3. Distribution of continental LIP emplacement environment from 2.7-2.0 Ga	81
Figure 3.4. Temporal correlation of continental emergence and other secular changes at the Archean-Proterozoic transition.	83
Figure A1. Carbonate $^{87}\text{Sr}/^{86}\text{Sr}$ isotopic ratios from 3.5 to 1.0 Ga.	89
Figure 4.1. Zircon $\delta^{18}\text{O}$ vs garnet $\delta^{18}\text{O}$.	129
Figure 4.2. Single spot $\delta^{34}\text{S}$ vs. $\Delta^{33}\text{S}$ of sediment-derived igneous rocks.	130
Figure 4.3. Oxygen and sulfur isotopic data vs. crystallization age of sediment-derived igneous rocks.	132
Figure A1. Terra-Wasserburg diagrams.	149
Figure A2. Cathodoluminescence images of representative zircon grains with O and U-Pb spots marked.	151
Figure A3. Back scatter electron images of representative pyrite grains with S spots marked.	151
Figure A4. Thin section photomicrographs.	152
Figure A5. Reflected light photomicrographs.	153
Figure A6. Backscatter electron image and element maps of garnet.	154
Figure A7. Backscatter electron image and element maps of garnet.	155
Figure A8. Sulfur and oxygen isotope data of standards and unknowns.	156
Figure 5.1. CL images of representative zircon grains.	181
Figure 5.2. $\delta^{18}\text{O}$ vs. $^{16}\text{O}^{1\text{H}}/^{16}\text{O}$ plots for zircon reference materials and unknowns.	186
Figure 5.3. Two sigma error of mean $\delta^{18}\text{O}$ value vs. $^{16}\text{O}^{1\text{H}}/^{16}\text{O}$ ratio.	187
Figure 5.4. Raman spectra and $\delta^{18}\text{O}$ vs. $^{16}\text{O}^{1\text{H}}/^{16}\text{O}$ plots.	188
Figure 5.5. Zircon water content ($^{16}\text{O}^{1\text{H}}/^{16}\text{O}$) vs. measurement parameters for crystal damage.	189
Figure 5.6. REE pattern and Ca and Fe concentrations.	190
Figure 5.7. Zircon Ca and Fe concentrations.	191

Figure 5.8. Zircon REE+Y and P concentrations	193
Figure 5.9. FWHM of the $\nu_3(\text{SiO}_4)$ Raman band vs. alpha dose	196
Figure 5.10. Zircon water content ($^{16}\text{O}^1\text{H}/^{16}\text{O}$) vs. $\delta^{18}\text{O}$ of detrital and igneous zircon from the Luliang complex, North China Craton.....	198
Figure 6.1. Illustration of a possible model for the coevolution of lithosphere, atmosphere, and biosphere at the Archean Proterozoic transition.....	229
Figure 6.2. Artist's concept of Kepler-186f	231
Figure 6.3. Poster is from the "Visions of the Future" poster series. Courtesy NASA/JPL-Caltech	232

LIST OF TABLES

Table 2.1. Geologic unit, location, lithology, mineralogy, magmatic crystallization ages, and zircon $\delta^{18}\text{O}$ of samples studied here.....	20
Table 2.2. Bulk rock major element concentrations.....	23
Table 2.3. Trace element concentrations.....	25
Table 2.A1. U-Pb measurement results of zircon reference materials for SIMS analytical runs.....	60
Table 2.A2. O isotope measurement results of zircon reference materials for SIMS analytical runs.....	60
Table 2.A3. Hf isotope measurement results of zircon reference materials for LA-ICPMS analytical runs.....	60
Table 2.B1. SIMS zircon U-Pb single spot results.....	65
Table 2.C1. Zircon SIMS O isotopes and LA-ICPMS Hf isotopes single spot results.....	69
Table 3.1. Criteria for subaerial vs. submarine continental LIP emplacement.....	79
Table 3.B1.1. Large igneous province database.....	92
Table 3.B1.2. Comments on the LIP events listed in Table B1.1.....	98
Table 4.1. Summary of sample locations, lithologies, and mineralogy.....	125
Table 4.2. Bulk rock major element concentrations.....	128
Table 4.3. Summary of O and S geochemistry, and crystallization ages.....	131
Table 4.A1. U-Pb measurement results of zircon reference materials for SIMS analytical runs.....	157
Table 4.A2. U-Pb measurement results of secondary zircon reference materials for LA-ICPMS analytical run.....	157
Table 4.A3. O isotope measurement results of zircon reference materials for SIMS analytical runs.....	157
Table 4.A4. S isotope measurement results of pyrite reference materials for SIMS analytical runs.....	158

Table 4.B1. SIMS zircon U-Pb single spot results.....	160
Table 4.B2. LA-ICPMS zircon U-Pb single spot results.....	162
Table 4.C1. SIMS pyrite sulfur single spot results	163
Table 4.D1. SIMS zircon oxygen single spot results	171
Table 4.D2. Laser fluorination garnet O isotope single aliquot results.	177
Table 5.1. List of igneous zircon samples, including location, lithology, and magmatic crystallization age.....	180
Table 5.2. Whole rock major element concentrations.	194
Table 5.A1.1 SIMS zircon O isotope, and U-Th-Pb data.....	204
Table 5.A1.2 Raman spectroscopic results	223
Table 5.A2 LA-ICPMS zircon trace element data	224
Table 5.A3 O isotope measurement results of zircon reference materials for SIMS analytical runs	225

LIST OF ABBREVIATIONS AND DEFINITIONS

$\delta^{18}\text{O}$. Deviation in the isotope ratio $^{18}\text{O}/^{16}\text{O}$ in permil relative to average sea water (SMOW).

$\Delta^{17}\text{O}$. Deviation of triple oxygen isotopic composition from a reference line. Defined as $\delta^{17}\text{O}-0.5305*\delta^{18}\text{O}$.

$\delta^{34}\text{S}$. Deviation in the isotope ratio $^{34}\text{S}/^{32}\text{S}$ in permil relative to the Cañon Diabolo Troilite (CDT).

$\Delta^{33}\text{S}$. Deviation of triple sulfur isotopic composition from a reference line. Defined as $\delta^{33}\text{S}-0.515*\delta^{34}\text{S}$.

ϵHf . Deviation of $^{176}\text{Hf}/^{177}\text{Hf}$ in parts per 10,000 from that of the chondritic uniform reservoir (CHUR).

Freeboard. The average elevation of continental crust above sea level.

GOE. Great Oxygenation Event.

LIP. Large igneous province.

PAL. Present atmospheric level.

S-MDF. Mass-dependent fractionation of sulfur isotopes.

S-MIF. Mass-independent fractionation of sulfur isotopes.

INTRODUCTION

1.1 What makes a planet habitable?

Defining planetary habitability (the conditions for a planet to provide an environment hospitable for life) is a major aspect in the search for extraterrestrial life (Seager, 2013). One key requirement for habitability is the location of a planet within the ‘habitable zone’, that is at the distance from their host star where surface temperatures of a planetary body are consistent with the presence of liquid water (Kasting et al., 1993). However, a planet that is located in the habitable zone does not necessarily on its own provide an environment capable supporting the development and sustenance of life, let alone complex life (Cockell et al., 2016). Mars for instance is located in the habitable zone of the Sun, and may have had a plate tectonic regime similar to that of the modern Earth (Breuer and Spohn, 2003), and liquid surface water for the first few 100 million years of its lifetime (Borg and Drake, 2005). Today however, Mars at best may hosts subsurface microbes (Westall et al., 2013). Assessing which features of Earth are essential for life, and how these features are controlled is an important step to constrain the habitability of exoplanets (planets orbiting stars other than the Sun) (Shahar et al., 2019). The life-friendly environment on Earth is rooted in the presence of a stable atmosphere, and hydrosphere, which are influenced by the planet’s bulk composition, mass, and interior dynamics (Figure 1.1) (Cockell et al., 2016; Shahar et al., 2019). Plate tectonics provides a mechanism for geologic turnover to cycle material between the interior and the surface, and play a crucial role in stabilizing Earth’s climate and hydrosphere (Walker et al., 1981). Furthermore, the temperature gradient at the core-mantle boundary induced by plate tectonics may be an important driver of the planetary dynamo responsible for the generation of the magnetic field that shields Earth from the solar wind (Cockell et al., 2016; Olson and Christensen, 2006). Planets like Earth with liquid surface water can sustain habitable environments for oxygenic photosynthesis, which ultimately leads to the rise of free

atmospheric oxygen (O_2 ; Cockell et al., 2016). An O_2 -rich atmosphere provides the base for aerobic respiration, a highly efficient metabolism that may be crucial for the development of complex multicellularity and intelligent life over geologic time scales (Catling et al., 2005). On Earth atmospheric oxygenation was coeval with a number of other secular changes to the planet's system (Condie, 2018) during a time interval known as the Archean Proterozoic transition (2.5 billion years before present). Atmospheric oxygenation was also a necessary precursor of fire, a stabilizing factor for our O_2 -rich atmosphere, and an important nutrient recycling process unique in our solar system to Earth (Lenton, 2001). Understanding how the evolution of the Earth's atmosphere is tied to the planet's interior at the Archean Proterozoic transition will advance our understanding of the requirements for the habitability of exoplanets, and the development of complex life (Shahar et al., 2019).

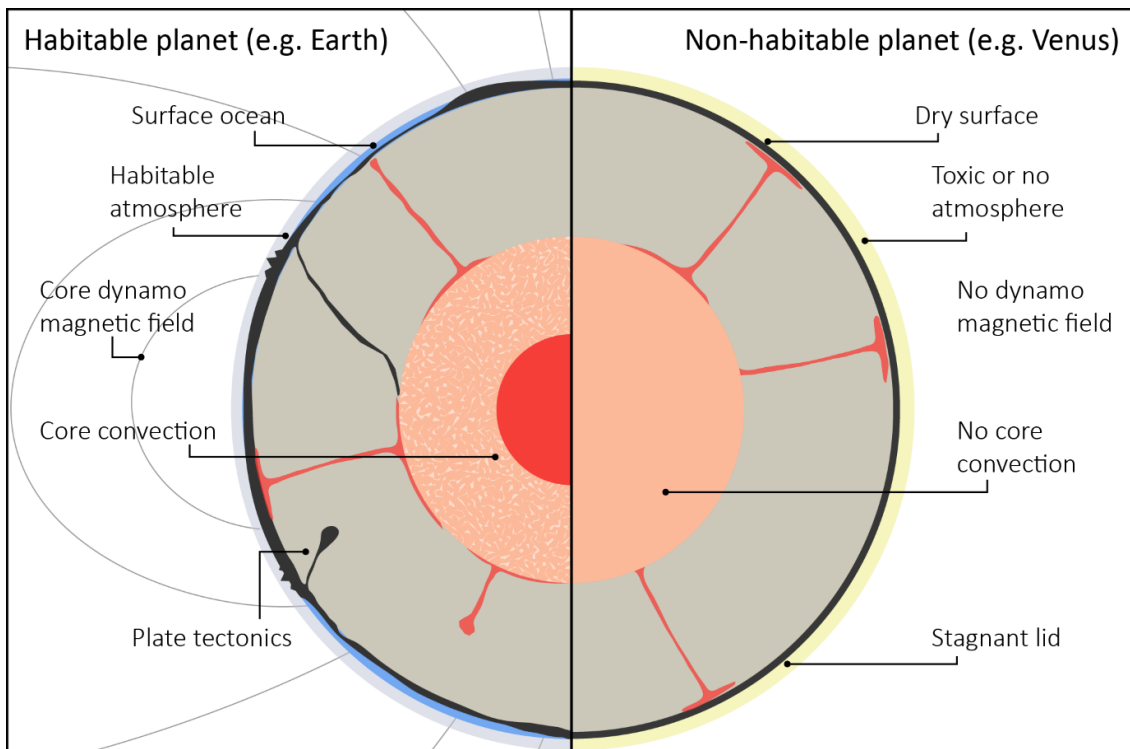


Figure 1.1. Characteristic features of long-term habitable and non-habitable planets (modified after Shahar et al., 2019). On the habitable planet (left) the interior maintains a stabilizing feedback between core, mantle, hydrosphere, and atmosphere that is important for long-term habitability (Foley and Driscoll, 2016). On the non-habitable planet (right) the stagnant lid insulates the planet's interior, preventing dynamo action (conversion

of mechanical into electrical energy) to generate a magnetic field, and leading to water loss into space, extreme surface temperatures (Nimmo, 2002; Phillips et al., 2001), and hence, an environment that is hostile to life.

1.2 The Archean Proterozoic Transition

The Archean Proterozoic transition marks a time in Earth history of fundamental geologic, climatic, and biologic upheavals (Condie, 2018; Kirschvink et al., 2000; Kopp et al., 2005), some of which permanently changed the surface environment of our planet (Figure 1.2). Among these events is a marked emergence of continental crust above sea-level (Bindeman et al., 2018; Kump and Barley, 2007), concomitant with a change in global zircon oxygen isotope ratio (Valley et al., 2005), the first recorded widespread, potentially global, glaciations (Rasmussen et al., 2013), and the oxygenation of the Earth atmosphere (Gumsley et al., 2017; Luo et al., 2016). Unravelling the causes and interplay of these events remains a major scientific challenge.



Figure 1.2. Artist's impression of the early Earth covered by a global ocean (left; image credit: Sci-News.com), and the Earth today with large subaerial continents (right; photo taken on September 4, 2019; image credit: NASA Earth Observatory/Joshua Stevens, NOAA National Environmental Satellite, Data, and Information Service.

The oxygenation of the Earth's atmosphere and oceans is arguably one of the most important things to ever happen on this planet to provide the base for the development of complex life

(Catling et al., 2005). At \sim 2.3 Ga atmospheric oxygen levels rose from negligible levels (<0.001% of the present atmospheric oxygen level; PAL; Pavlov and Kasting, 2002) to 10-40% PAL (Kump, 2008), or perhaps much higher approaching 100% PAL (Bekker and Holland, 2012; Harada et al., 2015; Lyons et al., 2014). The rise of atmospheric oxygen could easily be explained if oxygenic photosynthesis had evolved at that time (Fischer et al., 2016). However, the timing of the invention of oxygenic photosynthesis remains a matter of debate with suggestions ranging from >3.7 Ga (Rosing and Frei, 2004) to immediately preceding atmospheric oxygenation (Ward et al., 2016). Consequently, the mechanism that led to atmospheric oxygenation is controversial (Gaillard et al., 2011; Holland, 2002; Ward et al., 2016). Proposed scenarios for planetary oxygenation include: 1) an increase in O_2 production (i.e. through the invention of oxygenic photosynthesis) (Fischer et al., 2016; Ward et al., 2016), 2) a decrease in O_2 consumption (e.g. through changing redox state of volcanic gases, increased burial of organic carbon, or decreased pyrite weathering) (Bekker and Holland, 2012; Holland, 2002), and 3) a combination of both processes (through enhanced oxygenic photosynthesis combined with increased carbon burial) (Campbell and Allen, 2008). Following the rise of atmospheric oxygen the planet entered a period of severe, potentially global glaciations (Makganyene glaciation) (Warke et al., 2020) which may have been triggered by the decrease in atmospheric greenhouse gases associated with atmospheric oxygenation (Kopp et al., 2005),

Coeval with atmospheric oxygenation, the average zircon oxygen isotope ratio (expressed as $\delta^{18}O$, the deviation in the isotope ratio $^{18}O/^{16}O$ in permil relative to average seawater; VSMOW) increased (Spencer et al., 2019; Valley et al., 2005). The oxygen isotope ratio of zircon is a sensitive tracer of the incorporation of supracrustal material into felsic magmas as it reflects incorporation of material from the near surface environment where oxygen isotope fractionation is large. Igneous zircon in high-temperature equilibrium with the mantle has homogenous $\delta^{18}O$ values which average $5.3 \pm 0.6\text{‰}$ (Page et al., 2007). In contrast, supracrustal material has a wide range of $\delta^{18}O$ values ($\sim 0\text{--}40\text{‰}$) with most reservoirs being elevated in $\delta^{18}O$ relative to the mantle (Eiler, 2001). Hence, assimilation of supracrustal material generally results in magmatic zircon with $\delta^{18}O$ higher than that in equilibrium with primitive mantle magmas. Potential drivers for the Paleoproterozoic rise in average zircon $\delta^{18}O$ are changes in the

composition of supracrustal material and its availability for recycling or increased crustal reworking (Figure 1.3). One way to generate higher $\delta^{18}\text{O}$ felsic magmas is through enhanced assimilation of crustal material (Kirkland et al., 2010; Spencer et al., 2014) driven by a change in the geodynamic regime (i.e., the onset subduction-driven plate tectonics) at the Archean-Proterozoic transition (Condie, 2018; O'Neill et al., 2016). The timing of the onset of a modern plate tectonic regime with subduction-driven collisional tectonics is highly controversial with estimates ranging from Hadean (Hopkins et al., 2008) to Neoproterozoic (Stern, 2005). Importantly to note when considering this hypothesis, the ~ 2.35 Ga rise in average zircon $\delta^{18}\text{O}$ (Spencer et al., 2019) predates the $\sim 1.9\text{--}1.8$ Ga assembly of Earth's first widely accepted supercontinent Nuna (Bleeker, 2003). Also, the evolution of ϵ_{Hf} (deviation of $^{176}\text{Hf}/^{177}\text{Hf}$ in parts per 10,000 from that of CHUR; chondritic uniform reservoir) shows no correlation with zircon $\delta^{18}\text{O}$ (Spencer et al., 2019), indicating that enhanced crustal reworking alone cannot account for the shift in the oxygen isotope composition. Alternatively, changes in the oxygen isotope composition of recycled material (Payne et al., 2015; Valley et al., 2005) could have led to the increase in average zircon $\delta^{18}\text{O}$ without requiring more efficient recycling. Such a compositional change of supracrustal material could be related to the Paleoproterozoic emergence of continents above sea-level and concomitant changes in subaerial continental weathering pattern (Bindeman et al., 2018; Spencer et al., 2019).

Geochemical evidence and numerical models suggest that until the end of the Archean eon the subaerial exposure of continents was limited (Flament et al., 2013; Johnson and Wing, 2020), whereas presently, approximately 30% of the Earth's surface area is subaerial. Accordingly, continental flood basalts that erupted in submarine environments are common in the Archean and Paleoproterozoic, but rare to absent in the Phanerozoic (Arndt, 1999; Kump and Barley, 2007). Multiple lines of evidence support a widespread emergence of continents above sea-level at the Archean Proterozoic transition (Figure 1.4); including an increase in seawater $^{87}\text{Sr}/^{86}\text{Sr}$ ratio between 2.7 and 2.4 Ga (recorded by marine carbonate rocks) implying increasing continental influence on ocean chemistry through crustal erosive runoff (Flament et al., 2013; Shields and Veizer, 2002), a 2.43-2.32 Ga change in oxygen isotopic signatures in shales due to the onset of a modern hydrological cycle over large subaerial landmasses (Bindeman et al.,

2018), and the above mentioned ~ 2.35 Ga increase in average $\delta^{18}\text{O}$ of sediment-derived melts induced by enhanced subaerial weathering of exposed continents (Spencer et al., 2019).

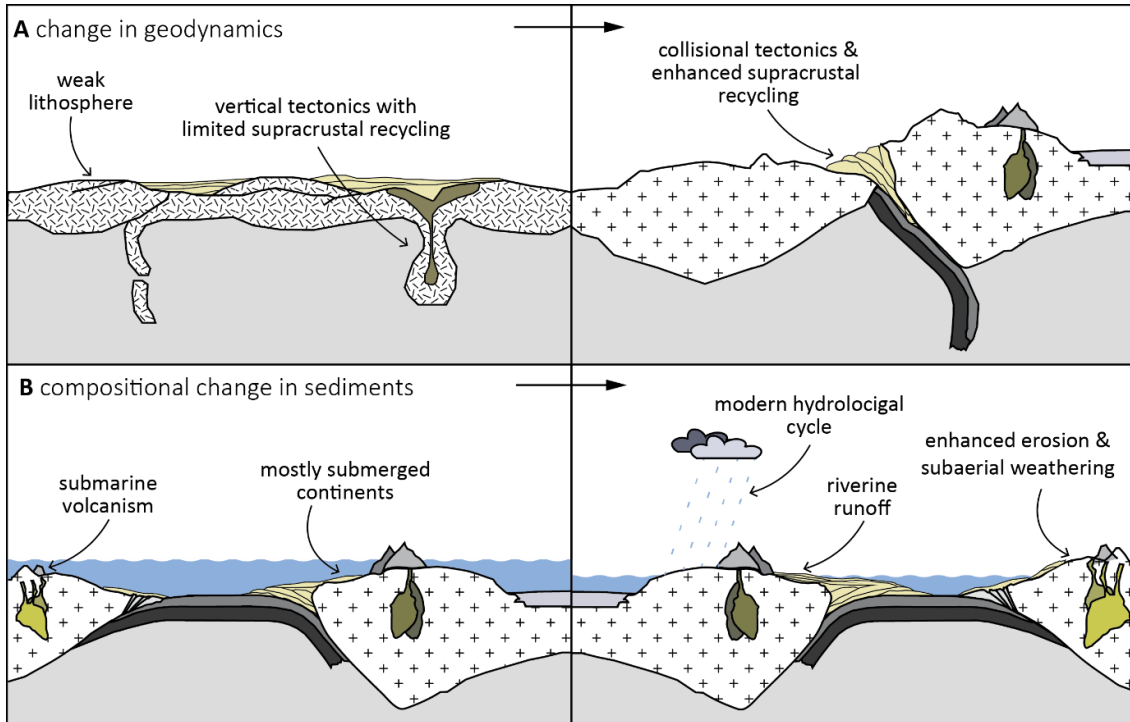


Figure 1.3. Schematic illustration of two contrasting models proposed to explain oxygen isotopic changes in felsic magmas (recorded by zircon $\delta^{18}\text{O}$) at the Archean-Proterozoic transition (Valley et al., 2005); **(A)** including enhanced recycling of supracrustal material (Kirkland et al., 2010; Spencer et al., 2014) driven by a change in the geodynamic regime (i.e., the onset subduction-driven plate tectonics) at the Archean-Proterozoic transition (Condie, 2018; O'Neill et al., 2016), **(B)** or a change in the oxygen isotope composition of recycled material (Payne et al., 2015) perhaps associated with the emergence of continents above sea-level (Kump and Barley, 2007), and concomitant enhanced subaerial erosion and weathering, and the onset of a modern hydrological cycle (Bindeman et al., 2018).

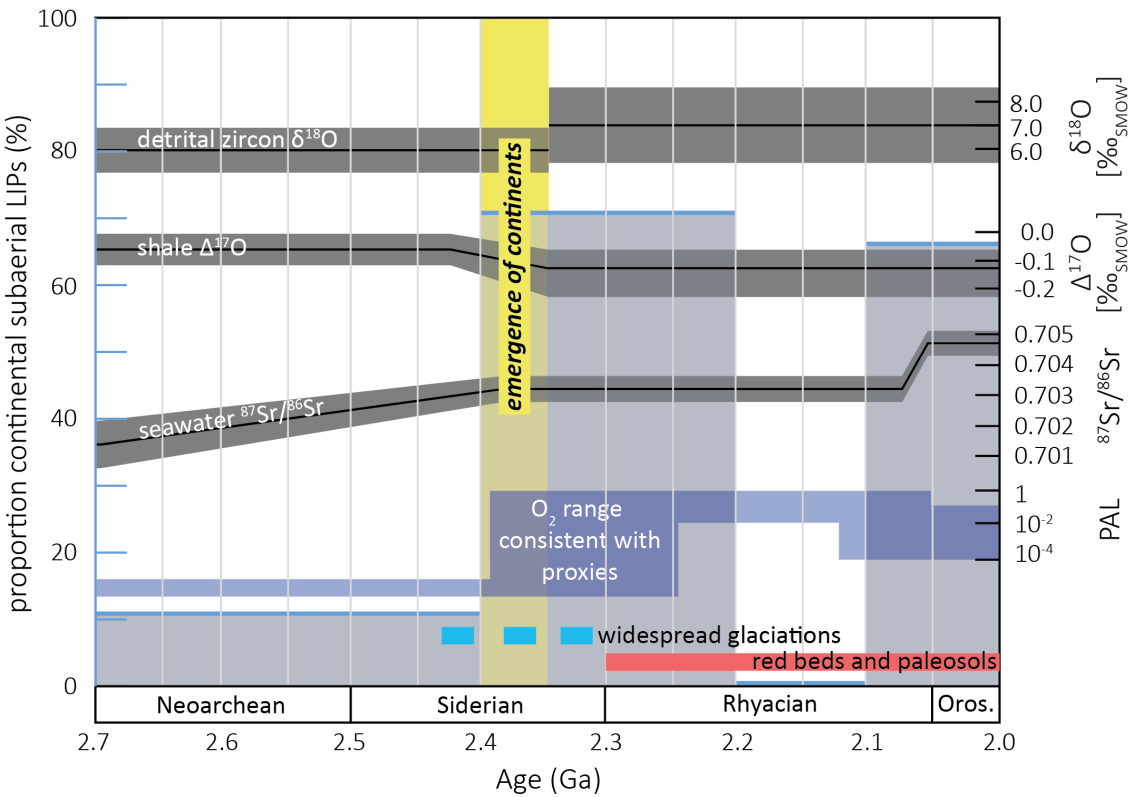


Figure 1.4. Temporal correlation of continental emergence, a rise of atmospheric oxygen, changes in geochemical proxies, and other secular changes at the Archean-Proterozoic transition. The widespread emergence of continents (yellow bar) as inferred from the continental large igneous province record (see Chapter 3) is coeval with an increase in atmospheric oxygen (blue curve), changes in geochemical proxies (i.e. detrital zircon $\delta^{18}\text{O}$, shale $\Delta^{17}\text{O}$, seawater $^{87}\text{Sr}/^{86}\text{Sr}$), widespread, potentially global glaciations (Rasmussen et al., 2013), and the first occurrence of red beds and paleosols (Beukes et al., 2002; Rainbird et al., 1990). The range of O_2 -level consistent with proxies is given in the present atmospheric level (PAL) after Lyons et al. (2014). Oxygen isotope data of detrital zircon is from Spencer et al. (2019) and shown as average with 1σ envelope. Oxygen isotope data of shale (expressed as $\Delta^{17}\text{O}$; defined as $\delta^{17}\text{O} - 0.5305 * \delta^{18}\text{O}$) is from Bindeman et al. (2018) and shown as average with 1σ envelope. The evolution of seawater $^{87}\text{Sr}/^{86}\text{Sr}$ is modelled using carbonate Sr isotope data from Kuznetsov et al. (2010), and Shields and Veizer (2002), and shown with 2σ envelope (see Chapter 3 for details).

1.3 Research Objectives & Sample Context

The objective of the work presented in this thesis is to elucidate the interplay of the evolution of the lithosphere, atmosphere, and biosphere at the Archean-Proterozoic transition. To unravel the temporal and causal relationship of global processes, such as the oxygenation of the

atmosphere, and the emergence of continents above sea-level, a global sample set was studied for this research (Figure 1.5). Samples for the work of this thesis are sediment-derived granitoids from various cratons or cratonic blocks, including the North China Craton, West African Craton, East European Craton, Superior Craton, and the Yavapai province. The magmatic crystallization ages of the granitoids studied here range from Neoarchean to Mesoproterozoic. Understanding the link between processes governing the Earth's surface environment and deep crust not only has implications for the history of our planet, but also the evolution of other habitable planets. Specifically, this research aims to:

- 1) Constrain the timing of the subaerial emergence of continents by combining geochemical proxies (e.g. O isotopes of sediment-derived magmatic zircon) with the geologic record (e.g. the continental large igneous province record).
- 2) Test the hypothesis of the coevolution of lithosphere, biosphere, and atmosphere by combining proxies for crustal recycling (i.e. zircon O, and Hf isotopic signatures, garnet O isotopic signatures, and bulk rock trace element signatures), continental freeboard (i.e. zircon, garnet, and shale O, and carbonate Sr isotopic signatures), and atmospheric oxygen level (i.e. pyrite S isotopic signatures).
- 3) Evaluate the extent to which geochemical proxies used to evaluate Earth evolution reflect primary magmatic signatures that can be temporally correlated. Specifically, how does the incorporation of water into radiation-damaged zircon affect the recorded oxygen isotope ratio?

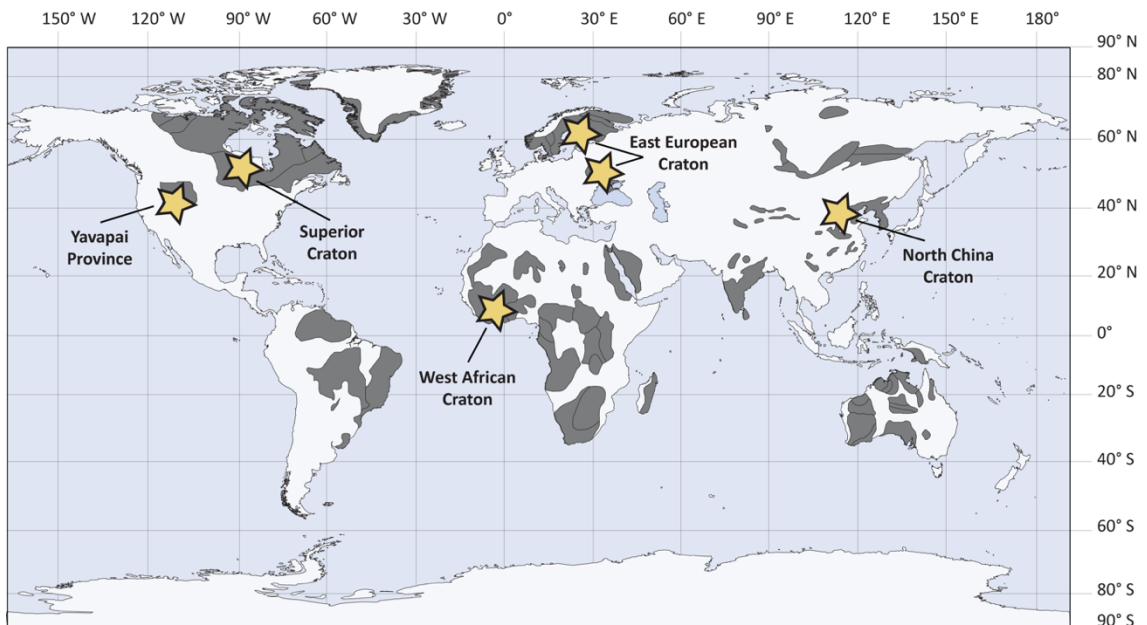


Figure 1.5. Map showing the exposure of Precambrian crust (dark grey areas) after Goldfarb et al. (2001). Sample locations are indicated by stars.

1.4 Thesis structure

This thesis is presented as a series of manuscripts submitted to peer-reviewed journals using complementary approaches to investigate a potential link between the emergence of continents above sea-level and Paleoproterozoic atmospheric oxygenation. The text and figures of works submitted for publication in peer-reviewed journals (Chapters 2-5) are reproduced in full but have been reformatted for consistency in the thesis.

Chapter 2. Emergence of continents above sea-level influences composition of sediment melts presents time-constrained oxygen, hafnium and trace element signatures in granitoids that track the incorporation of sediments into magmas across the Archean-Proterozoic boundary. The results of this study imply that Paleoproterozoic secular change in the oxygen isotope composition of global sediment melts (recorded by zircon $\delta^{18}\text{O}$) is caused by the widespread emergence of continents above sea-level.

Chapter 3. Large igneous provinces track 2.4 Ga subaerial emergence of continents investigates the continental large igneous province record across the Archean-Proterozoic transition. The eruptive emplacement environment (subaerial vs. submarine) of continental large igneous provinces tracks fluctuations in the emergent land area. The evaluation of the large igneous province record presented in this chapter unravels distinct time intervals of diminished or enhanced subaerial continental large igneous province volcanism between 2.7 to 2.0 Ga. The results of this study support a 2.4 Ga emergence of continents above sea-level in accord with geochemical proxies (e.g. the oxygen isotope record, as discussed in chapter 2), the sedimentary record, and numerical models.

Chapter 4. Coupling of the atmosphere and sediment melts across the Archean-Proterozoic transition presents triple sulfur and oxygen isotopic signatures in Archean and Proterozoic sediment-derived granitoids. The coupled evolution of sulfur and oxygen isotopic signatures presented in this chapter supports a temporal, and potentially causal link of subaerial continental emergence and atmospheric oxygenation.

Chapter 5. Effect of water on $\delta^{18}\text{O}$ in zircon constitutes a study on variations in the oxygen isotope ratio related to water uptake in natural zircon. Zircon preserves one of the most reliable records of the primary magmatic oxygen isotope signature and is the prime U-Pb geochronometer (Valley et al., 2003). Therefore, time-constrained zircon oxygen isotope geochemistry has found widespread usage in a variety of geologic studies, e.g. on the evolution of geodynamics and freeboard (e.g. as in chapter 2 and 4), and crustal growth. However, $\delta^{18}\text{O}$ values can be altered by the incorporation of water into radiation-damaged areas of zircon grains. This chapter examines the mechanisms responsible for water uptake in zircon, and their influence on the recorded $\delta^{18}\text{O}$ values. This chapter concludes with recommendations for the assessment of the potential disturbance of the zircon oxygen isotopic system through secondary processes.

Chapter 6. Conclusions: Models and questions concerning the emergence of continents above sea-level as a potential driver of atmospheric oxygenation summarize the

observations and conclusions of the various chapters, and their implications for planetary crustal evolution, and oxygenation of the Earth atmosphere. Furthermore, this chapter discusses how emergent land area may affect productivity and/or radiation of oxygenic phototrophs. This chapter concludes with a scrutiny of the limitations of our current data set and methodology, and highlights avenues for future work.

1.5 References

- Arndt, N., 1999. Why was flood volcanism on submerged continental platforms so common in the Precambrian? *Precambrian Res.* 97, 155–164. [https://doi.org/10.1016/S0301-9268\(99\)00030-3](https://doi.org/10.1016/S0301-9268(99)00030-3)
- Bekker, A., Holland, H.D., 2012. Oxygen overshoot and recovery during the early Paleoproterozoic. *Earth Planet. Sci. Lett.* 317–318, 295–304. <https://doi.org/10.1016/j.epsl.2011.12.012>
- Beukes, N.J., Dorland, H., Gutzmer, J., Nedachi, M., Ohmoto, H., 2002. Tropical laterites, life on land, and the history of atmospheric oxygen in the Paleoproterozoic. *Geology* 30, 491. [https://doi.org/10.1130/0091-7613\(2002\)030<0491:TLLOLA>2.0.CO;2](https://doi.org/10.1130/0091-7613(2002)030<0491:TLLOLA>2.0.CO;2)
- Bindeman, I.N., Zakharov, D.O., Palandri, J., Greber, N.D., Dauphas, N., Retallack, G.J., Hofmann, A., Lackey, J.S., Bekker, A., Data, E., 2018. Rapid emergence of subaerial landmasses and onset of a modern hydrologic cycle 2.5 billion years ago. *Nature* 557, 545–548. <https://doi.org/https://doi.org/10.1038/s41586-018-0131-1>
- Bleeker, W., 2003. The late Archean record: A puzzle in ca. 35 pieces. *Lithos* 71, 99–134. <https://doi.org/10.1016/j.lithos.2003.07.003>
- Borg, L., Drake, M.J., 2005. A review of meteorite evidence for the timing of magmatism and of surface or near-surface liquid water on Mars. *J. Geophys. Res.* 110, E12S03. <https://doi.org/10.1029/2005JE002402>
- Breuer, D., Spohn, T., 2003. Early plate tectonics versus single-plate tectonics on Mars: Evidence from magnetic field history and crust evolution. *J. Geophys. Res.* 108, 5072. <https://doi.org/10.1029/2002JE001999>
- Campbell, I.H., Allen, C.M., 2008. Formation of supercontinents linked to increases in atmospheric oxygen. *Nat. Geosci.* 1, 554–558. <https://doi.org/10.1038/ngeo259>
- Catling, D.C., Glein, C.R., Zahnle, K.J., McKay, C.P., 2005. Why O₂ Is Required by Complex Life on Habitable Planets and the Concept of Planetary “Oxygenation Time.” *Astrobiology* 5, 415–438. <https://doi.org/10.1089/ast.2005.5.415>
- Cockell, C.S., Bush, T., Bryce, C., Direito, S., Fox-Powell, M., Harrison, J.P., Lammer, H.,

- Landenmark, H., Martin-Torres, J., Nicholson, N., Noack, L., O’Malley-James, J., Payler, S.J., Rushby, A., Samuels, T., Schwendner, P., Wadsworth, J., Zorzano, M.P., 2016. Habitability: A Review. *Astrobiology* 16, 89–117. <https://doi.org/10.1089/ast.2015.1295>
- Condie, K.C., 2018. A planet in transition: The onset of plate tectonics on Earth between 3 and 2 Ga? *Geosci. Front.* 9, 51–60. <https://doi.org/10.1016/j.gsf.2016.09.001>
- Eiler, J.M., 2001. Oxygen Isotope Variations of Basaltic Lavas and Upper Mantle Rocks, in: Valley, J.W., Cole, D.R. (Eds.), *Stable Isotope Geochemistry. Reviews in Mineralogy and Geochemistry*. Mineralogical Society of America/Geochemical Society, Washington, DC, pp. 319–364.
- Fischer, W.W., Hemp, J., Johnson, J.E., 2016. Evolution of Oxygenic Photosynthesis. *Annu. Rev. Earth Planet. Sci.* 44, 647–683. <https://doi.org/10.1146/annurev-earth-060313-054810>
- Flament, N., Coltice, N., Rey, P.F., 2013. The evolution of the $^{87}\text{Sr}/^{86}\text{Sr}$ of marine carbonates does not constrain continental growth. *Precambrian Res.* 229, 177–188. <https://doi.org/10.1016/j.precamres.2011.10.009>
- Foley, B.J., Driscoll, P.E., 2016. Whole planet coupling between climate, mantle, and core: Implications for rocky planet evolution. *Geochemistry, Geophys. Geosystems* 17, 1885–1914. <https://doi.org/10.1002/2015GC006210>
- Gaillard, F., Scaillet, B., Arndt, N.T., 2011. Atmospheric oxygenation caused by a change in volcanic degassing pressure. *Nature* 478, 229–232. <https://doi.org/10.1038/nature10460>
- Goldfarb, R., Groves, D., Gardoll, S., 2001. Orogenic gold and geologic time: a global synthesis. *Ore Geol. Rev.* 18, 1–75. [https://doi.org/10.1016/S0169-1368\(01\)00016-6](https://doi.org/10.1016/S0169-1368(01)00016-6)
- Gumsley, A.P., Chamberlain, K.R., Bleeker, W., Söderlund, U., de Kock, M.O., Larsson, E.R., Bekker, A., 2017. Timing and tempo of the Great Oxidation Event. *Proc. Natl. Acad. Sci.* 114, 1811–1816. <https://doi.org/10.1073/pnas.1608824114>
- Harada, M., Tajika, E., Sekine, Y., 2015. Transition to an oxygen-rich atmosphere with an extensive overshoot triggered by the Paleoproterozoic snowball Earth. *Earth Planet. Sci. Lett.* 419, 178–186. <https://doi.org/10.1016/j.epsl.2015.03.005>
- Holland, H.D., 2002. Volcanic gases, black smokers, and the great oxidation event. *Geochim. Cosmochim. Acta* 66, 3811–3826. [https://doi.org/10.1016/S0016-7037\(02\)00950-X](https://doi.org/10.1016/S0016-7037(02)00950-X)
- Hopkins, M., Harrison, T.M., Manning, C.E., 2008. Low heat flow inferred from >4 Gyr zircons suggests Hadean plate boundary interactions. *Nature* 456, 493–496. <https://doi.org/10.1038/nature07465>
- Johnson, B.W., Wing, B.A., 2020. Limited Archaean continental emergence reflected in an early Archaean ^{18}O -enriched ocean. *Nat. Geosci.* 13, 243–248. <https://doi.org/10.1038/s41561-020-0538-9>

- Kasting, J.F., Whitmire, D.P., Reynolds, R.T., 1993. Habitable Zones around Main Sequence Stars. *Icarus* 101, 108–128. <https://doi.org/10.1006/icar.1993.1010>
- Kirkland, C.L., Whitehouse, M.J., Pease, V., Van Kranendonk, M., 2010. Oxygen isotopes in detrital zircons: Insight into crustal recycling during the evolution of the Greenland Shield. *Lithosphere* 2, 3–12. <https://doi.org/10.1130/L80.1>
- Kirschvink, J.L., Gaidos, E.J., Bertani, L.E., Beukes, N.J., Gutzmer, J., Maepa, L.N., Steinberger, R.E., 2000. Paleoproterozoic snowball earth: extreme climatic and geochemical global change and its biological consequences. *Proc. Natl. Acad. Sci. U. S. A.* 97, 1400–1405. <https://doi.org/10.1073/pnas.97.4.1400>
- Kopp, R.E., Kirschvink, J.L., Hilburn, I.A., Nash, C.Z., 2005. The Paleoproterozoic snowball Earth: A climate disaster triggered by the evolution of oxygenic photosynthesis. *Proc. Natl. Acad. Sci.* 102, 11131–11136. <https://doi.org/10.1073/pnas.0504878102>
- Kump, L.R., 2008. The rise of atmospheric oxygen. *Nature* 451, 277–278. <https://doi.org/10.1038/nature06587>
- Kump, L.R., Barley, M.E., 2007. Increased subaerial volcanism and the rise of atmospheric oxygen 2.5 billion years ago. *Nature* 448, 1033–1036. <https://doi.org/10.1038/nature06058>
- Kuznetsov, A.B., Melezhik, V.A., Gorokhov, I.M., Melnikov, N.N., Konstantinova, G.V., Kutyavin, E.P., Turchenko, T.L., 2010. Sr isotopic composition of Paleoproterozoic 13C-rich carbonate rocks: The Tulomozero Formation, SE Fennoscandian Shield. *Precambrian Res.* 182, 300–312. <https://doi.org/10.1016/j.precamres.2010.05.006>
- Lenton, T.M., 2001. The role of land plants, phosphorus weathering and fire in the rise and regulation of atmospheric oxygen. *Glob. Chang. Biol.* 7, 613–629. <https://doi.org/10.1046/j.1354-1013.2001.00429.x>
- Luo, G., Ono, S., Beukes, N.J., Wang, D.T., Xie, S., Summons, R.E., 2016. Rapid oxygenation of Earth's atmosphere 2.33 billion years ago. *Sci. Adv.* 2. <https://doi.org/10.1126/sciadv.1600134>
- Lyons, T.W., Reinhard, C.T., Planavsky, N.J., 2014. The rise of oxygen in Earth's early ocean and atmosphere. *Nature* 506, 307–315. <https://doi.org/10.1038/nature13068>
- Nimmo, F., 2002. Why does Venus lack a magnetic field? *Geology* 30, 987. [https://doi.org/10.1130/0091-7613\(2002\)030<0987:WDVLAM>2.0.CO;2](https://doi.org/10.1130/0091-7613(2002)030<0987:WDVLAM>2.0.CO;2)
- O'Neill, C., Lenardic, A., Weller, M., Moresi, L., Quenette, S., Zhang, S., 2016. A window for plate tectonics in terrestrial planet evolution? *Phys. Earth Planet. Inter.* 255, 80–92. <https://doi.org/10.1016/j.pepi.2016.04.002>
- Olson, P., Christensen, U.R., 2006. Dipole moment scaling for convection-driven planetary dynamos. *Earth Planet. Sci. Lett.* 250, 561–571.

<https://doi.org/10.1016/j.epsl.2006.08.008>

- Page, F.Z., Fu, B., Kita, N.T., Fournelle, J., Spicuzza, M.J., Schulze, D.J., Viljoen, F., Basei, M.A.S., Valley, J.W., 2007. Zircons from kimberlite: New insights from oxygen isotopes, trace elements, and Ti in zircon thermometry. *Geochim. Cosmochim. Acta* 71, 3887–3903. <https://doi.org/10.1016/j.gca.2007.04.031>
- Pavlov, A.A., Kasting, J.F., 2002. Mass-Independent Fractionation of Sulfur-Isotopes in Archean Sediments: Strong Evidence for an Anoxic Archean Atmosphere. *Astrobiology* 2.
- Payne, J.L., Hand, M., Pearson, N.J., Barovich, K.M., Mcinerney, D.J., 2015. Crustal thickening and clay: Controls on O isotope variation in global magmatism and siliciclastic sedimentary rocks. *Earth Planet. Sci. Lett.* 412, 70–76. <https://doi.org/10.1016/j.epsl.2014.12.037>
- Phillips, R.J., Bullock, M.A., Hauck, S.A., 2001. Climate and interior coupled evolution on Venus. *Geophys. Res. Lett.* 28, 1779–1782. <https://doi.org/10.1029/2000GL011821>
- Rainbird, R.H., Nesbitt, H.W., Donaldson, J.A., 1990. Formation and Diagenesis of a Sub-Huronian Saprolith: Comparison with a Modern Weathering Profile. *J. Geol.* 98, 801–822. <https://doi.org/10.1086/629455>
- Rasmussen, B., Bekker, A., Fletcher, I.R., 2013. Correlation of Paleoproterozoic glaciations based on U–Pb zircon ages for tuff beds in the Transvaal and Huronian Supergroups. *Earth Planet. Sci. Lett.* 382, 173–180. <https://doi.org/10.1016/j.epsl.2013.08.037>
- Rosing, M.T., Frei, R., 2004. U-rich Archaean sea-floor sediments from Greenland – indications of >3700 Ma oxygenic photosynthesis. *Earth Planet. Sci. Lett.* 217, 237–244. [https://doi.org/10.1016/S0012-821X\(03\)00609-5](https://doi.org/10.1016/S0012-821X(03)00609-5)
- Seager, S., 2013. Exoplanet Habitability. *Science* (80-.). 340, 577–581. <https://doi.org/10.1126/science.1232226>
- Shahar, A., Driscoll, P., Weinberger, A., Cody, G., 2019. What makes a planet habitable? *Science* (80-.). 364, 434–435. <https://doi.org/10.1126/science.aaw4326>
- Shields, G., Veizer, J., 2002. Precambrian marine carbonate isotope database: Version 1.1. *Geochemistry Geophys. Geosystems* 3. <https://doi.org/10.1029/2001GC000266>
- Spencer, C.J., Cawood, P.A., Hawkesworth, C.J., Raub, T.D., Prave, A.R., Roberts, N.M.W., 2014. Proterozoic onset of crustal reworking and collisional tectonics: Reappraisal of the zircon oxygen isotope record. *Geology* 42, 451–454. <https://doi.org/10.1130/G35363.1>
- Spencer, C.J., Partin, C.A., Kirkland, C.L., Raub, T.D., Liebmann, J., Stern, R.A., 2019. Paleoproterozoic increase in zircon $\delta^{18}\text{O}$ driven by rapid emergence of continental crust. *Geochim. Cosmochim. Acta* 257, 16–25. <https://doi.org/10.1016/j.gca.2019.04.016>

- Stern, R.J., 2005. Evidence from ophiolites, blueschists, and ultrahigh-pressure metamorphic terranes that the modern episode of subduction tectonics began in Neoproterozoic time. *Geology* 33, 557–560. <https://doi.org/10.1130/G21365.1>
- Valley, J.W., Bindeman, I.N., Peck, W.H., 2003. Empirical calibration of oxygen isotope fractionation in zircon. *Geochim. Cosmochim. Acta* 67, 3257–3266. [https://doi.org/10.1016/S0016-7037\(03\)00090-5](https://doi.org/10.1016/S0016-7037(03)00090-5)
- Valley, J.W., Lackey, J.S., Cavosie, A.J., Clechenko, C.C., Spicuzza, M.J., Basei, M.A.S., Bindeman, I.N., Ferreira, V.P., Sial, A.N., King, E.M., Peck, W.H., Sinha, A.K., Wei, C.S., 2005. 4.4 billion years of crustal maturation: Oxygen isotope ratios of magmatic zircon. *Contrib. to Mineral. Petrol.* 150, 561–580. <https://doi.org/10.1007/s00410-005-0025-8>
- Walker, J.C.G., Hays, P.B., Kasting, J.F., 1981. A negative feedback mechanism for the long-term stabilization of Earth's surface temperature. *J. Geophys. Res.* 86, 9776. <https://doi.org/10.1029/JC086iC10p09776>
- Ward, L.M., Kirschvink, J.L., Fischer, W.W., 2016. Timescales of Oxygenation Following the Evolution of Oxygenic Photosynthesis. *Orig. Life Evol. Biosph.* 46, 51–65. <https://doi.org/10.1007/s11084-015-9460-3>
- Warke, M.R., Di Rocco, T., Zerkle, A.L., Lepland, A., Prave, A.R., Martin, A.P., Ueno, Y., Condon, D.J., Claire, M.W., 2020. The Great Oxidation Event preceded a Paleoproterozoic “snowball Earth.” *Proc. Natl. Acad. Sci.* 202003090. <https://doi.org/10.1073/pnas.2003090117>
- Westall, F., Loizeau, D., Foucher, F., Bost, N., Betrand, M., Vago, J., Kmínek, G., 2013. Habitability on Mars from a Microbial Point of View. *Astrobiology* 13, 887–897. <https://doi.org/10.1089/ast.2013.1000>

EMERGENCE OF CONTINENTS ABOVE SEA-LEVEL INFLUENCES
COMPOSITION OF SEDIMENT MELTS

This chapter is submitted for publication as:

Liebmann, J., Spencer, C.J., Kirkland, C.K., Bucholz, C.E., He, X., Santosh, M., Xia, X.P., Martin, L., Evans, N. J. Emergence of continents above sea-level influences composition of sediment melts. *Submitted to Terra Nova.*

Abstract

The Archean-Proterozoic transition heralded a number of fundamental changes on Earth, including; the oxygenation of the atmosphere, a marked emergence of continents above sea-level, and an increase in $\delta^{18}\text{O}$ of felsic magmas. The potential drivers for the latter are changes in the composition of supracrustal material, or increased crustal reworking. Although the onset of subduction-induced continental collision and associated enhanced crustal recycling could produce high- $\delta^{18}\text{O}$ felsic magmas, temporally constrained zircon $\delta^{18}\text{O}$ reveals an increase in $\delta^{18}\text{O}$ at ~ 2.35 Ga that predates the oldest widely recognized supercontinent. In this work, we use the O and Hf isotope ratios of magmatic zircon crystals in Archean and Proterozoic sediment-derived granitoids of the North China Craton to track the incorporation of supracrustal material into magmas. The results are consistent with an increase of continental freeboard at ~ 2.35 Ga producing sedimentary reservoirs with comparatively elevated $\delta^{18}\text{O}$ that subsequently partially melted to generate the granitoids.

2.1 Introduction

In the past two decades, a number of works have discussed the secular evolution of oxygen isotopes in zircon (Valley et al., 2005; Kirkland et al., 2010; Roberts and Spencer, 2015). The oxygen isotope ratios ($^{18}\text{O}/^{16}\text{O}$) of a melt is sensitive to the incorporation of supracrustal material (Valley et al., 1994). Zircon preserves the most robust record of the oxygen isotopic composition of its parental magma due to its slow oxygen diffusion rate (Valley et al., 1994). Igneous zircon in high-temperature equilibrium with mantle has homogenous $\delta^{18}\text{O}$ values averaging $5.3 \pm 0.6\text{\textperthousand}$ (Page et al., 2007) relative to standard mean ocean water (VSMOW). Supracrustal material, in contrast, has a wide range of $\delta^{18}\text{O}$ values with most reservoirs being elevated in $\delta^{18}\text{O}$ relative to the mantle (Eiler, 2001). Hence, assimilation of supracrustal material generally results in magmatic zircon with $\delta^{18}\text{O}$ higher than that in equilibrium with the mantle. Igneous rocks that assimilated supracrustal material are known to exist since at least the Mesoarchean (e.g. Sylvester, 1994; Valley et al., 2005; Marschall et al., 2010; Bucholz and Spencer, 2019). Archean zircon has uniform $\delta^{18}\text{O}$ values averaging $5.8 \pm 1.0\text{\textperthousand}$ (1σ , $n=2,644$), whereas post-Archean zircon $\delta^{18}\text{O}$ is more variable and on average higher ($6.8 \pm 1.8\text{\textperthousand}$; 1σ , $n=13,314$) (Valley et al., 2005; Spencer et al., 2014). Statistical change-point analysis of 2.8-1.9 Ga detrital zircon data ($n=452$) suggest that the initial rise in average zircon $\delta^{18}\text{O}$ occurred at ~ 2.35 Ga (Spencer et al., 2019). One way to achieve higher $\delta^{18}\text{O}$ felsic magmas is through enhanced assimilation of supracrustal material (Kirkland et al., 2010; Spencer et al., 2014) driven by a change in the geodynamic regime (i.e. the onset of subduction-driven collisional tectonics) at the Archean-Proterozoic transition (O'Neill et al., 2016; Condie, 2018). Importantly however, the initial rise in average zircon $\delta^{18}\text{O}$ predates the ~ 1.9 -1.8 Ga assembly of Earth's first widely accepted supercontinent Nuna (Bleeker, 2003). Instead, the rise in average zircon $\delta^{18}\text{O}$ occurred in a period characterized by a global lull in tectono-magmatic activity (Condie et al., 2009; Spencer et al., 2018). Alternatively, increased $\delta^{18}\text{O}$ of recycled material (Valley et al., 2005; Payne et al., 2015) could have driven the increase in average zircon $\delta^{18}\text{O}$ without requiring more efficient recycling. The ~ 2.35 Ga shift in average zircon $\delta^{18}\text{O}$ is coincidental with the oxygenation of the Earth's atmosphere (Great Oxygenation Event; GOE) (Luo et al., 2016;

Gumsley et al., 2017) and an increase in continental freeboard (the average elevation of continental crust above sea-level) (Flament et al., 2013; Hollis et al., 2014) that is proposed to have led to a shift in the triple-oxygen isotope composition of shales (Bindeman et al., 2018).

A model involving crustal reworking has been invoked to explain the rise of average zircon $\delta^{18}\text{O}$ at ~ 2.35 Ga (Spencer et al., 2019). However, this explanation is based on detrital zircon that provides only limited information on the original source-rock given the inherent lack of contextual information, which may only partly be accessible through zircon chemistry (Hawkesworth and Kemp, 2006). In contrast, zircon from sediment-derived melts provide a clear link to the $\delta^{18}\text{O}$ of their sedimentary source-rocks. Existing bulk-rock and zircon $\delta^{18}\text{O}$ from sediment-derived granites show an on average increase across the Archean-Proterozoic transition (Bucholz and Spencer, 2019). However, the existing geochemical datasets for Precambrian sediment-derived granitoids are limited in size, particularly, for the critical age span of 2.6–1.8 Ga. This study utilizes zircon oxygen and hafnium isotope geochemistry, combined with bulk-rock trace element compositions of Archean to Paleoproterozoic sediment-derived granitoids of the North China Craton (NCC; Figure 2.1) to further characterize the zircon $\delta^{18}\text{O}$ record of sediment-derived melts across this critical transition in Earth history. Samples derive from 5 geologic units in an area extending 300 km E-W, and 80 km N-S (Table 2.1; Appendix A provides detailed sample context). The interpretation of isotopic signatures in igneous zircon in combination with protolith information allows a high fidelity in unravelling the impacts of potential tectonic and compositional drivers for the Paleoproterozoic increase in zircon $\delta^{18}\text{O}$.

2.2 Methods

Zircon was isolated using standard density and magnetic separation techniques. The resulting hand-picked zircon grains were mounted in epoxy. To reveal internal growth structures, cathodoluminescence (CL) images of zircon grains were taken using a Tescan MIRA3 field emission scanning electron microscope. Oxygen isotope analysis was conducted on a CAMECA IMS 1280 secondary ion mass spectrometer (SIMS). Oxygen isotope compositions are reported in the conventional delta notation; expressed as $\delta^{18}\text{O}$, the permil deviation of $^{18}\text{O}/^{16}\text{O}_{\text{sample}}$ relative to average sea water (VSMOW) (Baertschi, 1976). The reported zircon

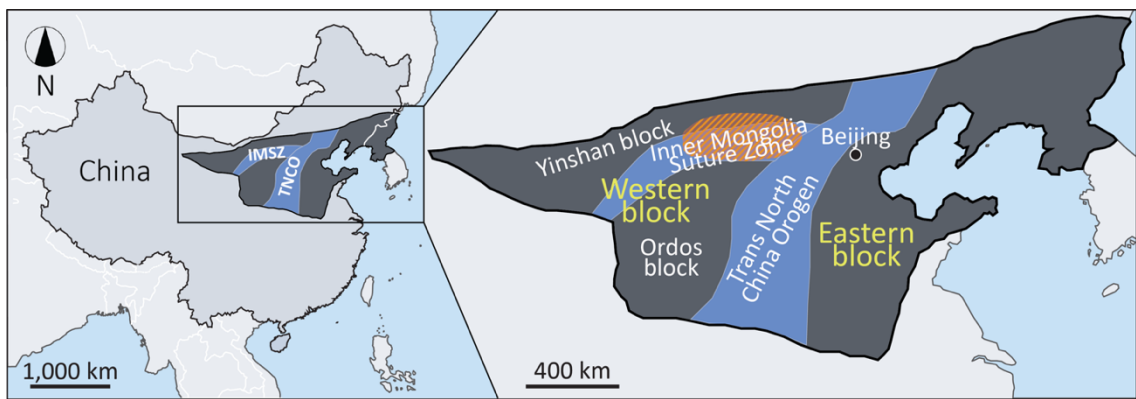


Figure 2.1. Simplified map of the North China Craton (shown in dark grey). Shaded area indicates area of sample collection. See Table 2.1 for GPS locations, and supplementary Figure A7 for a more detailed map.

$\delta^{18}\text{O}$ values for each sample are weighted means (weighted by uncertainty of individual analyses) quoted with 2σ uncertainty. Following analysis of oxygen isotopic composition, zircon U-Pb ages were obtained using an A.S.I. SHRIMP II sensitive high-resolution ion microprobe. Hafnium isotope analysis by laser ablation inductively coupled plasma mass spectrometry (LA-ICPMS) was conducted using a Resonetics RESOlution M50-A excimer laser coupled with a Nu Plasma II multi-collector ICP-MS. Unless indicated otherwise, spots of U-Pb, oxygen, and hafnium isotope analyses were located on the same zircon growth zone (Figure 2.2). To avoid signatures from inherited growth zones, only analyses located on magmatic rims of zircon grains were used to determine crystallization age, oxygen and hafnium isotopic composition of zircon in equilibrium with the melt.

Sample ID	Geologic unit	Latitude	Longitude	Rock type	Mineralogy	Age $\pm 2\sigma$ (Ma)	Zircon $\delta^{18}\text{O} \pm 2\sigma$	Zircon $\delta^{18}\text{O}$	n
					(‰SMOW)				
18IM11B	Jining Complex, IMSZ	40.604	112.500	Grt graniteoid	Pl+Alfs+Qz+Grt+Bt	1901 ± 17	10.80 ± 0.90 ¹		8
18IM12B	Jining Complex, IMSZ	40.839	112.565	Grt quartz rich graniteoid	Qz+Pl+Alfs+Grt	1929 ± 29	9.74 ± 1.16 ¹		18
18IM13C	Xiwulanbulang area, YB	41.084	110.924	Grt granite	Qz+Alfs+Pl+Grt+Bt(+Ms)	2536 ± 13	8.12 ± 0.70 ²		18
18IM14A	Daqingshan-Wulashan Complex, IMSZ	40.922	110.961	Grt granite	Qz+Alfs+Pl+Bt(+Grt)	1948 $\pm 2*$	4.65 ± 0.85 ²		17
18IM15B	Xiwulanbulang area, YB	40.994	110.947	Grt graniteoid	Qz+Pl+Alfs+Grt	2530 ± 60	8.75 ± 0.42 ²		11
18IM19	Daqingshan-Wulashan Complex, IMSZ	40.693	109.641	Grt granite	Alfs+Qz+Ph+Grt+Bt	2478 ± 18	7.21 ± 0.58 ²		35
18IM20	Daqingshan-Wulashan Complex, IMSZ	40.709	109.643	Grt graniteoid	Qz+Pl+Alfs+Grt+Bt	2374 $\pm 48*$	7.39 ± 0.70 ¹		17
18IM21C	Daqingshan-Wulashan Complex, IMSZ	40.698	109.721	Grt quartz rich granite	Qz+Alfs+Ph+Grt+Bt	1855 ± 16	6.71 ± 0.52 ¹		21
18IM23D	Daqingshan Wulashan Complex, IMSZ	40.811	110.238	Grt granite	Qz+Alfs+Pl+Grt	2453 ± 11	6.31 ± 0.63 ¹		13
18IM25C	Guyang area, YB	41.182	109.479	Mg Bt granite	Qz+Alfs+Pl+Ms(+Bt)	2493 ± 28	6.86 ± 0.89 ²		20
18IM3	Huanian Complex, TNCO	40.848	113.921	Grt granite	Qz+Alfs+Pl+Grt+Ms(+Bt)	1917 ± 70	11.41 ± 1.00 ¹		8

Table 2.1. Geologic unit, location, lithology, mineralogy, magmatic crystallization ages, and zircon $\delta^{18}\text{O}$ of samples studied here. Asterisks mark weighted mean ages calculated from the oldest statistical coherent population (see Appendix A for a detailed discussion of the U-Pb zircon geochronological data). Minerals are listed from most abundant to least. Minerals in parentheses are accessory phases. Zircon oxygen isotope analyses were conducted at ¹GIG and ²CIMA; n indicated number of single grain analyses per sample. Mineral abbreviations: Qtz, quartz; Alfs, alkali feldspar; Pl, plagioclase; Grt, garnet; Ms, muscovite, Bt, biotite.

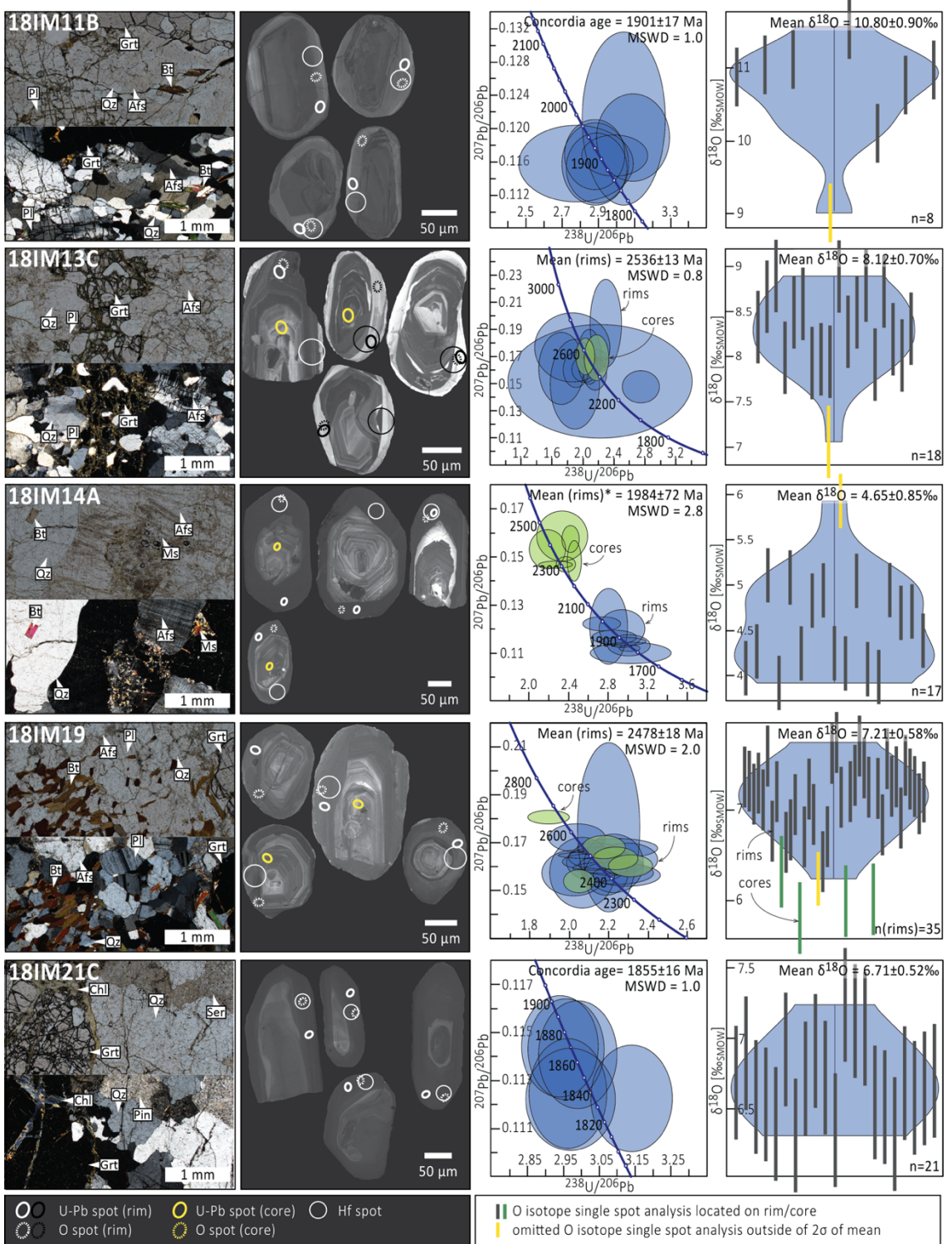


Figure 2.2. Thin section photomicrographs, CL images of representative zircon grains, concordia diagrams, and oxygen isotope violin plots of representative samples (see supplementary Figures A1-3 for complete sample

set). Spot locations of O, U-Pb, and Hf isotope analyses are marked in the CL images. Results of U-Pb analyses on zircon rims and cores are shown as blue and green ellipses, respectively, in concordia diagrams. Concordia ages, weighted mean ages, and weighted mean $\delta^{18}\text{O}$ are quoted with 2σ uncertainty. Quoted weighted mean ages are calculated from most concordant single spot $^{207}\text{Pb}/^{206}\text{Pb}^*$ ages. Weighted mean age marked with asterisk is calculated from the oldest statistical coherent population. See Appendix A for details of data analysis. Mineral abbreviations: Qz, quartz; Afs, alkali feldspar; Pl, plagioclase; Grt, garnet; Ms, muscovite; Bt, biotite; Ser, sericite; Chl, chlorite.

Bulk-rock major and trace element concentrations were determined using a Panalytical Zetium 4 kW X-ray fluorescence spectrometer (XRF). A detailed description of the methodology, and results for reference materials for SIMS, and LA-ICPMS analyses are provided in appendix A.

2.3 Results

Samples studied here include granitoids comprised of quartz, alkali feldspar, plagioclase, garnet, muscovite, and biotite in varying proportions. Magmatic crystallization ages of the granitoids range from 2536 ± 13 Ma to 1855 ± 10 Ma (Table 2.1). All samples are strongly peraluminous with an aluminium saturation index (ASI) ≥ 1.1 (defined as molar Al/[Ca-1.67P+Na+K]; Table 2.2) and contain at least one aluminous mineral, such as garnet or muscovite. Strongly peraluminous granitoids are generally interpreted to have formed through the partial melting of (meta-)sedimentary rocks (Chappell and White, 1992; Frost and Frost, 2008). Hence, both mineralogy and geochemistry of all samples support the derivation from sedimentary protoliths, in accord with previous petrogenetic interpretations (Zhao et al., 1999; Dan et al., 2012). All samples show Rb/Sr and Rb/Ba ratios below 1.5 and 0.5, respectively (Table 2.3). Samples with crystallization ages < 2.0 Ga show Rb/Ba ratios from 0.08 to 0.15 similar to those of samples > 2.3 Ga with Rb/Ba ratios of 0.03 to 0.07. The Rb/Sr ratios of both groups are indistinguishable and range from 0.03 to 1.4 (Figure 2.3).

Based on the timing of the increase in average $\delta^{18}\text{O}$ in detrital zircon at 2.35 Ga (Spencer et al., 2019), the granitoids of this study are grouped according to their magmatic crystallization age. Zircon from sediment-derived granitoids with crystallization ages > 2.3 Ga yield $\delta^{18}\text{O}$ values of $6.9 \pm 0.9\text{\textperthousand}$ to $8.6 \pm 0.4\text{\textperthousand}$ (Table 2.1). Sediment-derived granitoids with crystallization ages < 2.0

Ga have a wider range of zircon $\delta^{18}\text{O}$ from $4.7\pm0.9\text{\textperthousand}$ to $11.4\pm1.0\text{\textperthousand}$, but on average have higher $\delta^{18}\text{O}$ than their older counterparts (Figure 2.4).

Zircon $\delta^{18}\text{O}$ is typically interpreted in tandem with ϵHf (deviation of $^{176}\text{Hf}/^{177}\text{Hf}$ in parts per 10,000 from that of CHUR; chondritic uniform reservoir), as elevated $\delta^{18}\text{O}$ is often linked to enhanced crustal reworking and evolved Hf isotopic signatures (low ϵHf) (Hawkesworth and Kemp, 2006). The vast majority of single grain analyses yield ϵHf values between -10 and +15 (Figure 2.5). Of the 154 analyses, only two single grain analyses of sample 18IM3 show ϵHf values <-10 . There is no correlation between higher $\delta^{18}\text{O}$ values and evolved ϵHf values.

Detailed results of geochronology, Hf and O isotopic data, and whole rock major and trace element concentrations for individual samples is provided in Appendix A, and in supplementary data Tables B1 and C1.

Sample ID	Major element concentrations (reported as oxide wt %)												
	SiO ₂	TiO ₂	Al ₂ O ₃	Fe ₂ O ₃	MgO	CaO	Na ₂ O	K ₂ O	P ₂ O ₅	MnO	LOI	Total	ASI
18IM11B	61.93	1.06	18.04	6.58	2.18	2.88	2.80	3.58	0.07	0.06	0.22	99.38	1.3
18IM12B	69.05	0.14	14.73	5.97	1.90	2.85	2.32	1.03	0.03	0.13	0.77	98.92	1.5
18IM13C	70.74	0.33	14.84	3.06	0.87	3.04	3.29	1.73	0.10	0.01	1.00	99.01	1.2
18IM14A	77.72	0.29	10.59	1.62	0.54	0.77	1.31	5.15	0.07	0.04	0.72	98.82	1.2
18IM15B	65.23	0.58	15.48	7.01	2.12	3.52	2.84	0.96	0.09	0.09	1.34	99.25	1.3
18IM19	72.13	0.31	14.05	3.51	1.41	1.27	2.49	3.68	0.06	0.05	0.73	99.69	1.4
18IM20	63.52	0.26	17.78	6.13	1.81	2.63	3.50	3.05	0.07	0.07	0.85	99.69	1.3
18IM21C	81.84	0.04	8.75	2.84	0.65	1.11	2.19	0.76	0.18	0.18	0.93	99.48	1.4
18IM23D	71.76	0.11	14.05	2.83	0.79	0.60	2.01	6.51	0.12	0.04	0.50	99.32	1.2
18IM25C	74.42	0.06	13.17	0.95	0.17	0.95	2.71	5.80	0.02	0.00	0.89	99.15	1.1
18IM3	77.57	0.37	10.88	3.01	0.87	1.03	2.23	2.72	0.05	0.05	0.68	99.45	1.3

Table 2.2. Bulk rock major element concentrations. The aluminum saturation index (ASI) is calculated as molar Al/(Ca-1.67P+Na+K).

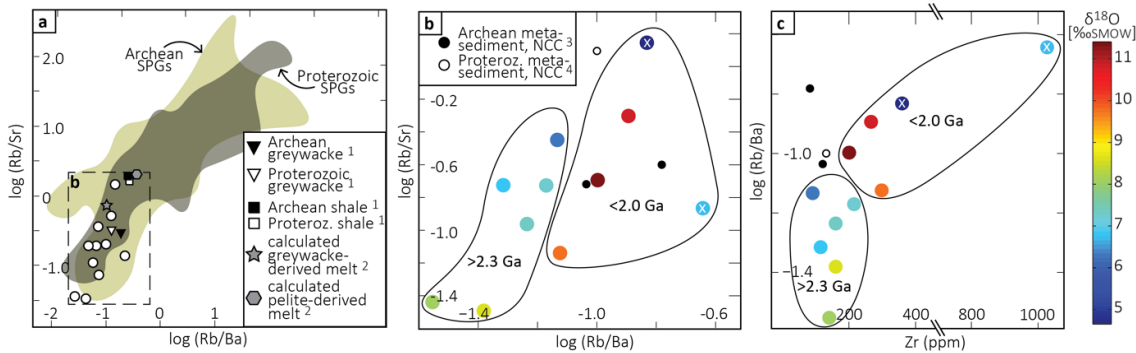


Figure 2.3. (A) Rb/Ba vs. Rb/Sr ratios of sediment-derived granitoids of this study (white circles), and Archean and Proterozoic strongly peraluminous granites (SPGs) from Buchholz and Spencer (2019) (Archean SPGs n= 255, Proterozoic SPGs n=586). Average compositions of Archean and Proterozoic greywacke and shales are from ¹⁾(Condie, 1993); compositions of calculated greywacke and pelite-derived melt are from ²⁾(Sylvester, 1998). Neither sediment-derived melts nor sediments show a systematic change in Rb/Ba or Rb/Sr ratio across the Archean-Proterozoic transition. Dashed rectangle marks section shown in (B). **(B)** Rb/Ba vs. Rb/Sr ratios, color-coded by their corresponding zircon $\delta^{18}\text{O}$ values. Rb/Ba and Rb/Sr ratios show no correlation with $\delta^{18}\text{O}$. Sediment-derived granitoids younger than 2.0 Ga show higher Rb/Ba ratios than their older counterparts (see section 4.3 for discussion). White X marks omitted samples whose bulk-rock composition may be affected by secondary processes (discussed in Appendix A2.4). Compositions of Archean and Proterozoic metasediments in the Yinshan block and Inner Mongolia Suture Zone, respectively, are from ³⁾(Wang and Guo, 2017) and ⁴⁾(Wan et al., 2018). **(C)** Rb/Ba ratio vs Zr concentration, color-coded by their corresponding zircon $\delta^{18}\text{O}$ values. Higher Rb/Ba ratios in ≤ 2.0 Ga samples compared to ≥ 2.3 Ga samples, are associated with higher Zr concentrations. Black and white circles show compositions of metasedimentary rocks in the sampling area potentially reflecting the composition of the source of the sediment-melts of this study (refer to caption and legend of (B) for references, and explanation of symbols, and Appendix A2.3 for further discussion on the sedimentary source). There is no evidence for distinct Zr concentrations of the source of the samples studied here, implying that the small differences in Rb/Ba ratios and Zr concentration of these samples may be caused by variable melting temperatures rather than variable composition of the source (discussed in Appendix A2.3); thus, further supporting that no systematic change in the clay-content of the source occurred.

Sample ID	Trace element concentrations (reported as ppm)																		
	Rb	Ba	Sr	Nb	Zr	Hf	Y	Zn	Cu	Ni	Co	Cr	V	La	Ce	Nd	Pb	Th	
18IM11B	118	925	237	15	267	<d.l.	25	88	12	18	15	54	109	74	113	53	22	24	
18IM12B	23	306	317	<d.l.	298	<d.l.	54	36	<d.l.	<d.l.	12	45	24	37	67	28	<d.l.	<d.l.	
18IM13C	18	658	504	<d.l.	141	<d.l.	<d.l.	33	<d.l.	<d.l.	<d.l.	<d.l.	32	18	47	14	<d.l.	<d.l.	
18IM14A	214	1448	153	<d.l.	360	<d.l.	25	27	<d.l.	<d.l.	<d.l.	<d.l.	16	142	304	131	35	69	
18IM15B	15	351	453	<d.l.	160	<d.l.	25	51	37	31	16	60	75	26	37	13	<d.l.	<d.l.	
18IM19	100	1476	530	<d.l.	215	<d.l.	17	38	26	77	10	109	70	40	59	26	22	<d.l.	
18IM20	53	911	486	<d.l.	162	<d.l.	36	43	19	<d.l.	13	59	35	76	158	70	24	23	
18IM21C	28	124	207	<d.l.	1026	28	112	25	<d.l.	<d.l.	<d.l.	78	14	700	1213	561	30	285	
18IM23D	140	1903	393	<d.l.	91	<d.l.	27	24	<d.l.	<d.l.	<d.l.	37	27	23	67	25	30	<d.l.	
18IM25C	97	2007	515	<d.l.	115	<d.l.	<d.l.	<d.l.	<d.l.	<d.l.	<d.l.	18	32	54	21	19	23		
18IM3	50	500	249	<d.l.	201	<d.l.	33	26	<d.l.	<d.l.	<d.l.	37	47	45	74	36	16	<d.l.	

Table 2.3. Trace element concentrations. The limit of detection for trace element concentrations is 10 ppm. Trace element concentrations below 30 ppm level are considered semi-quantitative.

2.4. Discussion

2.4.1 A Paleoproterozoic increase in zircon $\delta^{18}\text{O}$ in sediment-derived melts

Our results taken together with the data from Dan et al. (2012), Marschall et al. (2010), and Mikkola et al. (2011) demonstrate a $\sim 3.5\text{\textperthousand}$ increase in average zircon $\delta^{18}\text{O}$ from $6.7\text{\textperthousand}$ pre-2.3 Ga ($n=16$) to $10.1\text{\textperthousand}$ post-2.0 Ga ($n=5$) in sediment-derived granitoids (Figure 2.4). Two samples (18IM14A, 18IM21C) have been omitted from the calculation of the post-2.0 Ga zircon $\delta^{18}\text{O}$ average, as petrographic and geochemical evidence suggest that the zircon oxygen isotope compositions of these samples potentially reflect secondary processes (see Appendix A for details). Our results are in accord with previous studies on detrital and igneous zircon demonstrating an increase in average $\delta^{18}\text{O}$ across the Archean-Proterozoic boundary (Valley et al., 2005; Spencer et al., 2019).

2.4.2 Decoupled oxygen and hafnium isotopic signatures

The recycling of older crustal material (with lower $^{176}\text{Hf}/^{177}\text{Hf}$ ratio than the mantle) leads to lower εHf values and older depleted mantle model ages (TDM_{Hf}) for zircon from melts that assimilated such material as compared to zircon (of the same age) from more juvenile melts (Arndt and Goldstein, 1987). Neither of the two groups of granitoids of this study (i.e. the post-2.0 Ga and pre-2.3 Ga granitoids) show no correlation of radiogenic ^{176}Hf depletion (older

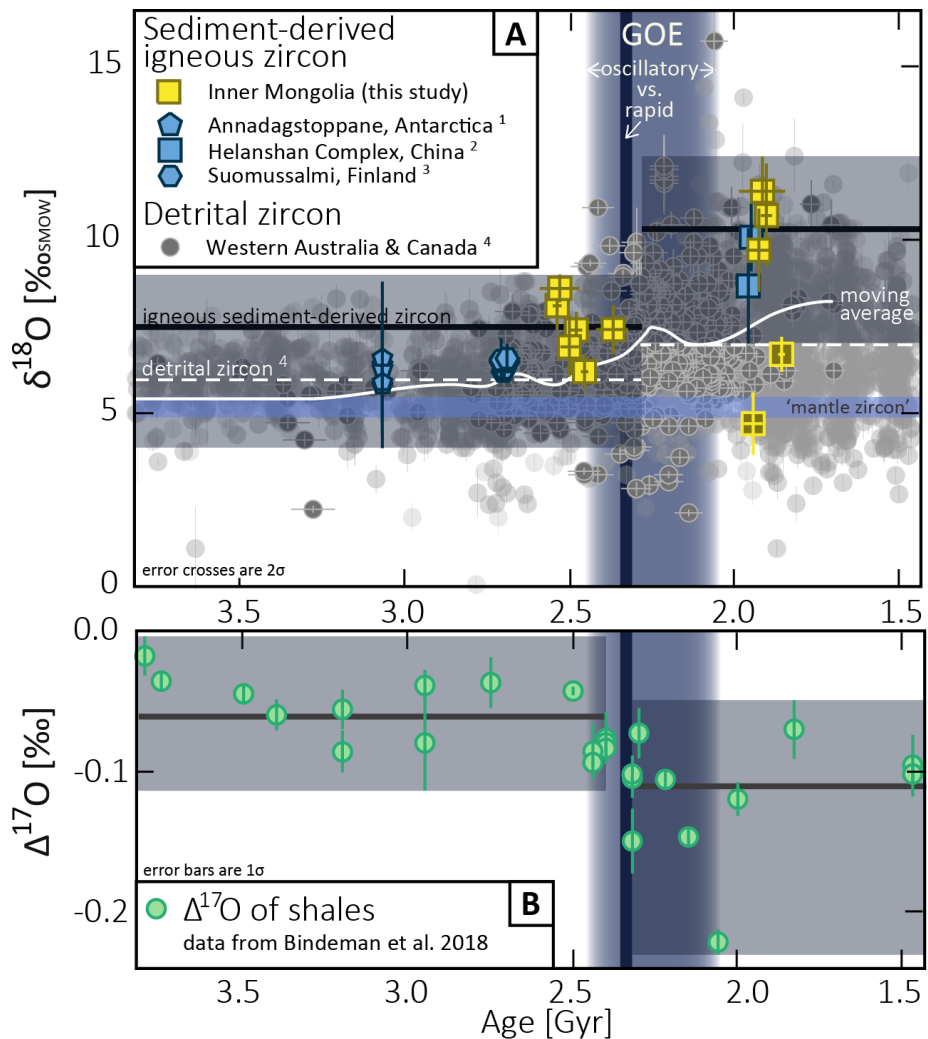


Figure 2.4. (A) Variation in zircon $\delta^{18}\text{O}$ with >1.5 Ga crystallization ages. Yellow symbols show data of sediment-derived igneous zircon from this study. Blue symbols refer to zircon data from strongly peraluminous granites from ¹Marschall et al., (2010), ²Dan et al., (2014), and ³Mikkola et al., (2011). Opaque grey symbols show data of detrital zircon from Spencer et al., (2019b). Transparent grey symbols show compiled global zircon $\delta^{18}\text{O}$ data from Spencer et al., (2017). Both detrital zircon and igneous zircon from sediment-derived melts show a shift in average oxygen isotope composition before and after ~ 2.35 Ga, as indicated by solid black and dashed white line, respectively. The $\sim 3.5\text{‰}$ shift in average zircon $\delta^{18}\text{O}$ of the sediment-derived granitoids of this study is more prominent than the deviation of 1.1‰ shown by detrital zircon (Spencer et al., 2019). This is not surprising given detrital zircon are sourced from diverse magmatic systems, with both mantle and supracrustal components. Time constraints for the change in average zircon $\delta^{18}\text{O}$ are from Spencer et al. (2019). Note that the solid black line shows the arithmetic mean of sediment-derived igneous zircon excluding samples 18IM14A, and 18IM21C (reversely colored symbols; see Appendix 4.2 for detailed discussion of reasons for

the exclusion of these two samples). Solid white line shows moving average of $\delta^{18}\text{O}$ for detrital zircon data (Spencer et al., 2019). The change in average zircon $\delta^{18}\text{O}$ is coeval with the Great Oxygenation Event (GOE), the timing of which is indicated by vertical blue line (rapid oxygenation) according to Luo et al., (2016), and by wider blue bar (oscillatory oxygenation) according to Gumsley et al., (2017), and a shift in average $\Delta^{17}\text{O}$ (defined as $\delta^{17}\text{O}-0.5305*\delta^{18}\text{O} [\text{\%}]$) of shales as shown in (B). Shale triple-oxygen isotope data are from Bindeman et al., (2018). Results of statistical step-change analysis (Pettitt test) shown as solid black line in B) are from Spencer et al., (2019b).

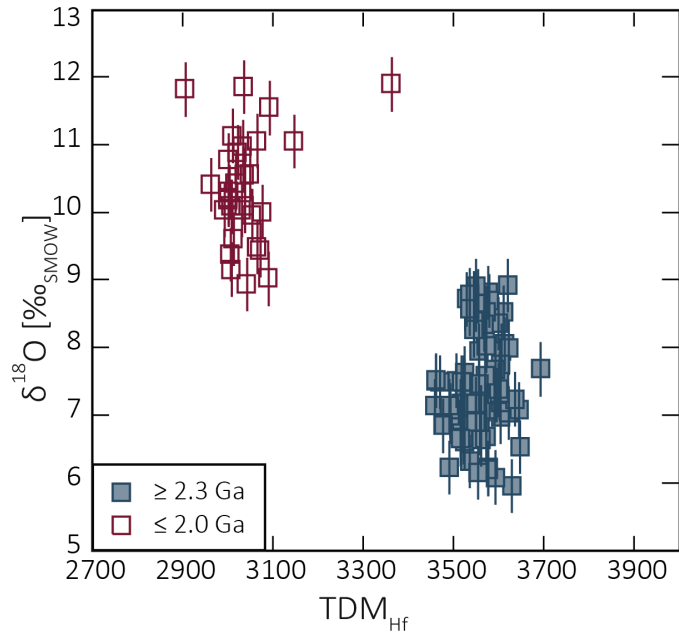


Figure 2.5. Depleted mantle model age (TDM_{Hf}) vs $\delta^{18}\text{O}$ of single grain analyses of igneous zircon from sediment-derived granitoids. Uncertainties are shown at two sigma level. TDM_{Hf} were calculated using the isotopic estimates of the depleted mantle from Vervoort et al. (2018), a ^{176}Lu decay constant of $1.867*10^{-11}$ years $^{-1}$ (Söderlund et al., 2004), and assuming an initial $^{176}\text{Lu}/^{177}\text{Hf}$ ratio of 0.01 (upper continental crust). While the absolute values calculated for TDM_{Hf} are highly sensitive to the assumed initial $^{176}\text{Lu}/^{177}\text{Hf}$ ratio, the relative differences of TDM_{Hf} are not affected. There is no correlation between depletion of radiogenic ^{176}Hf (leading to older TDM_{Hf} , and lower ϵ_{Hf}) and increasing $\delta^{18}\text{O}$ in the individual groups (i.e. the post-2.0 Ga and pre-2.3 Ga granitoids) indicating that enhanced crustal reworking alone did not cause the increase in $\delta^{18}\text{O}$.

TDM_{Hf}) and high $\delta^{18}\text{O}$ in zircon (Figure 2.5). Younger TDM_{Hf} in the post-2.0 Ga granitoids indicate on average shorter crustal residence time of the precursors of these rocks as compared to the pre-2.3 Ga granitoids (Arndt and Goldstein, 1987). The lack of a correlation between radiogenic ^{176}Hf depletion with increasing $\delta^{18}\text{O}$ values in the NCC granitoids is in accord with

a previous study on detrital zircon that demonstrated decoupled behaviour of zircon $\delta^{18}\text{O}$ and TDM_{HF} (Spencer et al., 2019). This has been interpreted as an indication that enhanced crustal reworking alone cannot account for the rise in zircon $\delta^{18}\text{O}$ (Spencer et al., 2019). This interpretation is supported by the timing of the ~ 2.35 Ga (Spencer et al., 2019) zircon $\delta^{18}\text{O}$ increase, that predates the ~ 1.9 – 1.8 Ga assembly of Earth’s first widely accepted supercontinent Nuna (Bleeker, 2003), and instead falls into a period characterized by a global lull in tectono-magmatic activity (Condie et al., 2009; Spencer et al., 2018).

2.4.3 Changes in sediment composition as a driver for the zircon $\delta^{18}\text{O}$ increase

If enhanced crustal recycling is unable to account for the Paleoproterozoic increase in zircon $\delta^{18}\text{O}$, the explanation of the data presented here necessitates an increase in $\delta^{18}\text{O}$ in recycled material. It has been suggested that an increased clay-component in sedimentary rocks and subsequent incorporation into sediment melts could have driven the increase in zircon $\delta^{18}\text{O}$ (e.g Payne et al., 2015). Clay-rich sediments and sediment melts tend to have higher Rb/Sr and Rb/Ba ratios than clay-poor ones (Sylvester, 1998). The NCC granitoids show Rb/Sr and Rb/Ba ratios that fall within the low end of Rb/Sr and Rb/Ba ratios reported for Archean to Phanerozoic sediment-derived granites elsewhere (Sylvester, 1998; Bucholz and Spencer, 2019), suggesting that the sediment-derived granitoids studied here may derive from the partial melting of relatively clay-poor sources (Sylvester, 1998). Rb/Ba, and Rb/Sr ratios only provide a first order assessment of the maturity of the sedimentary source (i.e. clay-content) of sediment-derived melts as these ratios are also controlled by the melting reaction, and may be affected by secondary processes (Harris and Inger, 1992; Ennis et al., 2000) (see Appendix A for a detailed discussion). Importantly however, neither the results of this study nor global data sets of sediments (Condie, 1993), and sediment-derived granitoids (Bucholz and Spencer, 2019) show evidence for a systematic increase in clay-component associated with the increase in zircon $\delta^{18}\text{O}$ (Figure 2.3), suggesting that sediment clay content was not a dominant control on the oxygen isotope composition of these melts.

2.4.4. The emergence of continents and its repercussion on sediment $\delta^{18}\text{O}$

Based on our results, we suggest that a change in the oxygen isotopic composition of supracrustal material available for recycling was the likely driver of the observed change in average zircon $\delta^{18}\text{O}$ at ~ 2.35 Ga (note, that time constraints for the change are from Spencer *et al.*, 2019b). Sediments are the dominant high- $\delta^{18}\text{O}$ reservoir on Earth with shales comprising the largest fraction (Veizer and Mackenzie, 2003). The average $\delta^{18}\text{O}$ value of shales increases from $11.4\text{\textperthousand}$ pre-2.43 Ga to $13.9\text{\textperthousand}$ post-2.31 Ga (Bindeman et al., 2018). The increase of shale $\delta^{18}\text{O}$ values through time can be attributed to a variety of causes, including the onset of a modern hydrological cycle due to the subaerial emergence of continents (Bindeman et al., 2018), progressive recycling of sediments (Windley, 1995), a decrease in ocean temperature (Knauth and Lowe, 2003), or a decreasing contribution of hydrothermal clays to shales (Knauth and Lowe, 2003). In addition, aggressive chemical weathering under a CO_2 -rich pre-GOE atmosphere may have stripped sediments of feldspar, the component required to form high- $\delta^{18}\text{O}$ authigenic clays (Savin and Epstein, 1970; Lowe and Tice, 2004). Furthermore, it has been suggested that increased freeboard led to the formation of Paleoproterozoic high- $\delta^{18}\text{O}$ sediments and that the recycling of such a newly formed reservoir caused a concomitant increase in zircon $\delta^{18}\text{O}$ (Payne et al., 2015; Spencer et al., 2019). Intriguingly, the increase of zircon $\delta^{18}\text{O}$ in sediment-derived melts is coeval with a change in the triple-oxygen isotope composition of shales between 2.43 and 2.31 Ga, which is reasonably linked with the rapid emergence of large subaerial landmasses and associated changes in continental weathering pattern (Bindeman et al., 2018; Bindeman, 2020). The emergence of continents could have supported authigenesis in marine Al-rich sediments derived from the erosion of elevated continental crust (Hazen et al., 2013) causing an increase in shale $\delta^{18}\text{O}$ (Savin and Epstein, 1970). Paleoproterozoic atmospheric oxygenation may have further supported the rise in average $\delta^{18}\text{O}$ of shales through enhanced and diversified clay production as a consequence of oxidative subaerial weathering (Hazen et al., 2013). An increase of continental freeboard during the early Paleoproterozoic Era is consistent with a shift from predominantly submarine to predominantly subaerial large igneous province volcanism (Kump and Barley, 2007). The lifespan of sedimentary basins ranges from <1 Myr for trench basins to >100 Myr for

intracratonic basins (Woodcock, 2004). Hence, the compositional response of sediment melts to the increase in sediment $\delta^{18}\text{O}$ may be retarded due to the lag time between sediment deposition and recycling. The timing of the $\delta^{18}\text{O}$ changes in shales (between 2.43 and 2.31 Ga; Bindeman, 2020) and detrital zircon (\sim 2.35 Ga; Spencer et al., 2019) indicate a lag time of <100 Myr between these two records. Importantly, the <2.0 Ga granitoids of this study are interpreted to have $<2.2\text{--}2.0$ Ga sedimentary precursors (see Appendix A), deposited well after (>100 Myr) the emergence of continents and the concomitant change in shale triple-oxygen isotope composition (Bindeman, 2020).

2.5 Concluding remarks

The results of this study imply that the Paleoproterozoic widespread emergence of continents above sea-level and concomitant formation of high- ^{18}O shales left an imprint on the composition of sediment melts (recorded by zircon $\delta^{18}\text{O}$). The coeval rise of atmospheric oxygen imply a potential link between continental emergence and atmospheric oxygenation, perhaps related to diminished submarine volcanism (Kump and Barley, 2007; Gaillard et al., 2011), or an increased supply of nutrients for photosynthetic microbes from emergent crust into the ocean (Hao et al., 2020).

2.6 References

- Arndt, N.T., and Goldstein, S.L., 1987, Use and abuse of crust-formation ages: *Geolog*, v. 15, p. 893–895, doi:10.1130/0091-7613(1987)15<893.
- Baertschi, P., 1976, Absolute ^{18}O content of standard mean ocean water: *Earth and Planetary Science Letters*, v. 31, p. 341–344, doi:10.1016/0012-821X(76)90115-1.
- Bindeman, I.N., 2020, Triple oxygen isotopes in evolving continental crust, granites, and clastic sediments: *Reviews in mineralogy and geochemistry*, v. 86, doi:10.2138/rmg.2020.86.X.
- Bindeman, I.N., Zakharov, D.O., Palandri, J., Greber, N.D., Dauphas, N., Retallack, G.J., Hofmann, A., Lackey, J.S., Bekker, A., and Data, E., 2018, Rapid emergence of subaerial landmasses and onset of a modern hydrologic cycle 2.5 billion years ago: *Nature*, v. 557, p. 545–548, doi:<https://doi.org/10.1038/s41586-018-0131-1>.
- Bleeker, W., 2003, The late Archean record: A puzzle in ca. 35 pieces: *Lithos*, v. 71, p. 99–134, doi:10.1016/j.lithos.2003.07.003.
- Bucholz, C.E., and Spencer, C.J., 2019, Strongly peraluminous granites across the Archean-

- Proterozoic transition: Journal of Petrology, doi:10.1093/petrology/egz033.
- Chappell, B.W., and White, A.J.R., 1992, I- and S-type granites in the Lachlan Fold Belt: Earth and Environmental Science Transactions of the Royal Society of Edinburgh, v. 83, p. 1–26, doi:10.1017/S0263593300007720.
- Condie, K.C., 2018, A planet in transition: The onset of plate tectonics on Earth between 3 and 2 Ga? Geoscience Frontiers, v. 9, p. 51–60, doi:10.1016/j.gsf.2016.09.001.
- Condie, K.C., 1993, Chemical composition and evolution of the upper continental crust: Contrasting results from surface samples and shales: Chemical Geology, v. 104, p. 1–37, doi:10.1016/0009-2541(93)90140-E.
- Condie, K.C., O'Neill, C., and Aster, R.C., 2009, Evidence and implications for a widespread magmatic shutdown for 250 My on Earth: Earth and Planetary Science Letters, v. 282, p. 294–298, doi:10.1016/j.epsl.2009.03.033.
- Dan, W., Li, X., Guo, J., Liu, Y., and Wang, X., 2012, Integrated in situ zircon U–Pb age and Hf–O isotopes for the Helanshan khondalites in North China Craton: Juvenile crustal materials deposited in active or passive continental margin? Precambrian Research, v. 222–223, p. 143–158, doi:10.1016/j.precamres.2011.07.016.
- Dan, W., Li, X.-H., Wang, Q., Wang, X.-C., Liu, Y., and Wyman, D.A., 2014, Paleoproterozoic S-type granites in the Helanshan Complex, Khondalite Belt, North China Craton: Implications for rapid sediment recycling during slab break-off: Precambrian Research, v. 254, p. 59–72, doi:10.1016/j.precamres.2014.07.024.
- Eiler, J.M., 2001, Oxygen Isotope Variations of Basaltic Lavas and Upper Mantle Rocks, in Valley, J.W. and Cole, D.R. eds., Stable Isotope Geochemistry. Reviews in Mineralogy and Geochemistry, Mineralogical Society of America/Geochemical Society, Washington, DC, p. 319–364.
- Ennis, D., Dunbar, N., Campbell, A., and Chapin, C., 2000, The effects of K-metasomatism on the mineralogy and geochemistry of silicic ignimbrites near Socorro, New Mexico: Chemical Geology, v. 167, p. 285–312, doi:10.1016/S0009-2541(99)00223-5.
- Flament, N., Coltice, N., and Rey, P.F., 2013, The evolution of the $^{87}\text{Sr}/^{86}\text{Sr}$ of marine carbonates does not constrain continental growth: Precambrian Research, v. 229, p. 177–188, doi:10.1016/j.precamres.2011.10.009.
- Frost, B.R., and Frost, C.D., 2008, A Geochemical Classification for Feldspathic Igneous Rocks: Journal of Petrology, v. 49, p. 1955–1969, doi:10.1093/petrology/egn054.
- Gaillard, F., Scaillet, B., and Arndt, N.T., 2011, Atmospheric oxygenation caused by a change in volcanic degassing pressure: Nature, v. 478, p. 229–232, doi:10.1038/nature10460.
- Gumsley, A.P., Chamberlain, K.R., Bleeker, W., Söderlund, U., de Kock, M.O., Larsson, E.R., and Bekker, A., 2017, Timing and tempo of the Great Oxidation Event: Proceedings of

- the National Academy of Sciences, v. 114, p. 1811–1816, doi:10.1073/pnas.1608824114.
- Hao, J., Knoll, A.H., Huang, F., Hazen, R.M., and Daniel, I., 2020, Cycling phosphorus on the Archean Earth: Part I. Continental weathering and riverine transport of phosphorus: *Geochimica et Cosmochimica Acta*, v. 273, p. 70–84, doi:10.1016/j.gca.2020.01.027.
- Harris, N.B.W., and Inger, S., 1992, Trace element modelling of pelite-derived granites: *Contributions to Mineralogy and Petrology*, v. 110, p. 46–56.
- Hawkesworth, C.J., and Kemp, A.I.S., 2006, Using hafnium and oxygen isotopes in zircons to unravel the record of crustal evolution: *Chemical Geology*, v. 226, p. 144–162, doi:10.1016/j.chemgeo.2005.09.018.
- Hazen, R.M., Sverjensky, D.A., Azzolini, D., Bish, D.L., Elmore, S.C., Hinnov, L., and Milliken, R.E., 2013, Clay mineral evolution: *American Mineralogist*, v. 98, p. 2007–2029, doi:10.2138/am.2013.4425.
- Hollis, J.A., Van Kranendonk, M.J., Cross, A.J., Kirkland, C.L., Armstrong, R.A., and Allen, C.M., 2014, Low $\delta^{18}\text{O}$ zircon grains in the Neoarchean Rum Jungle Complex, northern Australia: An indicator of emergent continental crust: *Lithosphere*, v. 6, p. 17–25, doi:10.1130/L296.1.
- Kirkland, C.L., Whitehouse, M.J., Pease, V., and Van Kranendonk, M., 2010, Oxygen isotopes in detrital zircons: Insight into crustal recycling during the evolution of the Greenland Shield: *Lithosphere*, v. 2, p. 3–12, doi:10.1130/L80.1.
- Knauth, L.P., and Lowe, D.R., 2003, High Archean climatic temperature inferred from oxygen isotope geochemistry of cherts in the 3.5 Ga Swaziland Supergroup, South Africa: *Geological Society of America Bulletin*, v. 115, p. 566–580, doi:10.1130/0016-7606(2003)115<0566:HAETIF>2.0.CO;2.
- Kump, L.R., and Barley, M.E., 2007, Increased subaerial volcanism and the rise of atmospheric oxygen 2.5 billion years ago: *Nature*, v. 448, p. 1033–1036, doi:10.1038/nature06058.
- Lowe, D.R., and Tice, M.M., 2004, Geologic evidence for Archean atmospheric and climatic evolution: Fluctuating levels of CO₂, CH₄, and O₂ with an overriding tectonic control: *Geology*, v. 32, p. 493–496, doi:10.1130/G20342.1.
- Luo, G., Ono, S., Beukes, N.J., Wang, D.T., Xie, S., and Summons, R.E., 2016, Rapid oxygenation of Earth's atmosphere 2.33 billion years ago: *Science Advances*, v. 2, doi:10.1126/sciadv.1600134.
- Marschall, H.R., Hawkesworth, C.J., Storey, C.D., Dhuime, B., Leat, P.T., Meyer, H.-P., and Tamm-Buckle, S., 2010, The Annandagstoppane Granite, East Antarctica: Evidence for Archean Intracrustal Recycling in the Kaapvaal-Grunehogna Craton from Zircon O and Hf Isotopes: *Journal of Petrology*, v. 51, p. 2277–2301, doi:10.1093/petrology/egg057.
- Mikkola, P., Huhma, H., Heilimo, E., and Whitehouse, M., 2011, Archean crustal evolution of

- the Suomussalmi district as part of the Kianta Complex, Karelia: Constraints from geochemistry and isotopes of granitoids: *Lithos*, v. 125, p. 287–307, doi:10.1016/j.lithos.2011.02.012.
- O'Neill, C., Lenardic, A., Weller, M., Moresi, L., Quenette, S., and Zhang, S., 2016, A window for plate tectonics in terrestrial planet evolution? *Physics of the Earth and Planetary Interiors*, v. 255, p. 80–92, doi:10.1016/j.pepi.2016.04.002.
- Page, F.Z., Fu, B., Kita, N.T., Fournelle, J., Spicuzza, M.J., Schulze, D.J., Viljoen, F., Basei, M.A.S., and Valley, J.W., 2007, Zircons from kimberlite: New insights from oxygen isotopes , trace elements , and Ti in zircon thermometry: *Geochimica et Cosmochimica Acta*, v. 71, p. 3887–3903, doi:10.1016/j.gca.2007.04.031.
- Payne, J.L., Hand, M., Pearson, N.J., Barovich, K.M., and Mcinerney, D.J., 2015, Crustal thickening and clay: Controls on O isotope variation in global magmatism and siliciclastic sedimentary rocks: *Earth and Planetary Science Letters*, v. 412, p. 70–76, doi:10.1016/j.epsl.2014.12.037.
- Roberts, N.M.W., and Spencer, C.J., 2015, The zircon archive of continent formation through time: Geological Society, London, Special Publications, v. 389, p. 197–225, doi:10.1144/SP389.14.
- Savin, S.M., and Epstein, S., 1970, The oxygen and hydrogen isotope geochemistry of clay minerals: *Geochimica et Cosmochimica Acta*, v. 34, p. 25–42, doi:10.1016/0016-7037(70)90149-3.
- Söderlund, U., Patchett, P.J., Vervoort, J.D., and Isachsen, C.E., 2004, The ^{176}Lu decay constant determined by Lu–Hf and U–Pb isotope systematics of Precambrian mafic intrusions: *Earth and Planetary Science Letters*, v. 219, p. 311–324, doi:10.1016/S0012-821X(04)00012-3.
- Spencer, C.J., Cawood, P.A., Hawkesworth, C.J., Raub, T.D., Prave, A.R., and Roberts, N.M.W., 2014, Proterozoic onset of crustal reworking and collisional tectonics: Reappraisal of the zircon oxygen isotope record: *Geology*, v. 42, p. 451–454, doi:10.1130/G35363.1.
- Spencer, C.J., Murphy, J.B., Kirkland, C.L., and Liu, Y., 2018, Was the supercontinent cycle activated by a Palaeoproterozoic tectono-magmatic lull? *Nature Geoscience*, doi:10.1038/s41561-017-0051-y.
- Spencer, C.J., Partin, C.A., Kirkland, C.L., Raub, T.D., Liebmann, J., and Stern, R.A., 2019, Paleoproterozoic increase in zircon $\delta^{18}\text{O}$ driven by rapid emergence of continental crust: *Geochimica et Cosmochimica Acta*, v. 257, p. 16–25, doi:10.1016/j.gca.2019.04.016.
- Spencer, C.J., Roberts, N.M.W., and Santosh, M., 2017, Growth, destruction, and preservation of Earth's continental crust: *Earth-Science Reviews*, v. 172, p. 87–106, doi:10.1016/j.earscirev.2017.07.013.

- Sylvester, P.J., 1994, Archean Granite Plutons, *in* p. 261–314, doi:10.1016/S0166-2635(08)70225-1.
- Sylvester, P.J., 1998, Post-collisional strongly peraluminous granites: *Lithos*, v. 45, p. 29–44, doi:10.1016/S0024-4937(98)00024-3.
- Valley, J.W. et al., 2005, 4.4 billion years of crustal maturation: Oxygen isotope ratios of magmatic zircon: Contributions to Mineralogy and Petrology, v. 150, p. 561–580, doi:10.1007/s00410-005-0025-8.
- Valley, J.W., Chiarenzelli, J.R., and McLelland, J.M., 1994, Oxygen isotope geochemistry of zircon: *Earth and Planetary Science Letters*, v. 126, p. 187–206, doi:10.1016/0012-821X(94)90106-6.
- Veizer, J., and Mackenzie, F.T., 2003, Evolution of Sedimentary Rocks, *in* Treatise on Geochemistry, Elsevier Ltd, p. 369–407.
- Vervoort, J.D., Kemp, A.I., and Fisher, C.M., 2018, Hf isotope constraints on evolution of the depleted mantle and growth of continental crust, *in* American Geophysical Union, Fall Meeting 2018,
- Wan, Y., Peng, P., Liu, S., Kröner, A., Guo, J., Dong, C., and Liu, D., 2018, Late Paleoproterozoic tectono-thermal event in the northwestern North China Craton: Evidence from U-Pb dating and O-Hf isotopic compositions of zircons from metasedimentary rocks north of Hohhot City, Inner Mongolia, northern China: *Journal of Asian Earth Sciences*, v. 167, p. 152–164, doi:10.1016/j.jseas.2017.09.012.
- Wang, D., and Guo, J., 2017, Late Archean high-pressure pelitic granulites in the Yinshan Block, North China Craton: *Precambrian Research*, v. 303, p. 251–267, doi:10.1016/j.precamres.2017.03.027.
- Windley, B.F., 1995, The Evolving Continents: Wiley & Sons, 377–385 p.
- Woodcock, N.H., 2004, Life span and fate of basins: *Geology*, v. 32, p. 685, doi:10.1130/G20598.1.
- Zhao, G., Wilde, S.A., Cawood, P.A., and Lu, L., 1999, Tectonothermal history of the basement rocks in the western zone of the North China Craton and its tectonic implications: *Tectonophysics*, v. 310, p. 37–53.

2.7 Author contributions

JL, CJS, CLK, CEB designed the research or contributed to designing the research. JL, CJS, XH, MS collected the samples or contributed to organizing the sample collection. JL, CEB, XX, LM, NE carried out the analyses. JL, CJS, CLK, CEB contributed to interpreting the results. JL wrote the manuscript. All authors provided comments on the manuscript.

Appendices

- A:** Supplementary information on sample context, methodology, data analysis, and supplementary Figures A1-A8, and supplementary Tables A1-A3.
- B:** Supplementary Table B1, U-Pb single spot results.
- C:** Supplementary Table C1, O and Hf isotope single spot results.

Appendix A

A1. Materials and Methods

A1.1 Sample context

Recent publications subdivide the Precambrian basement of the North China Craton (NCC) into three tectonic domains; Archean to Proterozoic Western and Eastern Blocks, and a central Paleoproterozoic collisional Trans-North China Orogen (Zhao and Zhai, 2013). The Western Block comprises the Yinshan Block in the north and the Ordos Block in the south, which amalgamated at ~1.95 Ga along the Inner Mongolia Suture Zone (IMSZ) (Santosh, 2010). The Neoarchean Yinshan Block comprises tonalite-trondhjemite-granodiorite (TTG) gneisses and minor supracrustal rocks that were metamorphosed at ~2.5 Ga (Zhao et al., 1999). The IMSZ is dominated by high-grade garnet-sillimanite pelitic gneisses and granulites, garnet-bearing quartzites, felsic paragneisses, calc-silicate rocks and marbles, which are considered to have been deposited in a continental margin setting (Dan et al., 2012). Based on zircon ϵ Hf it has been suggested that the protolith of this metasedimentary sequence was sourced from a 2.18-2.00 Ga continental arc (Dan et al., 2012). The metasedimentary series of the IMSZ is associated with minor TTG gneisses, sediment-derived granites, and mafic granulites (Zhao and Zhai, 2013). In this work we present data from eleven granitoids of the IMSZ, the Yinshan Block, and the Trans-North China Orogen. Samples derive from 5 geologic units in an area extending

300 km E-W, and 80 km N-S (Figure A8, GPS locations are provided in Table 2.1 in the main manuscript).

A1.2 Methods

Samples were prepared for zircon separation by trimming off weathered surfaces using a rock saw. The melanosome was removed from migmatic samples. The remaining fresh igneous rock material was washed in water. Subsequently, 0.5-1.0 kg of sample material was crushed. A ~10 g aliquot per sample was powdered using a tungsten carbide mill for bulk-rock geochemistry. Zircon crystals were extracted using standard separation techniques (Wilfley shaking table, Frantz magnetic separation, heavy liquid; Bromoform, CHBr₃). The resulting hand-picked zircon crystals were mounted in epoxy resin and polished to approximately half grain thickness to expose a cross section through the individual crystals. Zircon grains were mounted within a 5 mm radius from the centre of a 25 mm in diameter epoxy disk. The polished mounts were cleaned in an ultrasonic bath in multiple steps using isopropanol, ethanol, soap solution, and deionized water. Subsequently, the mounts were dried in an oven for ~24 hrs at 60°C. A 40 nm gold coat was applied to the mount surface. To reveal internal growth structures, CL images of zircon grains were taken prior to SIMS analysis using a Tescan MIRA3 field emission scanning electron microscope at the John de Laeter Centre, Curtin University, Western Australia. Unless indicated otherwise, spots of U-Pb, oxygen, and hafnium isotope analyses were located on the same zircon growth zone (Figures A1-3). To avoid signatures from inherited older growth zones, only analyses located on magmatic rims of zircon grains were used to determine crystallization age, oxygen and hafnium isotopic composition of zircon in equilibrium with the melt (Figures A1-3).

A1.2.1 SIMS zircon oxygen isotope analysis

Oxygen isotope analysis was conducted on a CAMECA IMS 1280 secondary ion mass spectrometer (SIMS) at the Centre for Microscopy, Characterisation and Analysis (CMCA) at the University of Western Australia and the Guangzhou Institute of Geochemistry (GIG), Chinese Academy of Sciences, China. Analytical methods have been described in detail by Yang et al. (2018). A Cs⁺ primary ion beam was accelerated at 10 keV with an intensity of 2–3 nA.

The spot diameter was \sim 10–15 μm . Prior to analysis, each site was pre-sputtered for 30–35 s to remove the Au-coat in a \sim 20 μm^2 area. The ^{18}O and ^{16}O ions were detected simultaneously by two faraday cups. Instrumental mass fractionation and drift were determined through repetitive analyses of zircon standard 91500 ($\delta^{18}\text{O} = 9.9 \pm 0.6\text{\textperthousand}$) (Wiedenbeck et al., 2004). Zircon standard Temora-2 ($\delta^{18}\text{O} = 8.2 \pm 0.03\text{\textperthousand}$) (Black et al., 2004) was used as secondary standard to monitor the quality of the corrections for instrumental mass fractionation and drift. The analysis of the secondary standard Temora-2 yielded $\delta^{18}\text{O}$ of $7.88 \pm 0.69\text{\textperthousand}$, $7.93 \pm 0.39\text{\textperthousand}$, $7.88 \pm 0.38\text{\textperthousand}$, and $7.98 \pm 0.33\text{\textperthousand}$ (2σ ; Figure A5 and Table A2) in accordance with the accepted value (see Schmitt et al. (2019) for a more thorough discussion of oxygen isotopic heterogeneity in different batches of Temora-2). The analysis of the primary standard indicates a precision of $\leq 0.2\text{\textperthousand}$ (1σ) for all runs. Oxygen isotope compositions are reported in the conventional delta notation; expressed as $\delta^{18}\text{O}$, the deviation in the isotope ratio $^{18}\text{O}/^{16}\text{O}$ in permil relative to average sea water (VSMOW) (Baertschi, 1976). To ensure that the oxygen isotope values reflect a primary signature, the zircon OH-content, an indicator of secondary alteration (Pidgeon et al., 2017) was determined qualitatively as compared to zircon standard 91500 (see Figure A5). Zircon mounts were held under vacuum for at least 3 days prior to this analysis. Zircon OH is reported as OH/O, determined as counts of $^{16}\text{O}^{1}\text{H}$ over counts of ^{16}O .

A1.2.2 SIMS zircon U-Pb analysis

Following analysis of oxygen isotopic composition, zircon U-Pb ages were obtained using an A.S.I. SHRIMP II sensitive high-resolution ion microprobe at the John de Laeter Centre, Curtin University, Western Australia. Operating procedures are described in detail by (Wingate and Kirkland, 2015). Zircon reference materials Temora-2 (417 ± 2 Ma, 130 ± 21 U ppm; (Black et al., 2004), 91500 (1065 ± 1 Ma, 81 ± 5 U ppm; (Wiedenbeck et al., 2004), and OG1 (3465 ± 0.6 Ma, 163 ± 48 U ppm; (Stern et al., 2009) were used for U-Pb, and U-concentration, and Pb-Pb standardisation, respectively. Secondary reference materials yielded weighted mean $^{238}\text{Pb}/^{206}\text{Pb}^*$ ages of 1075 ± 19 Ma ($n=5$, MSWD=0.52), and 1069 ± 31 Ma ($n=4$, MSWD=0.96) for 91500, and weighted mean $^{238}\text{U}/^{206}\text{Pb}^*$ ages of 3461 ± 21 Ma ($n=7$, MSWD=0.21), 3470 ± 110 Ma ($n=2$, MSWD=0.04). and 3466 ± 21 Ma ($n=6$, MSWD=0.13) for OG1. An acceleration voltage of 10 keV is used to direct a 15–20 μm diameter primary beam

of O_2^- ions onto the zircon grain to sputter secondary ions from its surface. Secondary ions are accelerated to 10 keV into a magnetic field that directs the secondary ion beam into an electron multiplier. During each run the magnetic field is cycled several times to count the secondary ions of 8 different mass species and to determine the background. The measured isotopic masses are 196 (species $[^{90}\text{Zr}_2^{16}\text{O}]^+$, count time 2 s), 204 ($^{204}\text{Pb}^+$, 10 s), 204.1 (background, 10 s), 206 ($^{206}\text{Pb}^+$, 10 s), 207 ($^{207}\text{Pb}^+$, 20–40 s), 208 ($^{208}\text{Pb}^+$, 10 s), 238 ($^{238}\text{U}^+$, 5 s), 248 ($[^{232}\text{Th}^{16}\text{O}]^+$, 5 s), and 254 ($[^{238}\text{U}^{16}\text{O}]^+$, 2 s). This cycle was repeated six times for each analysis. Prior to analysis, the primary ion beam was rastered over each site for 2–3 minutes to clean the area.

Raw data were reduced using the Microsoft Excel add-ins SQUID 2.50 and Isoplot 3.75 with the decay constants of Steiger and Jäger (1977). Measured $^{206}\text{Pb}^+ / ^{238}\text{U}^+$ ratios are calibrated to the accepted $^{206}\text{Pb} / ^{238}\text{U}$ ratio of the zircon standard, using a calibration curve of $\ln(^{206}\text{Pb}^+ / ^{238}\text{U}^+)$ vs. $\ln(\text{UO}^+ / \text{U}^+)$ with a fixed slope of 2.0 (Claoué-Long et al., 1995). Measured compositions were corrected for the presence of common Pb using measured $^{204}\text{Pb} / ^{206}\text{Pb}$ and the contemporaneous Pb isotopic composition determined according to the model of Stacey and Kramers (1975). To confirm that common Pb is mainly inherited to the zircon grain rather than related to surface contamination, counts for $^{204}\text{Pb}^+$ were monitored during each analysis to ensure that they remained low (≤ 5 counts/10 s for most grains) over the analysis time of ~ 16 min. Details of calibration and instrumental uncertainties for each analytical session are provided in supplementary Table A1. Calculated mean ages are quoted in the text at the two sigma level and include propagated internal and external uncertainty components. In order to detect potential low-temperature alteration, which may impact the zircon geochemistry (including O, U-Pb, and Hf isotopic signatures) (Pidgeon et al., 2017; Guitreau and Flahaut, 2019), measured and time-integrated Th/U ratios were monitored. Measured and time-integrated Th/U ratios were determined by direct measurement of ^{232}Th and ^{238}U abundances, and by calculation from the decay products of ^{232}Th and ^{238}U (i.e. ^{208}Pb , and ^{206}Pb), respectively (Guitreau and Flahaut, 2019).

A1.2.3 LA-ICPMS zircon Hf isotope analysis

Hafnium isotope analysis by laser ablation inductively coupled plasma mass spectrometry (LA-ICPMS) was conducted using a Resonetics RESOlution M50-A excimer laser coupled with a Nu Plasma II multi-collector ICP-MS at the John de Laeter Centre, Curtin University, Western Australia. Following two cleaning pulses and a 15–20 s period of background analysis, samples were spot ablated for 30 s at a 7 Hz repetition rate using a 33 µm beam. The sample cell was flushed by ultrahigh purity He and N₂. Hafnium, Lu, and Yb isotope (¹⁷²Yb, ¹⁷³Yb, ¹⁷⁵Lu, ¹⁷⁶Hf+Yb+Lu, ¹⁷⁷Hf, ¹⁷⁸Hf, ¹⁷⁹Hf, ¹⁸⁰Hf) intensities were measured simultaneously for 0.01 s. Reference zircon Mudtank (Woodhead and Herdt, 2005) was used to monitor accuracy and precision of internally corrected Hf isotope ratios. Zircon standards 91500 (Wiedenbeck et al., 2004) and Pleisovice (Sláma et al., 2008) were used as secondary standards. Raw data were reduced using Iolite (Paton et al., 2011). The quality of the corrections for isobaric interferences of ¹⁷⁶Yb with ¹⁷⁶Hf, and instrument stability and accuracy of mass bias corrections based on stable isotope ratios of the analysed standards have been assessed according to the workflow presented by (Spencer et al., 2019). Samples were analysed in four analytical sessions. The mean ¹⁷⁸Hf/¹⁷⁷Hf ratios of the standards were 1.46723 ± 0.00013 , 1.46718 ± 0.00017 , and 1.46721 ± 0.00008 ; the mean ¹⁸⁰Hf/¹⁷⁷Hf ratios of the standards were 1.88688 ± 0.00031 , 1.88691 ± 0.00024 , 1.88689 ± 0.00022 . The mean ratios of the stable isotopes of Hf obtained for the standards are in accordance with the predicted natural stable ratios of 1.46717 and 1.88666, respectively (Blichert-Toft and Albarède, 1997) (Figure A6). The measured ¹⁷⁶Hf/¹⁷⁷Hf ratios of the secondary standards reproduce the recommended values of 0.282306 ± 0.000008 for 91500 (Wiedenbeck et al., 2004), 0.282482 ± 0.000013 for Pleisovice (Sláma et al., 2008) within uncertainty (supplementary Table A3).

A1.2.4 XRF bulk rock major and trace element concentrations

Bulk-rock major and trace element concentrations were determined using a Panalytical Zetium 4 kW X-ray fluorescence spectrometer (XRF) at the California Institute of Technology, USA. Powdered samples were dried at 110°C overnight. Dried powders were then sintered at 1050°C for one hour and loss on ignition (L.O.I) was determined subsequently. After re-homogenising sample powders with an agate mortar and pestle, sample powders were fused into glass beads

at a flux to sample ratio of 10:1 using a di-lithium tetraborate-lithium metaborate flux. The concentrations of 10 major and 18 trace elements in the samples were measured by comparing their X-ray intensities to those obtained from standards beads. Full analytical methods and uncertainties are given in Bucholz and Spencer (2019).

A2. Detailed interpretation of results for individual samples

A2.1 U-Pb geochronology & O isotope geochemistry

Magmatic crystallization ages of the granitoids span ~600 million years. Nine samples yield concordia ages or weighted mean $^{207}\text{Pb}/^{206}\text{Pb}^*$ ages that range from 2536 ± 13 Ma (sample 18IM13C) to 1855 ± 10 Ma (sample 18IM21C). Two samples (18IM14A and 18IM20) show over dispersion in their single spot U-Pb ages relative to analytical uncertainty alone, indicating a more complex zircon growth or alteration history. For these two samples we report the age range of single spot analyses and consider the oldest statistically coherent population as the best estimate of their crystallization ages given the likelihood of radiogenic-Pb mobility. Measured and time-integrated Th/U ratios of magmatic rims of zircon agree well (within 0.15 (abs.) or 30% of each other; Figure A4), indicating that the geochemistry of the zircon crystals is unaffected by low-temperature alteration (Pidgeon et al., 2017; Guitreau and Flahaut, 2019). Results of single spot analyses are given in supplementary Table B1. Cathodoluminescence (CL) images of representative zircon grains and concordia plots for representative samples are shown in Figures A1–A3.

Zircon from sediment-derived granitoids with crystallization ages of >2.3 Ga yield zircon $\delta^{18}\text{O}$ that range from $6.9 \pm 0.9\text{\textperthousand}$ (sample 18IM25C) to $8.6 \pm 0.4\text{\textperthousand}$ (sample 18IM15B). Sediment-derived granitoids with crystallization ages of <2.0 Ga have a wider range of zircon $\delta^{18}\text{O}$ from $4.7 \pm 0.9\text{\textperthousand}$ (sample 18IM14A) to $11.4 \pm 1.0\text{\textperthousand}$ (sample 18IM3), but on average have higher $\delta^{18}\text{O}$ than their older counterparts.

In the following the interpretation of U-Pb geochronological and O isotopic data is described in detail for each sample of this study. U-Pb ages and O isotope compositions are reported with 2σ uncertainty unless stated otherwise.

A2.1.1 Sample 18IM11B

U-Pb geochronology

Sample 18IM11B is a medium-grained garnet-bearing granite. Zircon isolated from this sample is subhedral to euhedral, pink to brown in color, and up to 200 µm long. CL images reveal blurred oscillatory zoning of zircon cores overgrown by rims with a slightly higher CL response and weak indications of oscillatory zoning. A total of seven single spot analyses on seven zircon grains was obtained for sample 18IM11B. All analyses are located on zircon rims and are <8% discordant. All seven analyses yield a concordia age of 1901 ± 17 Ma (MSDW = 0.97) which is interpreted as the magmatic crystallization age of the granite.

O isotope geochemistry

A total of 13 single spot analyses on the rims of 13 zircon grains was obtained for sample 18IM11B. Four analyses have been omitted due to high $^{16}\text{O}^{1\text{H}}/^{16}\text{O}$ ratios as compared to the analysed primary standard. The remaining analyses yield a weighted mean $\delta^{18}\text{O}$ of $10.80 \pm 0.90\text{\textperthousand}$ ($n=8$); with one analysis outside of 2σ .

A2.1.2 18IM12B

U-Pb geochronology

Sample 18IM12B is a coarse-grained quartz-rich garnet-bearing granitoid. Zircon isolated from this sample is subhedral, pink, and up to 200 µm long. CL images reveal no to weakly developed oscillatory zoning of zircon cores overgrown by rims with low CL response some of them showing weak indications of oscillatory zoning. A total of seven single spot analyses on seven zircon grains was obtained for sample 18IM12B. All analyses are located on zircon rims and are concordant ($n=6$) to normally discordant ($n=1$). Analyses that are <10% discordant yield a weighted mean $^{207}\text{Pb}/^{206}\text{Pb}^*$ age of 1929 ± 42 Ma ($n=6$, MSWD=1.6) which is interpreted as the magmatic crystallization age of the quartz rich granitoid.

O isotope geochemistry

A total of 19 single spot analyses on the rims of 19 zircon grains was obtained for sample 18IM12B. One analyses has been omitted due to high $^{16}\text{O}^{1\text{H}}/^{16}\text{O}$ ratios as compared to the

analysed primary standard. The remaining analyses yield a weighted mean $\delta^{18}\text{O}$ of $9.74 \pm 1.16\text{\textperthousand}$ ($n=18$).

A2.1.3 Sample 18IM13C

U-Pb geochronology

Sample 18IM13C is a medium-grained garnet-kyanite bearing granite. Zircon isolated from this sample is euhedral, colorless to purple, and up to $300 \mu\text{m}$ long. CL images reveal complex growth patterns in zircon cores overgrown by rims with oscillatory zoning and an outer bright rim. In some grains the growth pattern of the core is truncated by the rim indicating that the cores underwent physical abrasion before overgrowth. A total of 15 single spot analyses on 12 zircon grains was obtained for sample 18IM13C. Thirteen analyses are located on zircon rims, two are located on zircon cores. Two analyses were omitted due to high common Pb content. The remaining 13 analyses are concordant ($n=9$) to normally or reversely discordant ($n=4$). Analyses of bright and dark zircon rims that are $< 10\%$ discordant form a single population and yield a weighted mean $^{207}\text{Pb}/^{206}\text{Pb}^*$ age of $2536 \pm 13 \text{ Ma}$ ($n=7$, MSWD=0.82) which is interpreted as the magmatic crystallization age of the granite. The two analyses of zircon cores yield $^{207}\text{Pb}/^{206}\text{Pb}^*$ ages of $2554 \pm 83 \text{ Ma}$, and $2544 \pm 104 \text{ Ma}$ (1σ) that overlap within error of that obtained for the zircon rims. Considering the truncated nature exhibited by some zircon core-rim boundaries the core ages are interpreted to date an inherited component.

O isotope geochemistry

A total of 19 single spot analyses on the rims of 19 zircon grains was obtained for sample 18IM13C. One analysis has been omitted due to a high $^{16}\text{O}^{1\text{H}}/^{16}\text{O}$ ratio as compared to the analysed primary standard. The remaining analyses yield a weighted mean $\delta^{18}\text{O}$ of $8.12 \pm 0.70\text{\textperthousand}$ ($n=18$); with one analysis outside of 2σ .

A1.4 Sample 18IM14A

U-Pb geochronology

Sample 18IM14A is a coarse-grained garnet-bearing granite. Zircon isolated from this sample is colorless to brown, euhedral and elongated, and up to $600 \mu\text{m}$ long. CL images reveal cores with oscillatory zoning overgrown by homogenous to weakly zoned rims with low-CL response

that truncate the growth pattern of the core. Some grains show a bright white growth zone between the core and rim. A total of 14 single spot analyses on 10 zircon grains was obtained for sample 18IM14A. Eight analyses are located on zircon rims, six are located on zircon cores. One rim analysis was omitted due to high common Pb content. The remaining analyses are concordant ($n=12$) to weakly normally discordant ($\sim 8\%$ discordant, $n=1$). All seven zircon rim analyses are $< 3\%$ discordant and yield $^{207}\text{Pb}/^{206}\text{Pb}^*$ ages that range from 1986 ± 20 Ma to 1796 ± 30 Ma (1σ) and show over dispersion in their single spot U-Pb ages relative to analytical uncertainty alone, indicating a more complex zircon growth or alteration history. Given the similar Th/U ratios of all rim analyses ($\text{Th}/\text{U} = 0.02\text{-}0.08$) and the likelihood of radiogenic Pb mobility we consider the oldest statistical coherent population as the best estimate of their crystallization age. The oldest statistically coherent population ($n=4$) yields a weighted mean $^{207}\text{Pb}/^{206}\text{Pb}^*$ age of 1948 ± 72 Ma (MSWD=2.8) which is interpreted as the magmatic crystallization age of the granite. Analyses $<8\%$ discordant located on zircon cores yield a weighted mean $^{207}\text{Pb}/^{206}\text{Pb}^*$ age of 2315 ± 28 Ma ($n=5$, MSWD=1.5) and are interpreted to date an inherited component.

Alternative interpretations are possible. Low zircon Th/U ratios (<0.1) as in sample 18IM14A have been observed in sediment-derived granites and migmatites in previous studies, and may be related to the simultaneous growth of monazite (Cesare et al., 2003; Villaros et al., 2012; Yakymchuk et al., 2018). However, the low Th/U ratios of the zircon rims of this sample could also indicate that these rims are metamorphic. This is further supported by the CL images revealing weak to non-existent oscillatory zoning in the rims indicating growth in a fluid-rich environment. If the zircon rims truly record metamorphism, the weighted mean $^{207}\text{Pb}/^{206}\text{Pb}^*$ age of 2315 ± 28 Ma of the zircon cores would reflect the magmatic crystallization age of the granite. This age, however, does not overlap with any of the magmatic events recognized previously in the Daquingshan area (Dong et al., 2014, and references therein), but is in agreement with the 2.30 to 1.95 Ga depositional ages suggested for the sedimentary protolith of the khondalite series (Liu et al., 2017, and references therein). Therefore, the age of 1948 ± 72 Ma obtained for the rims is interpreted to reflect magmatic crystallization.

O isotope geochemistry

A total of 18 single spot analyses on the rims of 18 zircon grains was obtained for sample 18IM14A. They yield a weighted mean $\delta^{18}\text{O}$ of $4.65 \pm 0.85\text{\textperthousand}$ ($n=17$); with one analysis outside of 2σ .

A2.1.5 Sample 18IM15B

U-Pb geochronology

Sample 18IM15B is a medium-grained garnet-bearing granite. Zircon isolated from this sample is colorless to brown, subhedral to euhedral, and up to $400\mu\text{m}$ long. CL images reveal two types of zircon grains in this sample. Type one has cores with oscillatory zoning, overgrown by a low-CL response, homogenous rim and a bright, thinner outer rim. Some cores of type 1 grains show brittle fractures that have been sealed by the overgrowing rim implying that the cores underwent physical stress before overgrowth. Grain type two shows a low-CL response soccer ball growth pattern overgrown by a thin, bright rim. A total of 15 single spot analyses on 12 zircon grains was obtained for sample 18IM15B. Nine analyses are located on zircon rims (two of them on low-CL response, inner rims, and seven of them on outer, bright rims), six are located on zircon cores. Two analyses were omitted due to high common Pb content. The remaining analyses are concordant ($n=12$) to normally discordant ($n=1$). The six analyses that are $< 10\%$ discordant located on zircon rims yield a weighted mean $^{207}\text{Pb}/^{206}\text{Pb}^*$ age of $2530 \pm 60\text{ Ma}$ (MSWD=0.73), which is interpreted as the magmatic crystallization age of the granite. All six analyses located on zircon cores are $< 5\%$ discordant and yield a concordia age of $2545 \pm 36\text{ Ma}$ (MSWD=0.67), which is indistinguishable from the age obtained from zircon rims. Considering that rims seal brittle fractures of cores, as shown by some grains, the concordia age of the cores is therefore interpreted to date an inherited component.

O isotope geochemistry

A total of 22 single spot analyses was obtained for sample 18IM15B. Eleven spots are located on the rims of 11 zircon grains. Seven spots are located on the cores of seven zircon grains. Four spots overlap multiple growth zones and are not considered further. The analyses located

on zircon rims yield a weighted mean $\delta^{18}\text{O}$ of $8.57 \pm 0.42\text{\textperthousand}$ ($n=11$). The analyses located on zircon cores yield a distinctly lower weighted mean $\delta^{18}\text{O}$ of $5.71 \pm 1.08\text{\textperthousand}$ ($n=17$).

A2.1.6 Sample 18IM19

U-Pb geochronology

Sample 18IM19 is a coarse-grained garnet rich granite. Zircon isolated from this sample is colorless to brown, subhedral, and up to $300 \mu\text{m}$ long. CL images reveal oscillatory zoning of the cores overgrown by low-CL response homogenous to weakly zoned rims. The zoning pattern of the cores is truncated by rims indicating that the cores underwent physical abrasion before overgrowth. A total of 23 single spot analyses on 18 zircon grains was obtained for sample 18IM19. Seventeen analyses are located on zircon rims, six are located on zircon cores. One analysis overlaps multiple growth zones and is not considered further. All remaining analyses are $< 8\%$ discordant. The most concordant analyses ($< 6\%$ discordant) that are located on zircon rims yield a weighted mean $^{207}\text{Pb}/^{206}\text{Pb}^*$ age of $2478 \pm 18 \text{ Ma}$ ($n=13$, MSWD=2.0), which is interpreted as the magmatic crystallization age of the granite. Analyses located on zircon cores yield $^{207}\text{Pb}/^{206}\text{Pb}^*$ ages that range from $2469 \pm 76 \text{ Ma}$ to $2657 \pm 17 \text{ Ma}$ (1σ) and do not define a single population. They are interpreted to date inherited detrital components which is in accordance with the truncated nature of the core-rim boundaries in these grains.

O isotope geochemistry

A total of 40 single spot analyses was obtained for sample 18IM19. Thirty-six spots are located on the rims of 36 zircon grains. Four spots are located on the cores of four zircon grains. The analyses located on zircon rims yield a weighted mean $\delta^{18}\text{O}$ of $7.21 \pm 0.58\text{\textperthousand}$ ($n=35$); with one analysis outside of 2σ . The analyses located on zircon cores yield a lower weighted $\delta^{18}\text{O}$ values that range from $5.72 \pm 0.37\text{\textperthousand}$ to $6.22 \pm 0.31\text{\textperthousand}$.

A2.1.7 Sample 18IM20

U-Pb geochronology

Sample 18IM20 is a coarse-grained garnet-rich granite. Zircons isolated from this sample are subhedral to euhedral, dark purple in color and up to $200 \mu\text{m}$ long. CL images reveal blurred growth pattern with a low-CL response in cores overgrown by oscillatory zoned rims that have

a stronger CL response. A total of 10 single spot analyses on the rims of 10 zircon grains was obtained for sample 18IM20. The analyses are concordant ($n=8$) to normally or reversely discordant ($n=2$). The eight analyses that are $< 10\%$ discordant yield $^{207}\text{Pb}/^{206}\text{Pb}^*$ ages that range from 2452 ± 94 Ma to 2231 ± 44 Ma (1σ) and show over dispersion in their single spot U-Pb ages relative to analytical uncertainty alone, indicating a more complex zircon growth or alteration history. Given the similar Th/U ratios of all rim analyses ($\text{Th}/\text{U} = 0.3\text{-}0.6$) and the likelihood of radiogenic Pb mobility, we consider the oldest statistically coherent population as the best estimate of their crystallization age. The oldest statistically coherent population ($n=5$) yields a weighted mean $^{207}\text{Pb}/^{206}\text{Pb}^*$ age of 2374 ± 48 Ma (MSWD=0.66) which is interpreted as the magmatic crystallization age of the granite.

O isotope geochemistry

A total of 17 single spot analyses on the rims of 17 zircon grains was obtained for sample 18IM20. They yield a weighted mean $\delta^{18}\text{O}$ of $7.39 \pm 0.70\text{\textperthousand}$ ($n=17$).

A2.1.8 Sample 18IM21C

U-Pb geochronology

Sample 18IM21C is a coarse-grained garnet-bearing quartz-rich granitoid. Zircon isolated from this sample is purple, euhedral, mostly elongated and up to $500 \mu\text{m}$ long. CL images reveal cores with blurred oscillatory zoning, overgrown by low-CL response rims that are homogenous to weakly zoned. A total of six single spot analyses on the rims of six zircon grains has been obtained for sample 18IM21C. All analyses are $< 3\%$ discordant and yield a concordia age of 1855 ± 16 Ma (MSWD=1.0) which is interpreted as the magmatic crystallization age of the quartz-rich granitoid.

O isotope geochemistry

A total of 22 single spot analyses on the rims of 22 zircon grains was obtained for sample 18IM21C. One analysis has been omitted due to a high $^{16}\text{O}^{1\text{H}}/^{16}\text{O}$ ratio as compared to the analysed primary standard. The remaining analyses yield a weighted mean $\delta^{18}\text{O}$ of $6.71 \pm 0.52\text{\textperthousand}$ ($n=21$).

A2.1.9 Sample 18IM23D

U-Pb geochronology

Sample 18IM23D is a coarse-grained garnet-bearing granite. Zircon isolated from this sample is purple, euhedral, and up to 150 µm long. CL images reveal diffuse zircon growth patterns in this sample. Growth pattern of cores tend to be more blurred, whereas rims of some grains exhibit a weak oscillatory zoning. A total of eight single spot analyses on the rims of eight zircon grains was obtained for sample 18IM23D. The analyses are concordant ($n=6$) to normally discordant ($n=2$). Analyses that are < 10% discordant yield a weighted mean $^{207}\text{Pb}/^{206}\text{Pb}^*$ age of 2453 ± 11 Ma ($n=6$, MSWD=0.86), which is interpreted as the magmatic crystallization age of the granite.

O isotope geochemistry

A total of 16 single spot analyses on the rims of 16 zircon grains was obtained for sample 18IM23D. Three analyses have been omitted due to high $^{16}\text{O}^{1\text{H}}/^{16}\text{O}$ ratios as compared to the analysed primary standard. The remaining analyses yield a weighted mean $\delta^{18}\text{O}$ of $6.31 \pm 0.63\text{\textperthousand}$ ($n=12$).

A2.1.10 Sample 18IM25C

U-Pb geochronology

Sample 18IM25C is a medium-grained muscovite-biotite granite. Zircon isolated from this sample is colourless to brown, euhedral, and up to 300 µm long. CL images reveal oscillatory zoning in cores. Cores are overgrown by rims with low-CL response close to the core that becomes brighter with more distinctive oscillatory zoning towards the outside of the grain. In some cases the growth pattern of the core is truncated by the rim implying that the cores underwent physical abrasion before rim overgrowth. A total of 16 single spot analyses on eight zircon grains was obtained for sample 18IM25C. Twelve analyses are located on zircon rims, four are located on zircon cores. One rim and one core analyses were omitted due to high common Pb content. The remaining analyses are concordant ($n=11$) to weakly normally discordant (7 to $\leq 10\%$ discordant, $n=3$). Analyses that are < 7% discordant located on zircon rims yield a weighted mean $^{207}\text{Pb}/^{206}\text{Pb}^*$ age of 2493 ± 28 Ma ($n=9$, MSWD=0.86) which is

interpreted as the magmatic crystallization age of the Ms Bt granite. Three analyses located on zircon cores are < 10% discordant and yield $^{207}\text{Pb}/^{206}\text{Pb}^*$ ages that overlap within 1σ of each other. They are interpreted to date inherited detrital components which is in accordance with the truncating nature of the core-rim boundaries exhibited by some zircon grains. The most concordant analysis located on an inherited core yields a $^{207}\text{Pb}/^{206}\text{Pb}^*$ age of 2532 ± 8 (1σ).

O isotope geochemistry

A total of 21 single spot analyses on the rims of 21 zircon grains was obtained for sample 18IM21C. One analysis has been omitted due to a high $^{16}\text{O}^{1\text{H}}/^{16}\text{O}$ ratio as compared to the analysed primary standard. The remaining analyses yield a weighted mean $\delta^{18}\text{O}$ of $6.86 \pm 0.89\text{\textperthousand}$ ($n=20$).

A2.1.11. Sample 18IM3

U-Pb geochronology

Sample 18IM3 is a coarse-grained garnet-bearing granite. Zircon isolated from this sample is pink, euhedral, and up to $150 \mu\text{m}$ long. CL images reveal blurred to metamict cores, overgrown by low-CL response rims with oscillatory zoning. Some grains exhibit ubiquitous oscillatory zoning. A total of six single spot analyses on six zircon grains was obtained for sample 18IM3. Five analyses are located on zircon rims, one is located on a zircon core. The analyses are concordant ($n=4$) to normally discordant ($n=2$). Analyses that are < 10% discordant located on zircon rims yield a weighted mean $^{207}\text{Pb}/^{206}\text{Pb}^*$ age of 1917 ± 70 Ma ($n=3$, MSWD=0.52) which is interpreted as the magmatic crystallisation age of the granite. The analysis located on a zircon core yields a $^{207}\text{Pb}/^{206}\text{Pb}^*$ age of 2890 ± 419 Ma (1σ) suggesting that this core is an inherited component.

O isotope geochemistry

A total of 14 single spot analyses on the rims of 14 zircon grains was obtained for sample 18IM3. Six analyses has been omitted due to high $^{16}\text{O}^{1\text{H}}/^{16}\text{O}$ ratios as compared to the analysed primary standard. The remaining analyses yield a weighted mean $\delta^{18}\text{O}$ of $11.41 \pm 1.00\text{\textperthousand}$ ($n=8$).

A2.2 Bulk rock trace element concentrations

Clay-rich sediments and sediment melts tend to have higher Rb/Sr and Rb/Ba ratios than clay-poor ones (Sylvester, 1998). However, Rb/Ba and Rb/Sr ratios of sediment-derived melts are not solely controlled by the maturity of the sedimentary source (i.e., clay-content), but also depend on the degree of partial melting, and the melting reaction (biotite vs muscovite breakdown, fluid-present vs –absent melting, equilibrium vs disequilibrium melting, etc.) (Harris and Inger, 1992). As Sr and Ba are compatible in feldspars whereas Rb is incompatible, Rb/Sr and Rb/Ba ratios of the melt are positively correlated with the amount of residual feldspar (Harris and Inger, 1992; Sylvester, 1998). Hence, sediment-derived melts commonly exhibit Rb/Sr and Rb/Ba ratios that are equal or higher than those of their sedimentary sources (Sylvester, 1998). Limited published trace element compositions of Archean metasedimentary rocks in the Yinshan Block show similar Rb/Ba ratios to and lower Rb/Sr ratios than those reported for Proterozoic metasedimentary rocks in the Inner Mongolia Suture Zone (Figure 2.3, main manuscript) (Wang and Guo, 2017; Wan et al., 2018). In contrast, granitoids studied here with crystallization ages <2.0 Ga show Rb/Ba ratios ranging from 0.08 to 0.15, which are slightly higher than those >2.3 Ga samples with Rb/Ba ratios of 0.03 to 0.07, whereas the Rb/Sr ratios of both groups are similar (0.03–1.40) (Figure 2.3, main manuscript). Rb/Ba ratios of the sediment-derived granitoids studied here show a positive correlation with Zr concentration (Figure 2.3, main manuscript). Zr concentrations reported for metasedimentary rocks in the sampling area show no significant difference between Archean and Proterozoic metasedimentary rocks (Wang and Guo, 2017; Wan et al., 2018). Assuming that these metasedimentary rocks resemble the source rocks of the NCC sediment-derived granitoids, the positive correlation of Zr concentration and Rb/Ba ratios implies that the relatively higher Rb/Ba ratios in <2.0 Ga samples (as compared to their ≥ 2.3 Ga counterparts) are likely the result of higher melting temperatures (Miller et al., 2003) (e.g. through vapour-absent instead of vapour-present melting, and associated changes in the modal composition of the residual; we refer the reader to (Harris and Inger, 1992) for a more detailed discussion of trace element distribution during the partial melting of sediments), rather than compositional differences of the source. Metasomatism and associated alteration of feldspar can affect the bulk rock Rb, Sr, and Ba concentrations (Ennis et al., 2000). A study by Ennis et al. (2000) on the effect of K-

metasomatism on the geochemistry of silicic ignimbrites reports enrichment of Rb and Ba, and depletion of Sr in metasomatized samples compared to unaltered samples. Thus, the Rb/Sr ratios of samples affected by K-metasomatism are elevated compared to unaltered samples. As the Rb/Sr ratios of the samples of this study are low compared to sediment-derived granites reported elsewhere, K-metasomatism is unlikely to have affected the samples of this study. This is further supported by petrographic evidence (Figures A1-3) suggesting that feldspars in the granitoids of this study are not affected by alteration (with the exception of samples 18IM14A, and 18IM21C that have been excluded as discussed below in section A2.4). Compared to the range of Rb/Sr (<0.2 to >80) and Rb/Ba ratios (<0.02 to >30) shown by global strongly peraluminous granites (Sylvester, 1998; Bucholz and Spencer, 2019), the variations in those ratios in the sediment-derived granitoids from the NCC are small. As Rb/Ba and Rb/Sr ratios of sediment-derived melts are not solely a function of the clay-content of the sedimentary source rock, they provide only a first order assessment of the composition of the source. Importantly, however, our data are in accord with previous studies that showed that neither the global average composition of greywacke and shales (Condie, 1993), nor strongly peraluminous granites record a shift to higher Rb/Ba or Rb/Sr ratios across the Archean-Proterozoic transition (Bucholz and Spencer, 2019), suggesting that sediment maturity of the source region was not a dominant control on the oxygen isotope composition of these melts.

A2.3 Temperature of melting

The granitoids from the NCC show a weak negative correlation of ϵ_{Hf} values and bulk-rock Zr concentration (Figure A8), indicating that the Hf isotopic system (of residual phases and melt) may have been in disequilibrium prior to melt extraction (Zhang et al., 2020). Available bulk-rock trace element data of Archean and Proterozoic metasedimentary rocks from the NCC (Wang and Guo, 2017; Wan et al., 2018) suggest that the Zr content of the sedimentary protoliths of the studied granitoids is similar for pre-2.3 Ga and post-2.0 Ga samples (~120 ppm) (discussed in section A2.2). Granitoids younger than 2.0 Ga, however, tend to have higher Zr concentrations than their older counterparts, indicating that the temperature of melting was higher for this group (Miller et al., 2003). If this is true, the proportion of zircon left in the residuum should be higher for the pre-2.3 Ga sediment-derived melts. Hence, ϵ_{Hf} for the pre-

2.3 Ga may be shifted towards more positive ϵ Hf values, and younger TDM_{Hf} leading to an underestimation of the amount crustal recycling for these samples. Importantly however, this does not change the fact, that there is no correlation between radiogenic ^{176}Hf depletion and higher $\delta^{18}\text{O}$ values. Although temperature and, thus, extent of melting will control the $\delta^{18}\text{O}$ of the melt, zircon crystallizing from the melt should have constant $\delta^{18}\text{O}$ values as zircon-melt fractionation factors are strongly temperature- and composition-dependent (Eiler, 2001; Lackey et al., 2008; Bucholz et al., 2017). Higher melt temperatures are associated with decreasing oxygen isotope fractionation between melt and zircon ($\Delta_{\text{melt-zircon}}$) (Bucholz et al., 2017). For granitic melts at 650°C $\Delta_{\text{melt-zircon}}$ is $\sim 2\text{\textperthousand}$, whereas $\Delta_{\text{melt-zircon}}$ for granitic melts at 900°C is $\sim 1\text{\textperthousand}$ (Bucholz et al., 2017). If the melt temperatures of the <2.0 Ga granitoids of this study were higher than those of the >2.3 Ga granitoids (as implied by bulk rock Zr concentrations) the absolute difference in melt $\delta^{18}\text{O}$ between these two groups would be overestimated by up to 1‰. However, the presence of primary hydrous silicate phases (i.e. muscovite, and biotite; Figures A1-3) indicate that these melts were hydrous to a certain extent, and hence, below 900°C. In addition, the increase in average zircon $\delta^{18}\text{O}$ of $\sim 3.5\text{\textperthousand}$ in the ≤ 2.0 Ga sediment-derived granitoids is too large to be the result of higher melt temperatures alone.

A2.4 Omitted samples

Sample 18IM14A shows a low zircon $\delta^{18}\text{O}$ value of $4.7 \pm 0.9\text{\textperthousand}$ which could be the results of 1) hydrothermal alteration of the protolith (Bindeman, 2008; Hollis et al., 2014), 2) zircon crystallization from a fluid during metamorphism (hence, reflecting the oxygen isotope composition of the fluid; Valley et al., 1994), 3) zircon crystallization from a highly fractionated magma derived from an igneous protolith (Wu et al., 2003). In addition, this sample shows anomalously high Zr, La, and Ce concentrations, and an elevated Rb/Sr ratio of 1.4 as compared to all other samples from this region (Rb/Sr ratios ≤ 0.5), which could be related to either of the three possible interpretations. Similar to 18IM14A, sample 18IM21C shows anomalously high Zr, La, and Ce concentrations, which could to be the result of post-crystallization hydrothermal alteration, or crystallization from a highly evolved magma. This sample was collected in close proximity to the Bayan Obo metallogenic province which underwent a series of hydrothermal events (Tian et al., 2020). Hydrothermal alteration in sample

18IM21C is supported by the occurrence of chlorite, and sericite replacing feldspar in this sample (Figure A2), which is commonly observed in hydrothermally altered granitoids (e.g. Plümper and Putnis, 2009). The high Zr concentration in this sample is likely the result of the crystallization from a highly evolved magma. Zircon of this sample may reflect the isotopic composition of the altering fluid rather than that of the sedimentary protolith. Given these uncertainties regarding the origin of the zircon oxygen isotope, and bulk rock compositions of samples 18IM14A and 18IM21C, they are not considered further. It should be noted however, that including these samples still yields an average increase in zircon $\delta^{18}\text{O}$ by 1.5‰ to 8.9‰ post-2.0 Ga.

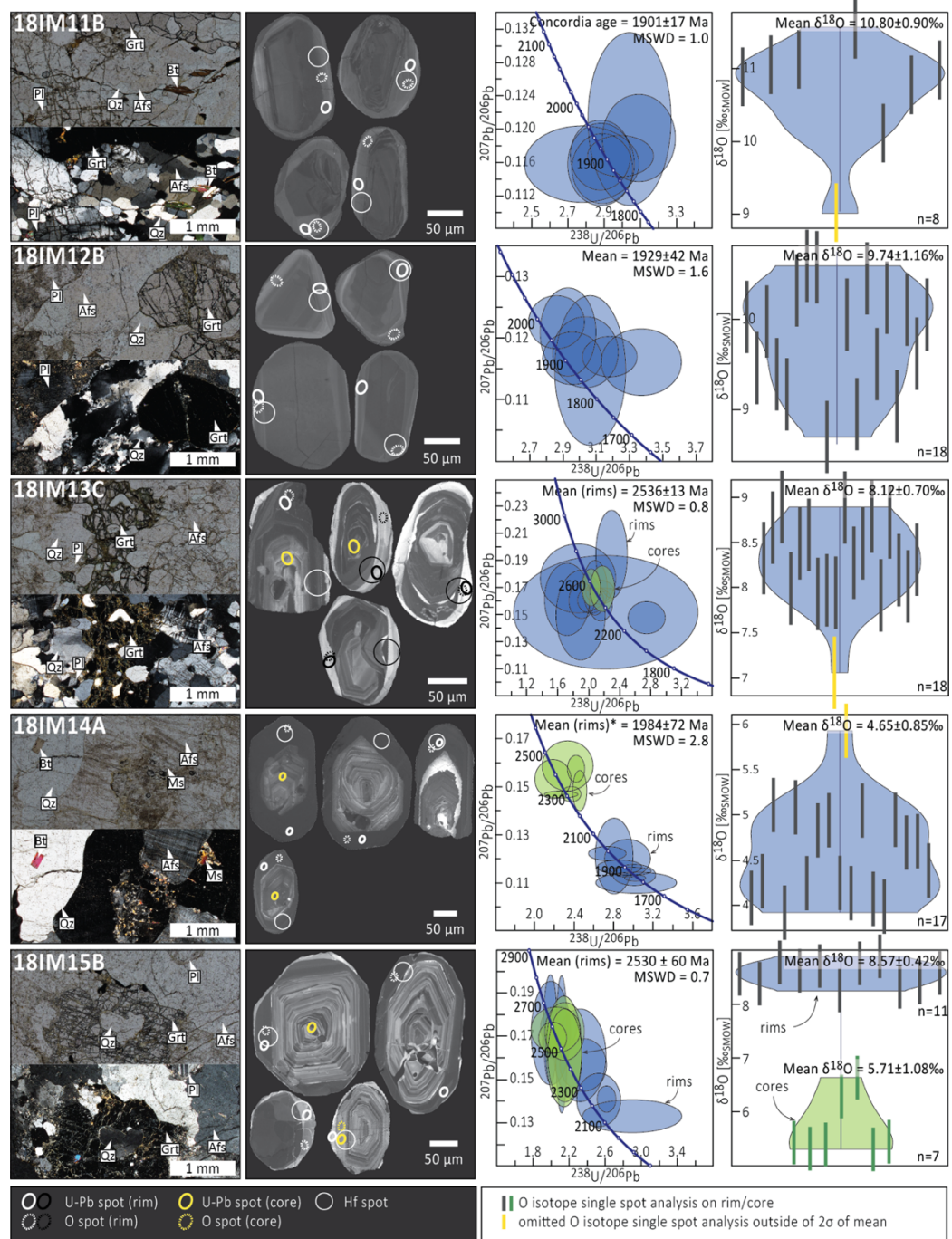


Figure A1. Thin section photomicrographs, CL images of representative zircon grains, concordia diagrams, and oxygen isotope violin plots of representative samples. Spot locations of O, U-Pb, and Hf isotope analyses are marked in the CL images. Results of U-Pb analyses on zircon rims and cores are shown as blue and green ellipses, respectively, in concordia diagrams. Concordia ages, weighted mean ages, and weighted mean $\delta^{18}\text{O}$ are quoted with 2σ uncertainty. Quoted weighted mean ages are calculated from most concordant single spot

$^{207}\text{Pb}/^{206}\text{Pb}^*$ ages. Weighted mean ages marked with asterisk are calculated from the oldest statistical coherent population. Mineral abbreviations: Qz, quartz; Afs, alkali feldspar; Pl, plagioclase; Grt, garnet; Ms, muscovite; Bt, biotite; Ser, sericite; Chl, chlorite.

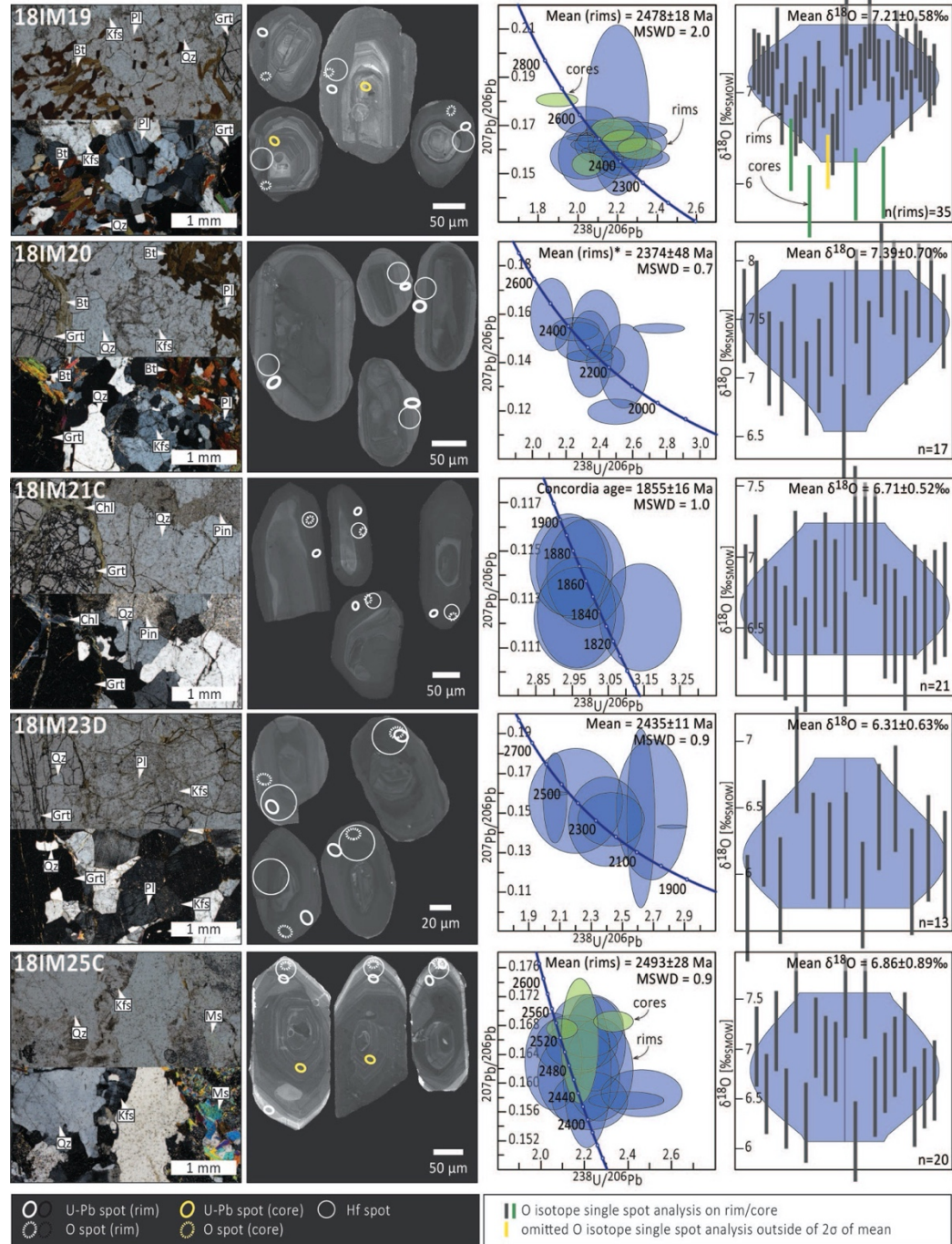


Figure A2. See caption of Figure A1.

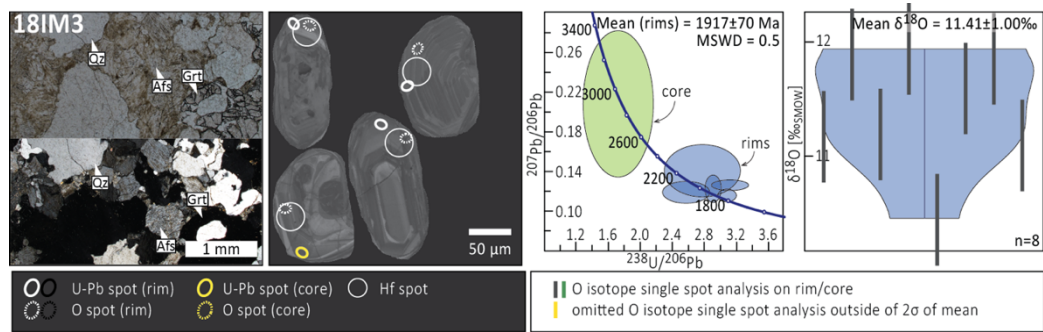


Figure A3. See caption of Figure A1.

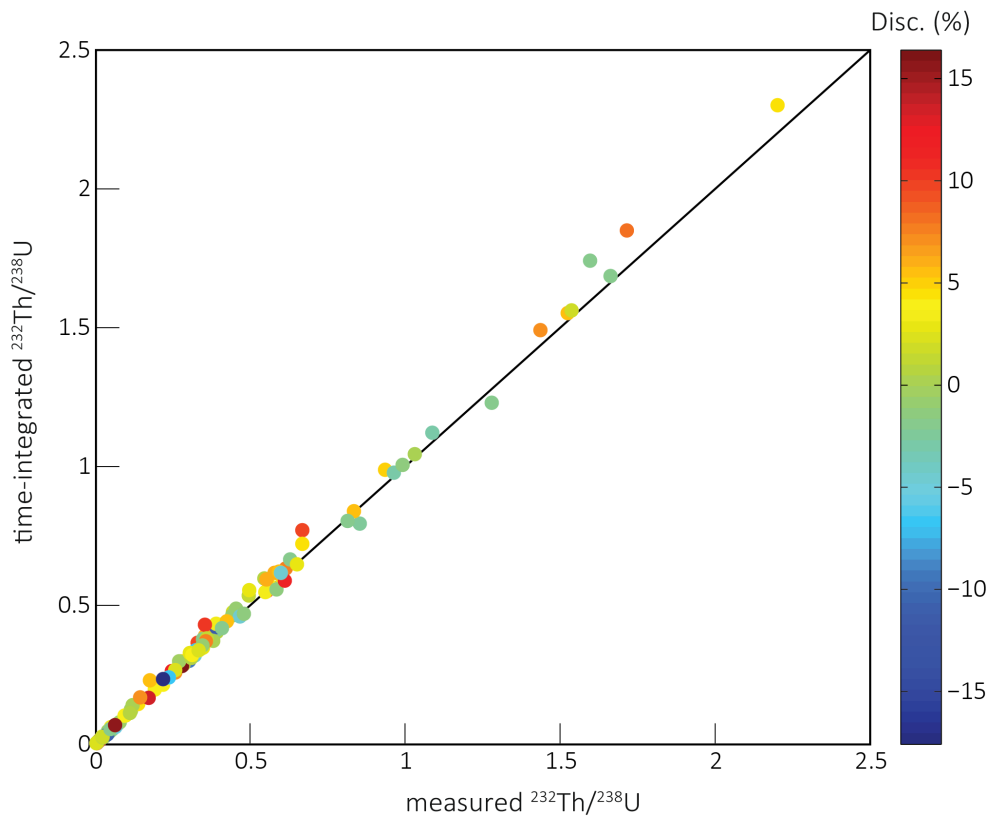


Figure A4. Measured vs. time-integrated Th/U ratios of single spot analyses color coded by discordance. Measured and time-integrated Th/U ratios agree well, indicating that no low-temperature alteration occurred in these grains (Guitreau and Flahaut, 2019; Pidgeon et al., 2017).

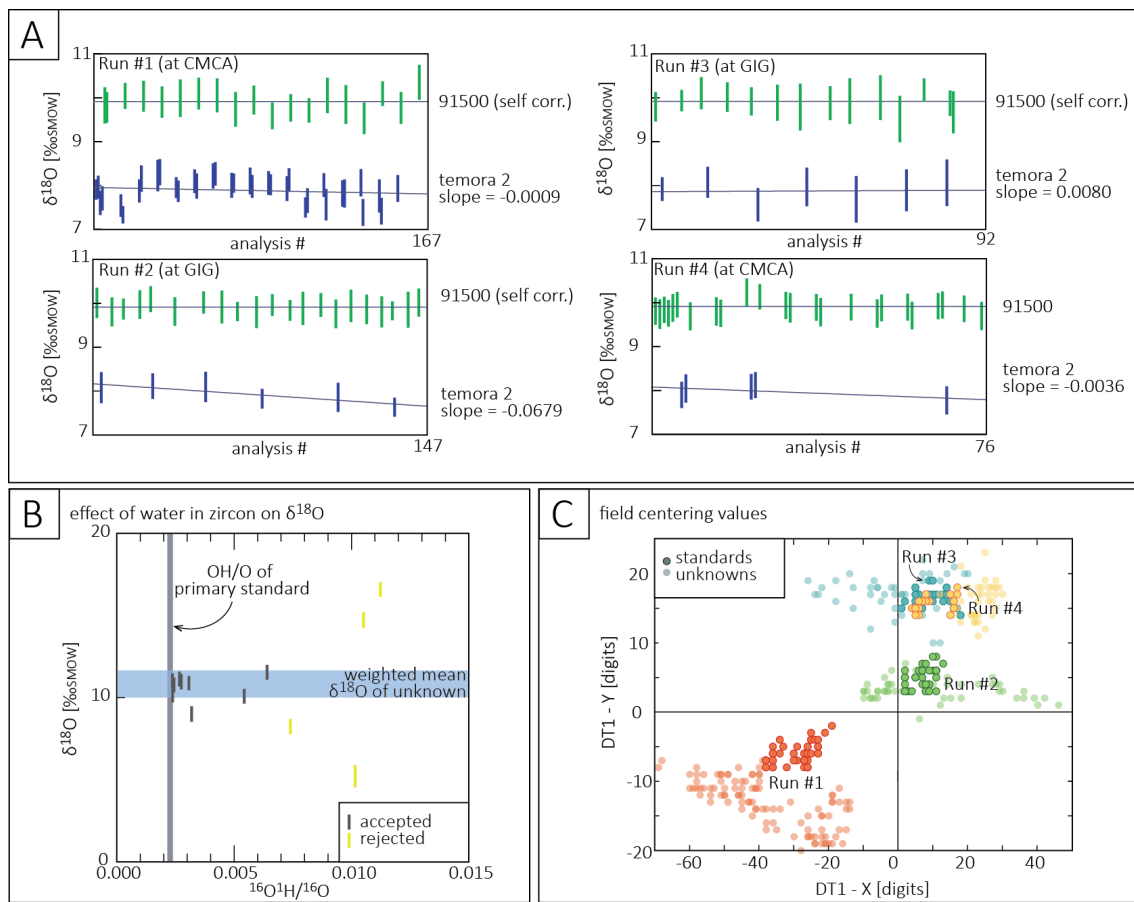


Figure A5. Oxygen isotope data of standards and unknowns. **(A)** Corrected $\delta^{18}\text{O}$ of standards over time show no significant drift. **(B)** OH/O vs $\delta^{18}\text{O}$ plot. Measured $\delta^{18}\text{O}$ shifts with increasing zircon OH-content. **(C)** Field centering values for standards and unknowns for each O isotope analytical run.

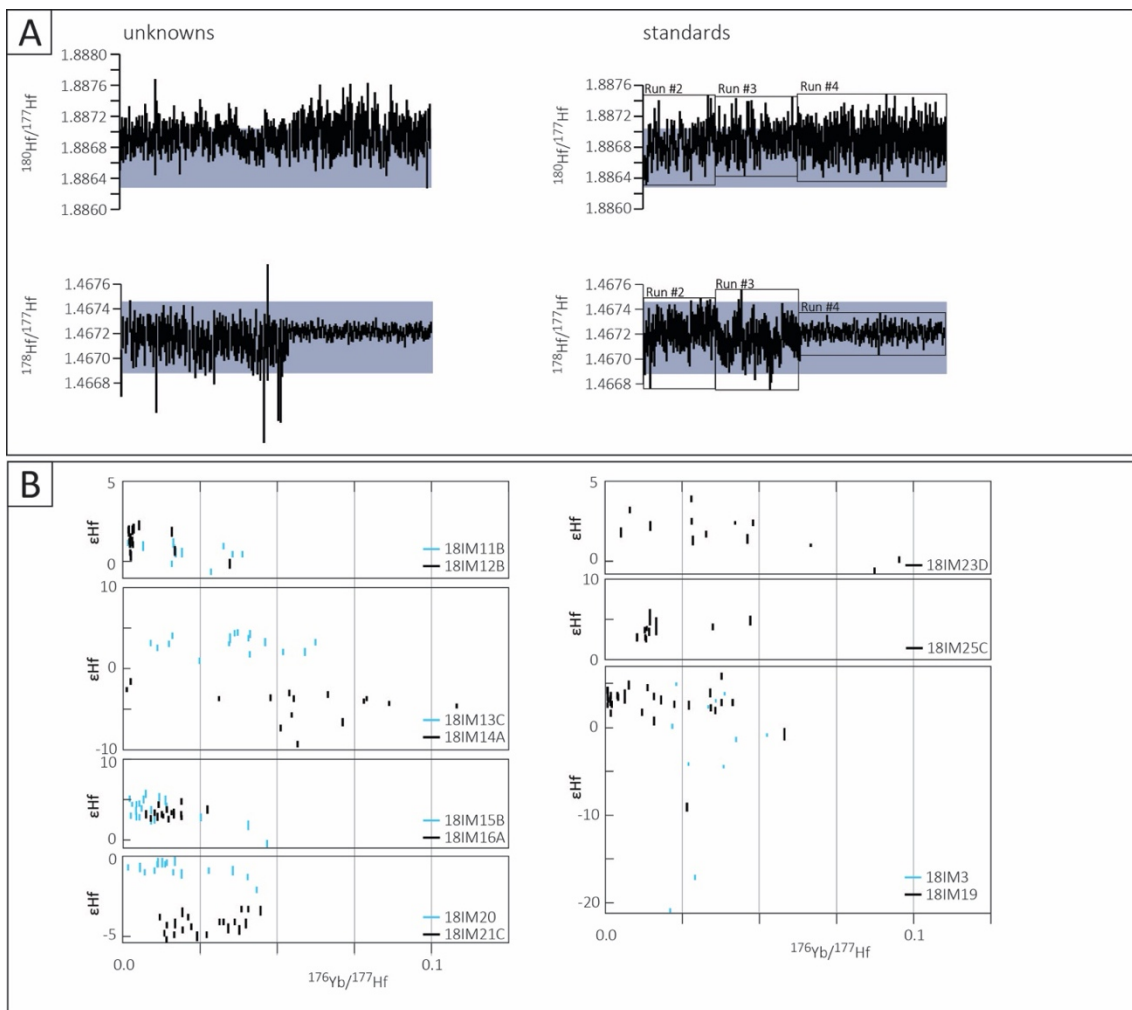


Figure A6. Hf isotope data of standards and unknowns. **(A)** Ratios of Hf stable isotopes of standards and unknowns. **(B)** ϵ Hf vs. $^{176}\text{Yb}/^{177}\text{Hf}$ of unknowns. ϵ Hf shows no correlation with $^{176}\text{Yb}/^{177}\text{Hf}$ indicating an effectual isobaric interference correction.

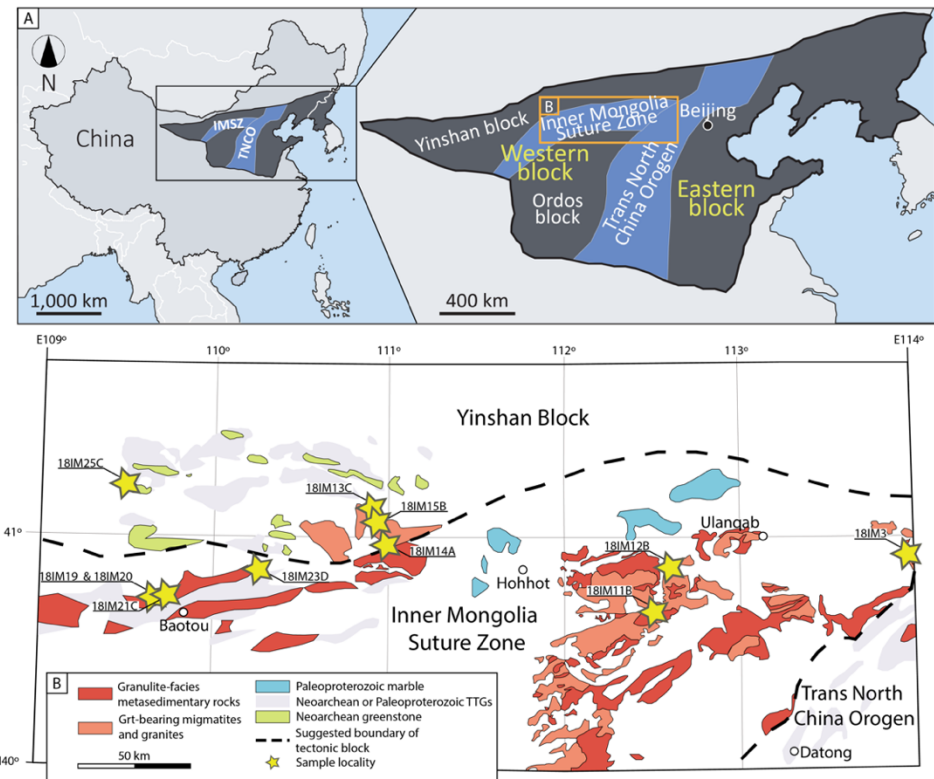


Figure A7. Map with sample locations. **(A)** Simplified map of the North China Craton. Rectangle marks area shown in **(B)**. **(B)** Sample locations are marked by yellow stars. Geological map after Guo et al. (2001); Santosh (2010); Wang et al. (2017).

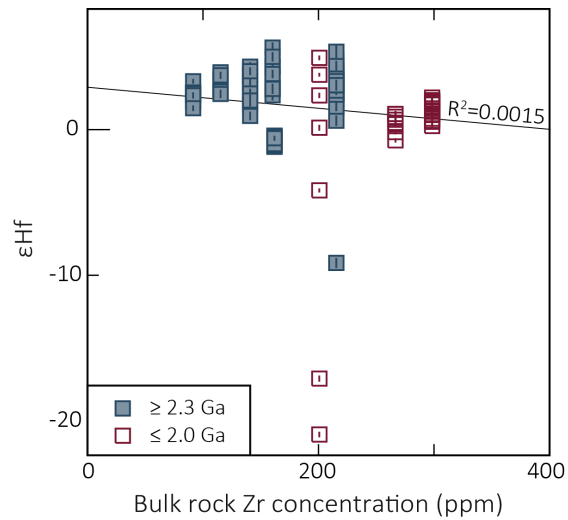


Figure A8. Bulk rock Zr concentration (ppm) vs. ϵHf . Measured ϵHf show a negative correlation with bulk rock Zr concentration, indicating that the Hf isotopic system (of residual phases and melt) may have been in disequilibrium prior to melt extraction (Zhang et al., 2020). Importantly however, this does not change the fact

that high $\delta^{18}\text{O}$ values in zircon are not associated radiogenic ^{176}Hf depletion and higher $\delta^{18}\text{O}$ values (discussed in Appendix A2.3). On average higher Zr concentrations in the <2.3 Ga granitoids may reflect higher melting temperatures as compared to their older counterparts (Miller et al., 2003). The effect of melting temperature on zircon Hf and O isotope, and bulk rock trace element geochemistry is discussed in detail in Appendix A2.2 and A2.3.

U-Pb	calibration standard		uncertainty/ reproducibility (1σ)		U concentration standard		secondary standard				
	session #	# analyses	spot-to-spot	$^{238}\text{U}/^{206}\text{Pb}^*$	# analyses	# analyses		weighted mean age (Ma)	2 σ	MSWD	
2	temora 2	16	2.65%	0.82%	OGC	7	OGC	7	3461 1)	21	0.21
3	91500	4	2.07%	0.50%	91500	4	OGC	2	3470 1)	110	0.04
4	91500	10	0.89%	0.50%	91500	10	OGC	6	3466 1)	21	0.13
5	temora 2	8	1.23%	0.55%	91500	5	91500	5	1075 2)	19	0.52
6	temora 2	6	1.38%	0.76%	91500	4	91500	4	1069 2)	31	0.96

Table A1. U-Pb measurement results of zircon reference materials for SIMS analytical runs. ¹⁾ weighted mean $^{207}\text{Pb}/^{206}\text{Pb}^*$ age; ²⁾ weighted mean $^{238}\text{U}/^{206}\text{Pb}^*$ age.

O isotopes	primary standard		secondary standard		# analyses	$\delta^{18}\text{O}$	2 σ	# analyses	$\delta^{18}\text{O}$	2 σ
	session #	# analyses	session #	# analyses						
1	91500	18	9.9	0.34	temora 2	35	7.88	0.69		
2	91500	21	9.9	0.38	temora 2	6	7.93	0.39		
3	91500	13	9.9	0.23	temora 2	7	7.88	0.38		
4	91500	24	9.9	0.26	temora 2	5	7.98	0.29		

Table A3. O isotope measurement results of zircon reference materials for SIMS analytical runs.

Hf isotopes	Mudtank				91500				Plesovice				stable isotope ratios			
	session #	$^{176}\text{Hf}/^{177}\text{Hf}$	2 σ	n	MSWD	$^{176}\text{Hf}/^{177}\text{Hf}$	2 σ	n	MSWD	$^{176}\text{Hf}/^{177}\text{Hf}$	2 σ	n	MSWD	$^{178}\text{Hf}/^{177}\text{Hf}$	2 σ	$^{180}\text{Hf}/^{177}\text{Hf}$
1	0.2825068	0.0000069	18	0.6	0.282295	0.000017	17	1.5	0.282463	0.000014	9	1.3	1.46704	0.00016	1.886778	0.00020
2	0.2825070	0.0000069	10	0.3	0.282287	0.000016	10	1.1	0.282466	0.000009	6	0.3	1.46723	0.00013	1.88688	0.00031
3	0.2825067	0.0000085	14	0.4	0.282297	0.000026	10	1.3	0.282495	0.000019	5	0.9	1.46718	0.00017	1.88691	0.00024
4	0.2825068	0.0000051	20	0.6	0.282309	0.000009	20	1.4	0.282488	0.000007	10	0.8	1.46721	0.00008	1.88689	0.00022

Table A4. Hf isotope measurement results of zircon reference materials for LA-ICPMS analytical runs.

A2. References

- Baertschi, P., 1976, Absolute ^{18}O content of standard mean ocean water: Earth and Planetary Science Letters, v. 31, p. 341–344, doi:10.1016/0012-821X(76)90115-1.
- Bindeman, I., 2008, Oxygen Isotopes in Mantle and Crustal Magmas as Revealed by Single Crystal Analysis: Reviews in Mineralogy and Geochemistry, v. 69, p. 445–478, doi:10.2138/rmg.2008.69.12.
- Black, L.P. et al., 2004, Improved $^{206}\text{Pb}/^{238}\text{U}$ microprobe geochronology by the monitoring of a trace-element-related matrix effect; SHRIMP, ID-TIMS, ELA-ICP-MS and oxygen isotope documentation for a series of zircon standards: Chemical Geology, v. 205, p. 115–140, doi:10.1016/j.chemgeo.2004.01.003.
- Blichert-Toft, J., and Albarède, F., 1997, The Lu-Hf isotope geochemistry of chondrites and the evolution of the mantle-crust system: Earth and Planetary Science Letters, v. 148, p. 243–258.
- Bucholz, C.E., Jagoutz, O., VanTongeren, J.A., Setera, J., and Wang, Z., 2017, Oxygen isotope trajectories of crystallizing melts: Insights from modeling and the plutonic record: Geochimica et Cosmochimica Acta, v. 207, p. 154–184, doi:10.1016/j.gca.2017.03.027.
- Bucholz, C.E., and Spencer, C.J., 2019, Strongly peraluminous granites across the Archean-Proterozoic transition: Journal of Petrology, doi:10.1093/petrology/egz033.
- Cesare, B., Gomez-Pugnaire, M.T., and Rubatto, D., 2003, Residence time of S-type anatexic magmas beneath the Neogene Volcanic Province of SE Spain: a zircon and monazite SHRIMP study: Contributions to Mineralogy and Petrology, v. 146, p. 28–43, doi:10.1007/s00410-003-0490-x.
- Claoue-Long, J.C., Compston, W., Roberts, J., and Fanning, C.M., 1995, Two Carboniferous ages: a comparison of SHRIMP zircon dating with conventional zircon ages and $^{40}\text{Ar}/^{39}\text{Ar}$ analysis, in Berggre, W.A., Kent, D. V., Aubrey, M.P., and Hardenbol, J. eds., Time Scales and Global Stratigraphic Correlation, Society for Sedimentary Geology, Special publication 54, p. 3–21.
- Condie, K.C., 1993, Chemical composition and evolution of the upper continental crust: Contrasting results from surface samples and shales: Chemical Geology, v. 104, p. 1–37, doi:10.1016/0009-2541(93)90140-E.
- Dan, W., Li, X., Guo, J., Liu, Y., and Wang, X., 2012, Integrated *in situ* zircon U–Pb age and Hf–O isotopes for the Helanshan khondalites in North China Craton: Juvenile crustal materials deposited in active or passive continental margin? Precambrian Research, v. 222–223, p. 143–158, doi:10.1016/j.precamres.2011.07.016.
- Dong, C., Wan, Y., Wilde, S.A., Xu, Z., Ma, M., Xie, H., and Liu, D., 2014, Earliest Paleoproterozoic supracrustal rocks in the North China Craton recognized from the Daqingshan area of the Khondalite Belt: Constraints on craton evolution: Gondwana

Research, v. 25, p. 1535–1553, doi:10.1016/j.gr.2013.05.021.

Eiler, J.M., 2001, Oxygen Isotope Variations of Basaltic Lavas and Upper Mantle Rocks, *in* Valley, J.W. and Cole, D.R. eds., Stable Isotope Geochemistry. Reviews in Mineralogy and Geochemistry, Mineralogical Society of America/Geochemical Society, Washington, DC, p. 319–364.

Ennis, D., Dunbar, N., Campbell, A., and Chapin, C., 2000, The effects of K-metasomatism on the mineralogy and geochemistry of silicic ignimbrites near Socorro, New Mexico: Chemical Geology, v. 167, p. 285–312, doi:10.1016/S0009-2541(99)00223-5.

Guitreau, M., and Flahaut, J., 2019, Record of low-temperature aqueous alteration of Martian zircon during the late Amazonian: Nature Communications, v. 10, p. 2457, doi:10.1038/s41467-019-10382-y.

Guo, J., Zhai, M., and Xu, R., 2001, Timing of the granulite facies metamorphism in the Sanggan area, North China craton: zircon U-Pb geochronology: Science in China Series D: Earth Sciences, v. 44, p. 1010–1018.

Harris, N.B.W., and Inger, S., 1992, Trace element modelling of pelite-derived granites: Contributions to Mineralogy and Petrology, v. 110, p. 46–56.

Hollis, J.A., Van Kranendonk, M.J., Cross, A.J., Kirkland, C.L., Armstrong, R.A., and Allen, C.M., 2014, Low $\delta^{18}\text{O}$ zircon grains in the Neoarchean Rum Jungle Complex, northern Australia: An indicator of emergent continental crust: Lithosphere, v. 6, p. 17–25, doi:10.1130/L296.1.

Lackey, J.S., Valley, J.W., Chen, J.H., and Stockli, D.F., 2008, Dynamic Magma Systems, Crustal Recycling, and Alteration in the Central Sierra Nevada Batholith: the Oxygen Isotope Record: Journal of Petrology, v. 49, p. 1397–1426, doi:10.1093/petrology/egn030.

Liu, J., Liu, F., Ding, Z., Liu, P., Chen, J., Liu, C., Wang, F., Yang, H., Cai, J., and Shi, J., 2017, Late Neoarchean–Paleoproterozoic arc-continent accretion along the Khondalite Belt, Western Block, North China Craton: Insights from granitoid rocks of the Daqingshan–Wulashan area: Precambrian Research, v. 303, p. 494–519, doi:10.1016/j.precamres.2017.06.006.

Miller, C.F., McDowell, S.M., and Mapes, R.W., 2003, Hot and cold granites? Implications of zircon saturation temperatures and preservation of inheritance: Geology, v. 31, p. 529, doi:10.1130/0091-7613(2003)031<0529:HACGIO>2.0.CO;2.

Paton, C., Hellstrom, J., Paul, B., Woodhead, J., and Hergt, J., 2011, Iolite: Freeware for the visualisation and processing of mass spectrometric data: Journal of Analytical Atomic Spectrometry, v. 26, p. 2508, doi:10.1039/c1ja10172b.

Pidgeon, R.T., Nemchin, A.A., and Whitehouse, M.J., 2017, The effect of weathering on U-Th-Pb and oxygen isotope systems of ancient zircons from the Jack Hills, Western Australia:

- Geochimica et Cosmochimica Acta, v. 197, p. 142–166, doi:10.1007/s11947-009-0181-3.
- Plümper, O., and Putnis, A., 2009, The Complex Hydrothermal History of Granitic Rocks: Multiple Feldspar Replacement Reactions under Subsolidus Conditions: Journal of Petrology, v. 50, p. 967–987, doi:10.1093/petrology/egp028.
- Santosh, M., 2010, Assembling North China Craton within the Columbia supercontinent: The role of double-sided subduction: Precambrian Research, v. 178, p. 149–167, doi:10.1016/j.precamres.2010.02.003.
- Schmitt, A.K., Magee Jr., C.W., Williams, I.S., Holden, P., Ireland, T.R., DiBugnara, D.L., and Bodorkos, S., 2019, Oxygen isotopic heterogeneity in the Temora-2 reference zircon; doi:10.11636/Record.2019.004.
- Sláma, J. et al., 2008, Plešovice zircon — A new natural reference material for U–Pb and Hf isotopic microanalysis: Chemical Geology, v. 249, p. 1–35, doi:10.1016/j.chemgeo.2007.11.005.
- Spencer, C.J., Kirkland, C.L., Roberts, N.M.W., Evans, N.J., and Liebmann, J., 2019, Strategies towards robust interpretations of in situ zircon Lu–Hf isotope analyses: Geoscience Frontiers, doi:10.1016/j.gsf.2019.09.004.
- Stacey, J.S., and Kramers, J.D., 1975, Approximation of terrestrial lead isotope evolution by a two-stage model: Earth and Planetary Science Letters, v. 26, p. 207–221, doi:10.1016/0012-821X(75)90088-6.
- Steiger, R.H., and Jäger, E., 1977, Subcommission on geochronology: Convention on the use of decay constants in geo- and cosmochronology: Earth and Planetary Science Letters, v. 36, p. 359–362, doi:10.1016/0012-821X(77)90060-7.
- Stern, R.A., Bodorkos, S., Kamo, S.L., Hickman, A.H., and Corfu, F., 2009, Measurement of SIMS Instrumental Mass Fractionation of Pb Isotopes During Zircon Dating: Geostandards and Geoanalytical Research, v. 33, p. 145–168, doi:10.1111/j.1751-908X.2009.00023.x.
- Sylvester, P.J., 1998, Post-collisional strongly peraluminous granites: Lithos, v. 45, p. 29–44, doi:10.1016/S0024-4937(98)00024-3.
- Tian, P., Yang, X., and Yuan, W., 2020, Formation and preservation of the Bayan Obo Fe-REE-Nb deposit, Inner Mongolia: Insights from evidences of petrogenesis, geochemistry and apatite fission track dating: Solid Earth Sciences, doi:10.1016/j.sesci.2020.08.002.
- Valley, J.W., Chiarenzelli, J.R., and McLelland, J.M., 1994, Oxygen isotope geochemistry of zircon: Earth and Planetary Science Letters, v. 126, p. 187–206, doi:10.1016/0012-821X(94)90106-6.
- Villaros, A., Buick, I.S., and Stevens, G., 2012, Isotopic variations in S-type granites: an inheritance from a heterogeneous source? Contributions to Mineralogy and Petrology, v.

163, p. 243–257, doi:10.1007/s00410-011-0673-9.

Wan, Y., Peng, P., Liu, S., Kröner, A., Guo, J., Dong, C., and Liu, D., 2018, Late Paleoproterozoic tectono-thermal event in the northwestern North China Craton: Evidence from U-Pb dating and O-Hf isotopic compositions of zircons from metasedimentary rocks north of Hohhot City, Inner Mongolia, northern China: *Journal of Asian Earth Sciences*, v. 167, p. 152–164, doi:10.1016/j.jseas.2017.09.012.

Wang, D., and Guo, J., 2017, Late Archean high-pressure pelitic granulites in the Yinshan Block, North China Craton: *Precambrian Research*, v. 303, p. 251–267, doi:10.1016/j.precamres.2017.03.027.

Wiedenbeck, M. et al., 2004, Further characterisation of the 91500 zircon crystal: *Geostandards and Geoanalytical Research*, v. 28, p. 9–39, doi:10.1111/j.1751-908X.2004.tb01041.x.

Wingate, M.T.D., and Kirkland, C.L., 2015, Introduction to geochronology information released in 2015: *Geological Survey of Western Australia*, p. 5p.

Woodhead, J.D., and Hergt, J.M., 2005, A Preliminary Appraisal of Seven Natural Zircon Reference Materials for In Situ Hf Isotope Determination: *Geostandards and Geoanalytical Research*, v. 29, p. 183–195, doi:10.1111/j.1751-908X.2005.tb00891.x.

Wu, F., Jahn, B., Wilde, S.A., Lo, C., Yui, T., Lin, Q., Ge, W., and Sun, D., 2003, Highly fractionated I-type granites in NE China (I): geochronology and petrogenesis: *Lithos*, v. 66, p. 241–273, doi:10.1016/S0024-4937(02)00222-0.

Yakymchuk, C., Kirkland, C.L., and Clark, C., 2018, Th/U ratios in metamorphic zircon: *Journal of Metamorphic Geology*, v. 36, p. 715–737, doi:10.1111/jmg.12307.

Yang, Q., Xia, X., Zhang, W., Zhang, Y., Xiong, B., Xu, Y., Wang, Q., and Wei, G., 2018, An evaluation of precision and accuracy of SIMS oxygen isotope analysis: *Solid Earth Sciences*, v. 3, p. 81–86, doi:10.1016/j.sesci.2018.05.001.

Zhang, C., Liu, D., Zhang, X., Spencer, C., Tang, M., Zeng, J., Jiang, S., Jolivet, M., and Kong, X., 2020, Hafnium isotopic disequilibrium during sediment melting and assimilation: *Geochemical Perspectives Letters*, p. 34–39, doi:10.7185/geochemlet.2001.

Zhao, G., Wilde, S.A., Cawood, P.A., and Lu, L., 1999, Tectonothermal history of the basement rocks in the western zone of the North China Craton and its tectonic implications: *Tectonophysics*, v. 310, p. 37–53.

Zhao, G., and Zhai, M., 2013, Lithotectonic elements of Precambrian basement in the North China Craton: Review and tectonic implications: *Gondwana Research*, v. 23, p. 1207–1240, doi:10.1016/j.gr.2012.08.016.

Appendix B

<i>Grp</i>	<i>Sample</i>	<i>Grain/spot</i>	^{28}U	^{20}Th	$^{20}\text{Th}/^{28}\text{U}$	$^{20}\text{Pb}^*$	$^{28}\text{Pb}^*$	$^{20}\text{Th}/^{28}\text{U}$	f^{28}	$^{28}\text{U}/^{28}\text{U}$	f^{28}	$^{20}\text{Pb}/^{28}\text{Pb}$	$^{28}\text{U}/^{28}\text{Pb}$	$^{20}\text{Pb}^*/^{28}\text{Pb}^*$	$^{28}\text{U}/^{28}\text{Pb}^*$	$^{20}\text{Pb}^*/^{28}\text{Pb}^*$	$^{28}\text{U}/^{28}\text{Pb}^*$	<i>date (Ma)</i>	<i>#</i>	<i>Disc session</i>			
<i>ID</i>	<i>ID</i>		(ppm)	(ppm)		(ppm)	(ppm)		(%)		(%)		(%)		(%)		(%)		#				
1	18IM11B	IM11B.7.1	105	150	1.436	29	12	1.491	0.00	3.091	0.082	0.11890	0.21504	3.091	0.082	0.11890	0.00216	1807	48	1940	35	6.9	5
1	18IM11B	IM11B.1.1	248	36	0.146	70	3	0.169	0.04	3.038	0.093	0.12147	0.42392	3.039	0.093	0.12147	0.00424	1834	56	1974	69	7.1	5
1	18IM11B	IM11B.3.1	142	47	0.334	41	4	0.338	0.05	2.988	0.075	0.11710	0.09742	2.990	0.075	0.11669	0.00102	1860	46	1906	17	2.4	5
1	18IM11B	IM11B.8.1	164	67	0.409	49	6	0.417	0.19	2.884	0.068	0.11667	0.16541	2.889	0.068	0.11524	0.00173	1916	45	1884	28	-1.7	5
1	18IM11B	IM11B.12.1	110	109	0.993	33	9	1.006	0.28	2.873	0.075	0.11784	0.18753	2.881	0.075	0.11573	0.00201	1921	50	1891	33	-1.6	5
1	18IM11B	IM11B.6.1	169	58	0.346	50	5	0.356	0.05	2.876	0.068	0.11724	0.17110	2.878	0.068	0.11686	0.00173	1923	46	1909	28	-0.7	5
1	18IM11B	IM11B.13.1	143	86	0.600	44	8	0.617	0.17	2.771	0.129	0.11704	0.17870	2.776	0.129	0.11577	0.00186	1983	92	1892	30	-4.8	5
1	18IM12B	IM12B.6.1	87	53	0.612	22	4	0.589	0.04	3.364	0.099	0.11622	0.21958	3.365	0.099	0.11591	0.00222	1677	49	1894	36	11.4	5
1	18IM12B	IM12B.7.1	244	87	0.358	66	7	0.371	0.03	3.175	0.067	0.11701	0.13258	3.176	0.067	0.11677	0.00133	1765	37	1907	22	7.5	5
1	18IM12B	IM12B.8.1	85	55	0.652	24	4	0.648	0.00	3.059	0.087	0.11454	0.49685	3.059	0.087	0.11454	0.00497	1824	52	1873	81	2.6	5
1	18IM12B	IM12B.11.1	83	182	2.202	23	16	2.302	0.05	3.029	0.080	0.11790	0.23306	3.030	0.080	0.11753	0.00236	1838	49	1919	39	4.2	5
1	18IM12B	IM12B.10.1	150	54	0.361	44	5	0.381	0.00	2.951	0.072	0.11652	0.17351	2.951	0.072	0.11652	0.00174	1881	46	1903	28	1.2	5
1	18IM12B	IM12B.13.1	167	52	0.314	49	5	0.321	0.07	2.923	0.068	0.12131	0.29111	2.925	0.068	0.12082	0.00293	1896	44	1968	48	3.7	5
1	18IM12B	IM12B.12.1	158	55	0.348	47	5	0.348	0.12	2.855	0.069	0.12333	0.16967	2.858	0.069	0.12241	0.00175	1934	46	1992	28	2.9	5
1	18IM13C	IM13C.22.1	109	7	0.065	45	1	0.069	0.04	2.278	0.082	0.19467	1.31750	2.279	0.082	0.19440	0.01318	2345	85	2780	188	15.6	2
1	18IM13C	IM13C.19.1	161	8	0.049	53	1	0.054	-0.02	2.208	0.484	0.15098	1.71360	2.207	0.484	0.15115	0.01713	2409	528	2359	267	-2.1	2
1	18IM13C	IM13C.10.1	55	12	0.220	23	1	0.234	0.12	1.886	0.129	0.14816	1.35014	1.884	0.129	0.14899	0.01350	2745	188	2334	211	17.6	2
1	18IM13C	IM13C.5.1	371	89	0.238	173	12	0.241	0.08	1.846	0.197	0.17693	1.03137	1.848	0.197	0.17637	0.01032	2788	297	2619	153	-6.5	2
1	18IM13C	IM13C.11.1	723	125	0.173	227	10	0.167	0.03	2.736	0.099	0.14792	0.48362	2.737	0.099	0.14768	0.00484	2008	72	2319	76	13.4	1
1	18IM13C	IM13C.8.1	899	275	0.306	360	33	0.328	0.08	2.141	0.071	0.16863	0.04369	2.143	0.071	0.16807	0.00046	2469	82	2538	7	2.7	1
1	18IM13C	IM13C.13.1	730	18	0.024	293	2	0.026	0.10	2.139	0.075	0.16688	0.35974	2.144	0.075	0.16620	0.00360	2471	87	2520	55	1.9	1
1	18IM13C	IM13C.10.2	336	38	0.112	139	4	0.112	0.04	2.074	0.063	0.16941	0.83261	2.073	0.063	0.16971	0.00832	2538	77	2555	125	0.7	1
1	18IM13C	IM13C.18.1	577	38	0.066	246	4	0.062	0.02	2.019	0.067	0.16015	0.38583	2.019	0.067	0.16030	0.00386	2594	86	2439	59	-5.5	1
1	18IM13C	IM13C.17.1	486	19	0.040	220	2	0.035	0.04	1.900	0.069	0.16052	0.533388	1.900	0.069	0.16027	0.00534	2726	99	2459	82	-10.9	3
1	18IM13C	IM13C.10.3	359	125	0.349	144	15	0.378	0.05	2.442	0.059	0.15741	0.48106	2.143	0.059	0.15706	0.00482	2468	68	2424	74	-1.8	3
X	18IM13C	IM13C.8.2	139	67	0.480	59	8	0.469	-0.02	2.025	0.048	0.16947	0.54951	2.024	0.048	0.16964	0.00550	2588	61	2554	83	-1.3	3
X	18IM13C	IM13C.7.2	420	40	0.095	167	5	0.103	0.01	2.165	0.065	0.16865	0.68698	2.166	0.065	0.16859	0.00687	2447	74	2344	104	3.8	3
D	18IM13C	IM13C.7.1	57	35	0.622	28	5	0.599	0.55	1.698	0.118	0.16489	1.07577	1.708	0.118	0.16104	0.01089	2671	206	2467	167	-20.5	2
D	18IM13C	IM13C.1.1	1007	341	0.338	226	14	0.230	0.22	2.415	0.070	0.16119	0.04378	2.420	0.070	0.15964	0.00068	2230	65	2452	11	9.1	1
I	18IM14A	IM14A.23.1	1313	42	0.032	364	3	0.032	0.01	3.020	0.167	0.10993	0.18303	3.021	0.167	0.10982	0.00183	1843	102	1796	30	-2.6	2
I	18IM14A	IM14A.20.1	946	36	0.038	276	3	0.038	0.02	2.940	0.096	0.11496	0.07091	2.941	0.096	0.11483	0.00071	1887	62	1877	12	-0.5	2
I	18IM14A	IM14A.10.1	807	59	0.073	231	5	0.074	0.01	3.003	0.088	0.11328	0.18404	3.004	0.088	0.11319	0.00184	1853	54	1851	30	-0.1	1

Table B1. SIMS zircon U-Pb single spot results. Group ID: I – inherited, X – magmatic, D – rejected.

<i>Gp</i>	<i>Sample</i>	<i>Grain/Spot</i>	$\approx U$	$\approx Th/\text{Th}^{204}U$	$\approx Pb/\text{Pb}^*$	$\approx Pb/\text{Pb}^*$	<i>time-int.</i>	δt_{B}	$\approx U/\text{U}^{204}$	$\approx Th/\text{Th}^{204}U$	$\approx Pb/\text{Pb}^*$	$\approx Pb/\text{Pb}^*$	$\approx U/\text{U}^{204}$	$\approx Pb/\text{Pb}^*$	$\approx U/\text{U}^{204}$	$\approx Pb/\text{Pb}^*$	<i>date (Ma)</i>	$\pm t_{\text{B}}$	$\approx Pb/\text{Pb}^*$	<i>date (Ma)</i>	$\pm t_{\text{B}}$	$\approx Pb/\text{Pb}^*$	<i>Disc. session</i>
<i>ID</i>	<i>ID</i>	<i>ID</i>	(ppm)	(ppm)	measured	(ppm)	(ppm)	(ppm)	(ppm)	(ppm)	(ppm)	(ppm)	(ppm)	(ppm)	(ppm)	(ppm)	(ppm)	(ppm)	(ppm)	(ppm)	(ppm)	(ppm)	
1	18IM14A	IM14A-2.1	2440	113	0.046	734	9	0.044	0.02	2.853	0.092	0.11675	0.12166	2.853	0.093	0.11659	0.090222	1937	63	1905	20	-1.7	1
1	18IM14A	IM14A-5.1	2347	57	0.024	721	5	0.024	0.04	2.796	0.078	0.12136	0.124725	2.797	0.078	0.12110	0.09648	1970	55	1972	105	0.1	1
1	18IM14A	IM14A-1.1	2447	135	0.055	770	12	0.053	0.03	2.730	0.078	0.12226	0.12244	2.731	0.078	0.12205	0.090123	2011	57	1986	20	-1.2	1
1	18IM14A	IM14A-10.2	765	61	0.080	218	5	0.080	0.03	3.012	0.044	0.11223	0.09044	3.013	0.044	0.11199	0.09052	1848	27	1832	8	-0.9	3
X	18IM14A	IM14A-20.2	496	294	0.593	174	31	0.622	0.02	2.453	0.030	0.14855	0.14849	2.454	0.030	0.14841	0.090345	2204	27	2328	54	5.5	3
X	18IM14A	IM14A-4.1	160	275	1.715	57	30	1.851	0.06	2.415	0.035	0.15787	0.23013	2.417	0.035	0.15746	0.090232	2232	33	2429	36	8.1	3
X	18IM14A	IM14A-23.2	467	717	1.537	169	76	1.562	0.01	2.569	0.039	0.14703	0.13295	2.570	0.039	0.14696	0.090133	2270	37	2311	21	1.8	3
X	18IM14A	IM14A-1.2	136	268	1.524	50	22	1.552	0.00	2.350	0.105	0.15576	0.23570	2.350	0.105	0.15876	0.090426	2302	103	2443	65	5.7	3
X	18IM14A	IM14A-7.1	442	360	0.814	168	39	0.804	0.00	2.266	0.069	0.14689	0.06117	2.266	0.069	0.14689	0.090061	2357	71	2310	19	-2.0	1
X	18IM14A	IM14A-11.1	149	190	1.280	58	21	1.229	-0.02	2.183	0.074	0.15311	0.33298	2.183	0.074	0.15327	0.090333	2431	82	2383	52	-2.0	1
D	18IM14A	IM14A-9.1	2335	89	0.038	684	23	0.115	1.55	2.888	0.093	0.13162	0.23986	2.934	0.093	0.12996	0.090523	1891	61	1957	53	3.4	1
1	18IM15B	IM15B-22.1	50	18	0.355	15	2	0.430	0.96	2.865	0.222	0.15973	0.22166	2.892	0.224	0.15271	0.090317	1914	148	2134	51	10.3	3
1	18IM15B	IM15B-6.1	53	14	0.425	12	1	0.442	-0.24	2.539	0.105	0.15476	0.48223	2.534	0.105	0.15642	0.090495	2282	101	2417	77	5.6	3
1	18IM15B	IM15B-10.1	98	157	1.597	41	20	1.741	0.17	2.037	0.056	0.16771	0.29106	2.041	0.056	0.16753	0.090297	2571	71	2523	45	-1.9	3
1	18IM15B	IM15B-8.1	35	22	0.629	15	3	0.665	0.11	1.994	0.088	0.17190	0.97414	1.996	0.088	0.17112	0.090978	2618	115	2549	147	-1.9	3
1	18IM15B	IM15B-4.1	96	56	0.586	41	6	0.558	0.04	1.991	0.032	0.17318	0.21132	1.992	0.032	0.17292	0.090222	2623	42	2586	153	-1.4	3
1	18IM15B	IM15B-17.1	342	166	0.311	159	12	0.311	0.01	2.113	0.026	0.16610	0.28599	2.113	0.026	0.16602	0.091289	2497	31	2518	195	0.8	3
1	18IM15B	IM15B-16.1	217	56	0.259	90	7	0.266	-0.03	2.081	0.082	0.17389	0.80039	2.081	0.082	0.17408	0.090460	2530	100	2597	69	2.6	3
X	18IM15B	IM15B-9.1	113	41	0.564	45	5	0.376	0.09	2.151	0.076	0.16172	0.87763	2.153	0.076	0.16106	0.090879	2459	87	2467	135	0.5	1
X	18IM15B	IM15B-4.1	54	36	0.669	22	4	0.721	0.23	2.142	0.088	0.17349	0.54291	2.147	0.089	0.17212	0.090550	2465	102	2578	82	4.4	1
X	18IM15B	IM15B-6.2	79	30	0.781	32	5	0.373	-0.04	2.138	0.081	0.16246	0.10668	2.137	0.081	0.16278	0.091047	2475	93	2485	160	0.4	1
X	18IM15B	IM15B-14.1	222	369	1.662	95	44	1.686	0.00	2.018	0.064	0.16917	0.28921	2.018	0.064	0.16917	0.090298	2595	82	2549	45	-1.8	1
X	18IM15B	IM15B-16.2	273	93	0.542	115	11	0.343	0.06	2.046	0.111	0.17330	0.42619	2.047	0.111	0.17290	0.090427	2564	139	2586	64	0.8	3
X	18IM15B	IM15B-17.2	67	31	0.468	25	3	0.460	0.10	2.260	0.089	0.14349	0.76842	2.262	0.089	0.14274	0.090771	2560	93	2261	122	-4.4	1
D	18IM15B	IM15B-13.1	135	35	0.263	44	5	0.241	0.78	2.591	0.091	0.14634	0.19998	2.611	0.091	0.14073	0.090249	2090	34	2236	49	6.5	3
D	18IM15B	IM15B-5.1	70	33	0.473	26	3	0.446	0.81	2.299	0.116	0.16458	0.85772	2.318	0.117	0.16990	0.090876	2312	116	2465	134	6.2	3
I	18IM19	IM19A-7.1	520	15	0.048	123	2	0.047	0.02	2.240	0.069	0.15640	0.33138	2.241	0.069	0.15625	0.09034	2379	73	2416	21	1.5	1
I	18IM19	IM19A-21.1	230	62	0.272	90	7	0.298	0.19	2.185	0.044	0.15807	0.35995	2.189	0.044	0.15673	0.090363	2425	49	2421	56	-0.2	3
I	18IM19	IM19C-2.1	405	21	0.052	152	3	0.062	0.00	2.293	0.069	0.15610	0.18965	2.293	0.069	0.15610	0.090190	2333	70	2414	29	3.3	1
I	18IM19	IM19A-10.1	161	4	0.024	61	0	0.027	0.04	2.245	0.075	0.15748	0.18471	2.246	0.075	0.15718	0.090186	2374	79	2426	29	2.1	1
I	18IM19	IM19C-6.1	697	346	0.553	267	44	0.594	0.05	2.244	0.083	0.16773	0.16539	2.245	0.083	0.16779	0.090166	2375	88	2532	25	6.2	1
I	18IM19	IM19A-7.1	520	15	0.048	123	2	0.047	0.02	2.240	0.069	0.15640	0.33138	2.241	0.069	0.15625	0.09034	2379	73	2416	21	1.5	1
I	18IM19	IM19A-18.1	564	3	0.095	219	0	0.004	0.02	2.214	0.066	0.16661	0.17628	2.214	0.066	0.16499	0.090176	2402	71	2461	27	2.4	1
I	18IM19	IM19C-2.1	678	6	0.099	268	1	0.009	0.00	2.176	0.064	0.15942	0.09126	2.176	0.064	0.15958	0.090091	2437	72	2449	14	0.5	1
I	18IM19	IM19A-11.1	531	3	0.096	212	0	0.005	0.02	2.156	0.064	0.16356	0.18319	2.156	0.064	0.16341	0.090183	2456	73	2491	28	1.4	1
I	18IM19	IM19A-3.1	482	55	0.121	181	7	0.149	0.066	2.145	0.065	0.16290	0.32956	2.146	0.065	0.16157	0.090350	2466	74	2472	51	0.5	1

Table B1. Continued.

<i>Gp</i>	<i>Sample</i>	<i>Grain/spot</i>	^{28}U	^{28}Th	$^{28}\text{Th}/^{28}\text{U}$	$^{28}\text{Pb}^*$	$^{28}\text{Pb}^*$	$^{28}\text{U}/^{28}\text{U}$	f^{84}	$^{28}\text{U}/^{28}\text{Pb}$	$^{28}\text{Pb}/^{28}\text{Pb}$	$\pm\text{is}$	$\pm\text{is}$	$^{28}\text{U}/^{28}\text{Pb}^*$	$^{28}\text{Pb}^*/^{28}\text{Pb}^*$	$^{28}\text{U}/^{28}\text{Pb}^*$	$^{28}\text{Pb}^*/^{28}\text{Pb}^*$	<i>Date (Ma)</i>	<i>±is</i>	<i>(%)</i>	<i>#</i>	<i>Disc session</i>	
<i>ID</i>	<i>ID</i>		(ppm)	(ppm)	measured	(ppm)	(ppm)	time-int.	(%)														
1	18IM19	IM19A-2.1	314	10	0.032	127	1	0.027	0.08	2.126	0.066	0.16239	0.153638	2.128	0.066	0.16185	0.00138	2483	77	2475	21	-0.3	1
1	18IM19	IM19A-6.1	476	20	0.042	195	3	0.047	0.05	2.099	0.063	0.16474	0.153632	2.100	0.063	0.16442	0.00055	2511	75	2502	8	-0.4	1
1	18IM19	IM19C-1.1	183	59	0.321	76	7	0.319	-0.05	2.068	0.067	0.15701	0.15801	2.067	0.066	0.15736	0.00598	2543	82	2427	92	-4.8	1
1	18IM19	IM19C-4.1	163	53	0.325	69	7	0.358	-0.10	2.027	0.066	0.15652	0.15893	2.025	0.066	0.15723	0.00390	2587	85	2426	60	-6.6	1
1	18IM19	IM19A-29.1	263	46	0.176	98	6	0.230	0.02	2.311	0.046	0.16033	0.15744	2.311	0.046	0.16020	0.00188	2318	46	2458	29	5.7	3
1	18IM19	IM19A-32.1	234	32	0.139	90	4	0.145	0.07	2.234	0.046	0.16379	0.15962	2.236	0.046	0.16328	0.00192	2383	49	2490	29	4.3	3
1	18IM19	IM19A-24.1	549	34	0.062	230	4	0.063	0.03	2.049	0.032	0.15404	0.15298	2.049	0.032	0.15380	0.00193	2562	40	2389	30	-7.3	3
1	18IM19	IM19C-3.1	155	95	0.615	60	11	0.633	0.04	2.201	0.064	0.17643	0.145731	2.202	0.064	0.17617	0.01438	2414	70	2617	214	7.8	1
X	18IM19	IM19A-21.2	114	40	0.354	43	5	0.389	-0.08	2.300	0.062	0.16224	0.27589	2.298	0.062	0.16277	0.00278	2329	63	2485	42	6.3	3
X	18IM19	IM19A-23.2	100	55	0.549	38	6	0.548	0.04	2.227	0.061	0.16155	0.49666	2.228	0.061	0.16128	0.00498	2390	65	2469	76	3.2	3
X	18IM19	IM19A-8.1	210	118	0.565	83	13	0.568	-0.04	2.176	0.044	0.16766	0.19610	2.175	0.044	0.16792	0.00197	2439	50	2537	30	3.9	3
X	18IM19	IM19A-5.1	152	146	0.964	69	19	0.978	0.15	1.894	0.043	0.18141	0.18040	1.897	0.043	0.18040	0.00113	2729	62	2657	17	-2.7	3
X	18IM19	IM19A-9.1	347	359	1.032	146	42	1.044	-0.01	2.042	0.058	0.17177	0.23891	2.042	0.058	0.17183	0.00239	2570	73	2576	36	0.2	3
D	18IM19	IM19A-6.2	207	160	0.775	73	17	0.842	0.00	2.439	0.048	0.14777	0.18602	2.439	0.048	0.14777	0.00186	2215	44	2320	29	4.5	3
1	18IM20	IM20-9.1	184	52	0.280	57	5	0.282	0.04	2.752	0.062	0.15417	0.08234	2.753	0.062	0.15389	0.00085	1998	45	2390	13	16.4	5
1	18IM20	IM20-3.1	146	57	0.390	49	6	0.434	0.08	2.543	0.059	0.13884	0.71242	2.545	0.060	0.13827	0.00714	2137	50	2206	114	3.1	5
1	18IM20	IM20-6.1	166	65	0.391	57	7	0.421	0.32	2.487	0.067	0.12158	0.19756	2.495	0.067	0.11923	0.00212	2173	58	1945	35	-11.7	5
1	18IM20	IM20-1.1	241	100	0.413	85	10	0.432	0.74	2.418	0.046	0.14570	0.24451	2.436	0.046	0.14053	0.00277	2217	42	2231	44	0.6	5
1	18IM20	IM20-8.1	118	68	0.579	43	7	0.617	0.02	2.380	0.058	0.15567	0.58235	2.381	0.058	0.15554	0.00583	2261	55	2408	90	6.1	5
1	18IM20	IM20-11.1	136	51	0.374	50	6	0.403	0.20	2.339	0.058	0.14399	0.09160	2.343	0.058	0.14252	0.0104	2291	56	2258	17	-1.5	5
1	18IM20	IM20-15.1	165	75	0.455	61	8	0.488	0.02	2.341	0.055	0.14344	0.75325	2.341	0.055	0.14329	0.00736	2293	54	2267	116	-1.1	5
1	18IM20	IM20-2.1	173	77	0.443	65	8	0.463	0.08	2.281	0.059	0.14896	0.32743	2.283	0.059	0.14840	0.00329	2342	61	2228	52	-0.6	5
1	18IM20	IM20-4.1	119	65	0.547	45	8	0.596	0.02	2.255	0.058	0.15436	0.19250	2.258	0.058	0.15355	0.00196	2364	60	2386	30	0.9	5
1	18IM20	IM20-5.1	142	56	0.392	58	7	0.410	0.02	2.115	0.051	0.15978	0.61056	2.115	0.051	0.15905	0.00611	2495	60	2452	94	-1.8	5
1	18IM21C	IM21C-4.1	155	15	0.098	43	1	0.103	0.91	3.136	0.046	0.11229	0.09073	3.136	0.046	0.11223	0.00091	1784	26	1836	15	2.8	4
1	18IM21C	IM21C-8.1	149	17	0.116	43	1	0.121	0.01	2.986	0.044	0.11411	0.09163	2.986	0.044	0.11405	0.00092	1862	28	1865	15	0.2	4
1	18IM21C	IM21C-3.1	161	18	0.111	47	2	0.112	0.03	2.965	0.051	0.11239	0.08598	2.966	0.051	0.11219	0.00087	1873	32	1835	14	-2.1	4
1	18IM21C	IM21C-5.1	135	10	0.074	39	1	0.073	-0.02	2.939	0.044	0.11231	0.09316	2.959	0.044	0.11243	0.00094	1877	28	1839	15	-2.1	4
1	18IM21C	IM21C-6.1	164	19	0.116	48	2	0.121	0.00	2.954	0.044	0.11428	0.08610	2.954	0.044	0.11428	0.00086	1880	28	1869	14	-0.6	4
1	18IM21C	IM21C-1.1	161	19	0.116	47	2	0.125	0.00	2.937	0.044	0.11440	0.08655	2.937	0.044	0.11440	0.00087	1889	28	1870	14	-1.0	4
1	18IM23D	IM23D-5.1	398	2	0.005	122	0	0.004	0.05	2.813	0.038	0.14335	0.03669	2.814	0.038	0.14298	0.00038	1960	27	2264	6	13.4	4
1	18IM23D	IM23D-4.1	253	3	0.014	81	0	0.013	0.01	2.684	0.093	0.15160	1.44850	2.685	0.093	0.15149	0.01449	2041	71	2363	226	13.6	4
1	18IM23D	IM23D-7.1	147	2	0.014	48	0	0.013	0.03	2.612	0.036	0.14739	1.84068	2.613	0.036	0.14714	0.01841	2089	29	2313	289	9.7	4
1	18IM23D	IM23D-8.1	131	2	0.013	46	0	0.013	0.01	2.424	0.086	0.14679	0.55586	2.424	0.086	0.14674	0.00556	2226	79	2308	87	3.5	4
1	18IM23D	IM23D-2.1	155	2	0.013	56	0	0.014	0.02	2.384	0.097	0.14570	0.91736	2.385	0.097	0.14558	0.00918	2257	91	2295	145	1.6	4

Table B1. Continued.

Table B1. Continued.

Appendix C

Sample	Grain ID	$\delta^{18}\text{O}$ ‰	2 σ	${}^{18}\text{O}/{}^{16}\text{O}$	1 σ	eHf	2 σ	TDM _{Hf}	${}^{18}\text{Ta} / {}^{18}\text{W}$ meas.	${}^{18}\text{Hf} / {}^{18}\text{W}$ 2 σ	${}^{18}\text{Ta} / {}^{18}\text{W}$ meas.	${}^{18}\text{Hf} / {}^{18}\text{W}$ 2 σ	2 σ	O run Hf run	comments				
18IM11B	18IM11B.04	14.71	0.47	0.01051	7.60E-06	-	-	-	-	-	-	-	-	3	X1				
18IM11B	18IM11B.11	5.21	0.68	0.01016	5.86E-05	-	-	-	-	-	-	-	-	3	X1				
18IM11B	18IM11B.14	8.24	0.46	0.00740	1.09E-05	-	-	-	-	-	-	-	-	3	X1				
18IM11B	18IM11B.17	16.59	0.45	0.01123	9.66E-06	-	-	-	-	-	-	-	-	3	X1				
18IM11B	18IM11B.13	9.00	0.47	0.00319	1.24E-05	0.87	0.23	3012	0.000860	0.000210	0.281628	0.000023	1.46725	0.00005	1.88705	0.00026	3	X1	
18IM11B	18IM11B.02	11.54	0.45	0.00640	2.23E-05	0.74	0.19	3093	0.000786	0.000049	0.281580	0.000019	1.46721	0.00004	1.88698	0.00029	3	X1	
18IM11B	18IM11B.03	11.05	0.43	0.00237	7.34E-06	-0.17	0.19	3064	0.000427	0.000040	0.281583	0.000019	1.46723	0.00004	1.88715	0.00031	3	X1	
18IM11B	18IM11B.05	10.08	0.45	0.00543	1.97E-05	0.37	0.21	3038	0.001145	0.000061	0.281624	0.000021	1.46720	0.00004	1.88710	0.00027	3	X1	
18IM11B	18IM11B.06	10.97	0.47	0.00275	1.90E-05	0.47	0.33	3032	0.000509	0.000098	0.281604	0.000033	1.46721	0.00004	1.88704	0.00023	3	X1	
18IM11B	18IM11B.09	10.88	0.43	0.00307	8.99E-06	0.68	0.25	3022	0.000429	0.000021	0.281607	0.000025	1.46722	0.00005	1.88674	0.00020	3	X1	
18IM11B	18IM11B.10	11.13	0.45	0.00267	2.13E-06	0.88	0.25	3012	0.000160	0.000024	0.281603	0.000025	1.46721	0.00006	1.88690	0.00033	3	X1	
18IM11B	18IM11B.08	10.77	0.45	0.00244	4.14E-06	1.07	0.21	3002	0.000058	0.000006	0.281604	0.000021	1.46718	0.00004	1.88684	0.00019	3	X1	
18IM11B	18IM11B.07	10.18	0.46	0.00238	7.84E-06	1.08	0.27	3002	0.000059	0.000004	0.281605	0.000027	1.46724	0.00004	1.88727	0.00036	3	X1	
18IM12B	18IM12B.03	6.92	0.41	0.00531	8.88E-06	-	-	-	-	-	-	-	-	-	3	X1			
18IM12B	18IM12B.18	9.02	0.41	0.00232	3.88E-06	0.25	0.27	3091	0.000059	0.000002	0.281555	0.000027	1.46722	0.00005	1.88709	0.00021	3	X1	
18IM12B	18IM12B.09	10.00	0.42	0.00221	4.65E-06	0.54	0.23	3076	0.000055	0.000000	0.281563	0.000023	1.46725	0.00004	1.88701	0.00023	3	X1	
18IM12B	18IM12B.19	9.44	0.41	0.00223	2.33E-06	0.61	0.26	3073	0.000049	0.000035	0.281581	0.000026	1.46725	0.00005	1.88707	0.00029	3	X1	
18IM12B	18IM12B.07	9.48	0.42	0.00232	5.85E-06	0.75	0.20	3066	0.000032	0.000001	0.281568	0.000020	1.46718	0.00006	1.88679	0.00023	3	X1	
18IM12B	18IM12B.11	9.95	0.43	0.00226	5.42E-06	1.01	0.20	3053	0.000077	0.000001	0.281577	0.000020	1.46723	0.00006	1.88691	0.00023	3	X1	
18IM12B	18IM12B.04	10.57	0.42	0.00219	1.58E-05	1.07	0.33	3049	0.000054	0.000029	0.281578	0.000033	1.46724	0.00005	1.88693	0.00035	3	X1	
18IM12B	18IM12B.02	8.93	0.42	0.00279	3.97E-06	1.23	0.25	3042	0.000072	0.000001	0.281582	0.000023	1.46723	0.00005	1.88691	0.00025	3	X1	
18IM12B	18IM12B.08	10.55	0.41	0.00250	2.55E-06	1.32	0.23	3037	0.000055	0.000004	0.281585	0.000023	1.46725	0.00007	1.88686	0.00027	3	X1	
18IM12B	18IM12B.13	10.03	0.40	0.00206	3.65E-06	1.46	0.24	3030	0.000056	0.000002	0.281589	0.000024	1.46721	0.00005	1.88698	0.00024	3	X1	
18IM12B	18IM12B.05	10.43	0.41	0.00219	6.26E-06	1.72	0.21	3017	0.000048	0.000001	0.281613	0.000025	1.46724	0.00004	1.88697	0.00023	3	X1	
18IM12B	18IM12B.14	9.60	0.40	0.00230	2.18E-06	1.80	0.25	3013	0.000044	0.000029	0.281601	0.000024	1.46718	0.00004	1.88695	0.00024	3	X1	
18IM12B	18IM12B.17	9.15	0.39	0.00209	2.68E-06	1.90	0.24	3008	0.000048	0.000002	0.281601	0.000024	1.46720	0.00005	1.88657	0.00030	3	X1	
18IM12B	18IM12B.12	10.08	0.43	0.00230	4.71E-06	1.90	0.25	3008	0.000044	0.000000	0.281601	0.000025	1.46726	0.00004	1.88702	0.00025	3	X1	
18IM12B	18IM12B.15	9.37	0.40	0.00242	1.52E-05	1.94	0.34	3006	0.000074	0.000002	0.281603	0.000034	1.46720	0.00005	1.88695	0.00028	3	X1	
18IM12B	18IM12B.1	10.29	0.40	0.00207	3.76E-06	2.00	0.25	3003	0.000082	0.000002	0.281606	0.000025	1.46714	0.00005	1.88697	0.00023	3	X1	
18IM12B	18IM12B.06	10.21	0.42	0.00204	3.48E-06	2.02	0.26	3002	0.000088	0.000002	0.281606	0.000026	1.46721	0.00005	1.88693	0.00025	3	X1	
18IM12B	18IM12B.10	10.03	0.41	0.00211	4.46E-06	2.20	0.26	2993	0.000142	0.000047	0.281613	0.000026	1.46720	0.00005	1.88678	0.00028	3	X1	
18IM12B	18IM12B.16	8.68	0.39	0.00258	1.34E-06	-	-	-	-	-	-	-	-	-	3	X1			
18IM13C	18IM13C.4	7.06	0.39	0.00077	1.65E-06	-	-	-	-	-	-	-	-	-	1	X2			
18IM13C	18IM13C.15	7.97	0.38	0.00112	2.04E-06	0.79	0.83	3338	0.000480	0.000160	0.281436	0.000083	1.46597	0.00048	1.88730	0.00051	1	X4	
18IM13C	18IM13C.2	8.34	0.37	0.00085	1.16E-06	8.54	1.50	3251	0.001447	0.000036	0.281530	0.000150	1.46560	0.00140	1.88742	0.00042	1	X4	
18IM13C	18IM13C.10	8.05	0.41	0.00084	1.21E-06	1.69	0.41	3592	0.001221	0.000031	0.281528	0.000038	1.46725	0.00017	1.88692	0.00018	1	X4	
18IM13C	18IM13C.19	7.95	0.40	0.00090	4.55E-07	3.18	0.39	3518	0.001786	0.000044	0.281535	0.000039	1.46714	0.00012	1.88713	0.00023	1	X4	
18IM13C	18IM13C.11	8.74	0.37	0.00082	2.51E-06	3.23	0.49	3516	0.001302	0.000061	0.281537	0.000049	1.46706	0.00017	1.88694	0.00016	1	X4	
18IM13C	18IM13C.14	7.99	0.43	0.00111	1.02E-05	2.00	0.54	3577	0.001700	0.000120	0.281358	0.000054	1.46711	0.00015	1.88701	0.00025	1	X4	
18IM13C	18IM13C.6	8.81	0.41	0.00155	4.56E-06	2.48	0.44	3553	0.000358	0.000017	0.281308	0.000044	1.46713	0.00014	1.88687	0.00019	1	X4	
18IM13C	18IM13C.13	8.22	0.40	0.00080	1.08E-06	3.12	0.37	3521	0.000274	0.00004	0.281352	0.000037	1.46719	0.00005	1.88712	0.00019	1	X4	
18IM13C	18IM13C.19	7.95	0.40	0.00093	4.55E-07	3.18	0.39	3518	0.001786	0.000046	0.281395	0.000039	1.46714	0.00010	1.88704	0.00023	1	X4	
18IM13C	18IM13C.1	8.74	0.37	0.00084	1.02E-05	2.26E-06	3.70	0.35	3492	0.001148	0.000016	0.281380	0.000035	1.46704	0.00013	1.88697	0.00016	1	X4
18IM13C	18IM13C.16	8.35	0.38	0.00084	7.92E-07	3.74	0.56	3490	0.000970	0.000170	0.281357	0.000056	1.46709	0.00005	1.88681	0.00019	1	X4	
18IM13C	18IM13C.7	8.69	0.40	0.00070	1.05E-06	4.01	0.35	3477	0.000528	0.000046	0.281360	0.000035	1.46695	0.00011	1.88692	0.00018	1	X4	

Table C1. Zircon SIMS O isotopes and LA-ICPMS Hf isotopes single spot results. X indicates rejected analyses; O isotope data rejected based on stable Hf isotope ratios (X4). OH/O (X1), $\delta^{18}\text{O}$ outside of 2σ (X2), spot overlaps multiple growth zones (X3); Hf isotope data rejected based on stable Hf isotope ratios (X4).

Sample	Grain	$\delta^{18}\text{O}$	2 σ	${}^{\text{17}}\text{O}/{}^{\text{18}}\text{O}$	1 σ	ϵ_{Hf}	2 σ	TDM _{Hf}	${}^{\text{17}}\text{Lu}/{}^{\text{177}}\text{Hf}$	2 σ	${}^{\text{18}}\text{Hf}/{}^{\text{177}}\text{Hf}$	2 σ	${}^{\text{18}}\text{Hf}/{}^{\text{177}}\text{Hf}$	2 σ	O run	Hf run	comments	
ID		%						meas.		meas.		meas.		meas.		#	#	
18IM13C	18IM13C.12	8.52	0.38	0.00113	1.33E-05	4.15	0.49	3470	0.001237	0.000029	0.281397	0.000049	1.46708	0.00017	1.88720	0.00022	1	2
18IM13C	18IM13C.18	8.02	0.38	0.00083	1.06E-06	4.32	0.41	3461	0.001091	0.000086	0.281395	0.000041	1.46702	0.00016	1.88696	0.00019	1	2
18IM13C	18IM13C.14	8.30	0.36	0.00089	8.31E-07	-	-	-	-	-	-	-	-	-	-	-	1	
18IM13C	18IM13C.3	8.58	0.39	0.00068	7.76E-07	-	-	-	-	-	-	-	-	-	-	-	1	
18IM13C	18IM13C.9	8.90	0.39	0.00081	1.93E-06	-	-	-	-	-	-	-	-	-	-	-	1	
18IM14A	18IM14A.4	5.93	0.30	-	-	-2.56	0.34	3143	0.000039	0.000001	0.281525	0.000034	1.46720	0.00013	1.88680	0.00014	4	3
18IM14A	18IM14A.5	4.83	0.30	-	-	-9.28	0.42	3478	0.001538	0.000046	0.281389	0.000042	1.46717	0.00013	1.88684	0.00018	4	3
18IM14A	18IM14A.14	4.94	0.30	-	-	-7.27	0.37	3378	0.001521	0.000067	0.281445	0.000037	1.46729	0.00011	1.88678	0.00015	4	3
18IM14A	18IM14A.9	3.99	0.30	-	-	-6.56	0.48	3343	0.002033	0.000083	0.281483	0.000048	1.46717	0.00015	1.88683	0.00025	4	3
18IM14A	18IM14A.18	4.94	0.30	-	-	-5.72	0.34	3301	0.001731	0.000015	0.281496	0.000034	1.46713	0.00014	1.88681	0.00017	4	3
18IM14A	18IM14A.12	4.27	0.31	-	-	-4.60	0.31	3245	0.003890	0.000058	0.281604	0.000031	1.46711	0.00014	1.88689	0.00014	4	3
18IM14A	18IM14A.16	4.08	0.30	-	-	-4.25	0.32	3228	0.002742	0.000073	0.281573	0.000032	1.46708	0.00011	1.88686	0.00017	4	3
18IM14A	18IM14A.15	4.25	0.29	-	-	-3.97	0.25	3213	0.002710	0.000120	0.281580	0.000025	1.46697	0.00010	1.88668	0.00012	4	3
18IM14A	18IM14A.2	4.69	0.28	-	-	-3.68	0.34	3199	0.000986	0.000095	0.281527	0.000034	1.46709	0.00009	1.88685	0.00017	4	3
18IM14A	18IM14A.1	5.05	0.28	-	-	-3.66	0.31	3198	0.002580	0.000023	0.281584	0.000031	1.46713	0.00017	1.88682	0.00018	4	3
18IM14A	18IM14A.10	5.08	0.29	-	-	-3.62	0.36	3196	0.001528	0.000057	0.281548	0.000036	1.46705	0.00015	1.88689	0.00013	4	3
18IM14A	18IM14A.6	5.12	0.29	-	-	-3.23	0.37	3176	0.002182	0.000074	0.281582	0.000037	1.46712	0.00015	1.88675	0.00016	4	3
18IM14A	18IM14A.17	3.92	0.29	-	-	-3.00	0.44	3165	0.001573	0.000089	0.281567	0.000044	1.46706	0.00024	1.88678	0.00021	4	3
18IM14A	18IM14A.7	4.13	0.32	-	-	-1.61	0.36	3095	0.000072	0.000001	0.281553	0.000036	1.46706	0.00014	1.88683	0.00015	4	3
18IM14A	18IM14A.19	4.39	0.31	-	-	-	-	-	-	-	-	-	-	-	-	-	4	
18IM14A	18IM14A.20	4.07	0.31	-	-	-	-	-	-	-	-	-	-	-	-	-	4	
18IM14A	18IM14A.3	4.71	0.32	-	-	-	-	-	-	-	-	-	-	-	-	-	4	
18IM14A	18IM14A.8	4.25	0.33	-	-	-	-	-	-	-	-	-	-	-	-	-	4	
18IM15B	18IM15B.1	5.37	0.36	0.00068	1.02E-06	-	-	-	-	-	-	-	-	-	-	-	1	
18IM15B	18IM15B.14	6.28	0.37	0.00068	1.34E-06	-	-	-	-	-	-	-	-	-	-	-	1	
18IM15B	18IM15B.2	5.41	0.36	0.00065	1.11E-06	-	-	-	-	-	-	-	-	-	-	-	1	
18IM15B	18IM15B.22	5.32	0.40	0.00067	1.09E-06	-	-	-	-	-	-	-	-	-	-	-	1	
18IM15B	18IM15B.4	5.43	0.39	0.00066	1.61E-06	-	-	-	-	-	-	-	-	-	-	-	1	
18IM15B	18IM15B.6	6.62	0.37	0.00068	1.19E-06	-	-	-	-	-	-	-	-	-	-	-	1	
18IM15B	18IM15B.9	5.31	0.39	0.00073	1.13E-06	-	-	-	-	-	-	-	-	-	-	-	1	
18IM15B	18IM15B.11	7.28	0.39	0.00076	1.72E-06	-	-	-	-	-	-	-	-	-	-	-	1	
18IM15B	18IM15B.16	7.69	0.38	0.00075	1.18E-06	-	-	-	-	-	-	-	-	-	-	-	4	
18IM15B	18IM15B.17	7.46	0.39	0.00071	1.09E-06	-	-	-	-	-	-	-	-	-	-	-	4	
18IM15B	18IM15B.5	6.11	0.37	0.00066	1.26E-06	-	-	-	-	-	-	-	-	-	-	-	4	
18IM15B	18IM15B.21	8.59	0.41	0.00085	4.69E-06	7.98	0.81	3343	0.000045	0.000004	0.281413	0.000081	1.46667	0.00049	1.88695	0.00016	1	2
18IM15B	18IM15B.19	8.34	0.39	0.00077	1.15E-06	2.36	0.45	3623	0.000274	0.000087	0.281266	0.000045	1.46713	0.00019	1.88699	0.00021	1	2
18IM15B	18IM15B.13	8.71	0.38	0.00077	1.10E-06	2.75	0.38	3603	0.000150	0.000007	0.281271	0.000038	1.46711	0.00017	1.88693	0.00021	1	2
18IM15B	18IM15B.5	8.76	0.37	0.00082	1.45E-06	2.80	0.45	3601	0.000097	0.00004	0.281270	0.000045	1.46721	0.00014	1.88712	0.00022	1	2
18IM15B	18IM15B.18	8.64	0.38	0.00070	1.26E-06	2.90	0.44	3506	0.000058	0.000001	0.281271	0.000044	1.46722	0.00016	1.88706	0.00020	1	2
18IM15B	18IM15B.20	8.91	0.40	0.00063	1.25E-06	3.61	0.52	3561	0.000272	0.000018	0.281301	0.000052	1.46717	0.00012	1.88685	0.00022	1	2
18IM15B	18IM15B.7	8.40	0.39	0.00085	1.10E-06	3.82	0.37	3550	0.000189	0.000041	0.281303	0.000037	1.46725	0.00012	1.88692	0.00019	1	2
18IM15B	18IM15B.12	8.38	0.36	0.00079	9.40E-07	4.33	0.35	3525	0.000096	0.000002	0.281313	0.000035	1.46713	0.00011	1.88663	0.00018	1	2
18IM15B	18IM15B.15	8.26	0.39	0.00077	1.12E-06	4.34	0.29	3524	0.000070	0.000001	0.281312	0.000029	1.46723	0.00012	1.88700	0.00015	1	2
18IM15B	18IM15B.8	8.78	0.37	0.00065	1.46E-06	5.00	0.42	3491	0.000057	0.000002	0.281330	0.000042	1.46719	0.00014	1.88700	0.00017	1	2
18IM15B	18IM15B.10	8.57	0.37	0.00075	9.73E-07	5.63	0.47	3460	0.000214	0.000003	0.281355	0.000047	1.46727	0.00016	1.88696	0.00018	1	2
18IM19	18IM19A.15	6.22	0.31	-	-	-	-	-	-	-	-	-	-	-	-	-	4	

Table C1. Continued.

Sample	Grain	$\delta^{18}\text{O}$	2 σ	${}^{16}\text{O}/{}^{18}\text{O}$	1 σ	ϵHf	2 σ	TDM _{Hf}	${}^{176}\text{Lu}/{}^{177}\text{Hf}$	2 σ	${}^{176}\text{Hf}/{}^{177}\text{Hf}$	2 σ	${}^{180}\text{Hf}/{}^{177}\text{Hf}$	2 σ	O run	Hf run	comments		
ID		%						meas.		meas.		meas.		meas.	#	#			
18IM19	18IM19A.1	5.89	0.31	-	-	-	-	-	-	-	-	-	-	-	4	-	core analysis		
18IM19	18IM19C.3	5.72	0.37	0.00091	1.91E-06	-	-	-	-	-	-	-	-	-	1	1	core analysis		
18IM19	18IM19C.18	5.96	0.37	0.00087	6.29E-07	-	-	-	-	-	-	-	-	-	1	1	core analysis		
18IM19	18IM19A.18	6.33	0.32	-	-	-	-	-	-	-	-	-	-	-	4	4	X4		
18IM19	18IM19A.2	6.73	0.28	-	-	5.54	0.49	3449	0.000330	0.000100	0.281367	0.000049	1.46670	0.00039	1.88686	0.00022	4	3	
18IM19	18IM19C.7	7.13	0.36	0.00102	9.47E-07	7.03	0.94	3574	0.00034	0.00015	0.281395	0.000094	1.46649	0.00055	1.88725	0.00020	1	2	X4
18IM19	18IM19C.8	7.29	0.37	0.00085	1.53E-06	9.88	1.30	3232	0.000137	0.00045	0.281480	0.000130	1.46598	0.00094	1.88727	0.00019	1	2	X4
18IM19	18IM19C.5	7.30	0.36	0.00092	1.13E-06	10.06	1.20	3223	0.000030	0.00009	0.281480	0.000120	1.46599	0.00068	1.88694	0.00024	1	2	X4
18IM19	18IM19C.9	7.25	0.37	0.00077	1.29E-06	13.18	1.40	3067	0.000078	0.00030	0.281570	0.000140	1.46648	0.00046	1.88710	0.00023	1	2	X4
18IM19	18IM19A.3	7.18	0.30	-	-	-9.15	0.45	4175	0.000690	0.00014	0.280971	0.000045	1.46721	0.00015	1.88673	0.00019	4	3	
18IM19	18IM19A.9	6.60	0.30	-	-	0.61	0.47	3693	0.000385	0.00091	0.281231	0.000047	1.46712	0.00019	1.88690	0.00018	4	3	
18IM19	18IM19A.10	7.16	0.32	-	-	1.54	0.38	3647	0.00044	0.00008	0.281244	0.000038	1.46721	0.00010	1.88698	0.00019	4	3	
18IM19	18IM19A.19	6.85	0.30	-	-	1.58	0.41	3645	0.000314	0.00089	0.281254	0.000041	1.46718	0.00015	1.88693	0.00017	4	3	
18IM19	18IM19A.6	7.12	0.29	-	-	1.80	0.43	3634	0.001010	0.00073	0.281294	0.000043	1.46722	0.00013	1.88695	0.00021	4	3	
18IM19	18IM19A.20	6.97	0.29	-	-	2.40	0.46	3605	0.000780	0.00056	0.281300	0.000046	1.46713	0.00011	1.88684	0.00018	4	3	
18IM19	18IM19A.11	7.23	0.30	-	-	2.46	0.39	3601	0.000042	0.00003	0.281267	0.000039	1.46712	0.00016	1.88688	0.00018	4	3	
18IM19	18IM19A.17	6.68	0.36	-	-	2.51	0.38	3599	0.000561	0.00063	0.281293	0.000038	1.46714	0.00011	1.88700	0.00017	4	3	
18IM19	18IM19A.8	7.07	0.37	-	-	2.66	0.36	3592	0.00032	0.00002	0.281272	0.000036	1.46712	0.00017	1.88697	0.00017	4	3	
18IM19	18IM19A.14	7.04	0.31	-	-	3.09	0.40	3570	0.00032	0.00001	0.281284	0.000040	1.46713	0.00012	1.88685	0.00018	4	3	
18IM19	18IM19A.5	6.81	0.30	-	-	3.38	0.78	3546	0.00052	0.00087	0.281298	0.000078	1.46729	0.00047	1.88703	0.00022	4	3	
18IM19	18IM19A.7	7.14	0.30	-	-	3.51	0.36	3549	0.00033	0.0000270	0.281344	0.000052	1.46699	0.00014	1.88691	0.00016	4	3	
18IM19	18IM19A.16	6.66	0.30	-	-	3.79	0.52	3535	0.000880	0.000270	0.281300	0.000050	1.46678	0.00029	1.88680	0.00014	4	3	
18IM19	18IM19A.13	7.16	0.30	-	-	4.71	0.50	3490	0.000210	0.000120	0.281338	0.000050	1.46678	0.00029	1.88680	0.00014	4	3	
18IM19	18IM19A.12	6.54	0.32	-	-	-	-	-	-	-	-	-	-	-	-	-			
18IM19	18IM19A.4	7.10	0.32	-	-	-	-	-	-	-	-	-	-	-	-	-			
18IM19	18IM19C.15	7.50	0.38	0.00088	1.69E-06	2.40	0.32	3604	0.000015	0.00000	0.281264	0.000032	1.46720	0.00013	1.88697	0.00018	1	2	
18IM19	18IM19C.16	7.14	0.37	0.00091	8.60E-07	2.68	0.39	3590	0.001074	0.00074	0.281322	0.000039	1.46724	0.00012	1.88701	0.00020	1	2	
18IM19	18IM19C.4	7.03	0.37	0.00081	1.08E-06	3.04	0.34	3573	0.000176	0.00001	0.281322	0.000034	1.46722	0.00011	1.88700	0.00018	1	2	
18IM19	18IM19C.6	7.19	0.38	0.00098	1.12E-06	3.05	0.48	3572	0.000476	0.000019	0.281304	0.000048	1.46734	0.00013	1.88684	0.00013	1	2	
18IM19	18IM19C.13	7.53	0.36	0.00073	1.19E-06	3.29	0.42	3560	0.000101	0.000024	0.281293	0.000042	1.46707	0.00014	1.88688	0.00020	1	2	
18IM19	18IM19C.14	7.30	0.37	0.00088	1.07E-06	3.33	0.37	3559	0.000016	0.000001	0.281290	0.000037	1.46717	0.00016	1.88700	0.00019	1	2	
18IM19	18IM19C.12	6.63	0.38	0.00106	1.44E-06	3.50	0.37	3550	0.000105	0.00003	0.281299	0.000037	1.46726	0.00013	1.88686	0.00019	1	2	
18IM19	18IM19C.10	7.17	0.36	0.00090	1.33E-06	4.07	0.37	3522	0.000118	0.00001	0.281311	0.000021	1.46711	0.00013	1.88679	0.00017	1	2	
18IM19	18IM19C.11	7.62	0.39	0.00085	1.14E-06	4.15	0.36	3518	0.000113	0.00000	0.281313	0.000036	1.46722	0.00013	1.88683	0.00020	1	2	
18IM19	18IM19C.11	7.42	0.39	0.00074	1.35E-06	4.40	0.42	3505	0.000393	0.00046	0.281338	0.000042	1.46711	0.00019	1.88693	0.00020	1	2	
18IM19	18IM19C.2	6.98	0.37	0.00078	1.27E-06	5.35	0.65	3458	0.000020	0.00002	0.281347	0.000065	1.46664	0.00031	1.88699	0.00020	1	2	
18IM19	18IM19C.17	7.40	0.36	0.00077	1.21E-06	-	-	-	-	-	-	-	-	-	-	-			
18IM19	18IM19C.19	7.69	0.37	0.00077	1.04E-06	-	-	-	-	-	-	-	-	-	-	-			
18IM19	18IM19C.20	7.57	0.38	0.00076	1.06E-06	-	-	-	-	-	-	-	-	-	-	-			
18IM20	18IM20.12	7.50	0.45	0.00250	5.48E-06	-1.18	0.26	3553	0.000570	0.000120	0.281317	0.000026	1.46724	0.00004	1.88699	0.00026	3	4	
18IM20	18IM20.14	7.72	0.48	0.00220	7.83E-06	-1.10	0.21	3549	0.000540	0.00094	0.281318	0.000021	1.46718	0.00005	1.88688	0.00019	3	4	
18IM20	18IM20.21	7.68	0.41	0.00239	2.86E-06	-1.09	0.16	3549	0.000214	0.000020	0.281304	0.000016	1.46720	0.00004	1.88685	0.00025	3	4	
18IM20	18IM20.06	6.53	0.42	0.00265	1.97E-06	-1.01	0.21	3545	0.000828	0.00080	0.281333	0.000021	1.46717	0.00005	1.88669	0.00026	3	4	
18IM20	18IM20.11	7.08	0.43	0.00293	5.09E-06	-1.00	0.28	3544	0.001005	0.00080	0.281341	0.000028	1.46724	0.00005	1.88704	0.00021	3	4	
18IM20	18IM20.15	7.23	0.42	0.00254	6.04E-06	-0.99	0.21	3544	0.000311	0.00086	0.281311	0.000021	1.46722	0.00004	1.88694	0.00027	3	4	
18IM20	18IM20.08	7.74	0.41	0.00244	3.00E-06	-0.85	0.26	3537	0.000192	0.00055	0.281310	0.000026	1.46718	0.00004	1.88697	0.00029	3	4	

Table C1. Continued.

Sample	Grain	$\delta^{18}\text{O}$ ‰	2σ	${}^{16}\text{O}/{}^{18}\text{O}$	3σ	ε Hf	2σ	TDM $_{\text{Hf}}$	${}^{176}\text{Lu}/{}^{177}\text{Hf}$	2σ	${}^{176}\text{Hf}/{}^{177}\text{Hf}$	2σ	${}^{178}\text{Hf}/{}^{177}\text{Hf}$	2σ	${}^{180}\text{Hf}/{}^{177}\text{Hf}$	2σ	O run	H run	comments
ID	ID					meas.			meas.		meas.		meas.		meas.		#	#	
18IM20	18IM20.02	7.32	0.42	0.00244	1.90E-06	-0.80	0.22	3534	0.000050	0.000005	0.281305	0.000022	1.46719	0.00004	1.88670	0.000018	3	4	
18IM20	18IM20.07	7.37	0.43	0.00245	1.72E-06	-0.62	0.21	3525	0.0000542	0.000054	0.281325	0.000021	1.46722	0.00005	1.88682	0.000020	3	4	
18IM20	18IM20.16	7.67	0.40	0.00248	3.93E-06	-0.59	0.22	3524	0.0000418	0.000035	0.281327	0.000022	1.46721	0.00004	1.88705	0.000018	3	4	
18IM20	18IM20.10	7.57	0.43	0.00252	4.28E-06	-0.48	0.23	3518	0.0000440	0.000093	0.281323	0.000023	1.46723	0.00005	1.88712	0.000028	3	4	
18IM20	18IM20.04	7.46	0.42	0.00252	2.32E-06	-0.47	0.27	3515	0.0000365	0.000099	0.281328	0.000027	1.46722	0.00004	1.88681	0.000027	3	4	
18IM20	18IM20.05	6.89	0.44	0.00255	2.19E-06	-0.41	0.26	3515	0.0000506	0.000061	0.281336	0.000026	1.46724	0.00004	1.88699	0.000024	3	4	
18IM20	18IM20.03	7.89	0.43	0.00281	1.78E-05	-	-	-	-	-	-	-	-	-	-	-	-	-	
18IM20	18IM20.09	7.39	0.44	0.00256	3.23E-06	-	-	-	-	-	-	-	-	-	-	-	-	-	
18IM20	18IM20.13	7.14	0.42	0.00273	3.06E-06	-	-	-	-	-	-	-	-	-	-	-	-	-	
18IM20	18IM20.17	7.06	0.43	0.00229	3.06E-06	-	-	-	-	-	-	-	-	-	-	-	-	-	
18IM21C	18IM21C.13	3.61	0.42	0.00508	2.62E-05	-	-	-	-	-	-	-	-	-	-	-	-	-	X1
18IM21C	18IM21C.18	6.68	0.43	0.00216	1.96E-06	-5.18	0.22	3262	0.000357	0.000010	0.281000	0.000022	1.46722	0.00005	1.88689	0.000025	2	4	
18IM21C	18IM21C.02	7.04	0.40	0.00207	5.07E-06	-4.95	0.27	3251	0.000604	0.000020	0.281000	0.000027	1.46726	0.00005	1.88711	0.000023	2	4	
18IM21C	18IM21C.19	6.87	0.42	0.00208	2.41E-06	-4.95	0.24	3251	0.000456	0.000000	0.281000	0.000024	1.46724	0.00004	1.88696	0.000031	2	4	
18IM21C	18IM21C.21	6.27	0.42	0.00313	3.03E-06	-4.92	0.24	3249	0.000748	0.000020	0.281000	0.000024	1.46720	0.00003	1.88697	0.000027	2	4	
18IM21C	18IM21C.11	6.65	0.41	0.00206	4.56E-06	-4.84	0.23	3245	0.000543	0.000000	0.281000	0.000023	1.46721	0.00005	1.88683	0.000031	2	4	
18IM21C	18IM21C.03	6.66	0.40	0.00182	4.45E-06	-4.57	0.27	3232	0.001180	0.000070	0.282000	0.000027	1.46725	0.00005	1.88717	0.000027	2	4	
18IM21C	18IM21C.08	7.09	0.41	0.00193	3.04E-06	-4.50	0.28	3229	0.000983	0.000040	0.282000	0.000028	1.46721	0.00005	1.88717	0.000024	2	4	
18IM21C	18IM21C.15	6.88	0.40	0.00211	2.11E-06	-4.39	0.20	3223	0.000632	0.000020	0.282000	0.000020	1.46722	0.00006	1.88698	0.000026	2	4	
18IM21C	18IM21C.04	7.21	0.39	0.00185	4.32E-06	-4.32	0.20	3219	0.000411	0.000010	0.282000	0.000020	1.46721	0.00005	1.88702	0.000025	2	4	
18IM21C	18IM21C.09	6.50	0.39	0.00190	7.70E-07	-4.21	0.27	3214	0.001200	0.0000120	0.282000	0.000027	1.46721	0.00005	1.88732	0.000029	2	4	
18IM21C	18IM21C.05	6.69	0.41	0.00178	5.12E-06	-4.17	0.29	3212	0.000462	0.000000	0.282000	0.000029	1.46720	0.00005	1.88689	0.000029	2	4	
18IM21C	18IM21C.12	6.61	0.41	0.00198	2.51E-06	-4.12	0.20	3209	0.000985	0.000050	0.282000	0.000020	1.46723	0.00004	1.88698	0.000020	2	4	
18IM21C	18IM21C.14	6.48	0.42	0.00220	5.35E-06	-4.08	0.20	3208	0.001070	0.000040	0.282000	0.000020	1.46719	0.00005	1.88713	0.000028	2	4	
18IM21C	18IM21C.20	6.53	0.42	0.00223	1.45E-06	-4.07	0.19	3207	0.000917	0.000090	0.282000	0.000019	1.46721	0.00005	1.88696	0.000029	2	4	
18IM21C	18IM21C.17	6.31	0.41	0.00195	4.66E-06	-3.82	0.24	3194	0.000320	0.000000	0.282000	0.000024	1.46717	0.00004	1.88681	0.000026	2	4	
18IM21C	18IM21C.07	6.55	0.39	0.00221	4.38E-06	-3.76	0.21	3191	0.000669	0.000050	0.282000	0.000021	1.46728	0.00005	1.88698	0.000030	2	4	
18IM21C	18IM21C.06	6.52	0.41	0.00212	1.67E-06	-3.55	0.26	3181	0.000532	0.000010	0.282000	0.000026	1.46720	0.00004	1.88678	0.000029	2	4	
18IM21C	18IM21C.16	6.66	0.41	0.00209	3.70E-06	-3.40	0.32	3173	0.001320	0.000070	0.282000	0.000032	1.46719	0.00006	1.88688	0.000036	2	4	
18IM21C	18IM21C.11	6.37	0.40	0.00209	2.82E-06	-3.33	0.19	3170	0.001240	0.000080	0.282000	0.000019	1.46718	0.00005	1.88700	0.000024	2	4	
18IM21C	18IM21C.10	6.86	0.39	0.00203	3.43E-06	-3.25	0.24	3166	0.001150	0.000040	0.282000	0.000024	1.46728	0.00003	1.88705	0.000028	2	4	
18IM21C	18IM21C.22	6.27	0.41	0.00223	2.53E-06	-	-	-	-	-	-	-	-	-	-	-	-		
18IM23D	18IM23D.11	6.58	0.41	0.00666	6.67E-06	-	-	-	-	-	-	-	-	-	-	-	-		
18IM23D	18IM23D.12	6.22	0.40	0.00661	7.47E-06	-	-	-	-	-	-	-	-	-	-	-	-		
18IM23D	18IM23D.17	6.29	0.44	0.00557	5.08E-06	-	-	-	-	-	-	-	-	-	-	-	-	X1	
18IM23D	18IM23D.14	6.31	0.42	0.00331	3.58E-06	-1.47	0.25	3622	0.001358	0.000093	0.281317	0.000025	1.46720	0.00004	1.88689	0.000035	2	4	
18IM23D	18IM23D.08	6.22	0.46	0.00220	4.27E-06	-1.93	0.25	3599	0.000117	0.000007	0.281272	0.000025	1.46716	0.00005	1.88712	0.000033	2	4	
18IM23D	18IM23D.13	5.95	0.41	0.00254	4.29E-06	-2.35	0.28	3578	0.000380	0.000080	0.281296	0.000028	1.46721	0.00005	1.88685	0.000030	2	4	
18IM23D	18IM23D.03	6.07	0.42	0.00255	4.59E-06	-2.48	0.13	3571	0.001369	0.000031	0.281346	0.000013	1.46719	0.00004	1.88695	0.000027	2	4	
18IM23D	18IM23D.09	6.22	0.41	0.00264	5.50E-06	-2.48	0.23	3571	0.001453	0.000042	0.281350	0.000023	1.46723	0.00006	1.88709	0.000030	2	4	
18IM23D	18IM23D.07	6.20	0.42	0.00219	3.41E-06	-2.55	0.21	3568	0.000792	0.000061	0.281321	0.000021	1.46726	0.00005	1.88691	0.000023	2	4	
18IM23D	18IM23D.04	6.14	0.42	0.00233	3.53E-06	-3.32	0.21	3550	0.000200	0.000005	0.281315	0.000021	1.46721	0.00004	1.88700	0.000029	2	4	
18IM23D	18IM23D.02	6.87	0.40	0.00377	3.32E-06	-	-	-	-	-	-	-	-	-	-	-	-		
18IM23D	18IM23D.05	5.89	0.42	0.00274	4.54E-06	-	-	-	-	-	-	-	-	-	-	-	-		
18IM23D	18IM23D.06	5.75	0.41	0.00231	3.04E-06	-	-	-	-	-	-	-	-	-	-	-	-		
18IM23D	18IM23D.1	6.61	0.41	0.00215	2.49E-06	-	-	-	-	-	-	-	-	-	-	-	-		

Table C1. Continued.

Sample	Grain	$\delta^{18}\text{O}$	2σ	$^{16}\text{O}/^{18}\text{O}$	1σ	ϵHf	2σ	TDM _{Hf}	$^{18}\text{La}/^{177}\text{Hf}$	2σ	$^{18}\text{Hf}/^{177}\text{Hf}$	2σ	$^{18}\text{Hf}/^{177}\text{Hf}$	2σ	O run	Hf run	commens.	#
ID	ID	%						meas.		meas.					meas.			#
18IM23D	18IM23D.10	5.85	0.41	0.00360	5.65E-06	-	-	-	-	-	-	-	-	-	-	-	-	2
18IM23D	18IM23D.16	6.44	0.42	0.00335	6.30E-06	-	-	-	-	-	-	-	-	-	-	-	-	2
18IM25C	18IM25C.13	4.49	0.37	0.01365	1.73E-04	-	-	-	-	-	-	-	-	-	-	-	-	X1
18IM25C	18IM25C.1	6.87	0.38	0.00116	4.14E-06	4.68	0.61	3508	0.0001416	0.000051	0.281385	0.000061	1.46677	0.00023	1.88719	0.00021	1	2
18IM25C	18IM25C.5	7.14	0.38	0.00073	1.17E-06	5.13	1.00	3486	0.0000420	0.000017	0.281350	0.00010	1.46663	0.00025	1.88711	0.00025	1	2
18IM25C	18IM25C.8	7.48	0.38	0.00076	8.81E-07	2.45	0.37	3620	0.0000427	0.000010	0.281275	0.000037	1.46725	0.00011	1.88706	0.00018	1	2
18IM25C	18IM25C.19	7.49	0.39	0.00079	1.01E-06	2.59	0.42	3612	0.0000385	0.000002	0.281277	0.000042	1.46717	0.00009	1.88694	0.00017	1	2
18IM25C	18IM25C.7	6.64	0.39	0.00083	1.35E-06	2.61	0.45	3611	0.0000309	0.000009	0.281274	0.000045	1.46719	0.00009	1.88687	0.00014	1	2
18IM25C	18IM25C.3	7.07	0.37	0.00074	1.07E-06	2.71	0.39	3607	0.0000315	0.000003	0.281277	0.000039	1.46722	0.00012	1.88701	0.00020	1	2
18IM25C	18IM25C.12	7.14	0.40	0.00072	2.26E-06	3.31	0.46	3577	0.0000399	0.000009	0.281298	0.000046	1.46720	0.00015	1.88692	0.00021	1	2
18IM25C	18IM25C.14	6.84	0.39	0.00072	1.28E-06	3.45	0.40	3570	0.0000378	0.000006	0.281301	0.000040	1.46711	0.00018	1.88686	0.00018	1	2
18IM25C	18IM25C.9	7.49	0.39	0.00074	1.10E-06	3.73	0.32	3556	0.0000384	0.000009	0.281309	0.000032	1.46723	0.00013	1.88678	0.00015	1	2
18IM25C	18IM25C.2	7.52	0.38	0.00079	8.83E-07	3.94	0.44	3545	0.0001015	0.000014	0.281345	0.000044	1.46710	0.00016	1.88681	0.00018	1	2
18IM25C	18IM25C.10	6.57	0.37	0.00088	1.79E-06	-	-	-	-	-	-	-	-	-	-	-	-	1
18IM25C	18IM25C.11	6.51	0.37	0.00244	2.13E-05	-	-	-	-	-	-	-	-	-	-	-	-	1
18IM25C	18IM25C.15	7.00	0.37	0.00074	1.25E-06	-	-	-	-	-	-	-	-	-	-	-	-	1
18IM25C	18IM25C.16	6.37	0.40	0.00104	1.65E-06	-	-	-	-	-	-	-	-	-	-	-	-	1
18IM25C	18IM25C.17	6.91	0.39	0.00087	5.26E-07	-	-	-	-	-	-	-	-	-	-	-	-	1
18IM25C	18IM25C.18	6.50	0.37	0.00110	2.29E-06	-	-	-	-	-	-	-	-	-	-	-	-	1
18IM25C	18IM25C.20	6.40	0.37	0.00182	4.83E-06	-	-	-	-	-	-	-	-	-	-	-	-	1
18IM25C	18IM25C.21	6.05	0.38	0.00109	1.33E-06	-	-	-	-	-	-	-	-	-	-	-	-	1
18IM25C	18IM25C.4	6.71	0.38	0.00069	1.13E-06	-	-	-	-	-	-	-	-	-	-	-	-	1
18IM25C	18IM25C.6	6.22	0.37	0.00085	1.34E-06	-	-	-	-	-	-	-	-	-	-	-	-	1
18IM3	18IM3.09	11.16	0.43	0.00479	1.31E-05	-	-	-	-	-	-	-	-	-	-	-	-	2
18IM3	18IM3.1	9.03	0.40	0.00782	2.43E-06	-	-	-	-	-	-	-	-	-	-	-	-	X1
18IM3	18IM3.10	9.77	0.41	0.00474	2.33E-05	-	-	-	-	-	-	-	-	-	-	-	-	X1
18IM3	18IM3.13	7.61	0.42	0.00422	7.92E-06	-	-	-	-	-	-	-	-	-	-	-	-	X1
18IM3	18IM3.17	8.40	0.50	0.00699	6.69E-06	-	-	-	-	-	-	-	-	-	-	-	-	X1
18IM3	18IM3.6	7.76	0.41	0.00684	5.69E-06	-	-	-	-	-	-	-	-	-	-	-	-	X1
18IM3	18IM3.12	11.13	0.40	0.00336	2.23E-05	0.13	0.28	3147	0.001550	0.000012	0.281580	0.000028	1.46719	0.00006	1.88760	0.00036	2	4
18IM3	18IM3.11	11.56	0.41	0.00237	9.37E-06	20.93	0.25	4192	0.000506	0.000023	0.280951	0.000025	1.46721	0.00004	1.88694	0.00033	2	4
18IM3	18IM3.08	11.15	0.43	0.00346	8.58E-06	-17.09	0.27	4003	0.000828	0.000040	0.281068	0.000027	1.46722	0.00004	1.88696	0.00029	2	4
18IM3	18IM3.15	11.89	0.45	0.00383	9.08E-06	-4.17	0.18	3362	0.000725	0.000015	0.281428	0.000018	1.46724	0.00006	1.88702	0.00027	2	4
18IM3	18IM3.14	11.05	0.40	0.00347	1.70E-06	0.13	0.26	3147	0.000649	0.000034	0.281546	0.000026	1.46721	0.00005	1.88710	0.00025	2	4
18IM3	18IM3.4	11.85	0.40	0.00270	2.40E-06	2.35	0.24	3035	0.000982	0.000044	0.281621	0.000024	1.46720	0.00005	1.88683	0.00028	2	4
18IM3	18IM3.16	10.41	0.41	0.00197	2.87E-06	3.77	0.16	2964	0.001035	0.00006	0.281663	0.000016	1.46720	0.00005	1.88688	0.00023	2	4
18IM3	18IM3.07	11.82	0.40	0.00216	3.03E-06	4.93	0.21	2905	0.000620	0.000035	0.281680	0.000021	1.46719	0.00007	1.88695	0.00020	2	4

Table C1. Continued.

Chapter 3

LARGE IGNEOUS PROVINCES TRACK 2.4 GA SUBAERIAL EMERGENCE OF CONTINENTS

This chapter is submitted for publication as:

Liebmann, J., Spencer, C.J., Kirkland, C.K., Ernst, R. E. Large igneous provinces track 2.4 Ga subaerial emergence of continents. *Submitted to Geophysical Research Letters.*

Abstract

Geologic observations and numerical models posit that Archean continents were mostly submarine. In contrast, approximately one-third of modern Earth's surface area consists of subaerial continental crust. To constrain the timing of continental emergence above sea-level, we reevaluate the geologic record of continental large igneous provinces (LIPs) from 2.7-2.0 Ga. Our results indicate increased subaerial continental volcanism at ~2.4 Ga, supporting widespread subaerial emergence of continents at this time. An increase in exposed continental crust significantly impacts atmospheric and oceanic geochemical cycles, and the supply of nutrients for marine bioproductivity. By implication, an increase in freeboard may have triggered the earliest global glaciation event and the first significant rise of atmospheric oxygen. This period of elevated freeboard was punctuated by a short-lived continental drowning event that coincides with the 2.22-2.06 Ga global carbon-isotope excursion (Lomagundi-Jatuli event). Such drowning event potentially facilitated the substantial burial of organic carbon.

3.1 Introduction

Approximately 30% of Earth's present surface area consists of subaerial continental crust. Archean siliciclastic sediments (e.g. Eriksson et al., 1999) indicate that ancient continents were at least locally raised above sea-level. However, geochemical proxies and numerical models suggest that the subaerial exposure of Archean continental crust was limited (Flament et al., 2013; Johnson and Wing, 2020). Furthermore, continental flood basalts that erupted in submarine environments are common in the Archean and Paleoproterozoic, but are rare to absent in the Phanerozoic (Arndt, 1999; Kump and Barley, 2007). Multiple lines of evidence support an increase in freeboard (the average elevation of continental crust above sea level) in the early Paleoproterozoic era; including shifting of oxygen isotopic values in shales due to the onset of a modern hydrological cycle over large subaerial landmasses (Bindeman et al., 2018), and changes in oxygen isotopes of sediment-derived melts induced by enhanced subaerial weathering of exposed continents (Spencer et al., 2019). Furthermore, $^{87}\text{Sr}/^{86}\text{Sr}$ ratios of marine carbonate rocks increase between 2.7 and 2.4 Ga implying increasing continental influence on ocean chemistry through crustal erosive runoff (Flament et al., 2013; Shields and Veizer, 2002). Also, the volcano-sedimentary record of cratons that make up parts of the present-day continents of Africa, India, Australia, North and South America, and Europe indicate a rapid increase in freeboard at ~ 2.4 Ga (Eriksson et al., 1999; Eriksson and Condie, 2014). Broadly coincidental, the oldest known widespread, low-latitude glaciation occurred (Rasmussen et al., 2013), and atmospheric O_2 rose to $>10^{-5}$ present atmospheric level (Pavlov and Kasting, 2002), referred to as 'Great Oxidation Event' (Holland, 2002). Based on the global large igneous province (LIP) record and the assumption that all post-Archean continental LIPs are emplaced subaerially, Kump & Barley (2007) proposed that subaerial volcanism increased at 2.5 Ga, and that the associated change in the redox state of emitted volcanic gases facilitated atmospheric oxygenation. Large igneous provinces represent high volume, short duration intraplate magmatic events (Ernst, 2014). They typically consist of flood basalts and a plumbing system of dyke swarms, sills, and layered intrusions. To constrain the timing of the shift from predominantly submarine to predominantly subaerial continental volcanism, and to test the hypothesis of a 2.4 Ga widespread emergence of continents above sea-level, we reevaluate the global continental LIP record to determine submarine vs. subaerial volcanic emplacement.

3.2 Data Source and Eruptive Loci Criteria

We consider all 2.7-2.0 Ga continental LIPs in the compilations of Prokoph et al. (2004), and Condie et al. (2015) updated with recent literature (Figure 3.1, Supplementary Table B1). LIPs that have been classified as oceanic (e.g. oceanic plateaus, ocean basin flood basalts), and LIPs that do not show evidence for crustal contamination and hence are likely to be oceanic have been excluded from this evaluation (see Figure 3.2, and Table B1 for a complete list of oceanic and continental LIP events from 2.7-2.0 Ga). Ninety percent of continental flood basalts show evidence for interaction with continental material en route to the surface (Kerr et al., 2000). Geochemical indications for continental contamination include enrichment in light rare earth elements, and large ion lithophile elements as these elements are strongly enriched in the upper continental crust (Kerr et al., 2000; and references therein). Kerr et al. (2000), and Doucet et al. (2020) provide discrimination criteria for oceanic LIPs.

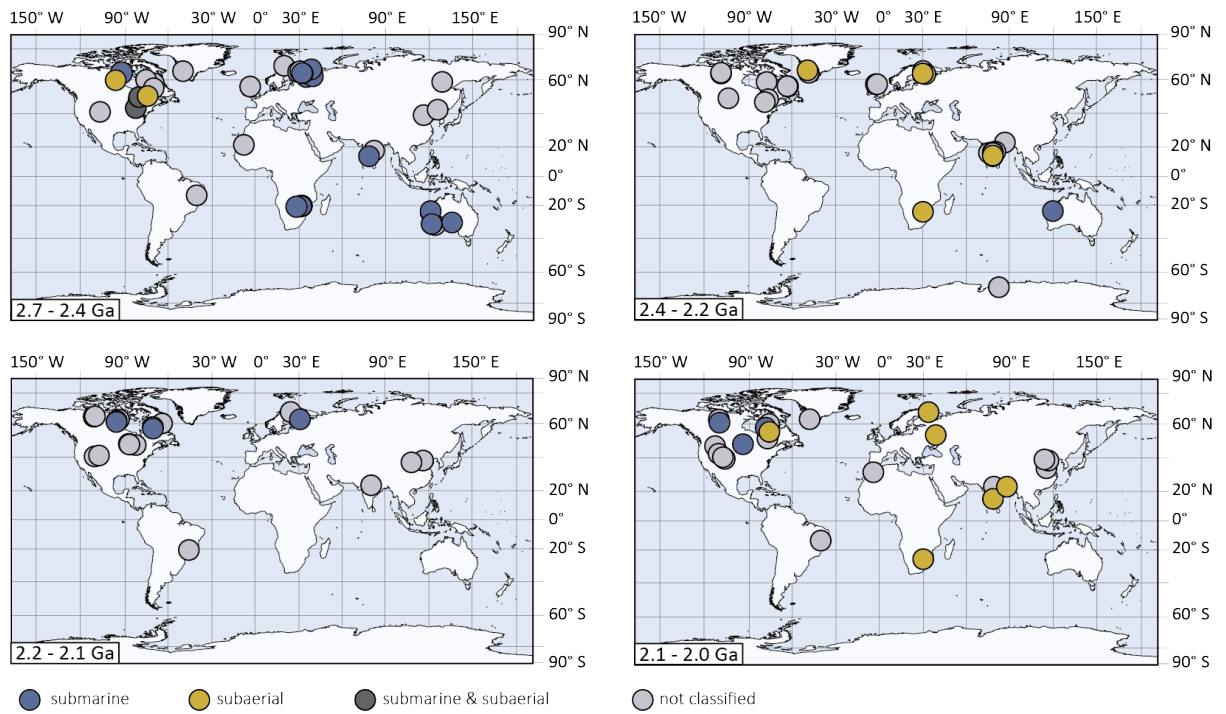


Figure 3.1. Location and locus of emplacement of continental LIP events from 2.7 to 2.0 Ga.

The most robust criteria for subaerial vs. submarine volcanic emplacement are the eruptive characteristics of extrusive igneous rocks that form a LIP. The presence of pillow lavas and hyaloclastites is strong evidence that indicates a submarine emplacement, whereas amygdalooidal flow tops, and columnar jointing are commonly observed in subaerial lava flows (Kerr et al., 2000). Another indicator of the emplacement environment includes sediments intercalated with the extrusive rocks of the LIP. Alluvial, aeolian, and lacustrine deposits, weathered horizons, and initial emplacement on eroded land surfaces are characteristic of subaerial environments (Eriksson et al., 1999; Kerr et al., 2000). In contrast, marine clay, carbonates, chert, and other marine chemical sediments indicate submarine environments (Eriksson et al., 1999). Intercalated terrigenous sediments deposited in marine environments (e.g. turbidites, tidal sandstones) indicate a partly emerged, partly submerged continent, making any definitive categorization problematic. Hence, intercalated terrigenous continental shelf sediments are not used in this study to discriminate subaerial and submarine LIP emplacement. For many Precambrian LIPs, the intrusive rocks of the magmatic system are the only preserved remnants. Where possible, the locus of emplacement of those LIPs (e.g. dyke swarms) is determined based on correlation to coeval extrusive magmatism on the same craton or intracratonic sedimentary successions with reasonable age constraints. A summary of the criteria for subaerial vs. submarine emplacement is provided in Table 3.1.

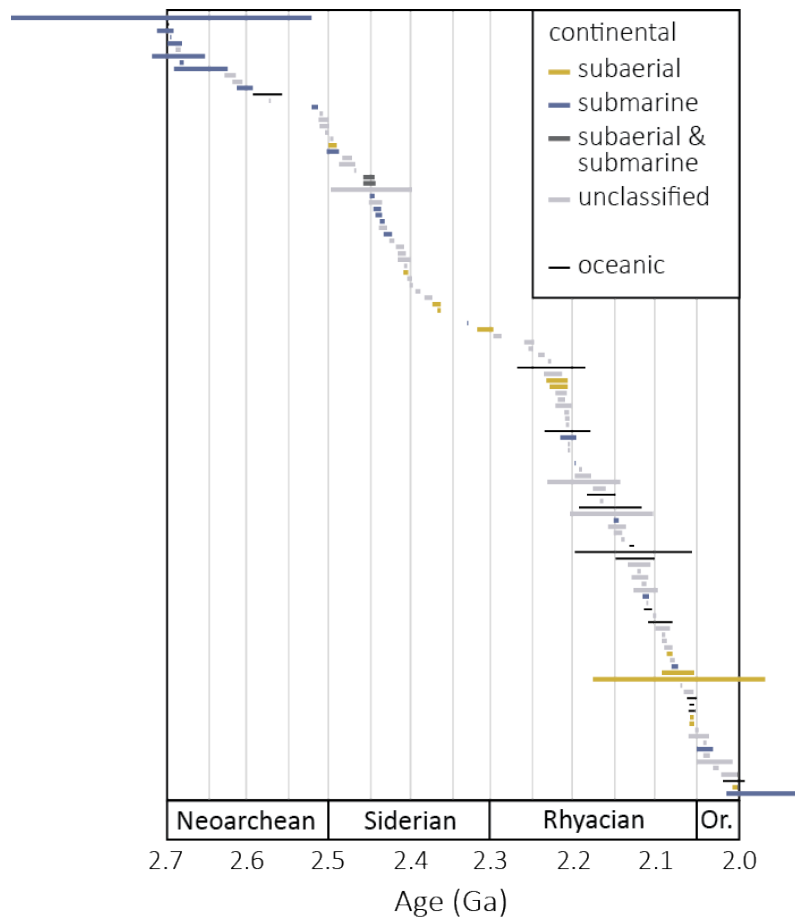


Figure 3.2. Temporal distribution of oceanic and continental LIPs from 2.7 to 2.0 Ga. Lengths of the bars reflect age uncertainties rather than durations of LIP events. LIP events are typically short lived (<5 Myr) or consist of multiple short pulses over a maximum of a few 10s of Myr (Ernst, 2014).

3.3 Subaerial Emergence of Continents Tracked by Continental LIP Record

The locus of emplacement could be identified for 38 out of 106 continental LIPs from 2.7-2.0 Ga. Considering only the classified events, the fraction of subaerial LIPs rises from 11% at 2.7-2.4 Ga to 71% at 2.4-2.2 Ga, then falls to 0% at 2.2-2.1 Ga, and rises again to 67% at 2.1-2.0 Ga (Figure 3.3). Kump and Barley (2007) posit that all post-Archean continental LIPs are subaerial. The fraction of subaerial LIPs is likely underestimated as higher erosional rates and hiatuses in continental sedimentation are a predicted consequence for high freeboard. Continental erosional process complicates the identification of LIP emplacement environment. Nonetheless, relative changes in proportions are unlikely to be caused by preservation bias and

are interpreted to reflect changes in emergent land area. This is supported by temporal correlation of changes in freeboard (as determined based on the continental LIP record) with changes in geochemical parameters sensitive to alterations in freeboard, as well as sedimentological evidence (Figures 3.3 and 3.4). The time intervals of increased and diminished subaerial LIP volcanism are in good agreement with

subaerial criteria	submarine criteria
subaerial lava flows (e.g. amygdaloidal flow tops, columnar jointing)	submarine lava flows (e.g. pillows, hyaloclastites)
intercalated continental sediments (e.g. alluvial, lacustrine, aeolian deposits)	intercalated oceanic sediments (e.g. marine clay, carbonates, chert)
emplacement on weathered horizons or eoded land surfaces	
LIP event coeval with subaerial intracratonic sedimentary succession and/or subaerial extrusive magmatism on the same craton	LIP event coeval with submarine intracratonic sedimentary succession and/or submarine extrusive magmatism on the same craton

Table 3.1. Criteria for subaerial vs. submarine continental LIP emplacement.

the time intervals of global low and high freeboard, respectively, as proposed by Eriksson et al., (1999) based on the global supracratonic volcano-sedimentary record (Figure 3.3). Precambrian sedimentation patterns indicate deposition in predominant oceanic settings or epeiric seas, and generally low-freeboard conditions prior to ~2.42 Ga (Eriksson et al., 2005; Eriksson and Condie, 2014). However, local exceptions of high freeboard occur, and have been speculated to reflect mantle plume-related uplift (Eriksson et al., 2005). The first marked increase in subaerial continental LIP volcanism at ~2.4 Ga closely matches the 2.35 Ga change in the oxygen isotope composition of sediment melts (Spencer et al., 2019), the 2.43-2.31 Ga shift in the oxygen isotope composition of shales (Bindeman et al., 2018; Spencer et al., 2019), and broadly overlaps with a change in $^{87}\text{Sr}/^{86}\text{Sr}$ ratio of marine carbonate rocks (Flament et al., 2013; Shields and Veizer, 2002), all of which are reasonably linked to the widespread emergence of continents above sea-level (Figure 3.4). A pervasive erosional event at <2.42 Ga led Eriksson

and Condie, (2014) to postulate a relatively rapid global-scale drop in sea-level potentially related to a ~2.4-2.2 Ga tectono-magmatic slowdown (Condie et al., 2009; Spencer et al., 2018). This proposed lull in mantle activity and concomitant reduced plate-velocities (Spencer et al., 2018) and mid-ocean ridge activity (Eriksson and Condie, 2014) may have led to cooling and thickening of the oceanic lithosphere, causing rapid subsidence of the ocean floor and a drop in eustatic sea-level (Eriksson and Condie, 2014; Miller et al., 2005). The subsequent drowning event from 2.20-2.10 Ga is coeval with a peak in preserved oceanic LIPs (Figure 3.4), and a flare-up of juvenile magmatism (Spencer et al., 2018) providing a potential geodynamic driver for global relative sea-level rise (Ernst and Youbi, 2017). It has been suggested that peaks in the oceanic LIP record reflect increased mantle-plume activity in the oceanic realm (Doucet et al., 2020). Emplacement of oceanic plateaus induces a moderately rapid sea-level rise of 60 m/My, and subsequent slow sea-level fall (10 m/My) due to thermal subsidence (Miller et al., 2005). Furthermore, a global positive carbon isotope excursion in sedimentary carbonates (Lomagundi-Jatuli event) from 2.20-2.06 (Martin et al., 2013) temporally overlaps with the widespread flooding of continents (Figure 3.4). Although the mechanism that is responsible for this excursion event is not known, it is generally assumed that the Lomagundi-Jatuli event was caused by increased organic carbon burial or decreased carbonate deposition (Bekker and Holland, 2012; Martin et al., 2013). Widespread continental drowning may have facilitated the burial of large quantities of organic carbon. The short episode of increased subaerial volcanism from 2.50-2.45 Ga (recorded by continental LIPs in the Superior and Hearne Cratons) could be related to mantle upwelling during the ~2.45 Ga rifting of Superia (Bleeker, 2003), and associated dynamic topography that led to continental uplift and high freeboard (Gurnis, 1988).

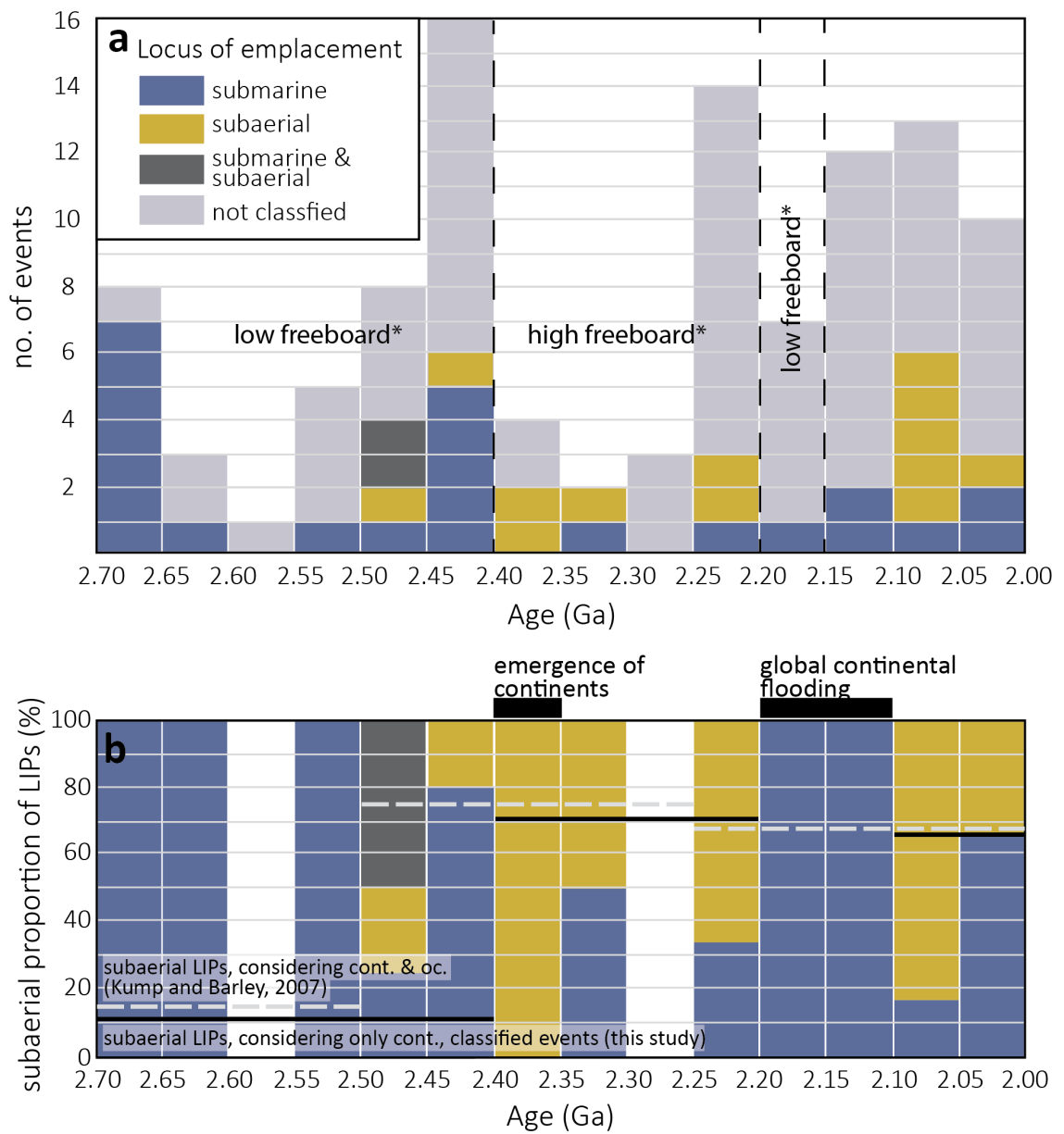


Figure 3.3. Distribution of continental LIP emplacement environment from 2.7-2.0 Ga. (A) Absolute numbers of continental LIP events recorded from 2.7-2.0 Ga, color-coded by locus of emplacement. Bin-width is 50 Ma. Compilation of LIP events is provided in Supplementary Table B1. *Time intervals of low and high freeboard, respectively, as inferred from the global supracrustal volcano-sedimentary record are from Eriksson et al. (1999), and Eriksson and Condie (2014). (B) Proportions of emplacement loci through time. Solid black line represents average fraction of subaerial LIP events for the time intervals 2.7-2.4 Ga, 2.4-2.2 Ga, and 2.1-2.0 Ga. LIP events that could not be classified are excluded. Dashed grey line indicates proportion of subaerial LIPs after Kump and Barley (2007). Note that the assessment by Kump and Barley (2007) includes continental and

oceanic LIPs, whereas this study only considers continental LIPs. Black bars indicate timings of first marked continental emergence, and a global continental flooding event.

3.4 Repercussion of Continental Emergence on Climate, Atmosphere, and Biosphere

The revaluation of the continental LIP record presented here supports an increase in freeboard at ~ 2.4 Ga (hereafter referred to as widespread continental emergence). Importantly, this does not imply that continents were completely submerged prior to 2.4 Ga, nor that freeboard was necessarily constant after 2.4 Ga. Widespread continental emergence is temporally associated to the oldest known widespread glaciation at ~ 2.4 Ga (Kopp et al., 2005; Rasmussen et al., 2013), and atmospheric oxygenation (Holland, 2002). Two contrasting models have been suggested for the Paleoproterozoic rise of O₂; namely, a long-lived oscillatory rise from ~ 2.45 -2.25 Ga (Gumsley et al., 2017), or a rapid (1-10 Ma) rise at 2.33 Ga (Luo et al., 2016). Elevated and emerged continental crust may increase the supply of nutrients (e.g. P and Fe) into oceans, increasing that available for oxyphotobacteria (Campbell and Allen, 2008). The proportion of submarine to subaerial volcanism would also change, which in turn alters the redox state of volcanic gases towards more oxidizing (Gaillard et al., 2011; Kump and Barley, 2007). The rise of O₂ may have triggered potentially global glaciations (Kopp et al., 2005). Furthermore, larger areas of subaerial landmasses increase the albedo of the Earth and enhance silicate weathering and associated removal of CO₂ from the atmosphere (Rosing et al., 2010, and references therein).

The timing of the advent of oxygenic photosynthesis is highly controversial; estimates range from >3.7 Ga (Rosing and Frei, 2004) to immediately preceding atmospheric oxygenation (Ward et al., 2016). Consequently, there is no agreement on the mechanism that led to the rise of O₂. Proposed causes for atmospheric oxygenation include 1) an increase in O₂ production (i.e. through

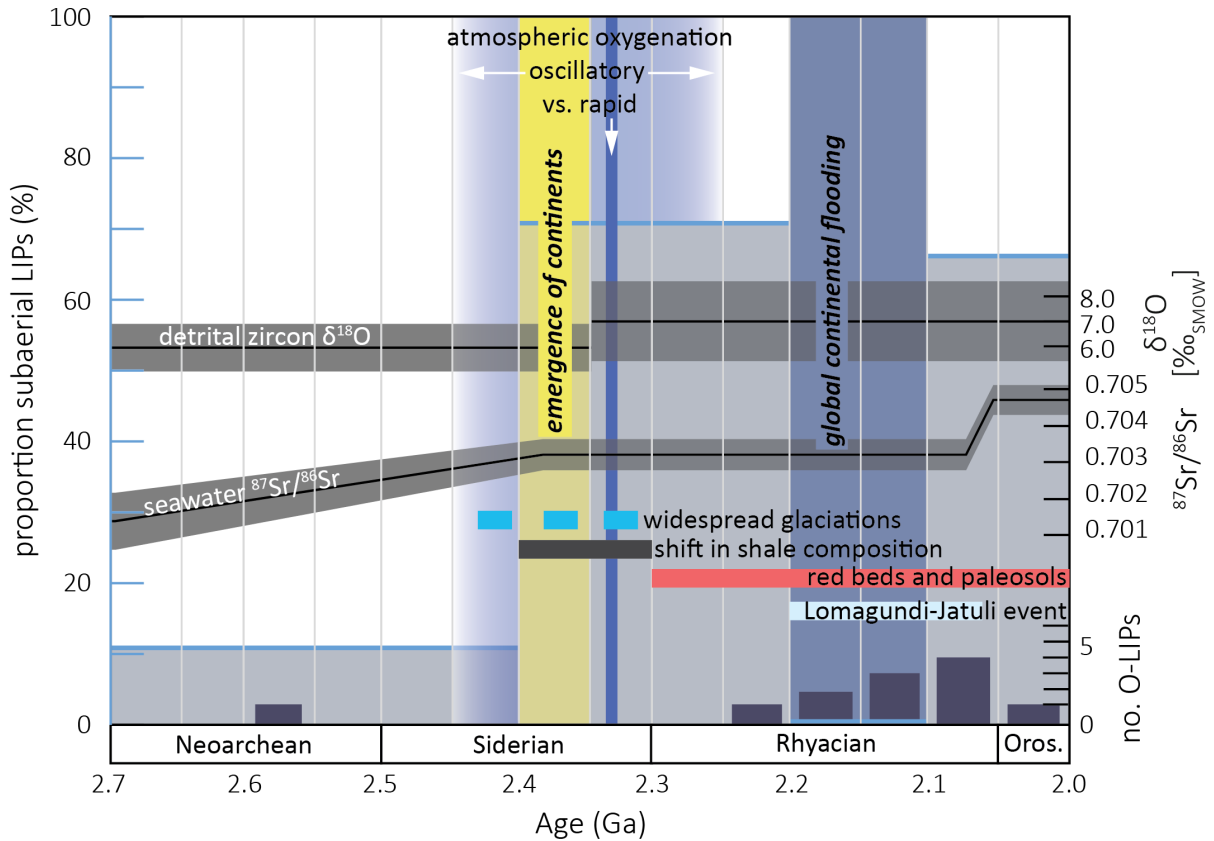


Figure 3.4. Temporal correlation of continental emergence and other secular changes at the Archean-Proterozoic transition. Fraction of subaerial LIPs is shown as grey boxes. The widespread emergence of continents above sea-level at ~ 2.4 (indicated by yellow bar; i.e. initial marked increase in freeboard; note that freeboard may have continued to increase up until ~ 2.2 Ga) is temporally associated with atmospheric oxygenation (Gumsley et al., 2017; Luo et al., 2016), a shift in the oxygen isotope composition of shales (Bindeman et al., 2018), widespread glaciations (Rasmussen et al., 2013), and the first occurrence of red beds and paleosols (Rainbird et al., 1990). Furthermore the oxygen isotope composition of detrital zircon (expressed as $\delta^{18}\text{O}$; deviation in the isotope ratio $^{18}\text{O}/^{16}\text{O}$ in ‰ relative to average sea water; SMOW) is subject to a rapid change at 2.35 Ga (shown as black line with grey 1σ envelope; Spencer et al., 2019). The evolution of seawater $^{87}\text{Sr}/^{86}\text{Sr}$ ratio as modelled based on the carbonate Sr isotope record using step change analysis is shown as black line with 2σ envelope (see supplementary Figure A1 for details). Seawater $^{87}\text{Sr}/^{86}\text{Sr}$ ratios increase between 2.7 and 2.4 Ga, and at ~ 2.1 Ga. Note that the rate at which the increase in seawater $^{87}\text{Sr}/^{86}\text{Sr}$ ratio occurred between 2.7 and 2.4 Ga (i.e. rapid vs. slow rise) is not well constrained due to limited availability of carbonate Sr isotope data for this time interval. A 2.2-2.1 Ga global continental flooding event (indicated by blue bar) is coeval with the Lomagundi-Jatuli event (Martin et al., 2013), and also a peak in recorded oceanic LIPs. Number of oceanic LIPs are from Doucet et al. (2020), and this study (supplementary Table B1).

the radiation of oxyphotobacteria) (Ward et al., 2016), 2) a decrease in O₂ consumption (e.g. through changing redox state of volcanic gases, increased burial of organic carbon, or decreased pyrite weathering) (Bekker and Holland, 2012; Holland, 2002), and 3) a combination of both (through enhanced oxygenic photosynthesis combined with increased carbon burial) (Campbell and Allen, 2008). Phosphorous is a limiting nutrient on long-term primary production (Tyrrell, 1999). A shift in ocean nutrient availability from phosphorous to iron limiting may have resulted in ecological conditions favourable for oxygenic photoautotrophs over anoxygenic photoautotrophs (Jones et al., 2015). Hydrolysis of apatite during the weathering of igneous and sedimentary rocks is the major source of phosphorous in the biosphere (Brantley, 2008). Numerical models imply a strong influence of emergent continental land area on P flux into the ocean (Hao et al., 2020). Previous studies have invoked a model for atmospheric oxygenation that involves changes in terrestrial silicate weathering controlling the long-term supply of phosphorous into the oceans and primary production of oxygen (e.g. Campbell and Allen, 2008; Lee et al., 2016; Mills et al., 2014). While the overall trends in P flux are similarly modelled for slow and rapid continental emergence, respectively, the timing of a secular increase in P flux is strongly dependent on the timing of widespread continental emergence causing the rate of physical erosion to exceed the rate of chemical weathering (Hao et al., 2020). An increase in subaerial continental land area at ~2.4 Ga could have fuelled O₂ production through a flush of essential nutrients into the ocean, concomitant with an increase in oxygenic photosynthesis (either in terms of radiation or bioproductivity).

The implication of our study is that the widespread emergence of continents above sea-level constitutes a potential trigger for the boost – or even first invention – of oxygenic photosynthesis, leading to the oxygenation of the atmosphere. The shift towards less reducing volcanic gases associated with diminishing submarine volcanism may have further facilitated the early Paleoproterozoic rise of O₂ (Gaillard et al., 2011; Kump and Barley, 2007).

3.5 References

- Arndt, N., 1999. Why was flood volcanism on submerged continental platforms so common in the Precambrian? *Precambrian Res.* 97, 155–164. [https://doi.org/10.1016/S0301-9268\(99\)00030-3](https://doi.org/10.1016/S0301-9268(99)00030-3)

- Bekker, A., Holland, H.D., 2012. Oxygen overshoot and recovery during the early Paleoproterozoic. *Earth Planet. Sci. Lett.* 317–318, 295–304. <https://doi.org/10.1016/j.epsl.2011.12.012>
- Bindeman, I.N., Zakharov, D.O., Palandri, J., Greber, N.D., Dauphas, N., Retallack, G.J., Hofmann, A., Lackey, J.S., Bekker, A., Data, E., 2018. Rapid emergence of subaerial landmasses and onset of a modern hydrologic cycle 2.5 billion years ago. *Nature* 557, 545–548. [https://doi.org/https://doi.org/10.1038/s41586-018-0131-1](https://doi.org/10.1038/s41586-018-0131-1)
- Bleeker, W., 2003. The late Archean record: A puzzle in ca. 35 pieces. *Lithos* 71, 99–134. <https://doi.org/10.1016/j.lithos.2003.07.003>
- Brantley, S.L., 2008. Kinetics of Mineral Dissolution, in: Kinetics of Water-Rock Interaction. Springer New York, New York, NY, pp. 151–210. https://doi.org/10.1007/978-0-387-73563-4_5
- Campbell, I.H., Allen, C.M., 2008. Formation of supercontinents linked to increases in atmospheric oxygen. *Nat. Geosci.* 1, 554–558. <https://doi.org/10.1038/ngeo259>
- Condie, K.C., Davaille, A., Aster, R.C., Arndt, N., 2015. Upstairs-downstairs: supercontinents and large igneous provinces, are they related? *Int. Geol. Rev.* 57, 1341–1348. <https://doi.org/10.1080/00206814.2014.963170>
- Condie, K.C., O'Neill, C., Aster, R.C., 2009. Evidence and implications for a widespread magmatic shutdown for 250 My on Earth. *Earth Planet. Sci. Lett.* 282, 294–298. <https://doi.org/10.1016/j.epsl.2009.03.033>
- Doucet, L.S., Li, Z.-X., Ernst, R.E., Kirscher, U., El Dien, H.G., Mitchell, R.N., 2020. Coupled supercontinent–mantle plume events evidenced by oceanic plume record. *Geology* 48, 159–163. <https://doi.org/10.1130/G46754.1>
- Eriksson, P.G., Catuneanu, O., Sarkar, S., Tirsgaard, H., 2005. Patterns of sedimentation in the Precambrian. *Sediment. Geol.* 176, 17–42. <https://doi.org/10.1016/j.sedgeo.2005.01.003>
- Eriksson, P.G., Condie, K.C., 2014. Cratonic sedimentation regimes in the ca. 2450–2000 Ma period: Relationship to a possible widespread magmatic slowdown on Earth? *Gondwana Res.* 25, 30–47. <https://doi.org/10.1016/j.gr.2012.08.005>
- Eriksson, P.G., Mazumder, R., Sarkar, S., Bose, P.K., Altermann, W., van der Merwe, R., 1999. The 2.7–2.0 Ga volcano-sedimentary record of Africa, India and Australia: evidence for global and local changes in sea level and continental freeboard. *Precambrian Res.* 97, 269–302. [https://doi.org/10.1016/S0301-9268\(99\)00035-2](https://doi.org/10.1016/S0301-9268(99)00035-2)
- Ernst, R.E., 2014. Large igneous provinces. Cambridge University Press.
- Ernst, R.E., Youbi, N., 2017. How Large Igneous Provinces affect global climate, sometimes cause mass extinctions, and represent natural markers in the geological record. *Palaeogeogr. Palaeoclimatol. Palaeoecol.* 478, 30–52.

<https://doi.org/10.1016/j.palaeo.2017.03.014>

- Flament, N., Coltice, N., Rey, P.F., 2013. The evolution of the $^{87}\text{Sr}/^{86}\text{Sr}$ of marine carbonates does not constrain continental growth. *Precambrian Res.* 229, 177–188. <https://doi.org/10.1016/j.precamres.2011.10.009>
- Gaillard, F., Scaillet, B., Arndt, N.T., 2011. Atmospheric oxygenation caused by a change in volcanic degassing pressure. *Nature* 478, 229–232. <https://doi.org/10.1038/nature10460>
- Gumsley, A.P., Chamberlain, K.R., Bleeker, W., Söderlund, U., de Kock, M.O., Larsson, E.R., Bekker, A., 2017. Timing and tempo of the Great Oxidation Event. *Proc. Natl. Acad. Sci.* 114, 1811–1816. <https://doi.org/10.1073/pnas.1608824114>
- Gurnis, M., 1988. Large-scale mantle convection and the aggregation and dispersal of supercontinents. *Nature* 332, 695–699.
- Hao, J., Knoll, A.H., Huang, F., Hazen, R.M., Daniel, I., 2020. Cycling phosphorus on the Archean Earth: Part I. Continental weathering and riverine transport of phosphorus. *Geochim. Cosmochim. Acta* 273, 70–84. <https://doi.org/10.1016/j.gca.2020.01.027>
- Holland, H.D., 2002. Volcanic gases, black smokers, and the great oxidation event. *Geochim. Cosmochim. Acta* 66, 3811–3826. [https://doi.org/10.1016/S0016-7037\(02\)00950-X](https://doi.org/10.1016/S0016-7037(02)00950-X)
- Johnson, B.W., Wing, B.A., 2020. Limited Archaean continental emergence reflected in an early Archaean ^{18}O -enriched ocean. *Nat. Geosci.* 13, 243–248. <https://doi.org/10.1038/s41561-020-0538-9>
- Jones, C., Nomosatryo, S., Crowe, S.A., Bjerrum, C.J., Canfield, D.E., 2015. Iron oxides, divalent cations, silica, and the early earth phosphorus crisis. *Geology* 43, 135–138. <https://doi.org/10.1130/G36044.1>
- Kerr, A.C., White, R. V., Saunders, A.D., 2000. LIP Reading: Recognizing Oceanic Plateaux in the Geological Record. *J. Petrol.* 41, 1041–1056. <https://doi.org/10.1093/petrology/41.7.1041>
- Kopp, R.E., Kirschvink, J.L., Hilburn, I.A., Nash, C.Z., 2005. The Paleoproterozoic snowball Earth: A climate disaster triggered by the evolution of oxygenic photosynthesis. *Proc. Natl. Acad. Sci.* 102, 11131–11136. <https://doi.org/10.1073/pnas.0504878102>
- Kump, L.R., Barley, M.E., 2007. Increased subaerial volcanism and the rise of atmospheric oxygen 2.5 billion years ago. *Nature* 448, 1033–1036. <https://doi.org/10.1038/nature06058>
- Lee, C.-T.A., Yeung, L.Y., McKenzie, N.R., Yokoyama, Y., Ozaki, K., Lenardic, A., 2016. Two-step rise of atmospheric oxygen linked to the growth of continents. *Nat. Geosci.* 9, 417–424. <https://doi.org/10.1038/ngeo2707>
- Luo, G., Ono, S., Beukes, N.J., Wang, D.T., Xie, S., Summons, R.E., 2016. Rapid oxygenation

of Earth's atmosphere 2.33 billion years ago. *Sci. Adv.* 2.
<https://doi.org/10.1126/sciadv.1600134>

Martin, A.P., Condon, D.J., Prave, A.R., Melezhik, V.A., Lepland, A., Fallick, A.E., 2013. Dating the termination of the Palaeoproterozoic Lomagundi-Jatuli carbon isotopic event in the North Transfennoscandian Greenstone Belt. *Precambrian Res.* 224, 160–168.
<https://doi.org/10.1016/j.precamres.2012.09.010>

Miller, K.G., Kominz, M.A., Browning, J. V., Wright, J.D., Mountain, G.S., Katz, M.E., Sugarman, P.J., Cramer, B.S., Christie-Blick, N., Pekar, S.F., 2005. The Phanerozoic Record of Global Sea-Level Change. *Science* (80-.). 310, 1293–1298.
<https://doi.org/10.1126/science.1116412>

Mills, B., Lenton, T.M., Watson, A.J., 2014. Proterozoic oxygen rise linked to shifting balance between seafloor and terrestrial weathering. *Proc. Natl. Acad. Sci.* 111, 9073–9078.
<https://doi.org/10.1073/pnas.1321679111>

Pavlov, A.A., Kasting, J.F., 2002. Mass-Independent Fractionation of Sulfur-Isotopes in Archean Sediments: Strong Evidence for an Anoxic Archean Atmosphere. *Astrobiology* 2.

Prokoph, A., Ernst, R.E., Buchan, K.L., 2004. Time-Series Analysis of Large Igneous Provinces: 3500 Ma to Present. *J. Geol.* 112, 1–22. <https://doi.org/10.1086/379689>

Rainbird, R.H., Nesbitt, H.W., Donaldson, J.A., 1990. Formation and Diagenesis of a Sub-Huronian Saprolith: Comparison with a Modern Weathering Profile. *J. Geol.* 98, 801–822.
<https://doi.org/10.1086/629455>

Rasmussen, B., Bekker, A., Fletcher, I.R., 2013. Correlation of Paleoproterozoic glaciations based on U–Pb zircon ages for tuff beds in the Transvaal and Huronian Supergroups. *Earth Planet. Sci. Lett.* 382, 173–180. <https://doi.org/10.1016/j.epsl.2013.08.037>

Rosing, M.T., Bird, D.K., Sleep, N.H., Bjerrum, C.J., 2010. No climate paradox under the faint early Sun. *Nature* 464, 744–747. <https://doi.org/10.1038/nature08955>

Rosing, M.T., Frei, R., 2004. U-rich Archaean sea-floor sediments from Greenland – indications of >3700 Ma oxygenic photosynthesis. *Earth Planet. Sci. Lett.* 217, 237–244.
[https://doi.org/10.1016/S0012-821X\(03\)00609-5](https://doi.org/10.1016/S0012-821X(03)00609-5)

Shields, G., Veizer, J., 2002. Precambrian marine carbonate isotope database: Version 1.1. *Geochemistry Geophys. Geosystems* 3. <https://doi.org/10.1029/2001GC000266>

Spencer, C.J., Murphy, J.B., Kirkland, C.L., Liu, Y., Mitchell, R.N., 2018. Was the supercontinent cycle activated by a Palaeoproterozoic tectono-magmatic lull? *Nat. Geosci.* 11, 97–101. <https://doi.org/10.1038/s41561-017-0051-y>

Spencer, C.J., Partin, C.A., Kirkland, C.L., Raub, T.D., Liebmann, J., Stern, R.A., 2019. Paleoproterozoic increase in zircon $\delta^{18}\text{O}$ driven by rapid emergence of continental crust.

- Geochim. Cosmochim. Acta 257, 16–25. <https://doi.org/10.1016/j.gca.2019.04.016>
- Tyrrell, T., 1999. The relative influences of nitrogen and phosphorus on oceanic primary production. Nature 400, 525–531. <https://doi.org/10.1038/22941>
- Ward, L.M., Kirschvink, J.L., Fischer, W.W., 2016. Timescales of Oxygenation Following the Evolution of Oxygenic Photosynthesis. Orig. Life Evol. Biosph. 46, 51–65. <https://doi.org/10.1007/s11084-015-9460-3>

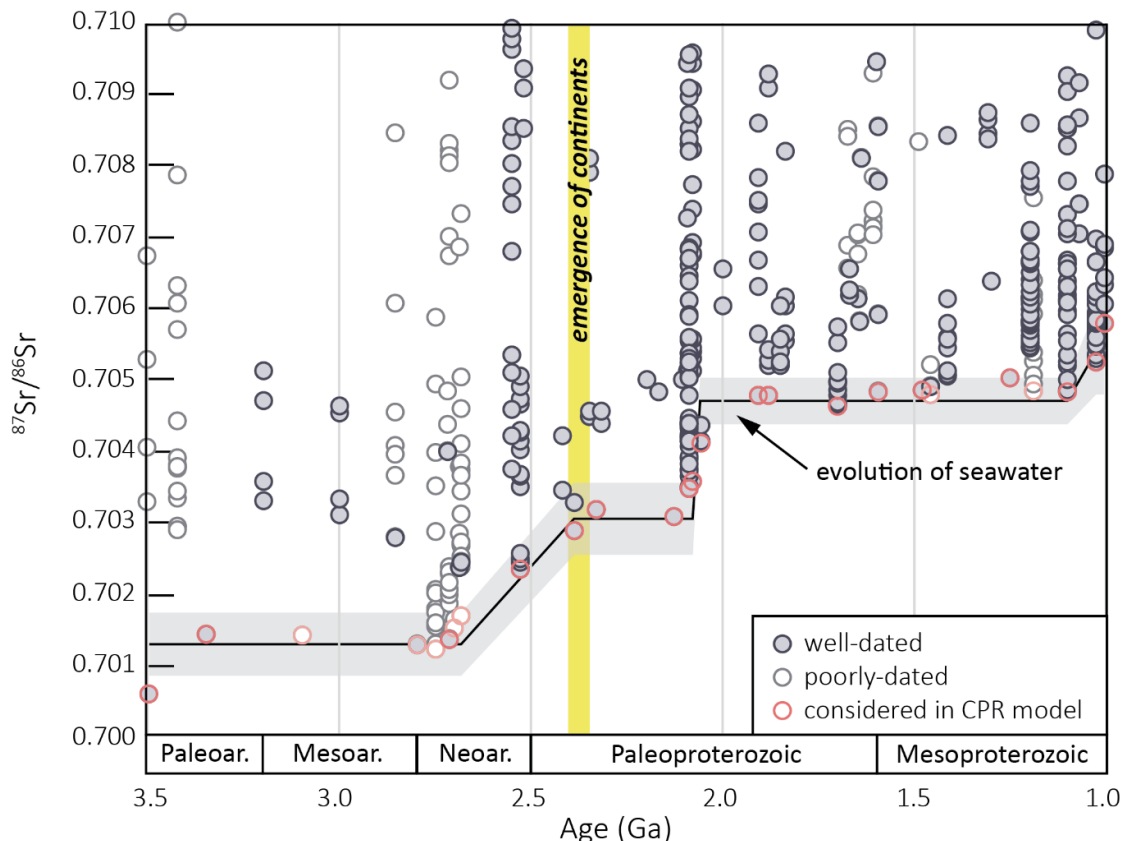
3.6 Author contributions

JL, CJS, CLK designed the research or contributed to designing the research. REE provided a recent compilation of LIP events. JL wrote the manuscript. All authors contributed to interpreting the data, and provided comments on the manuscript.

Appendices

- A:** Supplementary information on classification of LIP events without preserved extrusive rocks and supplementary Figure A1.
- B:** Supplementary Table B1, Large igneous province database.

Appendix A



Supplementary Figure A1. Carbonate $^{87}\text{Sr}/^{86}\text{Sr}$ isotopic ratios from 3.5 to 1.0 Ga. Data are from Shields and Veizer (2002), and Kuznetsov et al. (2010). Well and poorly time-constrained (uncertainty >50 Ma) samples are shown as grey and white circles, respectively. Note that lowest recorded carbonate $^{87}\text{Sr}/^{86}\text{Sr}$ ratio represents the best maximum estimate of seawater $^{87}\text{Sr}/^{86}\text{Sr}$ ratio at any particular time, as postdepositional alteration commonly leads to increased $^{87}\text{Sr}/^{86}\text{Sr}$ (Shields and Veizer, 2002). Statistical change-point analysis indicates increases in seawater $^{87}\text{Sr}/^{86}\text{Sr}$ between ~ 2.7 and 2.4 Ga and at ~ 2.1 Ga (black line: modelled median seawater $^{87}\text{Sr}/^{86}\text{Sr}$ ratio; grey field: 2σ envelope). Note, however, that the rate at which the increase in seawater $^{87}\text{Sr}/^{86}\text{Sr}$ ratio occurred between ~ 2.7 and 2.4 Ga (i.e. rapid vs. long-lived, consistent rise) cannot be constrained due to limited availability of carbonate Sr isotope data for this time interval. The conjugate partitioned recursion (CPR) algorithm of Jensen (2013) was used for change-point analysis.

A1. Case-description of classification of eruptive environment of LIP events without preserved extrusive rocks

For many Precambrian LIPs, the intrusive rocks of the magmatic system are the only preserved remnants, making a classification of the eruptive environment based on the first three criteria in Table 3.1 unfeasible. The ~2.41 Ga Du Chef (Ciborowski et al., 2014) and ~2.22 Ga Ungava events (Buchan et al., 2007) in the Superior craton, the ~2.37 Ga Graedefjord (Nilsson et al., 2013) and ~2.23 Ga Kikkertavik events (Sahin and Hamilton, 2019) in the North Atlantic craton, and the ~2.37 Ga Bangalore event in the Dharwar craton (French and Heaman, 2010) are examples for such events. Based on magmatic barcode comparison between the North Atlantic craton, Dharwar craton, and Superior craton, Nilsson et al., (2019) suggested that the three cratons have been situated adjacent to each other from 2.37 Ga to 2.17 Ga within a Paleoproterozoic supercraton. Therefore, the intracratonic Huronian Supergroup of the Superior Craton whose deposition is coeval with some of the LIP events listed above can be used to constrain their eruptive environment. Deposition of the <2.45 Ga to >2.31 Ga fluvial-lacustrine-glacial Lower Huronian Supergroup (Young, 2013; Rasmussen et al., 2013) is coeval with the Du Chef, Graedefjord, and Bangalore events. Hence, these LIPs likely erupted in a subaerial environment. The minimum age of the fluvial to shallow marine upper Huronian Supergroup is constraint by the intrusion of the ~2.22 Ga Nipissing dykes (Rasmussen et al., 2013) which form part of the Ungava LIP event (Buchan et al., 2007). As the deposition of the upper Huronian Supergroup precedes the Ungava event, the eruptive environment of this LIP cannot be determined based on the Huronian Supergroup. The Kikkertavik event is slightly older than the Ungava event, and therefore potentially erupted coevally with deposition of the upper Huronian supergroup. However, this assumption is not well founded. In addition, the depositional environment of the upper Huronian Supergroup alternates between fluvial and marine making any definitive categorization of the Kikkertavik event problematic.

A2. References

- Buchan, K.L., Goutier, J., Hamilton, M.A., Ernst, R.E., and Matthews, W.A., 2007, Paleomagnetism, U-Pb geochronology, and geochemistry of Lac Esprit and other dyke swarms, James Bay area, Quebec, and implications for Paleoproterozoic deformation of the Superior Province: Canadian Journal of Earth Sciences, v. 44, p. 643–664,

doi:10.1139/e06-131.

- Ciborowski, T.J.R., Kerr, A.C., McDonald, I., Ernst, R.E., Hughes, H.S.R., and Minifie, M.J., 2014, The geochemistry and petrogenesis of the Paleoproterozoic du Chef dyke swarm, Québec, Canada: *Precambrian Research*, v. 250, p. 151–166, doi:10.1016/j.precamres.2014.05.008.
- French, J.E., and Heaman, L.M., 2010, Precise U-Pb dating of Paleoproterozoic mafic dyke swarms of the Dharwar craton, India: Implications for the existence of the Neoarchean supercraton Sclavia: *Precambrian Research*, v. 183, p. 416–441, doi:10.1016/j.precamres.2010.05.003.
- Jensen, G., 2013, Closed-Form Estimation of Multiple Change-Point Models: PeerJ PrePrints, doi:<https://doi.org/10.7287/peerj.preprints.90v3>.
- Kuznetsov, A.B., Melezhik, V.A., Gorokhov, I.M., Melnikov, N.N., Konstantinova, G.V., Kutyavin, E.P., and Turchenko, T.L., 2010, Sr isotopic composition of Paleoproterozoic ^{13}C -rich carbonate rocks: The Tulomozero Formation, SE Fennoscandian Shield: *Precambrian Research*, v. 182, p. 300–312, doi:10.1016/j.precamres.2010.05.006.
- Nilsson, M.K.M., Klausen, M.B., and Petersson, A., 2019, Break-up related 2170–2120 Ma mafic dykes across the North Atlantic craton: Final dismembering of a North Atlantic-Dharwar craton connection? *Precambrian Research*, v. 329, p. 70–87, doi:10.1016/j.precamres.2018.12.028.
- Nilsson, M.K.M., Klausen, M.B., Söderlund, U., and Ernst, R.E., 2013, Precise U-Pb ages and geochemistry of Palaeoproterozoic mafic dykes from southern West Greenland: Linking the North Atlantic and the Dharwar cratons: *Lithos*, v. 174, p. 255–270, doi:10.1016/j.lithos.2012.07.021.
- Rasmussen, B., Bekker, A., and Fletcher, I.R., 2013, Correlation of Paleoproterozoic glaciations based on U–Pb zircon ages for tuff beds in the Transvaal and Huronian Supergroups: *Earth and Planetary Science Letters*, v. 382, p. 173–180, doi:10.1016/j.epsl.2013.08.037.
- Sahin, T., and Hamilton, M.A., 2019, New U-Pb baddeleyite ages for Neoarchean and Paleoproterozoic mafic dyke swarms of the southern Nain Province, Labrador: implications for possible plate reconstructions involving the North Atlantic craton: *Precambrian Research*, doi:10.1016/j.precamres.2019.02.001.
- Shields, G., and Veizer, J., 2002, Precambrian marine carbonate isotope database: Version 1.1: *Geochemistry Geophysics Geosystems*, v. 3, doi:10.1029/2001GC000266.
- Young, G.M., 2013, Climatic catastrophes in Earth history: two great Proterozoic glacial episodes: *Geological Journal*, v. 48, p. 1–21, doi:10.1002/gj.2467.

Appendix B

Table B1.1. Large igneous province database. Type: C – continental; O – oceanic. Comments are provided in Table B1.2.

Age (Ma)	2σ	Eruptive environment	Type	Location	Name	Subaerial Subaqueous						
						1	2	3	4	5	6	Reference
2050	2		C	North Atlantic Craton	Kangamuit dykes, MD3 dikes, Igusuaraliksuaq							Cadman et al., 2001;
												Nilsson et al., 2010;
												Sahin and Hamilton, 2019
2056	3	Subaerial	C	Kapvaal Craton	Bushveld event, Rooiberg Group	x	x					Buchanan et al., 2002; Ernst and Bleeker, 2010;
												Lenhardt and Eriksson, 2012
2056	2.3	Subaerial	C	Karelia Craton	Otanmaki, Keivisa-Kuetsjärvi-Umba	x	x					Melezhik and Fallick, 2004;
												Lahhinen et al., 2008;
												x Martin et al., 2013;
												Salminen et al., 2013
2056	4	Submarine/ subaerial	O	Fennoscandian Shield	Katasjøk komatiites	x	x	x				Pharaor et al., 1987;
2056	6	Submarine/ subaerial	O	Fennoscandian Shield	Peturamaa greenstone	x	x	x				Barnes and Olfen, 1990
2056	3	Submarine	O	Fennoscandian Shield	Jeesiorova greenstone	x	x					Hanski et al., 2001
2060	6		C	Wyoming Province	MD3S dykes, Tobacco Root Mountains, Montana							Hanski et al., 2001
2069	1		C	Superior Craton	Lac Esprit dykes							Brady et al., 2004
2072	106	Subaerial	C	Singhbhum Craton	Dhanjori Formation volcanics	x						Ernst and Bleeker, 2010;
												Mitchell et al., 2014
2073	20	Subaerial	C	Samartha	Voronezh	x						Roy et al., 2002;
												Mazumder et al., 2012
												Terentiev and Santosh, 2016;
												Terentiev, 2019
2077	4	Submarine	C	Superior Craton	Fort Frances dyke swarm (Kenora-Kabetogama)							Sims and Peterman, 1983;
												Ainsdell, 2005; Buchan et al., 2010
2080	3		C	North China Craton	Hutuo mafic dykes							x 2007; Ernst and Bleeker, 2010
2083.5	3.5	Subaerial	C	Dharwar craton	Devarambada dyke swarm							Wang et al., 2010
2085	5		C	Sao Francisco Craton	Medrado sill							x Soderlund et al., 2019
2090	3		C	North China Craton	Zaihuang sills, Menglianggu dykes							Olivera et al., 2004
2091	2		C	Superior Craton	Cauchon dyke swarm, (Molson dyke swarm, older dykes)							Peng et al., 2015;
												Yang et al. 2019
2092	9		C	Wyoming Craton	Snowy Pass gabbros							Halls and Heaman, 2000
												Prieto and Van Schmus, 1989;
												Roscoe and Card, 1993;
												Ernst and Bleeker, 2010

Table B1.1. Continued.

Age (Ma)	2σ	Eruptive environment	Type	Location	Name	Subaerial Subaqueous						
						1	2	3	4	5	6	Reference
2095	15	Submarine	O	West African Craton	Baundian, Western Subprovince of Birman		x	x	x	x		Abouchami et al., 1990; Hirdes et al., 1996; Kerr et al., 2000; Hirdes and Davis, 2002
2102	2		C	Superior Craton	Marathon diabase dykes, reversed, Superior Province							Buchanan et al., 1996; Hamilton et al., 2002
2110	5	Submarine	O (?) *	Guiana Shield	Inini greenstone belt, Paramaca series, Guiana	x	x	x	x	x		Gruau et al., 1985; Heenan and LeCheminant, 1993; Aspler and Chiarenzelli, 1997; Aspler et al., 2002
2111	1		C	Hearne Craton	Griffin mafic event							
2113	4	Submarine	C	Karelia Craton	Tohmajarvi, Kuhitelysvaara	x	x	x	x	x		Vuollo and Huhma, 2005; Hanski and Melezhik, 2011
2113	15		C	Wyoming Craton	Bear Mountain dykes							Ernst and Bleeker, 2010
2115	3		C	North China Craton	Haicheng sill							Wang et al., 2016
2120	10		C	Slave Craton	Indian dike swarm							Buchan et al., 2016
2121	2		C	North Atlantic Craton.	Labrador Coast, Tikkigatsagak dykes							Sahin, 2017, PhD thesis
2121	14		C	Superior Craton	Marathon-normal palaeomagnetic dykes							Buchan et al., 1996; Hamilton et al., 2002; Halls et al., 2008
2126	24	Submarine	O	West African Craton	Bouourum greenstones, Burkina Faso	x	x	x	x	x		Abouchami et al., 1990; Kerr et al., 2000
2128	72	Submarine/ subaerial	O	West African Craton	Mako greenstone, Senegal	x	x	x	x	x		Hirdes and Davis, 2002; Gueye et al., 2007, 2008; Diene et al., 2012
2130	3	Submarine	O	Guiana Shield	Pastora greenstones, Guiana	x	x	x	x	x		Kerr et al., 2000; Hildebrand et al., 2014
2141	2		C	North Atlantic Craton	Avavallik dykes, Labrador							Nilsson et al., 2010; Sahin, 2017, PhD thesis
2147	5		C	North China Craton	Hengling dykes							Peng et al., 2012
2148	11		C	Fennoscandian Shield	Rantaavaara							Hanski et al., 2001
2149	3	Submarine	C	Superior craton	Riviere du Gne							Rohon et al., 1993; Matrice et al., 2009; Ernst and Bleeker, 2010
2155	51		C	Bundelkhand Craton	Bundelkhand dykes event A, N India							Rao et al., 2005
2156.5	38.5	Submarine	O	West African Craton	Nangodi greenstone, W Africa	x	x	x	x	x		Sylvester and Attoh, 1992; de Kock et al., 2012
2167	2		C	Superior Craton	Biscotasing dyke swarm							Ernst and Bleeker, 2010

Table B1.1. Continued.

Age (Ma)	2σ	Eruptive environment	Type	Location	Name	Subaerial Subaqueous						
						1	2	3	4	5	6	Reference
2167.5	17.5	Submarine	O	West African Craton	Birman, Eastern Subprovince of Birman	x	x	x	x			Abouchami et al., 1990;
2170	8		C	Wyoming craton	Wind River							Hirdes et al., 1996
2189	45		C	Sao Francisco Craton	Paroapeba dykes, SE Brazil							Hartl et al., 2003;
2190	10		C	Rae Craton	Tulernau-MacQuoid dykes							Ernst and Bleeker, 2010;
2193	2		C	Slave Craton	Dogrib dyke swarm							de Oliveira Chaves and Neves, 2005
~2200		Submarine	C	Hearne Craton	Happotyik	x	x	x	x			Sandeman et al., 2003
2207.5	1.5		C	Dharwar craton	Mahabubnagar-Dandeli, Bandepalem							French and Heaman, 2010;
2207.5	1.5		C	Dharwar craton	Amantapur-Kunigal dyke swarm							Söderlund et al., 2019
2208	10	Submarine	C	Pilbara	Cheela Springs, Turee Creek, NW Australia	x	x	x	x			Müller et al., 2005;
2209	28	Submarine	O (?) *	Brasília belt	Críxas greenstone belt, Goiás, Brazil	x	x	x	x			Martin and Morris, 2010;
2209	2		C	Superior Craton	Klotz dyke swarm, Quebec							Subba and Teixeira, 1983;
2209.3	2.8		C	Dharwar Craton	Somala dykes							Kuyumjian and Jost, 2006;
2210	3		C	Slave Craton	MacKay event							Jost et al., 2010
2214	10		C	Isukasia terrain	BN-1 dykes, SW Greenland							Buchan et al., 2007
2216.5	4.5		C	Dharwar Craton	Kandlamachigum dykes							Buchan et al., 2010
2217	7		C	Superior Craton	Ungava event							French and Heaman, 2010;
2220	11	Subaerial	C	Fennoscandian Shield	Koli sills, Jämtland	x						Söderlund et al., 2019
2222	13	Predominantly subaerial	C	Kapvapp Craton	Ongeluk-Hekpoort	x	x	x	x			Cornell et al., 1996;
2227	11		C	North Atlantic Craton	Kikkertavik Dike Swarm, Labrador							Obreholzer and Eriksson, 2000
2229	42		O	West African Craton	Tsalabya greenstones, Mauritania							Cadman et al., 1993;
2231	2		C	Slave Craton	Malley dyke swarm							Sahin and Hamilton, 2019
2241	4		C	East Antarctica	Vestfold Hills-2							Abouchami et al., 1990
2254	3		C	Dharwar craton	Ippaguda Dhimbahalli dyke swarm							Buchan et al., 2012
						x	x	x	x			Lauzon et al., 1993;
												Hock and Seitz, 1995
												Söderlund et al., 2019

Table B1.1. Continued.

Age (Ma)	2σ	Eruptive environment	Type	Location	Name	Subaerial Subaqueous						
						1	2	3	4	5	6	Reference
2256	6		C	Singhbhum Craton	Kapitipada dyke swarm, E India							Srivastava et al., 2019
2295	5		C	Kardia Craton	Iisalmi dykes, E Finland							Vuollo and Huhma, 2005
2310	10	Subaerial	C	Kardia Craton	Kuito-Tavakkoski	x						Salmiemi et al., 2013;
2332	Submarine		C	Churchill Province	Pallatin - Nishiku	x						Stepanova et al., 2015
2367	2	Subaerial	C	Dharwar Craton	Bangalore, Karimnagar dyke swarms							Girard, 1999
2370	5	Subaerial	C	North Atlantic Craton	Grædlefjord dykes, SW Greenland	x						Halls et al., 2007;
2380	5		C	Lewisian Gneiss Complex, Scotland	Unipool, Lochan Featne dykes (Scourie late stage)		x					Kumar et al., 2012
2393	3		C	Lewisian Gneiss Complex, Scotland	Scourie main stage			x				Nilsson et al., 2013
2401	2		C	Yigarni	Ezayinia dyke swarm, Western Australia				x			Davies and Heaman, 2014
2403	3		C	West Trossachs Basement Complex	Ringvassoy dyke swarm, N Norway					x		Davies and Heaman, 2014
2408	2		C	Zimbabwe Craton	Sebangau Poort dykes						x	Pisarevsky et al., 2015
2408	3	Subaerial	C	Superior craton	Du Chef							Küllerud et al., 2006
2410	8		C	Aldan Shield	Khodolodikan gneiss, Siberia					x		Lavrak and Mishkin, 2010
2413	5		C	Lewisian Gneiss Complex, Scotland	Cleithead Beag, Beaunoch dykes (oldest Scourie suite)						x	Davies and Heaman, 2014
2415	5		C	Yigarni	Widgienootha dykes, Jimberiana intrusion							Nenchin and Pidgeon, 1998;
2425	3		C	Kardia Craton	Rasinkylä intrusion/dykes, E Karelia							French et al., 2002;
2430	5	Submarine	C	Kardia Craton	Buratovskiy dyke swarm, Russia						x	Smirnov et al., 2013
2436	5		C	Kola-Karelia	Koillismaa layered gneissic complex, Kynsijärvi pluton						x	Mikkola et al., 2010
2437	3	Submarine	C	Baltic shield	Vetreny belt basalts/komataites	x					x	Bailly et al., 2009
2441	4	Submarine	C	Kola-Karelia	Baltic LIP (BLIP)/ Sunman LIP II	x					x	Lauri et al., 2003
2442.8	4.8	Submarine	C	Kola Craton	Imandra-Varzuga layered intrusion/dykes						x	Puchtel et al., 1997
2445	8		C	North China Craton	Miyun dykes, N China craton						x	Ernst and Buchan, 2001;
2449	3	Submarine	C	Yigarni Craton	Weeli Welli, Woongarra	x	x	x	x		x	Kulikov et al., 2010
~2450			C	Bastar Craton	Dantewara dyke swarm						x	Smolkin et al., 1997
2452.5	7.5	Submarine/ subaerial	C	Superior Craton	Matachewan 2nd pulse	x	x	x	x		x	Söderlund et al., 2019
2453	7	Submarine/ subaerial	C	Superior Craton	Thessalon Formation	x	x	x	x		x	Ernst and Bleeker, 2010;
2470	1.2		C	Kalahari Craton	Mitsigwe dyke						x	Ciborowski et al., 2015

Table B1.1. Continued.

Age (Ma)	2σ	Eruptive environment	Type	Location	Name	Subaerial Subaqueous						
						1	2	3	4	5	6	Reference
2480	10		C	Superior Craton	Matachewan 1st pulse							Ernst and Bleeker, 2010;
2480	6		C	Wyoming Craton	Blue draw							Ciborowski et al., 2015
2497.5	7.5	Submarine	C	Kola-Karelia	Baltic LIP (BLIP)/ Surianian LIP I	x						Ciborowski et al., 2013
2498	5	Subaerial	C	Hearne Craton	Kuminak dykes, Spi Group basalts	x	x					Ernst and Buchan, 2001;
2499	2		C	North Atlantic Craton	Kilaarsarfik	x	x					Kulikov et al., 2010
2505	2		C	Superior Craton	Farnigan dykes			x				Sandeman and Ryan, 2008;
2508	6		C	Superior Craton	Irsnaq dykes				x			Sandeman et al., 2013
2509	6		C	Superior craton	Mistassini					x		Nilsson et al., 2010
2512	2		C	Zimbabwe craton	Crystal Springs						x	Buchan et al., 1998
2520	4	Submarine	C	Gawler Craton	Harris greenstone komatiite							Maurice et al., 2009
2575	1		C	Zimbabwe craton	Great Dyke of Zimbabwe						x	Buchan et al., 2007;
2578	18		O	North China Craton	Qingyuan greenstone belt							Suhin and Hamilton, 2019
2606	10	Submarine	C	Limpopo belt	Stockford dyke							Soderlund et al., 2010
2615	6		C	Yilgarn Craton	Yandindilling dyke swarm							Hoatson et al., 2005;
2624	7		C	Sao Francisco Craton	Uiana dyke swarm (younger dykes)						x	Zang, 2007
2660	33	Submarine	C	Zimbabwe Craton	Zederbergs, Belingwe greenstone							Obethir et al., 2002
2683.5	2.5	Submarine	C	Hearne Craton	Hearne Central supracrustal belt (assemblage II)	x	x	x	x			Li and Wei, 2017
2687.5	32.5	Submarine	C	Yilgarn Craton	Eastern Goldfields greenstone belts	x						Xie et al., 2017
2688	3		C	West African Craton	Mousserd-Tichla dyke swarm					x		Stark et al., 2018
2692	9	Submarine	C	Zimbabwe Craton	Reliance, Belingwe greenstone	x	x					Olivera et al., 2013
2701	10	Submarine	C	Hearne Craton	Hearne Central supracrustal belt (assemblage I)	x						Prendergast, 2004;
2706	184	Submarine	C	Dharwar craton	Sultapura greenstone	x	x					Prendergast and Wingate, 2013
~2700		Submarine	O (?) *	Paramirim Craton	Morro de Ferro greenstone belt	x	x	x	x			Sandeman et al., 2004
~2700		Submarine	C	Rae Craton	Prince Albert Group volcanics	x						Manikyamba et al., 2008
											x	Brenner et al. 1990
												Fryer and Jenner, 1978

Table B1.1. Continued.

Name	Comments
Minto-Povungnituk	Geochronology of Minto dykes is affected by crustal contamination, whereas Povungnituk was likely emplaced onto oceanic crust (see Kastek et al., 2018).
Nastapoka Group, Richmond Gulf	Has been linked to subaerial Eskimo basalts (see Legault et al., 1994). Form part of the rift-related Povungnituk Group (Kastek et al., 2018).
Nauracoota Formation, WA	Interpreted as oceanic plateau (see Pirajno and Adamides, 2000; Pirajno et al., 2016).
Otannmäki, Kyrönjärvi-Kuetsjärvi-Uumba	Kuetsjärvi volcanics are coeval with alluvial-fluvial Kertsjärvä Sedimentary Formation (Melezhik and Fallick, 2004).
Karasiök konnäitüü	Konnäitüü are overain and underlain by clastic sediments deposited in fluvial or shallow marine environments. Overlap with Kervitsa-Kuertejärvi-Uumba events. Interpreted as oceanic LIP (see Barnes and Offen, 1990)
Peuramaa greenstone	Interpreted as oceanic LIP (see Hanski et al., 2001)
Jeesioroya greenstone	Interpreted as oceanic LIP (see Hanski et al., 2001)
Dhanjori Formation volcanics	Intracontinental rift setting has been suggested for Dhanjori volcanism with fluvial sedimentation (Mazmunder et al., 2012).
Voronezh	Emplaced in Paleoproterozoic (~2.1 Ga) flyschoid metasediments of the Vorontsovka group, coeval with/immediately succeeding closure of ocean basin and continental collision (see Teiteniev and Santos, 2016)
Fort Frances dyke swarm (Kenora-Kabetogama)	Coeval with rift related Mills Lac volcanic rocks (with pillow basalts and intercalated oceanic sediments; see Sims and Peterman, 1983) and Courtney Lake porphyries (Ansdel, 2005).
Devarabanda dyke swarm	Coeval with alluvial-fluvial sedimentation of ~2.1 Ga Dhonjoni formation (Mazmunder et al., 2012).
Bandanian, Western Subprovince of Birman	Interpreted as oceanic LIP (see Kerr et al., 2000; Lompo, 2009).
Inini greenstone belt, Paranaica series, Guyana	Linked to Marowijne Group (Surinam) and Barana-Mazaruni Supergroup (Guyana). No evidence for continental contamination (Graau et al., 1985).
Tohmajärvi, Kihllysäärä	Magmaism coeval with deposition of "marine Jatuli" (Hanski and Melezhik, 2011). Underlain by thinned continental crust (Huhma et al., 1990; Hanski and Melezhik, 2011).
Bouroum greenstones, Burkina Faso	Interpreted as oceanic LIP (see Kerr et al., 2000; Lompo, 2009).
Mako greenstone, Senegal	Interpreted as oceanic LIP (see Kerr et al., 2000; Lompo, 2009).
Pastora greenstones, Guyana	Interpreted as oceanic LIP (see Kerr et al., 2000).
Rivière du Gué	Cogenetic to 2142 +/- 4 Ma rhyolites and basalts of Mistramisk Formation (Labrador Trough). Mistramisk basalts show pillows and are intercalated marine sediments (Rohon et al. 1993).
Nangodi greenstone, W Africa	Interpreted as oceanic LIP (see Kerr et al., 2000; Lompo, 2009).
Birman, Eastern Subprovince of Birman	Interpreted as oceanic LIP (see Kerr et al., 2000; Lompo, 2009).
Happoijärvi	Happoijärvi Member is undated. Interpreted as continental mafic suite (Sandeman et al. 2013).
Cheda Springs, Turee Creek, NW Australia	Conformably overain by Wooy dolomite (Müller et al. 2005). Geochemistry indicates interaction with continental lithosphere (Martin and Morris 2010).
Crixas greenstone belt, Goiás, Brazil	No geochemical evidence for crustal contamination (see Kuyumjian and Jost, 2006).

Table B1.2. Comments on the LIP events listed in Table B1.1.

Name	Comments
Koli sils, Jatilian	Potentially coeval with subaerial Runkaus volcanics (Perttunen 1985).
Ongeluk-Heekpoort	The Heekpoort sequence is subaerial with no "significant subaqueous eruption" (Oberholzer et al. 2000). The comagmatic Ongeluk lavas are a shallow marine volcanic sequence and indicate subaqueous extrusion in the Griqualand West basin (Cornell and Schütte, 1995).
Tsalabya greenstones, Mauritania	Interpreted as oceanic LIP (see Kerr et al., 2000; Lompo, 2009).
Kuito-Tavakkosi	Kuito dykes are potentially linked to subaerial Runkaus formation basalts (Huuhma et al. 1990)
Pallatin - Nishnuku	Interpreted as underlain by continental crust (see Girard 1999).
Bangalore, Karimnagar dyke swarms	Coeval with predominantly fluvial-lacustrine-glacial sedimentation of the lower Huronian supergroup, Superior (Young, 2013). Magmatic barcode comparison between the Dharwar and Superior craton suggest that the two cratons have been situated adjacent to each other from 2.37 to Ga to 2.17 Ga (Nilsson et al., 2019).
Graedelfjord dykes, SW Greenland	Coeval with predominantly fluvial-lacustrine-glacial sedimentation of the lower Huronian supergroup, Superior (Young, 2013). Magmatic barcode comparison between the North Atlantic craton and Superior craton suggest that the two cratons have been situated adjacent to each other from >2.5 Ga to 2.0 Ga (Nilsson et al., 2010).
Du Chef	Coeval with predominantly fluvial-lacustrine-glacial sedimentation of the lower Huronian supergroup (Young 2013).
Burakovskiy dyke swarm, Russia	Coeval with submarine Vetenry basalts.
Vetenry belt basalts / komatiites	Geochemical evidence for continental contamination (Puchtel et al. 1997).
Baltic LIP (BLIP)/ Sunian LIP II	Geochemical evidence for continental contamination (Kulikov et al. 2010).
Imandra-Vazuga layered intrusion/dykes	Linked to submarine Vetenry basalts. Presumably related to continental rifting without formation of oceanic crust (Smolkin et al. 1997).
Weeli Wollie, Woongarra	Erupted onto continental shelf (Barley et al. 1997)
Dantewara dyke swarm	Assumed to be part of global 2.5-2.4 episode of boninite-norite magmatism. However, the only published age for this dyke swarm is a minimum age of 2118 ± 2 Ma (Srivastava et al 2011).
Baltic LIP (BLIP)/ Sunian LIP I	Geochemical evidence for continental contamination (Kulikov et al. 2010).
Kaminak dykes, Spi Group basalts	Kaminak dykes are genetically linked to subaerial Spi-Group basalts (see Sandeman and Ryan, 2008).
Harris greenstone komatiite	Erupted onto thinned continental crust (Hoarson et al., 2005).
Qingyun greenstone belt	Interpreted as oceanic plateau (Li and Wei, 2017).
Stockford dyke	Emplacement coeval with submarine sedimentation of the Ghap Group, Transvaal Supergroup (Knoll and Beukes, 2009)

Table B1.2. Continued.

B1. References

- Abouchami, W., Boher, M., Michard, A., and Albarede, F., 1990, A Major 2.1 Ga Event of Mafic Magmatism in West Africa: An Early Stage of Crustal Accretion: *Journal of Geophysical Research*, v. 95, p. 17,605-17,629.
- Ans dell, K.M., 2005, Tectonic evolution of the Manitoba-Saskatchewan segment of the Paleoproterozoic Trans-Hudson Orogen, Canada: *Canadian Journal of Earth Sciences*, v. 42, p. 741–759, doi:10.1139/e05-035.
- Aspler, L.B., and Chiarenzelli, J.R., 1997, Initiation of ~2.45-2.1 Ga intracratonic basin sedimentation of the Hurwitz Group, Keewatin Hinterland, Northwest territories, Canada: *Precambrian Research*, v. 81, p. 265–297, doi:10.1016/S0301-9268(96)00038-1.
- Aspler, L.B., Cousins, B.L., and Chiarenzelli, J.R., 2002, Griffin gabbro sills (2.11 Ga), Hurwitz Basin, Nunavut, Canada: Long-distance lateral transport of magmas in western Churchill Province crust: *Precambrian Research*, v. 117, p. 269–294, doi:10.1016/S0301-9268(02)00090-6.
- Bailly, L., Auge, T., Cocherie, A., Trofimov, N.N., Golubev, A.I., Tkachev, A. V., and Cherkasov, S. V, 2009, New Data on the Age of the Burakovskiy Layered Intrusion, Karelia: *Doklady Earth Sciences*, v. 426, p. 534–538, doi:10.1134/S1028334X09040059.
- Barley, M.E., Pickard, A.L., and Sylvester, P.J., 1997, Emplacement of a large igneous province as a possible cause of banded iron formation 2.45 billion years ago: *Nature*, v. 385, p. 55–58, doi:10.1038/385055a0.
- Barnes, S.J., and Often, M., 1990, Ti-rich komatiites from northern Norway: Contributions to Mineralogy and Petrology, v. 105, p. 42–54, doi:10.1007/BF00320965.
- Brady, J.B., Mohlman, H.K., Harris, C., Carmichael, S.K., Jacob, L.J., and Chaparro, W.R., 2004, General geology and geochemistry of metamorphosed Proterozoic mafic dikes and sills, Tobacco Root Mountains, Montana, in Brady, J.B., Burger, H.R., Cheney, J.T., and Harms, T.A. eds., Precambrian geology of the Tobacco Root Mountains, Montana: Boulder, Colorado, Geological Society of America Special Paper 377, Geological Society of America, p. 89–104, doi:10.1130/0-8137-2377-9.89.
- Brenner, T.L., Teixeira, N.A., Oliveira, J.A.L., Franke, N.D., and Thompson, J.F.H., 1990, The O’Toole nickel deposit, Morro do Ferro greenstone belt, Brazil: *Economic Geology*, v. 85, p. 904–920, doi:10.2113/gsecongeo.85.5.904.
- Buchan, K.L., Goutier, J., Hamilton, M.A., Ernst, R.E., and Matthews, W.A., 2007, Paleomagnetism, U-Pb geochronology, and geochemistry of Lac Esprit and other dyke swarms, James Bay area, Quebec, and implications for Paleoproterozoic deformation of the Superior Province: *Canadian Journal of Earth Sciences*, v. 44, p. 643–664, doi:10.1139/e06-131.
- Buchan, K.L., Halls, H.C., and Mortensen, J.K., 1996, Paleomagnetism, U-Pb geochronology, 100

and geochemistry of Marathon dykes, Superior Province, and comparison with the Fort Frances swarm: Canadian Journal of Earth Sciences, v. 33, p. 1583–1595, doi:10.3166/ISI.21.4.67-81.

Buchan, K.L., LeCheminant, A.N., and van Breemen, O., 2012, Malley diabase dykes of the Slave craton, Canadian Shield: U–Pb age, paleomagnetism, and implications for continental reconstructions in the early Paleoproterozoic: Canadian Journal of Earth Sciences, v. 49, p. 435–454, doi:10.1139/e11-061.

Buchan, K.L., LeCheminant, A.N., and van Breemen, O., 2009, Paleomagnetism and U–Pb geochronology of the Lac de Gras diabase dyke swarm, Slave Province, Canada: implications for relative drift of Slave and Superior provinces in the Paleoproterozoic: Canadian Journal of Earth Sciences, v. 46, p. 361–379, doi:10.1139/E09-026.

Buchan, K.L., Mitchell, R.N., Bleeker, W., Hamilton, M.A., and LeCheminant, A.N., 2016, Paleomagnetism of ca. 2.13–2.11 Ga Indin and ca. 1.885 Ga Ghost dyke swarms of the Slave craton: Implications for the Slave craton APW path and relative drift of Slave, Superior and Siberian cratons in the Paleoproterozoic: Precambrian Research, v. 275, p. 151–175, doi:10.1016/j.precamres.2016.01.012.

Buchan, K.L., Mortensen, J.K., Card, K.D., and Percival, J.A., 1998, Paleomagnetism and U–Pb geochronology of diabase dyke swarms of Minto block, Superior Province, Quebec, Canada: Canadian Journal of Earth Sciences, v. 35, p. 1054–1069, doi:10.1139/e98-054.

Buchanan, P.C., Reimold, W.U., Koebert, C., and Kruger, F.J., 2002, Geochemistry of intermediate to siliceous volcanic rocks of the Rooiberg Group, Bushveld Magmatic Province, South Africa: Contributions to Mineralogy and Petrology, v. 144, p. 131–143, doi:10.1007/s00410-002-0386-1.

Cadman, A.C., Heaman, L., Tarney, J., Wardle, R., and Krogh, T.E., 1993, U–Pb geochronology and geochemical variation within two Proterozoic mafic dyke swarms, Labrador: Canadian Journal of Earth Sciences, v. 30, p. 1490–1504.

Cadman, A., Tarney, J., Bridgwater, D., Mengel, F., Whitehouse, M., and Windley, B., 2001, The petrogenesis of the Kangâmiut dyke swarm, W. Greenland: Precambrian Research, v. 105, p. 183–203, doi:10.1016/S0301-9268(00)00111-X.

Ciborowski, T.J.R., Kerr, A.C., Ernst, R.E., McDonald, I., Minifie, M.J., Harlan, S.S., and Millar, I.L., 2015, The early proterozoic Matachewan large Igneous Province: Geochemistry, petrogenesis, and implications for earth evolution: Journal of Petrology, v. 56, p. 1459–1494, doi:10.1093/petrology/egv038.

Ciborowski, T.J.R., Kerr, A.C., McDonald, I., Ernst, R.E., Hughes, H.S.R., and Minifie, M.J., 2014, The geochemistry and petrogenesis of the Paleoproterozoic du Chef dyke swarm, Québec, Canada: Precambrian Research, v. 250, p. 151–166, doi:10.1016/j.precamres.2014.05.008.

- Ciborowski, T.J.R., Kerr, A.C., McDonald, I., Ernst, R.E., and Minifie, M.J., 2013, The geochemistry and petrogenesis of the Blue Draw Metagabbro: *Lithos*, v. 174, p. 271–290, doi:10.1016/j.lithos.2012.06.035.
- Cornell, D.H., Schütte, S.S., and Eglington, B.L., 1996, The Ongeluk basaltic andesite formation in Griqualand West, South Africa: submarine alteration in a 2222 Ma proterozoic sea: *Precambrian Research*, v. 79, p. 101–123, doi:10.1016/0301-9268(95)00090-9.
- Cox, D.M., 2000, 2.01-Ga Kennedy dike swarm, southeastern Wyoming: Record of a rifted margin along the southern Wyoming province: *Rocky Mountain Geology*, v. 35, p. 7–30, doi:10.2113/35.1.7.
- Davies, J.H.F.L., and Heaman, L.M., 2014, New U–Pb baddeleyite and zircon ages for the Scourie dyke swarm: A long-lived large igneous province with implications for the Paleoproterozoic evolution of NW Scotland: *Precambrian Research*, v. 249, p. 180–198, doi:10.1016/j.precamres.2014.05.007.
- Diene, M., Gueye, M., Diallo, D.P., and Dia, A., 2012, Structural Evolution of a Precambrian Segment: Example of the Paleoproterozoic Formations of the Mako Belt (Eastern Senegal, West Africa): *International Journal of Geosciences*, v. 3, p. 153–165, doi:10.4236/ijg.2012.31017.
- Ernst, R., and Bleeker, W., 2010, Large igneous provinces (LIPs), giant dyke swarms, and mantle plumes: significance for breakup events within Canada and adjacent regions from 2.5 Ga to the PresentThis article is one of a selection of papers published in this Special Issue on the the them (R. Clowes, Ed.): *Canadian Journal of Earth Sciences*, v. 47, p. 695–739, doi:10.1139/E10-025.
- Ernst, R.E., and Buchan, K.L., 2001, Large mafic magmatic events through time and links to mantle-plume heads, in *Mantle plumes: their identification through time*, Geological Society of America, doi:10.1130/0-8137-2352-3.483.
- French, J.E., and Heaman, L.M., 2010, Precise U-Pb dating of Paleoproterozoic mafic dyke swarms of the Dharwar craton, India: Implications for the existence of the Neoarchean supercraton Sclavia: *Precambrian Research*, v. 183, p. 416–441, doi:10.1016/j.precamres.2010.05.003.
- French, J.E., Heaman, L.M., and Chacko, T., 2002, Feasibility of chemical U-Th-total Pb baddeleyite dating by electron microprobe: *Chemical Geology*, v. 188, p. 85–104, doi:10.1016/S0009-2541(02)00074-8.
- Fryer, B.J., and Jenner, G.A., 1978, Geochemistry and origin of the Archean Prince Albert Group volcanics, western Melville Peninsula, Northwest Territories, Canada: *Geochimica et Cosmochimica Acta*, v. 42, p. 1645–1654, doi:10.1016/0016-7037(78)90253-3.
- Furnes, H., Dilek, Y., and de Wit, M., 2015, Precambrian greenstone sequences represent different ophiolite types: *Gondwana Research*, v. 27, p. 649–685,

doi:10.1016/j.gr.2013.06.004.

Girard, R., 1999, Evidence d'un magmatisme d'arc protérozoïque inférieur (2.3 Ga) sur le plateau de la rivière George: *Geoscience Canada*, v. 17.

Gruau, C., Martin, H., Leveque, B., Capdevila, R., and Marot, A., 1985, Rb-Sr and Sm-Nd geochronology of lower Proterozoic granite-greenstone terrains in French Guiana, South America: *Precambrian Research*, v. 30, p. 63–80.

Gueye, M., Ngom, P.M., Diène, M., Thiam, Y., Siegesmund, S., Wemmer, K., and Pawlig, S., 2008, Intrusive rocks and tectono-metamorphic evolution of the Mako Paleoproterozoic belt (Eastern Senegal, West Africa): *Journal of African Earth Sciences*, v. 50, p. 88–110, doi:10.1016/j.jafrearsci.2007.09.013.

Gueye, M., Siegesmund, S., Wemmer, K., Pawlig, S., Drobe, M., Nolte, N., and Layer, P., 2007, New evidences for an early Birimian evolution in the West African Craton: An example from the Kédougou-Kénieba inlier, southeast Senegal: *South African Journal of Geology*, v. 110, p. 511–534, doi:10.2113/gssajg.110.4.511.

Halls, H.C., Davis, D.W., Stott, G.M., Ernst, R.E., and Hamilton, M.A., 2008, The Paleoproterozoic Marathon Large Igneous Province: New evidence for a 2.1 Ga long-lived mantle plume event along the southern margin of the North American Superior Province: *Precambrian Research*, v. 162, p. 327–353, doi:10.1080/14616734.2018.1473886.

Halls, H.C., and Heaman, L.M., 2000, The paleomagnetic significance of new U-Pb age data from the Molson dyke swarm, Cauchon Lake area, Manitoba: *Canadian Journal of Earth Sciences*, v. 37, p. 957–966, doi:10.1139/e00-010.

Halls, H.C., Kumar, A., Srinivasan, R., and Hamilton, M.A., 2007, Paleomagnetism and U-Pb geochronology of easterly trending dykes in the Dharwar craton, India: feldspar clouding, radiating dyke swarms and the position of India at 2.37 Ga: *Precambrian Research*, v. 155, p. 47–68, doi:10.1016/j.precamres.2007.01.007.

Hamilton, M.A., Davis, D.W., Buchan, K.L., and Halls, H.C., 2002, Precise U-Pb dating of reversely magnetized Marathon diabase dykes and implications for emplacement of giant dyke swarms along the southern margin of the Superior Province, Ontario: *Geological Survey of Canada*, v. F6.

Hanski, E., Huhma, H., Rastas, P., and Kamenetsky, V.S., 2001, The Palaeoproterozoic Komatiite-Picrite Association of Finnish Lapland: *Journal of Petrology*, v. 42, p. 855–876, doi:10.1093/petrology/42.5.855.

Hanski, E., Huhma, H., and Vuollo, J., 2010, SIMS zircon ages and Nd isotope systematics of the 2.2 Ga mafic intrusions in northern and eastern Finland: *Bulletin of the Geological Society of Finland*, v. 82, p. 31–62, doi:10.17741/bgsf/82.1.002.

- Hanski, E., and Melezhik, V.A., 2011, Litho- and Chronostratigraphy of the Palaeoproterozoic Karelian Formations, in Melezhik, V.A., Prave, A.R., Hanski, E., Fallick, A.E., Lepland, A., Kump, L.R., and Strauss, H. eds., *Reading the Archive of Earth's Oxygenation*, Springer, p. 39–110, doi:DOI 10.1007/978-3-540-88558-0.
- Harlan, S.S., Geisman, J.W., and Premo, W.R., 2003, Paleomagnetism and geochronology of an Early Proterozoic quartz diorite in the southern Wind River Range, Wyoming, USA: *Tectonophysics*, v. 362, p. 105–122, doi:10.1016/S0040-1951(02)00633-9.
- Heaman, L.M., and LeCheminant, A.N., 1993, Paragenesis and U-Pb systematics of baddeleyite (ZrO_2): *Chemical Geology*, v. 110, p. 95–126, doi:10.1016/0009-2541(93)90249-I.
- Hildebrand, R.S., Buchwaldt, R., and Bowring, S.A., 2014, On the allochthonous nature of auriferous greenstones, Guayana shield, Venezuela: *Gondwana Research*, v. 26, p. 1129–1140, doi:10.1016/j.gr.2013.09.011.
- Hirdes, W., and Davis, D., 2002, U–Pb Geochronology of Paleoproterozoic Rocks in the Southern Part of the Kedougou-Kéniéba Inlier, Senegal, West Africa: Evidence for Diachronous Accretionary Development of the Eburnean Province: *Precambrian Research*, v. 118, p. 83–99, doi:10.1016/S0301-9268(02)00080-3.
- Hirdes, W., Davis, D.W., Lüdtke, G., and Konan, G., 1996, Two generations of Birimian (Paleoproterozoic) volcanic belts in northeastern Côte d'Ivoire (West Africa): consequences for the “Birimian controversy”: *Precambrian Research*, v. 80, p. 173–191, doi:10.1016/S0301-9268(96)00011-3.
- Hoatson, D.M., Sun, S.-S., Duggan, M.B., Davies, M.B., Daly, S.J., and Purvis, A.C., 2005, Late Archean Lake Harris Komatiite, Central Gawler Craton, South Australia: Geologic Setting and Geochemistry: *Economic Geology*, v. 100, p. 349–374, doi:10.2113/gsecongeo.100.2.349.
- Hoek, J.D., and Seitz, H.M., 1995, Continental mafic dyke swarms as tectonic indicators: an example from the Vestfold Hills, East Antarctica: *Precambrian Research*, v. 75, p. 121–139, doi:10.1016/0301-9268(95)80002-Y.
- Hofmann, A., and Kusky, T., 2004, The Belingwe Greenstone Belt: Ensilic or Oceanic?, in p. 487–538, doi:10.1016/S0166-2635(04)13015-6.
- Huhma, H., Cliff, R.A., Perttunen, V., and Sakkö, M., 1990, Sm-Nd and Pb isotopic study of mafic rocks associated with early Proterozoic continental rifting: the Per?pohja schist belt in northern Finland: *Contributions to Mineralogy and Petrology*, v. 104, p. 369–379, doi:10.1007/BF00321491.
- Jost, H., Chemale, F., Dussin, I.A., Tassinari, C.C.G., and Martins, R., 2010, A U–Pb zircon Paleoproterozoic age for the metasedimentary host rocks and gold mineralization of the Crixás greenstone belt, Goiás, Central Brazil: *Ore Geology Reviews*, v. 37, p. 127–139, doi:10.1016/j.oregeorev.2010.01.003.

- Kastek, N., Ernst, R.E., Cousins, B.L., Kamo, S.L., Bleeker, W., Söderlund, U., Baragar, W.R.A., and Sylvester, P., 2018, U-Pb Geochronology and Geochemistry of the Povungnituk Group of the Cape Smith Belt: Part of a Craton-Scale Circa 2.0 Ga Minto-Povungnituk Large Igneous Province, Northern Superior Craton: *Lithos*, v. 320–321, p. 315–331, doi:10.1016/j.lithos.2018.09.026.
- Kerr, A.C., White, R. V., and Saunders, A.D., 2000, LIP Reading: Recognizing Oceanic Plateaux in the Geological Record: *Journal of Petrology*, v. 41, p. 1041–1056, doi:10.1093/petrology/41.7.1041.
- Ketchum, K.Y., Heaman, L.M., Bennett, G., and Hughes, D.J., 2013, Age, petrogenesis and tectonic setting of the Thessalon volcanic rocks, Huronian Supergroup, Canada: *Precambrian Research*, v. 233, p. 144–172, doi:10.1016/j.precamres.2013.04.009.
- Knoll, A.H., and Beukes, N.J., 2009, Introduction: Initial investigations of a Neoarchean shelf margin-basin transition (Transvaal Supergroup, South Africa): *Precambrian Research*, v. 169, p. 1–14, doi:10.1016/j.precamres.2008.10.009.
- de Kock, G.S., Théveniaut, H., Botha, P.M.W., and Gyapong, W., 2012, Timing the structural events in the Palaeoproterozoic Bolé–Nangodi belt terrane and adjacent Maluwe basin, West African craton, in central-west Ghana: *Journal of African Earth Sciences*, v. 65, p. 1–24, doi:10.1016/j.jafrearsci.2011.11.007.
- Kouyaté, D., Söderlund, U., Youbi, N., Ernst, R., Hafid, A., Ikenne, M., Soulaimani, A., Bertrand, H., El Janati, M., and R'kha Chaham, K., 2013, U-Pb baddeleyite and zircon ages of 2040Ma, 1650Ma and 885Ma on dolerites in the West African Craton (Anti-Atlas inliers): Possible links to break-up of Precambrian supercontinents: *Lithos*, v. 174, p. 71–84, doi:10.1016/j.lithos.2012.04.028.
- Krogh, T.E., 1994, PreciseU-Pb ages for Grenvilan and pre-Grenan thrusting of Proterozoic and Archean metamorphic assemblages in the Grenville Front tectonic zone, Canada: *Tectonics*, v. 13, p. 963–982.
- Kulikov, V.S., Bychkova, Y. V., Kulikova, V., and Ernst, R., 2010, The Vetreny Poyas (Windy Belt) subprovince of southeastern Fennoscandia: An essential component of the ca. 2.5–2.4Ga Sumian large igneous provinces: *Precambrian Research*, v. 183, p. 589–601, doi:10.1016/j.precamres.2010.07.011.
- Kullerud, K., Skjerlie, K.P., Corfu, F., and de la Rosa, J.D., 2006, The 2.40 Ga Ringvassøy mafic dykes, West Troms Basement Complex, Norway: The concluding act of early Palaeoproterozoic continental breakup: *Precambrian Research*, v. 150, p. 183–200, doi:10.1016/j.precamres.2006.08.003.
- Kumar, A., Hamilton, M.A., and Halls, H.C., 2012, A Paleoproterozoic giant radiating dyke swarm in the Dharwar Craton, southern India: *Geochemistry, Geophysics, Geosystems*, v. 13, doi:10.1029/2011GC003926.

- Kuyumjian, R.M., and Jost, H., 2006, Low- and high-alumina komatiites of Goiás, Central Brazil: *Journal of South American Earth Sciences*, v. 20, p. 315–326, doi:10.1016/j.jsames.2005.11.003.
- Lahtinen, R., Garde, A.A., and Melezhik, V.A., 2008, Paleoproterozoic evolution of Fennoscandia and Greenland: *Episodes*, v. 31, p. 20–28, doi:10.18814/epiugs/2008/v31i1/004.
- Lanyon, R., Black, L.P., and Seitz, H.M., 1993, U-Pb zircon dating of mafic dykes and its application to the Proterozoic geological history of the Vestfold Hills, East Antarctica: *Contributions to Mineralogy and Petrology*, v. 115, p. 184–203, doi:10.1007/BF00321219.
- Lauri, L.S., Karinen, T., and Räsänen, J., 2003, The earliest Paleoproterozoic supracrustal rocks in Koillismaa, northern Finland - Their petrographic and geochemical characteristics and lithostratigraphy: *Bulletin of the Geological Society of Finland*, v. 75, p. 29–50, doi:10.17741/bgsf/75.1-2.003.
- Lavrik, S.N., and Mishkin, M.A., 2010, Geochemistry and genesis of metamorphosed volcanic rocks in the Kholodnikan greenstone belt, southern Aldan Shield: *Geochemistry International*, v. 48, p. 593–605, doi:10.1134/S0016702910060066.
- Legault, F., Francis, D., Hynes, A., and Budkewitsch, P., 1994, The petrogenesis of proterozoic continental volcanism in the Belcher Islands with implications for the evolution of the circum Ungava fold belt: *Canadian Journal of Earth Sciences*, v. 31.
- Lenhardt, N., and Eriksson, P.G., 2012, Volcanism of the Palaeoproterozoic Bushveld Large Igneous Province: The Rooiberg Group, Kaapvaal Craton, South Africa: *Precambrian Research*, v. 214–215, p. 82–94, doi:10.1016/j.precamres.2011.12.003.
- Li, Z., and Wei, C., 2017, Two types of Neoarchean basalts from Qingyuan greenstone belt, North China Craton: Petrogenesis and tectonic implications: *Precambrian Research*, v. 292, p. 175–193, doi:10.1016/j.precamres.2017.01.014.
- Lompo, M., 2009, Geodynamic evolution of the 2.25–2.0 Ga Palaeoproterozoic magmatic rocks in the Man-Leo Shield of the West African Craton. A model of subsidence of an oceanic plateau: *Geological Society, London, Special Publications*, v. 323, p. 231–254, doi:10.1144/SP323.11.
- Manikyamba, C., Kerrich, R., Khanna, T.C., Keshav Krishna, A., and Satyanarayanan, M., 2008, Geochemical systematics of komatiite–tholeiite and adakitic-arc basalt associations: The role of a mantle plume and convergent margin in formation of the Sandur Superterrane, Dharwar craton, India: *Lithos*, v. 106, p. 155–172, doi:10.1016/j.lithos.2008.07.003.
- Martin, A.P., Condon, D.J., Prave, A.R., Melezhik, V.A., Lepland, A., and Fallick, A.E., 2013, Dating the termination of the Palaeoproterozoic Lomagundi-Jatuli carbon isotopic event in the North Transfennoscandian Greenstone Belt: *Precambrian Research*, v. 224, p. 160–168, doi:10.1016/j.precamres.2012.09.010.

- Martin, D.M.B., and Morris, P.A., 2010, Tectonic setting and regional implications of ca 2.2 Ga mafic magmatism in the southern Hamersley Province, Western Australia: Australian Journal of Earth Sciences, v. 57, p. 911–931, doi:10.1080/08120099.2010.510172.
- Maurice, C., David, J., O’Neil, J., and Francis, D., 2009, Age and tectonic implications of Paleoproterozoic mafic dyke swarms for the origin of 2.2 Ga enriched lithosphere beneath the Ungava Peninsula, Canada: Precambrian Research, v. 174, p. 163–180, doi:10.1016/j.precamres.2009.07.007.
- Mazumder, R., Eriksson, P.G., De, S., Bumby, A.J., and Lenhardt, N., 2012, Palaeoproterozoic sedimentation on the Singhbhum Craton: global context and comparison with Kaapvaal: Geological Society, London, Special Publications, v. 365, p. 51–76, doi:10.1144/SP365.4.
- Melezhik, V.A., and Fallick, A.E., 2004, Palaeoproterozoic, rift-related, 13 C-rich, lacustrine carbonates, NW Russia. Part I: Sedimentology and major element geochemistry: Earth and Environmental Science Transactions of the Royal Society of Edinburgh, v. 95, p. 393–421, doi:10.1017/S0263593300001140.
- Mikkola, P., Kontinen, A., Huhma, H., and Lahaye, Y., 2010, Three Paleoproterozoic A-type granite intrusions and associated dykes from Kainuu, East Finland: Bulletin of the Geological Society of Finland, v. 82, p. 81–100, doi:10.17741/bgsf/82.2.002.
- Mitchell, R.N., Bleeker, W., van Breemen, O., Lecheminant, T.N., Peng, P., Nilsson, M.K.M., and Evans, D.A.D., 2014, Plate tectonics before 2.0 Ga: Evidence from paleomagnetism of cratons within supercontinent Nuna: American Journal of Science, v. 314, p. 878–894, doi:10.2475/04.2014.03.
- Müller, S.G., Krapež, B., Barley, M.E., and Fletcher, I.R., 2005, Giant iron-ore deposits of the Hamersley province related to the breakup of Paleoproterozoic Australia: New insights from in situ SHRIMP dating of baddeleyite from mafic intrusions: Geology, v. 33, p. 577–580, doi:10.1130/G21482.1.
- Nemchin, A.A., and Pidgeon, R.T., 1998, Precise conventional and SHRIMP baddeleyite U-Pb age for the Binneringie Dyke, near Narrogin, Western Australia: Australian Journal of Earth Sciences, v. 45, p. 673–675, doi:10.1080/0812009808728424.
- Nilsson, M.K.M., Klausen, M.B., and Petersson, A., 2019, Break-up related 2170–2120 Ma mafic dykes across the North Atlantic craton: Final dismembering of a North Atlantic-Dharwar craton connection? Precambrian Research, v. 329, p. 70–87, doi:10.1016/j.precamres.2018.12.028.
- Nilsson, M.K.M., Klausen, M.B., Söderlund, U., and Ernst, R.E., 2013, Precise U-Pb ages and geochemistry of Palaeoproterozoic mafic dykes from southern West Greenland: Linking the North Atlantic and the Dharwar cratons: Lithos, v. 174, p. 255–270, doi:10.1016/j.lithos.2012.07.021.
- Nilsson, M.K.M., Söderlund, U., Ernst, R.E., Hamilton, M.A., Scherstén, A., and Armitage,

- P.E.B., 2010, Precise U–Pb baddeleyite ages of mafic dykes and intrusions in southern West Greenland and implications for a possible reconstruction with the Superior craton: *Precambrian Research*, v. 183, p. 399–415, doi:10.1016/j.precamres.2010.07.010.
- Oberholzer, J.D., and Eriksson, P.G., 2000, Subaerial volcanism in the Palaeoproterozoic Hekpoort Formation (Transvaal Supergroup), Kaapvaal craton: *Precambrian Research*, v. 101, p. 193–210, doi:10.1016/S0301-9268(99)00088-1.
- Oberthür, T., Davis, D.W., Blenkinsop, T.G., and Höhndorf, A., 2002, Precise U–Pb mineral ages, Rb–Sr and Sm–Nd systematics for the Great Dyke, Zimbabwe—constraints on late Archean events in the Zimbabwe craton and Limpopo belt: *Precambrian Research*, v. 113, p. 293–305, doi:10.1016/S0301-9268(01)00215-7.
- de Oliveira Chaves, A., and Neves, J.M.C., 2005, Radiometric ages, aeromagnetic expression, and general geology of mafic dykes from southeastern Brazil and implications for African–South American correlations: *Journal of South American Earth Sciences*, v. 19, p. 387–397, doi:10.1016/j.jsames.2005.04.005.
- Oliveira, E.P., Silveira, E.M., Söderlund, U., and Ernst, R.E., 2013, U–Pb ages and geochemistry of mafic dyke swarms from the Uauá Block, São Francisco Craton, Brazil: LIPs remnants relevant for Late Archaean break-up of a supercraton: *Lithos*, v. 174, p. 308–322, doi:10.1016/j.lithos.2012.05.025.
- Oliveira, E.P., Windley, B.F., McNaughton, N.J., Pimentel, M., and Fletcher, I.R., 2004, Contrasting copper and chromium metallogenetic evolution of terranes in the Palaeoproterozoic Itabuna-Salvador-Curaçá orogen, São Francisco craton, Brazil: New zircon (SHRIMP) and Sm-Nd (model) ages and their significance for orogen-parallel escape tectonic: *Precambrian Research*, v. 128, p. 143–165, doi:10.1016/j.precamres.2003.09.018.
- Peng, P., 2015, Precambrian mafic dyke swarms in the North China Craton and their geological implications: *Science China Earth Sciences*, v. 58, p. 649–675, doi:10.1007/s11430-014-5026-x.
- Peng, P., Guo, J., Zhai, M., Windley, B.F., Li, T., and Liu, F., 2012, Genesis of the Hengling magmatic belt in the North China Craton: Implications for Paleoproterozoic tectonics: *Lithos*, v. 148, p. 27–44, doi:10.1016/j.lithos.2012.05.021.
- Pharaoh, T.C., Warren, A., and Walsh, N.J., 1987, Early Proterozoic metavolcanic suites of the northernmost part of the Baltic Shield, in Pharaoh, T.C., Beckinsale, R.D., and Rickard, D. eds., *Geochemistry and Mineralization of Proterozoic Volcanic Suites*, Geological Society Special Publication, p. 41–58.
- Prajno, F., and Adamides, N.G., 2000, Geology and mineralization of the Palaeoproterozoic Yerrida Basin, Western Australia: doi:10.13140/2.1.3850.2720.
- Prajno, F., Chen, Y., Li, N., Li, C., and Zhou, L., 2016, Besshi-type mineral systems in the

- Palaeoproterozoic Bryah Rift-Basin, Capricorn Orogen, Western Australia: Implications for tectonic setting and geodynamic evolution: *Geoscience Frontiers*, v. 7, p. 345–357, doi:10.1016/j.gsf.2015.09.003.
- Pisarevsky, S.A., De Waele, B., Jones, S., Söderlund, U., and Ernst, R.E., 2015, Paleomagnetism and U-Pb age of the 2.4Ga Erayinia mafic dykes in the south-western Yilgarn, Western Australia: Paleogeographic and geodynamic implications: *Precambrian Research*, v. 259, p. 222–231, doi:10.1016/j.precamres.2014.05.023.
- Premo, W.R., and Van Schmus, W.R., 1989, Zircon geochronology of Precambrian rocks in southeastern Wyoming and northern Colorado: *Geological Society of America Special Paper* 235, p. 13–48, doi:10.1130/SPE235-p13.
- Prendergast, M.D., 2004, The Bulawayan Supergroup: a late Archaean passive margin-related large igneous province in the Zimbabwe craton: *Journal of the Geological Society*, v. 161, p. 431–445, doi:10.1144/0016-764902-092.
- Prendergast, M.D., and Wingate, M.T.D., 2013, Zircon geochronology of late Archean komatiitic sills and their felsic country rocks, south-central Zimbabwe: A revised age for the Reliance komatiitic event and its implications: *Precambrian Research*, v. 229, p. 105–124, doi:10.1016/j.precamres.2012.02.004.
- Puchtel, I.S., Haase, K.M., Hofmann, A.W., Chauvel, C., Kulikov, V.S., Garbe-Schönberg, C.-D., and Nemchin, A.A., 1997, Petrology and geochemistry of crustally contaminated komatiitic basalts from the Vetreny Belt, southeastern Baltic Shield: Evidence for an early Proterozoic mantle plume beneath rifted Archean continental lithosphere: *Geochimica et Cosmochimica Acta*, v. 61, p. 1205–1222, doi:10.1016/S0016-7037(96)00410-3.
- Rao, J.M., Rao, G.V.S.P., Widdowson, M., and Kelley, S.P., 2005, Evolution of Proterozoic mafic dyke swarms of the Bundelkhand Granite Massif, central India: *Current Science*, p. 502–506, doi:<https://www.jstor.org/stable/24110222>.
- Rohon, M.-L., Vialette, Y., Clark, T., Roger, G., Ohnenstetter, D., and Vidal, P., 1993, Aphebian mafic–ultramafic magmatism in the Labrador Trough (New Quebec): its age and the nature of its mantle source: *Canadian Journal of Earth Sciences*, v. 30, p. 1582–1593, doi:10.1139/e93-136.
- Roscoe, S.M., and Card, K.D., 1993, The reappearance of the Huronian in Wyoming rifting and drifting of ancient continents: *Canadian Journal of Earth Sciences*, v. 30, p. 2475–2480, doi:10.1080/09613219308727250.
- Roy, A., Sarkar, A., Jeyakumar, S., Aggrawal, S.K., and Ebihara, M., 2002, Sm-Nd age and mantle source characteristics of the Dhanjori volcanic rocks, Eastern India.: *GEOCHEMICAL JOURNAL*, v. 36, p. 503–518, doi:10.2343/geochemj.36.503.
- Saboya, L.A., and Teixeira, N.A., 1983, Ultramafic flows of the Crixas greenstone belt, Goias - Brazil: *Precambrian Research*, v. 22, p. 23–40.

- Sahin, T., 2017, An integrated geochronological, petrological, geochemical and paleomagnetic study of Paleoproterozoic and Mesoproterozoic mafic dyke swarms in the Nain Craton, Labrador: PhD thesis, v. Department.
- Sahin, T., and Hamilton, M.A., 2019, New U-Pb baddeleyite ages for Neoarchean and Paleoproterozoic mafic dyke swarms of the southern Nain Province, Labrador: implications for possible plate reconstructions involving the North Atlantic craton: Precambrian Research, doi:10.1016/j.precamres.2019.02.001.
- Said, N., Kerrich, R., Cassidy, K., and Champion, D.C., 2012, Characteristics and geodynamic setting of the 2.7 Ga Yilgarn heterogeneous plume and its interaction with continental lithosphere: evidence from komatiitic basalt and basalt geochemistry of the Eastern Goldfields Superterrane: Australian Journal of Earth Sciences, v. 59, p. 737–763, doi:10.1080/08120099.2012.695294.
- Salminen, P., Melezhik, V.A., Hanski, V.A., Lepland, A., Romashkin, A.E., and Rychanchik, D. V, 2013, 6.2. 2 Kuetsjärvi Sedimentary Formation: FAR-DEEP Hole 5A, neighbouring quarry and related outcrops.In: Reading the Archive of Earth's Oxygenation (2). Publisher: Springer-Verlag
- Sandeman, H.A., Cousens, B.L., and Hemmingway, C.J., 2003, Continental tholeiitic mafic rocks of the Paleoproterozoic Hurwitz Group, Central Hearne sub-domain, Nunavut: insight into the evolution of the Hearne sub-continental lithosphere: Canadian Journal of Earth Sciences, v. 40, p. 1219–1237, doi:10.1139/e03-035.
- Sandeman, H., Hanmer, S., Davis, W., Ryan, J., and Peterson, T., 2004, Neoarchaean volcanic rocks, Central Hearne supracrustal belt, Western Churchill Province, Canada: geochemical and isotopic evidence supporting intra-oceanic, supra-subduction zone extension: Precambrian Research, v. 134, p. 113–141, doi:10.1016/j.precamres.2004.03.014.
- Sandeman, H.A., Heaman, L.M., and LeCheminant, A.N., 2013, The Paleoproterozoic Kaminak dykes, Hearne craton, western Churchill Province, Nunavut, Canada: Preliminary constraints on their age and petrogenesis: Precambrian Research, v. 232, p. 119–139, doi:10.1016/j.precamres.2012.06.002.
- Sandeman, H.A., and Ryan, J.J., 2008, The Spi Lake Formation of the central Hearne domain, western Churchill Province, Canada: an axial intracratonic continental tholeiite trough above the cogenetic Kaminak dyke swarmGeological Survey of Canada Contribution 20070462. (L. Corriveau, Ed.): Canadian Journal of Earth Sciences, v. 45, p. 745–767, doi:10.1139/E08-015.
- Sheen, A.I., Heaman, L.M., Kjarsgaard, B., Ootes, L., Pearson, D.G., and Creaser, R.A., 2019, Athapuscow aulacogen revisited: Geochronology and geochemistry of the 2046 Ma Union Island Group mafic magmatism, East Arm of Great Slave Lake, Northwest Territories, Canada: Precambrian Research, v. 321, p. 85–102, doi:10.1016/j.precamres.2018.11.012.
- Shi, Y., Wilde, S.A., Zhao, X., Ma, Y., Du, L., and Liu, D., 2012, Late Neoarchean magmatic

- and subsequent metamorphic events in the northern North China Craton: SHRIMP zircon dating and Hf isotopes of Archean rocks from Yunmengshan Geopark, Miyun, Beijing; *Gondwana Research*, v. 21, p. 785–800, doi:10.1016/j.gr.2011.07.009.
- Sims, P.K., and Peterman, Z.E., 1983, Evolution of Penokean foldbelt, Lake Superior region, and its tectonic environment: Early Proterozoic Geology of the Great Lakes Region, v. 160, p. 3–14.
- Smirnov, A. V., Evans, D.A.D., Ernst, R.E., Söderlund, U., and Li, Z.X., 2013, Trading partners: Tectonic ancestry of southern Africa and western Australia, in Archean supercratons Vaalbara and Zimgarn: *Precambrian Research*, v. 224, p. 11–22, doi:10.1016/j.precamres.2012.09.020.
- Smithies, R.H., Ivanic, T.J., Lowrey, J.R., Morris, P.A., Barnes, S.J., Wyche, S., and Lu, Y.-J., 2018, Two distinct origins for Archean greenstone belts: *Earth and Planetary Science Letters*, v. 487, p. 106–116, doi:10.1016/j.epsl.2018.01.034.
- Smolkin, V.F., 1997, The Paleoproterozoic (2.5–1.7 Ga) Midcontinent Rift System of the northeastern Fennoscandian Shield: *Canadian Journal of Earth Sciences = Journal Canadien des Sciences de la Terre*, v. 34, p. 426–443, doi:10.1139/e17-036.
- Söderlund, U. et al., 2019, Emplacement ages of Paleoproterozoic mafic dyke swarms in eastern Dharwar craton, India: Implications for paleoreconstructions and support for a ~30° change in dyke trends from south to north: *Precambrian Research*, v. 329, p. 26–43, doi:10.1016/j.precamres.2018.12.017.
- Söderlund, U., Hofmann, A., Klausen, M.B., Olsson, J.R., Ernst, R.E., and Persson, P.-O., 2010, Towards a complete magmatic barcode for the Zimbabwe craton: Baddeleyite U–Pb dating of regional dolerite dyke swarms and sill complexes: *Precambrian Research*, v. 183, p. 388–398, doi:10.1016/j.precamres.2009.11.001.
- Srivastava, R.K., Heaman, L.M., French, J.E., and Filho, C.F.F., 2011, Evidence for a Paleoproterozoic event of metamorphism in the Bastar craton, Central India: P-T-t constraints from mineral chemistry and U-Pb geochronology of mafic dykes: *Episodes*, v. 34, p. 13–24, doi:10.18814/epiugs/2011/v34i1/003.
- Srivastava, R.K., Söderlund, U., Ernst, R.E., Mondal, S.K., and Samal, A.K., 2019, Precambrian mafic dyke swarms in the Singhbhum craton (eastern India) and their links with dyke swarms of the eastern Dharwar craton (southern India): *Precambrian Research*, v. 329, p. 5–17, doi:10.1016/j.precamres.2018.08.001.
- St-Onge, M.R., Scott, D.J., and Lucas, S.B., 2000, Early partitioning of Quebec: Microcontinent formation in the Paleoproterozoic: *Geology*, v. 28, p. 323–326, doi:10.1130/0091-7613(2000)028<0323:EPOQMF>2.3.CO;2.
- Stark, J.C., Wilde, S.A., Söderlund, U., Li, Z.-X., Rasmussen, B., and Zi, J.-W., 2018, First evidence of Archean mafic dykes at 2.62 Ga in the Yilgarn Craton, Western Australia:

Links to cratonisation and the Zimbabwe Craton: Precambrian Research, v. 317, p. 1–13, doi:10.1016/j.precamres.2018.08.004.

Stepanova, A. V., Salnikova, E.B., Samsonov, A. V., Egorova, S. V., Larionova, Y.O., and Stepanov, V.S., 2015, The 2.31Ga mafic dykes in the karelian craton, eastern fennoscandian shield: U-Pb age, source characteristics and implications for continental break-up processes: Precambrian Research, v. 259, p. 43–57, doi:10.1016/j.precamres.2014.10.002.

Sylvester, P.J., and Attoh, K., 1992, Lithostratigraphy and Composition of 2.1 Ga Greenstone Belts of the West African Craton and Their Bearing on Crustal Evolution and the Archean-Proterozoic Boundary: The Journal of Geology, v. 100, p. 377–393, doi:10.1086/629593.

Terentiev, R.A., 2019, Petrogenesis of Synplutonic High-Mg Porphyritic Dikes from Mafic-Granitoid Plutons of the Voronezh Crystalline Massif, East European Platform: Geochemistry International, v. 57, p. 384–399, doi:10.1134/S0016702919040128.

Terentiev, R.A., and Santosh, M., 2016, Detrital zircon geochronology and geochemistry of metasediments from the Vorontsovka terrane: implications for microcontinent tectonics: International Geology Review, v. 58, p. 1108–1126, doi:10.1080/00206814.2016.1147386.

Vuollo, J., and Huhma, H., 2005, Paleoproterozoic dykes in NE Finland, in Lehtinen, M., Nurmi, P.A., and Rämö, O.T. eds., Precambrian Geology of Finland- Key to the Evolution of the Fennoscandian Shield., Elsevier B.V., p. 195–236.

Vuollo, J., and Piirainen, T., 1992, The 2.2 ga old koli layered sill: The low-al tholeiitic (karjalitic) magma type and its differentiation in Northern Karelia, Eastern Finland: Gff, v. 114, p. 132–142, doi:10.1080/11035899209453466.

Wang, X., Peng, P., Wang, C., and Yang, S., 2016, Petrogenesis of the 2115 Ma Haicheng mafic sills from the Eastern North China Craton: Implications for an intra-continental rifting: Gondwana Research, v. 39, p. 347–364, doi:10.1016/j.gr.2016.01.009.

Wang, Z., Wilde, S.A., and Wan, J., 2010, Tectonic setting and significance of 2.3–2.1Ga magmatic events in the Trans-North China Orogen: New constraints from the Yanmenguan mafic-ultramafic intrusion in the Hengshan–Wutai–Fuping area: Precambrian Research, v. 178, p. 27–42, doi:10.1016/j.precamres.2010.01.005.

Xie, H., Kröner, A., Brandl, G., and Wan, Y., 2017, Two orogenic events separated by 2.6Ga mafic dykes in the Central Zone, Limpopo Belt, southern Africa: Precambrian Research, v. 289, p. 129–141, doi:10.1016/j.precamres.2016.11.009.

Yang, L., Hou, G., Liu, S., Tian, W., and Gao, L., 2019, 2.09 Ga mafic dykes from Western Shandong, Eastern block of North China Craton, and their tectonic implications: Precambrian Research, v. 325, p. 39–54, doi:10.1016/j.precamres.2019.02.007.

Youbi, N., Ernst, R.E., Söderlund, U., Boumehdi, M.A., Bensalah, M.K., and Aarab, E.M., 2016, Morocco, North Africa: a Dyke Swarm Bonanza: *Acta Geologica Sinica - English Edition*, v. 90, p. 15–15, doi:10.1111/1755-6724.12855.

Young, G.M., 2013, Climatic catastrophes in Earth history: two great Proterozoic glacial episodes: *Geological Journal*, v. 48, p. 1–21, doi:10.1002/gj.2467.

Zang, W.-L., 2007, Deposition and deformation of late Archaean sediments and preservation of microfossils in the Harris Greenstone Domain, Gawler Craton, South Australia: *Precambrian Research*, v. 156, p. 107–124, doi:10.1016/j.precamres.2007.03.002.

COUPLING OF THE ATMOSPHERE AND SEDIMENT MELTS ACROSS THE ARCHEAN PROTEROZOIC TRANSITION

This chapter is submitted for publication as:

Liebmann, J., Spencer, C.J., Kirkland, C.K., Bucholz, C.E., Xia, X.P., Martin, L., Kitchen, N. and Shumlyanskyy, L. Coupling of the atmosphere and sediment melts across the Archean-Proterozoic transition. *Submitted to Geochimica et Cosmochimica Acta.*

Abstract

The Archean-Proterozoic transition marks a time of fundamental geologic, biologic, and atmospheric changes to the Earth system, including oxygenation of the atmosphere (termed the Great Oxygenation Event; GOE), and the emergence of continents above sea-level. The impacts of the GOE on Earth's surface environment are imprinted on the geologic record, including the attenuation of mass-independent fractionation of sulfur isotopes (S-MIF). Temporally overlapping geologic and geochemical observations (e.g. a change in oxygen isotope ratio of sediments) imply the widespread subaerial emergence of continents was coeval with atmospheric oxygenation. Here we present triple sulfur isotope ratios in pyrite and oxygen isotope ratios in garnet and zircon in a global suite of Archean and Proterozoic sediment-derived granitoids. These crustal melts record an increase in average $^{18}\text{O}/^{16}\text{O}$ isotope ratio and a disappearance of S-MIF in the Paleoproterozoic. The coupled behaviour of sulfur and oxygen isotope signatures imply a potential causal link between the emergence of continents and Paleoproterozoic atmospheric oxygenation.

4.1 Introduction

The oxygenation of the Earth's atmosphere and oceans irreversibly changed many major biogeochemical cycles (e.g. Fe, S, Mn) (Pufahl and Hiatt, 2012) and provided the base for a highly efficient aerobic metabolism that allowed the development of complex life (Catling et al., 2005). During the Great Oxygenation Event (GOE) (~2.3 Ga; Luo et al., 2016, c.f. Gumsley et al., 2017) atmospheric oxygen increased from <0.001% of the present atmospheric level (PAL) (Pavlov and Kasting, 2002) to 10-40% PAL (Kump, 2008), or perhaps much higher approaching 100% PAL (Harada et al., 2015, and references therein). The mechanism that led to atmospheric oxygenation remains controversial. Proposed scenarios for oxygenation include 1) an increase in O₂ production (i.e. through the emergence of oxygenic photosynthesis) (Ward et al., 2016), 2) a decrease in O₂ consumption (e.g. through changing redox state of volcanic gases, increased burial of organic carbon, or decreased pyrite weathering) (Holland, 2002; Bekker and Holland, 2012), and 3) a combination of both processes (through enhanced oxygenic photosynthesis combined with increased carbon burial) (Campbell and Allen, 2008). One source of dispute is the timing of the invention of oxygenic photosynthesis; suggestions range from >3.7 Ga (Rosing and Frei, 2004) to immediately preceding atmospheric oxygenation (Ward et al., 2016). Previous studies imply that the widespread emergence of continents above sea-level is temporally correlated with atmospheric oxygenation (Kump and Barley, 2007). Furthermore, it has been proposed that the subaerial emergence of continents may have led to a flux of life-essential nutrients into the ocean supporting a boost in photosynthetic activity (Campbell and Allen, 2008; Hao et al., 2020).

Multiple sulfur isotopic signatures are a sensitive tracer for atmospheric oxygen levels (Farquhar et al., 2000). Some sulfides and sulfates in metasedimentary rocks deposited prior to the GOE display mass-independent fractionation of sulfur (S-MIF), whereas those deposited after the GOE display almost wholly mass-dependent fractionation (S-MDF) (Farquhar et al., 2000; Johnston, 2011). It has been postulated that S-MIF was generated in the atmosphere through ultraviolet photolysis of gas molecules (Lyons, 2007). The establishment of an ozone shield as a consequence of atmospheric oxygenation led to blocking of UV radiation and attenuation of the photolysis of volcanic sulfur species (Farquhar et al., 2000). In addition, enhanced oxidative

weathering of sulfides and the formation of oceanic sulfates stimulated the activity of sulfur-metabolizing bacteria supporting the generation of S-MDF signatures (Guo et al., 2009). Recent studies show that fluctuations in atmospheric oxygen level are also captured in the igneous rock record; namely, through recycling of S-MIF in the crust (Bekker et al., 2009; Bucholz et al., 2020), and a change in oxygen fugacity of strongly peraluminous granites (Bucholz et al., 2018).

Broadly coeval with atmospheric oxygenation, the average oxygen isotope ratio of global felsic magmas (recorded by zircon $\delta^{18}\text{O}$) increases (Valley et al., 2005). The oxygen isotopic composition of a magma is sensitive to the recycling of supracrustal material (Taylor, 1980). Igneous zircon in high-temperature equilibrium with the mantle has remarkably homogenous $\delta^{18}\text{O}$ values which average $5.3 \pm 0.6\text{\textperthousand}$ (Page et al., 2007) relative to standard mean ocean water (VSMOW). Supracrustal material (e.g. sedimentary and volcanic rocks), in contrast, has a wide range of $\delta^{18}\text{O}$ values (~ 0 – $40\text{\textperthousand}$) with most reservoirs being elevated in $\delta^{18}\text{O}$ relative to the mantle (Savin and Epstein, 1970). Hence, assimilation of supracrustal material commonly results in magmas with elevated $\delta^{18}\text{O}$ compared to primitive mantle-derived magmas. An increase in average $\delta^{18}\text{O}$ of zircon in the Paleoproterozoic has been recognized for over a decade (Valley et al., 2005). Contrasting models have been suggested to account for this increase in $\delta^{18}\text{O}$; 1) the formation of high $\delta^{18}\text{O}$ sediments (and sediment-derived melts) potentially linked to enhanced subaerial weathering and erosion related to the widespread emergence of continents above sea-level (1; Spencer et al., 2019), and 2) enhanced crustal recycling associated with the onset of collisional tectonics (Spencer et al., 2014). However, high- $\delta^{18}\text{O}$ sediment melts do not show a concomitant depletion in radiogenic ^{176}Hf , as would be expected if the increase in $\delta^{18}\text{O}$ was related to enhanced supracrustal recycling (1). Therefore, a change in sediment oxygen isotope composition potentially associated with the subaerial emergence of continents (Bindeman et al., 2018) seems to be the likely driver for the Paleoproterozoic increase in average zircon $\delta^{18}\text{O}$ (Spencer et al., 2019; Liebmann et al., submitted to *Terra Nova*).

We explore a potential link between the emergence of continents above sea-level and atmospheric oxygenation through a coupled analysis of proxies for atmospheric oxygen level and sedimentary recycling in Archean to Mesoproterozoic sediment-derived granitoids (i.e.

granitoids that partially or wholly derive from the partial melting of metasediments). Here we present pyrite multiple sulfur isotope ratios in tandem with zircon and garnet oxygen isotope ratios for a global sample set. The combination of these proxies allows us to provide new insights into the coupled behaviour of geodynamic, biogenic, and atmospheric evolution.

4.2 Materials and Methods

4.2.1 Sample context

Samples of this study derive from various localities within the Superior, North China, West African, and East European Cratons, and the Yavapai province (USA). A list of all samples including location is given in Table 1.

Superior Craton

The Superior Craton forms the Archean core of the Canadian Shield and can be divided into the Western and Eastern Superior Province, which are further subdivided into 17 distinct tectonic terranes (Percival et al., 2006). (Meta-)granitoid- and greenstone-dominated terranes evolved independently from 3.7-2.75 Ga, followed by accretionary events associated with the trapping of sedimentary basins and high-temperature metamorphism, leading to the formation of a coherent Superior Craton by 2.60 Ga (Percival et al., 2006). Peraluminous granites are widespread within the Superior Craton, and their occurrence is described in detail by (Breaks et al., 2005).

North China Craton

The North China Craton comprises Archean to Paleoproterozoic basement overlain by Mesoproterozoic to Cenozoic cover sequences (Zhao and Zhai, 2013). Recent publications subdivide the Precambrian basement of this region into three tectonic domains; Archean to Proterozoic Western and Eastern Blocks and a central Paleoproterozoic collisional Trans-North China Orogen (Zhao and Zhai, 2013). The Western Block comprises the Yinshan Block in the north and the Ordos Block in the south. The Neoarchean Yinshan Block comprises tonalite-trondhjemite-granodiorite (TTG) gneisses and minor supracrustal rocks that were metamorphosed at ~2.5 Ga (Zhao et al., 1999).

Baoulé-Mossi domain, West African Craton

The Paleoproterozoic (~2.3-2.0 Ga) Baoulé-Mossi domain in the southern portion of the West African Craton comprises sedimentary basins and volcanic/volcaniclastic rocks that are intruded by multiple generations of granitic rock (Parra-Avila et al., 2019, and references therein). The emplacement of felsic intrusions across the Baoulé-Mossi domain is associated with the 2.2-1.8 Eburnean Orogeny (Lombo, 2009). No agreement has been reached upon the tectonic model for the Paleoproterozoic evolution. Proposed scenarios include plume-related, subduction-related, and continental collision-related models (Parra-Avila et al., 2019, and references therein).

Ukrainian Shield, East European Craton

The Ukrainian Shield is a region of exposed Archean and Proterozoic crust within Samartia in the southwestern part of the East European Craton. The Ukrainian Shield is comprised by several tectonic blocks separated by suture zones described in detail by (Claesson et al., 2006). High grade metamorphism and associated magmatism occurred in multiple domains of the Ukrainian Shield at ~2.8 and 2.1-2.0 Ga and may reflect an active-margin setting (Claesson et al., 2006).

Svecofennian domain, Baltic Shield, East European Craton

The Svecofennian Orogeny in Finland between 1.91 and 1.87 Ga involved accretion of island arc complexes and older crustal fragments to the Archean basement of the Karelian Craton (Väisänen et al., 2000). In southernmost Finland, ~2.0-1.8 Ga old crust was intruded by sediment-derived granites at 1.84-1.83 Ga associated with high-temperature, low-pressure granulite facies metamorphism and migmatization (Huhma, 1986). This complex, referred to as the late Svecofennian granite-migmatite zone, includes the Sulkava, West Uusuma, and Turku areas (Ehlers et al., 1993). Granitic material is abundant in the Turku area. Mostly, these magmas occur as garnet and cordierite bearing leucosome in magmatic metapelites (Väisänen et al., 2000).

Yavapai province

The Yavapai province (or Colorado province) south of the Wyoming Craton comprises ~1.79-1.66 Ga volcanic-plutonic suites and sediments that are interpreted to have formed in a convergent margin setting (Reed et al., 1987). These rocks experienced multiple deformational episodes associated with metamorphism and plutonism between 1.71 and 1.62 Ga described in detail by Hoffman, (1988). The deformational episodes were followed by two pulses of calc-alkaline to alkaline magmatism at 1.50-1.42 Ga and 1.40-1.34 Ga (Hoffman, 1988).

4.2.2 Methodology

Samples were prepared by trimming off weathered surfaces using a rock saw. Melosome was removed from migmatite samples. The remaining material was washed in water and crushed. A ~10 g aliquot per sample was powdered using a tungsten carbide ring mill for bulk-rock geochemistry. Zircon, pyrite, and garnet crystals were extracted using standard separation techniques (Jasper Canyon shaking table, Frantz magnetic separation, heavy liquids [lithium heteropolytungstates and diiodomethane]). Hand-picked zircon and pyrite crystals were mounted in epoxy resin and polished to approximately half grain thickness to expose an interior cross section through the individual crystals. Grains were mounted within a 5 mm radius from the centre of a 25 mm diameter epoxy resin disk for SIMS analysis. The polished mounts were cleaned in an ultrasonic bath in multiple steps using isopropanol, ethanol, soap solution, and deionized water. Subsequently, the mounts were dried in an oven for ~24 hrs at 60°C. A 40 nm gold coat was applied to the mount surface. To reveal internal growth structures, CL images of zircon grains were taken prior to SIMS analysis using a Tescan MIRA3 field emission scanning electron microscope. SIMS U-Pb and oxygen isotope analyses were located on the same zircon growth zone (see supplementary Figure A2). Magmatic rims of zircon grains were targeted for SIMS analyses to avoid inherited older growth zones. SIMS U-Pb analysis was conducted subsequent to SIMS oxygen isotope analysis. Backscatter electron (BSE) images and energy dispersive X-ray analysis (EDX) of pyrite grains were obtained prior to SIMS analysis using a Hitachi TM3030 tabletop scanning electron microscope (SEM) coupled with a SwiftED3000 EDX spectrometer. Field Emission Scanning Electron Microscope (FESEM) element maps and BSE images of garnet grains were obtained using a Tescan Integrated Mineral

Analyzer (TIMA). The mineralogy of the samples was studied in thin section using a polarized light microscope. CL and BSE imaging, EDX analysis, and element mapping was conducted using the facilities of the John de Laeter Centre, Curtin University, Western Australia.

SIMS zircon oxygen and pyrite sulfur isotope ratios

Oxygen and sulfur isotope analysis were conducted on a CAMECA IMS 1280 secondary ion mass spectrometer (SIMS) at the Centre for Microscopy, Characterisation, and Analysis (CMCA) at the University of Western Australia and at the Guangzhou Institute of Geochemistry (GIG), Chinese Academy of Sciences, China. Analytical methods have been described in detail by Yang et al. (2018) for oxygen isotope analysis and by LaFlamme et al. (2016) for sulfur isotope analysis. A Cs⁺ primary ion beam was accelerated at 10 keV with an intensity of 2–3 nA. The spot diameter was ~10–15 μm. Prior to analysis, each site was pre-sputtered for 30–35 s to remove the Au-coat in a ~20 μm² area. Secondary optics were centered automatically before each analysis.

Oxygen and sulfur isotope compositions are reported in the conventional delta notation; expressed as $\delta^{18}\text{O}$ and $\delta^{34}\text{S}$, respectively. The delta notation reflects the permil deviation in the isotope ratio of the sample ($^{18}\text{O}/^{16}\text{O}$, $^{34}\text{S}/^{32}\text{S}$, and $^{33}\text{S}/^{32}\text{S}$ in this case) relative to a reference material. Reference materials are standard mean ocean water (VSMOW) (Baertschi, 1976) for $\delta^{18}\text{O}$, and the Cañon Diabolo Troilite (VCDT) (Ding et al., 2001) for $\delta^{34}\text{S}$ and $\delta^{33}\text{S}$. The triple sulfur isotopic composition of pyrite is expressed as $\Delta^{33}\text{S}$, defined as $\delta^{33}\text{S}-0.515*\delta^{34}\text{S}$.

For zircon oxygen isotope analysis, the ^{18}O and ^{16}O ions were detected simultaneously by two faraday cups. Instrumental mass fractionation and drift were determined through repetitive analyses of zircon standard 91500 ($\delta^{18}\text{O} = 9.9 \pm 0.6\text{\textperthousand}$) (Wiedenbeck et al., 2004). Zircon reference materials Temora-2 ($\delta^{18}\text{O} = 8.2 \pm 0.03\text{\textperthousand}$) (Black et al., 2004), and Penglai ($\delta^{18}\text{O} = 5.31 \pm 0.1\text{\textperthousand}$) (Li et al., 2010) were used as a secondary reference to monitor the quality of the applied corrections. The analysis of the secondary standard Temora-2 yielded $\delta^{18}\text{O}$ of $8.0 \pm 0.5\text{\textperthousand}$, and $7.8 \pm 0.4\text{\textperthousand}$ (2σ) in accordance with the accepted value (but see Schmitt et al. (2019) for a discussion of oxygen isotopic heterogeneity in different batches of Temora-2). The

analysis of the secondary standard Penglai yielded $\delta^{18}\text{O}$ of $5.0 \pm 0.3\text{\textperthousand}$ (2σ) in accordance with the accepted value. The analysis of the primary standard indicates a precision of $\leq 0.2\text{\textperthousand}$ (1σ) for all runs. To ensure that the oxygen isotope values reflect a primary signature, the zircon OH-content, an indicator of secondary alteration (Pidgeon et al., 2017) was determined qualitatively as compared to zircon standard 91500 (see supplementary Figure A8) for all but six samples. Zircon mounts were held under vacuum for at least 3 days prior to this analysis. Zircon OH is reported as OH/O, determined as counts of $^{16}\text{O}^1\text{H}$ over counts of ^{16}O .

For pyrite sulfur isotope analysis, the ^{34}S , ^{33}S , and ^{32}S ions were detected simultaneously by three faraday cups. Instrumental mass fractionation and drift were determined through repeated analyses of pyrite standard Sierra ($\delta^{34}\text{S} = 2.17 \pm 0.28\text{\textperthousand}$, $\Delta^{33}\text{S} = -0.02 \pm 0.01\text{\textperthousand}$) (LaFlamme et al., 2016). Pyrite standards Ruttan ($\delta^{34}\text{S} = 1.2 \pm 0.35\text{\textperthousand}$, $\Delta^{33}\text{S} = 0 \pm 0.22\text{\textperthousand}$) (Crowe and Vaughan, 1996) and Balmat ($\delta^{34}\text{S} = 16.02 \pm 1.18\text{\textperthousand}$, $\Delta^{33}\text{S} = 0 \pm 0.23\text{\textperthousand}$) (Whitehouse, 2013) were used as secondary standards to monitor the quality of the applied corrections. The analysis of Ruttan pyrite yielded $\delta^{34}\text{S}$ of $1.2 \pm 0.3\text{\textperthousand}$, and $\Delta^{33}\text{S}$ of $-0.01 \pm 0.08\text{\textperthousand}$; the analysis of Balmat pyrite yielded $\delta^{34}\text{S}$ of $16.3 \pm 0.2\text{\textperthousand}$, and $\Delta^{33}\text{S}$ of $-0.03 \pm 0.08\text{\textperthousand}$ (2σ) in accordance with the accepted values. The analysis of the primary standard indicates a precision of $\leq 0.15\text{\textperthousand}$ (1σ) for $\delta^{34}\text{S}$ and $\leq 0.04\text{\textperthousand}$ (1σ) for $\Delta^{33}\text{S}$ for all runs.

Oxygen and sulfur isotope measurement results and field centering values of reference materials are given in supplementary Figure A8, and supplementary Tables A3 and A4. Images of representative zircon and pyrite grains are given in supplementary Figures A2 and A3. Delta values of each sample are reported as weighted means (weighted based on error of single spot analysis) with 2σ errors unless stated otherwise.

Laser fluorination oxygen isotope geochemistry

Garnet grains were handpicked under a binocular to ensure they were free of inclusions and alteration. Approximately 1.6-1.8 mg of garnet was used per analysis. Laser fluorination oxygen isotope analysis was conducted at the California Institute of Technology using a CO₂ laser with BrF₅ as fluorinating agent following the procedure described by (Sharp, 1990; Valley et al., 1995). All samples were analyzed in duplicate and yielded $\delta^{18}\text{O}$ within 0.01-0.36‰ of the

replicate for each sample. Six to seven measurements per analytical session of Gore mountain garnet (UWG-2) (Valley et al., 1995) were interspersed with measurements of the unknowns. The analyses of UWG-2 indicate a precision of $\leq 0.07\%$ (1σ) for all runs. Delta values are reported as weighted means with 2σ errors unless stated otherwise. Garnet of all samples is almandine-rich and occurs as euhedral to subhedral grains (supplementary Figures A6 and A7).

SIMS zircon U-Pb geochronology

For eight samples of this study zircon U-Pb ages were obtained using an A.S.I. SHRIMP II sensitive high-resolution ion microprobe at the John de Laeter Centre, Curtin University, Western Australia. Operating procedures are described in detail by (Wingate and Kirkland, 2015). Zircon reference materials Temora-2 (417 ± 2 Ma, 130 ± 21 U ppm; Black et al., 2004), 91500 (1065 ± 1 Ma, 81 ± 5 U ppm; Wiedenbeck et al., 2004), and OG1 (3465 ± 0.6 Ma, 163 ± 48 U ppm; Stern et al., 2009) were used for U-Pb standardization, U concentration, and Pb-Pb referencing, respectively. Secondary reference material OG1 yielded weighted mean $^{207}\text{Pb}/^{206}\text{Pb}^*$ ages of 3452 ± 35 Ma (MSWD=0.6; n=4), and 3470 ± 13 Ma (MSWD=0.47; n=6); and 91500 yielded a $^{238}\text{U}/^{206}\text{Pb}^*$ age of 1078 ± 31 Ma (MSWD=0.68, n=5) within uncertainty of the accepted values. Details of calibration and instrumental uncertainties can be found in the supplementary Table A1. An acceleration voltage of 10 keV was used to direct a 15-20 μm diameter primary beam of O_2^- ions onto the zircon grain to sputter secondary ions from its surface. Secondary ions were accelerated to 10 keV into a magnetic field that directs the secondary ion beam into an electron multiplier. During each run the magnetic field was cycled several times to count the secondary ions of eight different mass species and to determine the background. The measured isotopic masses were 196 (species $[^{90}\text{Zr}_2^{16}\text{O}]^+$, count time 2 s), 204 ($^{204}\text{Pb}^+$, 10 s), 204.1 (background, 10 s), 206 ($^{206}\text{Pb}^+$, 10 s), 207 ($^{207}\text{Pb}^+$, 20–40 s), 208 ($^{208}\text{Pb}^+$, 10 s), 238 ($^{238}\text{U}^+$, 5 s), 248 ($[^{232}\text{Th}^{16}\text{O}]^+$, 5 s), and 254 ($[^{238}\text{U}^{16}\text{O}]^+$, 2 s). This cycle was repeated six times for each analysis. Prior to analysis, the primary ion beam was rastered over each site for 2-3 minutes to clean the area.

Raw data were reduced using the Microsoft Excel add-ins SQUID 2.50 and Isoplot 3.75 with the decay constants of Steiger and Jäger (1977). Measured $^{206}\text{Pb}^+/^{238}\text{U}^+$ ratios are calibrated to

the accepted $^{206}\text{Pb}/^{238}\text{U}$ ratio of the zircon standard, using a calibration curve of $\ln(^{206}\text{Pb}^+ / ^{238}\text{U}^+)$ vs. $\ln(\text{UO}^+/ \text{U}^+)$ with a fixed slope of 2.0 (Claoue-Long et al., 1995). Measured compositions were corrected for the presence of common Pb using measured $^{204}\text{Pb}/^{206}\text{Pb}$ and the contemporaneous Pb isotopic composition determined according to the terrestrial Pb model of Stacey and Kramers (1975). To confirm that common Pb is mainly inherited to the zircon grain rather than related to surface contamination, counts for $^{204}\text{Pb}^+$ were monitored during each analysis to ensure that they remained low (≤ 5 counts/10 s for most grains) over the analysis time of ~ 16 min. Calculated mean ages are quoted in the text at the 2σ level (unless stated otherwise) and include propagated internal and external uncertainty components. No $^{207}\text{Pb}/^{206}\text{Pb}$ fractionation correction was deemed necessary as OG1 yielded weighted mean $^{207}\text{Pb}/^{206}\text{Pb}^*$ ages of 3452 ± 35 Ma (MSWD=0.6; n=4), and 3470 ± 13 Ma (MSWD=0.47; n=6) within uncertainty of the accepted value.

LA ICP-MS zircon U-Pb geochronology

For one sample of this study (sample 15K-2) U-Pb isotopic data were collected by laser ablation inductively coupled plasma mass spectrometry (LA ICP-MS) at the GeoHistory Facility, John de Laeter Centre, Curtin University. Zircon was ablated using a Resonetics RESOlution M-50A-LR system, incorporating a COMPex 102–193 nm excimer UV laser coupled to an Agilent 8900 QQQ mass spectrometer. Following two cleaning pulses and a 30 s period of background analysis, samples were spot ablated for 30 s at a 5 Hz repetition rate using a $38 \mu\text{m}$ beam and laser energy at the sample surface of 2 J/cm^2 . An additional 15 s of baseline was collected after ablation. The sample cell was flushed with ultrahigh purity He (300 mL min^{-1}) and N₂ (1.0 mL min^{-1}) and high purity Ar was employed as the plasma carrier gas (flow rate 0.98 L min^{-1}). The time-resolved mass spectra were reduced using the U-Pb geochronology data reduction schemes in Iolite 3.7TM (Paton et al., 2011) with final ages calculated using Isoplot. Zircon standard OG1 (3465 ± 0.6 Ma) (Stern et al., 2009) was used as a primary reference material. Secondary zircon standards yielded weighted mean ages within uncertainty of their accepted values (see supplementary Table A2).

XRF bulk-rock geochemistry

Bulk-rock major and trace element concentrations of 12 samples of this study were determined using a Panalytical Zetium 4 kW X-ray fluorescence spectrometer (XRF) at the California Institute of Technology, USA. Powdered samples were dried at 110°C overnight. Dried powders were then sintered at 1050°C for one hour and loss on ignition (L.O.I) was determined subsequently. After re-homogenizing sample powders with an agate mortar and pestle, sample powders were fused into glass beads at a flux to sample ratio of 10:1 using a di-lithium tetraborate-lithium metaborate flux. The concentrations of 10 major and 18 trace elements in the samples were measured by comparing their X-ray intensities to those obtained from standards beads. Full analytical methods and uncertainties are given in (Bucholz and Spencer, 2019).

ICP-MS bulk-rock geochemistry

Bulk-rock major element concentrations of one sample (15K-2) was determined in solution by ICP-MS analysis at Bureau Veritas Minerals, Canada. Approximately 0.25 g of sample material was dissolved through multi-acid digestion ($\text{HNO}_3\text{-HClO}_4\text{-HF}$). Subsequently, the solution was dried down, and the residue was dissolved in HCl prior to analysis.

Sample ID	Locality	Latitude	Longitude	Lithology	Mineralogy	Reference
17FIN01	Svecofennian domain	60.498	22.262	Grt migmatite	Grt+Qz+Af _s +Pl+Bt	this study
17FIN02	Svecofennian domain	60.47	22.368	Grt migmatite	Grt+Qz+Af _s +Pl+Bt	this study
17FIN03B	Svecofennian domain	60.425	22.382	Grt migmatite	Grt+Qz+Af _s +Pl+Bt	this study
17FIN04A	Svecofennian domain	60.461	22.176	Grt migmatite	Grt+Qz+Af _s +Pl+Bt	this study
17FIN05B	Svecofennian domain	60.546	22.128	Grt migmatite	Grt+Qz+Af _s +Pl+Bt	this study
17FIN06	Svecofennian domain	60.482	22.018	Grt migmatite	Grt+Qz+Af _s +Pl+Bt	this study
19GH11B	West African Craton	-1.609	5.14	Bt Ms granite	Ms+Qz+Af _s +Pl+Bt	this study
19GH9	West African Craton	-1.377	5.34	Bt Ms granite	Ms+Qz+Af _s +Pl+Bt	this study
19GH3	West African Craton	-1.156	5.16	Grt granite	Grt+Qz+Af _s +Pl+Bt	this study
18IM19	North China Craton	40.693	109.641	Grt granite	Grt+Qz+Af _s +Pl+Bt	Liebmam et al. subm. to Terra Nova
18IM20	North China Craton	40.709	109.643	Grt granitoid	Grt+Qz+Af _s +Pl+Bt	Liebmam et al. subm. to Terra Nova
18IM23D	North China Craton	40.811	110.258	Grt granite	Grt+Qz+Af _s +Pl	Liebmam et al. subm. to Terra Nova
18IM25C	North China Craton	41.182	109.479	Ms Bt granite	Ms+Qz+Af _s +Pl(+Bt)	Liebmam et al. subm. to Terra Nova
18IM11B	North China Craton	40.604	112.5	Grt granitoid	Grt+Qz+Af _s +Pl+Bt	Liebmam et al. subm. to Terra Nova
18IM12B	North China Craton	40.839	112.565	Grt quartz rich granitoid	Grt+Qz+Af _s +Pl	Liebmam et al. subm. to Terra Nova
18IM13C	North China Craton	41.084	110.924	Grt granite	Grt+Qz+Af _s +Pl(+Ms)	Liebmam et al. subm. to Terra Nova
18IM15B	North China Craton	40.994	110.947	Grt granitoid	Grt+Qz+Af _s +Pl	Liebmam et al. subm. to Terra Nova
18IM3	North China Craton	40.848	113.921	Grt granite	Grt+Ms+Qz+Af _s +Pl(+Bt)	Liebmam et al. subm. to Terra Nova
15K-2	Ukrainian Shield	50.98	28.68	Granite	Qz+Pl+Bt	this study
CO-17-8	Yavapai province	39.776	105.78	Bt Ms granite	Ms+Qz+Af _s +Pl+Bt	Buchholz and Spencer, 2019
SP-16-20a	Superior Craton	49.815	93.02	Bt Ms granite	Ms+Qz+Af _s +Pl+Bt	Buchholz et al. 2018
SP-16-2b	Superior Craton	47.661	92.939	Bt Ms granite	Ms+Qz+Af _s +Pl+Bt	Buchholz et al. 2018
SP-16-34	Superior Craton	49.848	92.694	Bt Ms Grt granite	Ms+Qz+Grt+Af _s +Pl+Bt	Buchholz et al. 2018
SP-17-43	Superior Craton	50.741	93.209	Bt Ms Grt granite	Ms+Qz+Grt+Af _s +Pl+Bt	this study
SP-17-33	Superior Craton	50.284	94.495	Bt Grt granite	Grt+Bt+Qz+Af _s +Pl	this study
SP-17-38	Superior Craton	49.863	93.771	Ms Grt granite	Grt+Ms+Qz+Af _s +Pl	this study
SP-17-82	Superior Craton	51.2	92.383	Ms Grt granite	Grt+Ms+Qz+Af _s +Pl	Buchholz and Spencer, 2019
SP-17-71	Superior Craton	50.994	92.328	Ms Grt granite	Grt+Ms+Qz+Af _s +Pl	Buchholz and Spencer, 2019
SP-17-13	Superior Craton	48.906	89.213	Bt Grt granite	Grt+Qz+Af _s +Pl+Bt	this study
SP-17-50	Superior Craton	50.847	92.105	Bt Ms Grt granite	Grt+Ms+Qz+Af _s +Pl+Bt	this study

Table 4.1. Summary of sample locations, lithologies, and mineralogy. Minerals in parentheses are accessory phases. Mineral abbreviations: Qz, quartz; Af_s, alkali feldspar; Pl, plagioclase; Grt, garnet; Ms, muscovite; Bt, biotite.

4.3 Results

4.3.1 Bulk-rock geochemistry and mineralogy

Samples include granitoids comprised of quartz + alkali feldspar + plagioclase ± biotite in varying proportions, and contain one or more peraluminous indicator minerals, such as garnet or muscovite. The samples for which bulk-rock geochemical data is available are strongly peraluminous with an aluminium saturation index (ASI) ≥ 1.1 (defined as molecular Al/[Ca - 1.67P + Na + K]). For comparison ACNK values (defined as molecular Al/[Ca + Na + K]) are also reported in Table 2. With the exception of sample 15K-2, ASI and ACNK yield identical values to the first decimal place. The mineralogy of all samples is summarized in Table 1. Bulk rock major element concentrations are given in Table 2. Thin section photomicrographs can be found in supplementary Figure A4.

4.3.2 Geochronology

Magmatic crystallization ages of the 30 sediment-derived granitoids in this study are Neoarchean to Mesoproterozoic, ranging from 2664 ± 45 Ma to 1447 ± 50 Ma. For nine of these samples the magmatic crystallization age was determined in this study (as zircon concordia, upper intercept, or weighted mean $^{207}\text{Pb}^*/^{206}\text{Pb}^*$ ages). For nine samples zircon U-Pb SIMS ages were determined in previous studies (Liebmann et al., submitted to Terra Nova). For the remaining 12 samples for which no or only metamict zircon was extracted, preferred ages use robust published dates from the same batholith or are estimates based on the age of proximal magmatism. A detailed description of the geochronology is given in Appendix A; a summary is given in Table 3. Single-spot zircon U-Pb results can be found in supplementary Table B1.

4.3.3 Zircon and garnet oxygen isotope geochemistry

Zircon $\delta^{18}\text{O}$ values range from $4.93 \pm 0.82\text{\textperthousand}$ to $11.41 \pm 1.00\text{\textperthousand}$. Similarly, garnet $\delta^{18}\text{O}$ values range from $7.06 \pm 0.09\text{\textperthousand}$ to $11.50 \pm 0.12\text{\textperthousand}$. Note, that no garnet was extracted from the two samples with the lowest zircon $\delta^{18}\text{O}$ values (19GH9, and 19GH11B). Zircon records a lower range of $\delta^{18}\text{O}$ values for samples with crystallization ages >2.3 Ga ($2\sigma=0.5\text{\textperthousand}$, number of samples=3) as compared to samples with crystallization ages <2.3 Ga ($2\sigma=4.1\text{\textperthousand}$, n=12),

whereas the range of garnet $\delta^{18}\text{O}$ stays approximately the same (>2.3 Ga garnet: $2\sigma=1.2\text{\textperthousand}$, $n=10$; <2.3 Ga garnet: $2\sigma=1.1\text{\textperthousand}$, $n=10$). On average $\delta^{18}\text{O}$ values increase post- 2.3 Ga; from $7.15\text{\textperthousand}$ to $9.08\text{\textperthousand}$ in zircon, from $7.22\text{\textperthousand}$ to $10.24\text{\textperthousand}$ in garnet, and from $7.19\text{\textperthousand}$ to $9.30\text{\textperthousand}$ combining the data of both zircon and garnet. Equilibrium fractionation of oxygen isotopes between zircon and almandine-rich garnet is small at temperatures typical for granitoid melts ($<0.1\text{\textperthousand}$ at temperatures >650 °C) (Valley et al., 2003). The garnet-zircon pairs of all samples indicate oxygen isotopic equilibrium (Figure 4.1). Two samples (17FIN02 and 17FIN04A) yield heterogeneous single spot zircon $\delta^{18}\text{O}$ values ($2\sigma > 3\text{\textperthousand}$) and are

Sample ID	Major element concentrations (reported as oxide wt %)										Reference				
	SiO ₂	TiO ₂	Al ₂ O ₃	Fe ₂ O ₃	MgO	CaO	Na ₂ O	K ₂ O	P ₂ O ₅	MnO	LOI	Total	ASI	ACNK	
19GH11B	73.78	0.08	14.74	0.55	0.15	1.25	3.39	5.63	0.01	0.02	99.81	1.1	1.1	this study	
19GH9	73.23	0.11	15.67	1.06	0.28	2.91	5.02	1.14	0.03	0.02	0.63	100.09	1.1	1.1	this study
19GH3	73.16	0.05	16.96	0.33	0.14	0.91	4.36	2.34	0.08	0.01	1.31	99.64	1.5	1.5	this study
17FIN01D	74.00	0.04	13.38	2.13	0.28	0.26	2.05	7.40	0.11	0.02	0.58	100.26	1.1	1.1	this study
17FIN02	61.87	0.85	17.24	7.95	2.94	1.18	2.45	3.84	0.06	0.03	1.41	99.81	1.7	1.7	this study
17FIN03B	60.20	0.82	17.37	8.76	2.41	2.15	3.73	3.53	0.07	0.08	0.69	99.81	1.3	1.3	this study
17FIN04A	71.01	0.23	14.58	3.56	0.95	1.62	3.02	4.40	0.08	0.07	0.49	100.01	1.2	1.2	this study
17FIN05B	56.62	0.89	18.71	8.63	3.91	1.42	2.63	5.86	0.08	0.04	1.24	100.02	1.4	1.4	this study
17FIN06A	64.84	0.66	15.99	6.92	2.21	1.62	2.92	3.45	0.07	0.05	1.16	99.89	1.4	1.4	this study
17FIN06B	70.66	0.06	15.00	3.88	0.72	1.47	3.14	4.28	0.10	0.04	0.71	100.06	1.2	1.2	this study
18IM19	72.13	0.31	14.05	3.51	1.41	1.27	2.49	3.68	0.06	0.05	0.73	99.69	1.4	1.4	this study
15K-2	62.29	0.57	17.36	5.97	1.76	3.23	5.15	2.19	0.33	0.06	0.90	99.81	1.1	1.0	this study
18IM11B	61.93	1.06	18.04	6.58	2.18	2.88	2.80	3.58	0.07	0.06	0.22	99.38	1.3	1.3	Liebmann et al. subm. to Terra Nova
18IM12B	69.05	0.14	14.73	5.97	1.90	2.85	2.32	1.03	0.03	0.13	0.77	98.92	1.5	1.5	Liebmann et al. subm. to Terra Nova
18IM13C	70.74	0.33	14.84	3.06	0.87	3.04	3.29	1.73	0.10	0.01	1.00	99.01	1.2	1.2	Liebmann et al. subm. to Terra Nova
18IM14A	77.72	0.29	10.59	1.62	0.54	0.77	1.31	5.15	0.07	0.04	0.72	98.82	1.2	1.2	Liebmann et al. subm. to Terra Nova
18IM15B	65.23	0.58	15.48	7.01	2.12	3.52	2.84	0.96	0.09	0.09	1.34	99.25	1.3	1.3	Liebmann et al. subm. to Terra Nova
18IM19	72.13	0.31	14.05	3.51	1.41	1.27	2.49	3.68	0.06	0.05	0.73	99.69	1.4	1.4	Liebmann et al. subm. to Terra Nova
18IM20	63.52	0.26	17.78	6.13	1.81	2.63	3.50	3.05	0.07	0.07	0.85	99.69	1.3	1.3	Liebmann et al. subm. to Terra Nova
18IM21C	81.84	0.04	8.75	2.84	0.65	1.11	2.19	0.76	0.18	0.93	99.48	1.4	1.4	Liebmann et al. subm. to Terra Nova	
18IM23D	71.76	0.11	14.05	2.83	0.79	0.60	2.01	6.51	0.12	0.04	0.50	99.32	1.2	1.2	Liebmann et al. subm. to Terra Nova
18IM25C	74.42	0.06	13.17	0.95	0.17	0.95	2.71	5.80	0.02	0.00	0.89	99.15	1.1	1.1	Liebmann et al. subm. to Terra Nova
18IM3	77.57	0.37	10.88	3.01	0.87	1.03	2.23	2.72	0.05	0.05	0.68	99.45	1.3	1.3	Liebmann et al. subm. to Terra Nova
SP-16-20a	74.14	0.10	13.97	0.92	0.27	0.65	2.70	6.62	0.12	0.01	0.35	99.86	1.1	1.1	Buchholz et al. 2018
SP-16-2b	72.83	0.18	14.50	1.33	0.31	1.11	4.05	4.58	0.07	0.03	0.53	99.53	1.1	1.1	Buchholz et al. 2018
SP-16-34	75.30	0.08	14.30	0.73	0.25	0.84	2.80	5.00	0.05	0.02	0.61	99.97	1.3	1.2	Buchholz et al. 2018
SP-17-71	75.31	0.05	14.11	0.71	0.06	0.60	5.45	1.58	0.11	0.17	0.97	98.08	1.3	1.2	Buchholz and Spencer, 2019
SP-17-82	75.45	0.05	14.27	0.44	0.01	0.32	4.85	3.74	0.02	0.08	0.74	99.18	1.2	1.1	Buchholz and Spencer, 2019
CO-17-8	70.54	0.39	14.37	2.95	0.49	1.24	2.56	5.78	0.28	0.03	1.25	99.58	1.3	1.1	Buchholz and Spencer, 2019

Table 4.2. Bulk rock major element concentrations. The aluminium saturation index (ASI) is calculated as molecular Al/(Ca + Na + K); ACNK is calculated as molecular Al/(Ca - 1.67P + Na + K); ACNK is calculated as molecular Al/(Ca + Na + K).

interpreted to reflect secondary signatures (Pidgeon et al., 2017). This is further supported by CL images revealing that some areas in some zircon grains are affected by metamictization (supplementary Figure A2). Therefore, the oxygen isotopic composition recorded by garnet from these two samples provides the best estimate of their parental magma $\delta^{18}\text{O}$. Data tables with single spot O isotopic data are given in the supplementary Table D1, a summary of weighted means is given in Table 3.

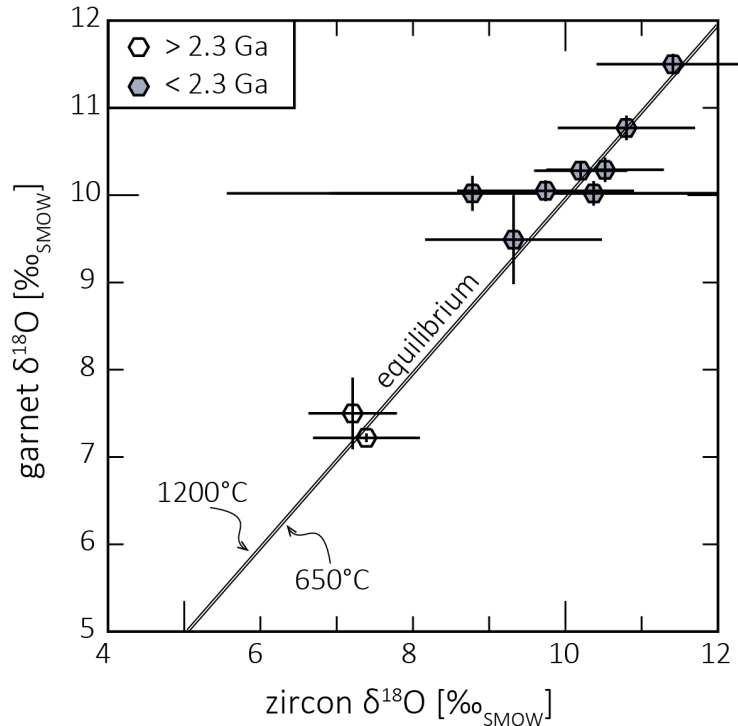


Figure 4.1. Zircon $\delta^{18}\text{O}$ vs garnet $\delta^{18}\text{O}$ color-coded by crystallization age of sediment-derived igneous rocks. Isotherms at 650°C and 1200°C are after Valley et al., (2003). Oxygen isotope data is shown as weighted averages. Single spot results of O isotope analysis are given in the appendix. Error bars are shown at 2σ level. Note that large error bars for zircon $\delta^{18}\text{O}$ are due to heterogeneity in these samples interpreted to be related to secondary processes (discussed in the text).

4.3.4 Sulfur isotope geochemistry

Pyrite grains are euhedral to sub-euhedral, chemically homogenous, and largely free of inclusions and intergrown phases. BSE and reflected light images of representative pyrite grains for each sample are given in the supplementary Figures A3 and A5. Pyrite $\delta^{34}\text{S}$ values range

from $-13.33 \pm 0.36\text{‰}$ to $9.72 \pm 0.99\text{‰}$, but are mostly (11 out of 13 samples) between -4‰ and 4‰ . Single spot pyrite $\delta^{34}\text{S}$ and $\Delta^{33}\text{S}$ values cluster tightly around discrete values for each sample, and seemingly define single populations (Figure 4.2). Four samples show pyrite $\Delta^{33}\text{S}$ outside of the S-MDF range (Figure 4.2). These samples include three ~ 2.7 Ga granites from the Superior province that exhibit positive $\Delta^{33}\text{S}$ values of $0.13 \pm 0.06\text{‰}$ to $0.18 \pm 0.05\text{‰}$, and a ~ 2.5 Ga granite from the North China Craton with negative $\Delta^{33}\text{S}$ value of $-0.29 \pm 0.12\text{‰}$. Data tables with single spot sulfur isotopic data are given in the supplementary Table C1, a summary of weighted means is given in Table 3.

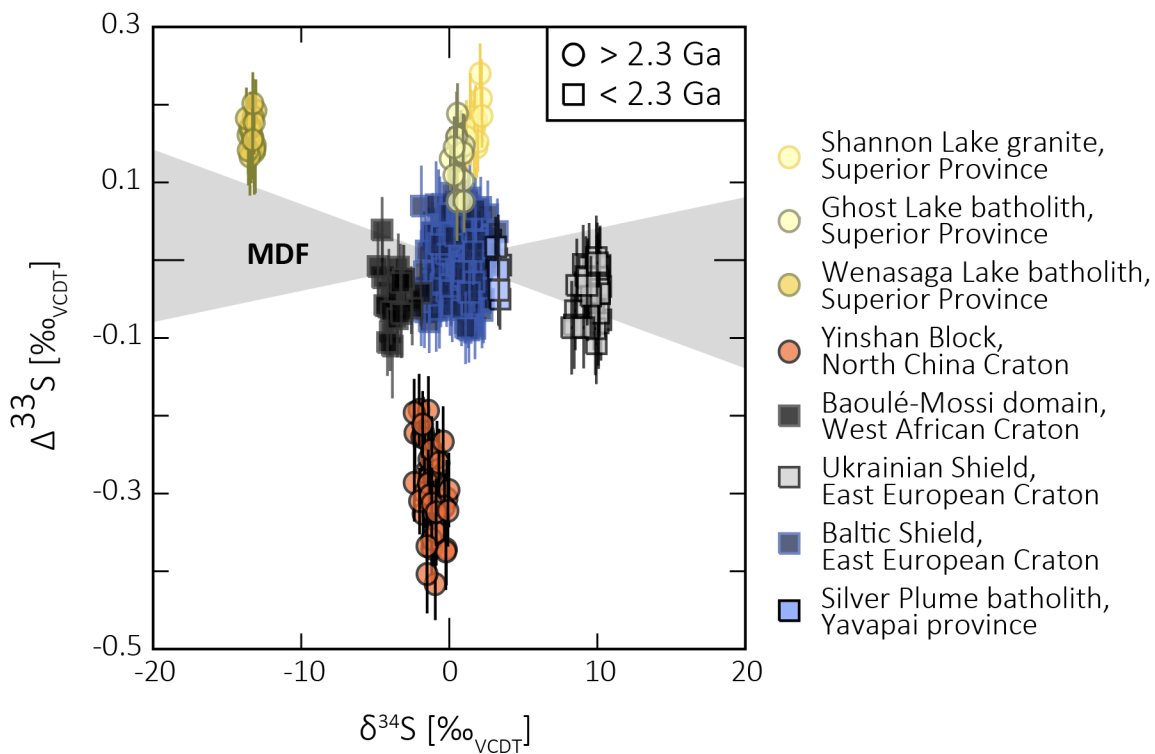


Figure 4.2. Single spot $\delta^{34}\text{S}$ vs. $\Delta^{33}\text{S}$ of sediment-derived igneous rocks. Error bars for $\Delta^{33}\text{S}$ are shown at 1σ level. Errors of $\delta^{34}\text{S}$ at 2σ level are smaller than the symbols. Grey area marks the range of $\Delta^{33}\text{S}$ values that can be produced through mass-dependent fractionation processes (LaFlamme et al., 2018). Single spot results of sulfur isotope analysis are given in the appendix.

Sample ID	Locality	Age ± 2σ Ma	zircon $\delta^{18}\text{O}$ [‰]	$\delta^{18}\text{O}$ [‰] 2σ	garnet $\delta^{18}\text{O}$ [‰]	$\delta^{18}\text{O}$ [‰] 2σ	pyrite $\delta^{34}\text{S}$ [‰] 2σ	$\Delta^{33}\text{S}$ [‰] 2σ	Reference
17FIN01	Svecofennian domain	1850 ¹⁾	-	-	10.39	0.2	1.54	0.99	-0.01
17FIN02	Svecofennian domain	1896 ± 26	8.78	3.22	9.87	0.24	-0.87	0.9	-0.02
17FIN03B	Svecofennian domain	1824 ± 13	9.32	1.16	9.48	0.51	-0.09	0.88	0.01
17FIN04A	Svecofennian domain	1850 ¹⁾	10.37	3.46	10.02	0.1	0.85	1.41	0.01
17FIN05B	Svecofennian domain	1836 ± 11	10.52	0.77	10.3	0.11	1.61	0.55	-0.01
17FIN06	Svecofennian domain	1815 ± 16	10.2	0.61	10.28	0.11	1.58	0.93	-0.01
19GH11B	West African Craton	2188 ± 20	5.34	0.83	-	-	-3.71	1.51	-0.05
15K-2	Ukrainian Shield	2144 ± 28	8.86	0.81	-	-	9.72	0.99	-0.04
CO-17-8	Yarapai province	1447 ± 50	8.74	0.61	-	-	3.31	0.26	-0.02
SP-16-20a	Superior Craton	2654 ± 24	-	-	-	-	0.6	0.56	0.13
SP-16-2b	Superior Craton	2664 ± 45	-	-	-	-	1.79	0.61	0.18
SP-17-43	Superior Craton	2690 ²⁾	-	-	7.06	0.09	-13.33	0.36	0.04
18IM19	North China Craton	2478 ± 18	7.21	0.58	7.5	0.41	-1.26	1.29	-0.29
18IM20	North China Craton	2374 ± 48	7.39	0.7	7.22	0.05	-	-	-
18IM11B	North China Craton	1901 ± 17	10.8	0.9	10.77	0.14	-	-	-
18IM12B	North China Craton	1929 ± 29	9.74	1.16	10.05	0.12	-	-	-
18IM3	North China Craton	1917 ± 70	11.41	1	11.52	0.12	-	-	-
18IM25C	North China Craton	2493 ± 28	6.86	0.89	-	-	-	-	-
18IM13C	North China Craton	2536 ± 13	8.12	0.7	-	-	-	-	-
18IM15B	North China Craton	2530 ± 60	8.57	0.42	-	-	-	-	-
18IM23D	North China Craton	2453 ± 11	6.31	0.63	-	-	-	-	-
19GH9	West African Craton	2183 ± 14	4.93	0.82	-	-	-	-	-
19GH3	West African Craton	2180 ¹⁾	-	-	9.72	0.09	-	-	-
SP-16-34	Superior Craton	2654 ± 24	-	-	7.99	0.1	-	-	-
SP-17-33	Superior Craton	2650 ¹⁾	-	-	7.85	0.13	-	-	-
SP-17-38	Superior Craton	2650 ¹⁾	-	-	6.93	0.11	-	-	-
SP-17-82	Superior Craton	2650 ¹⁾	-	-	6.06	0.12	-	-	-
SP-17-71	Superior Craton	2650 ¹⁾	-	-	6.92	0.09	-	-	-
SP-17-13	Superior Craton	2660 ± 10 ³⁾	-	-	7.15	0.1	-	-	-
SP-17-50	Superior Craton	2650 ¹⁾	-	-	7.55	0.09	-	-	-

Table 4.3. Summary of O and S geochemistry, and crystallization ages. Isotopic data is given as weighted average. 1) expected age (see Appendix A. 2) age from Corfu et al. (1995), 3) age from Percival (1989).

4.4 Discussion and conclusion

The presence of aluminous mineral phases and/or ASI ≥ 1.1 strongly suggest that the studied granitoids were derived from the partial melting of metasedimentary protoliths (Chappell and White, 1992; Frost and Frost, 2008). The partial or entire derivation of these granitoids from metasedimentary protoliths is in accord with previous interpretations of the regional geology (Väisänen et al., 2000; Percival et al., 2006; Zhao and Zhai, 2013; Parra-Avila et al., 2019). Zircon and garnet tend to preserve a record of the oxygen isotope composition of their parental melt due to slow intracrystalline diffusion rates of oxygen in these minerals (Valley et al., 1994; Vielzeuf, 2005). Given the small equilibrium fractionation (smaller than the analytical uncertainty) of oxygen isotopes between almandine-rich garnet and zircon at temperatures typical for granitoid melts (Valley et al., 2003) (Figure 4.1) $\delta^{18}\text{O}$ values recorded by garnet and zircon, respectively, in the sediment-derived granitoids of this study are directly comparable. The range and average $\delta^{18}\text{O}$ values of sediment-melts increases post-2.3 Ga (Figure 4.3), in accord with previous studies that interpret the rise of average $\delta^{18}\text{O}$ to be the result of widespread continental emergence and a concomitant change in sediment composition (Liebmann et al., submitted to Terra Nova; Spencer et al., 2019). Low $\delta^{18}\text{O}$ values in sediment melts (equal or lower than the mantle value of $5.3 \pm 0.6\text{\textperthousand}$; Page et al., 2007),

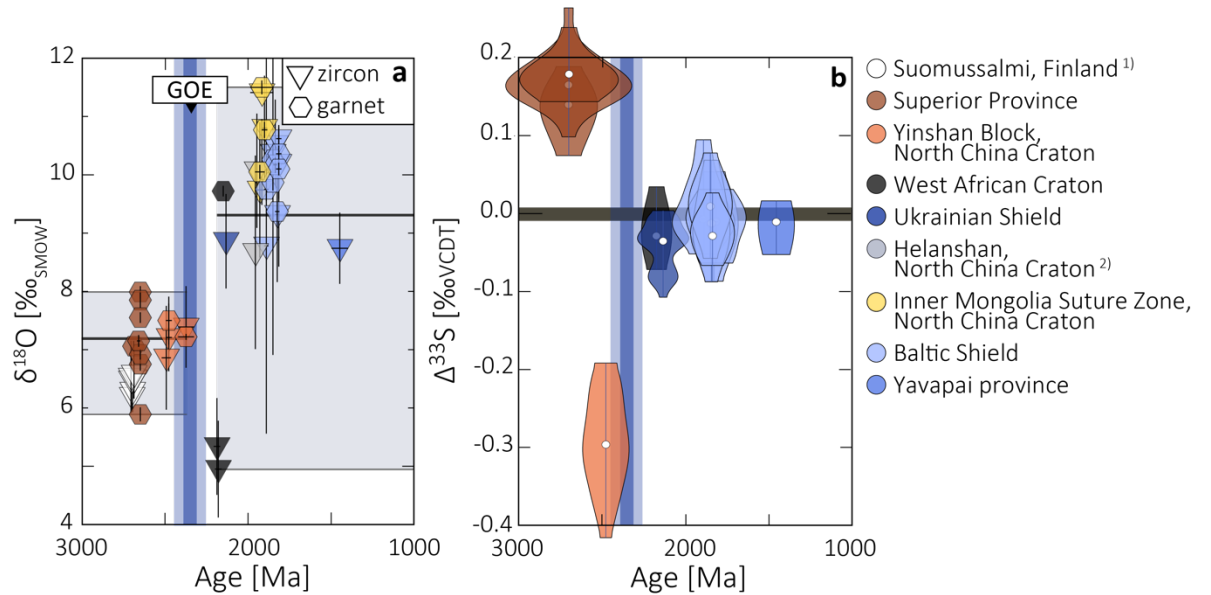


Figure 4.3. Oxygen and sulfur isotopic data vs. crystallization age of sediment-derived igneous rocks. Timing of atmospheric oxygenation is shown as blue bar (thin blue bar after Luo et al., 2016, and thick blue bar after Gumsley et al., 2017). Legend on the right applies to both parts of the figure. (A) Zircon and garnet $\delta^{18}\text{O}$ vs. crystallization age of sediment-derived igneous rocks. Oxygen isotope data is shown as weighted averages. Grey bars mark average $\delta^{18}\text{O}$ (as recorded by zircon and garnet) pre- and post-2.3 Ga, respectively. Single spot results of O isotope analysis are given in the appendix. Error bars for oxygen isotope data and age are 2σ . Zircon oxygen isotope data from Suomussalmi and Helanshan are from 1) Mikkola et al. (2011), and 2) Dan et al. (2014). (B) Pyrite $\Delta^{33}\text{S}$ vs. crystallization age of sediment-derived igneous rocks shown as violin plots; white circles mark medians. Black bar marks $\Delta^{33}\text{S} = 0\text{\textperthousand}$.

like in 19GH9 and 19GH11B, are interpreted to reflect hydrothermal alteration of the protolith (Hollis et al., 2014). It has been proposed that interaction of a melt with hydrothermal low- $\delta^{18}\text{O}$ meteoric water – a mechanism that requires large emergent land masses – may be the process responsible for such low $\delta^{18}\text{O}$ melts (Hollis et al., 2014).

Archean continents were at least locally raised above sea-level as evident from siliciclastic sediments and subaerial volcanism (e.g. Eriksson et al., 1999). However, geochemical proxies and numerical models suggest that the subaerial exposure of Archean continents was limited (Flament et al., 2013; Johnson and Wing, 2020). The widespread emergence of continents (i.e. a change from locally subaerial continents to large-scale subaerial exposure of continents) at the Archean-Proterozoic transition is supported by changes to geochemical proxies at this time, such as an increase in seawater $^{87}\text{Sr}/^{86}\text{Sr}$ (Flament et al., 2013), a decrease in shale $\Delta^{17}\text{O}$ (Bindeman et al., 2018; Bindeman, 2020), as well as an increase in subaerial large igneous province volcanism (Kump and Barley, 2007).

Pyrite-bearing sediment-derived granitoids with crystallization ages >2.3 Ga yield non-zero $\Delta^{33}\text{S}$ values, whereas those younger than 2.3 Ga uniformly show $\Delta^{33}\text{S}$ of 0\textperthousand . Although the $\Delta^{33}\text{S}$ values of the >2.3 Ga granitoids are small compared to those in pre-GOE sedimentary rocks (up to $\sim 12\text{\textperthousand}$) (Johnston, 2011), the magnitude of non-zero $\Delta^{33}\text{S}$ values observed here is too large to be the result of S-MDF processes alone (Figure 4.2). Hence, the S-MIF signatures in the >2.3 Ga pyrite-bearing granitoids record the recycling of sedimentary sulfur species formed under the anoxic pre-GOE atmosphere, as has been demonstrated for S-MIF carrying strongly

peraluminous granites in previous studies (Bucholz et al., 2020). Three of the >2.3 Ga granitoids of this study show positive $\Delta^{33}\text{S}$ values, one sample shows a negative $\Delta^{33}\text{S}$ value. The pre-GOE pyrite record is skewed towards positive $\Delta^{33}\text{S}$ values (Johnston, 2011). Positive $\Delta^{33}\text{S}$ anomalies are commonly found in Archean sedimentary pyrite that may have formed from reduced sulfur species (e.g. S_8 aerosols) produced through photodissociation in the oxygen-poor atmosphere (Farquhar et al., 2000; Farquhar et al., 2002). Based on the dominance of negative $\Delta^{33}\text{S}$ values in Archean barites, it has been posited that oceanic sulfates (formed from oxidized sulfur species produced through photodissociation; e.g. SO_4 aerosols) carry the complementary negative $\Delta^{33}\text{S}$ signatures required by isotopic mass balance (Farquhar et al., 2000). However, recent studies report positive $\Delta^{33}\text{S}$ anomalies in Archean oceanic sulfate (Paris et al., 2014). The inconsistent sulfur isotopic budget is a yet unsolved scientific problem, and the complementary negative $\Delta^{33}\text{S}$ reservoir remains cryptic.

The low $\delta^{34}\text{S}$ value ($\sim -13\text{\textperthousand}$) of pyrite in sample SP-17-43 from the Wenasaga Lake batholith, Superior province, could derive from the contribution of organic sulfur. Mircobial sulfate reduction commonly produces sulfides that are strongly depleted in the heavy ^{34}S isotope (Johnston et al., 2007). The S-MIF signature in this sample ($\Delta^{33}\text{S} = 0.16 \pm 0.04\text{\textperthousand}$) indicates atmospheric influence. Therefore, the recorded sulfur isotopic composition of this sample may be the result of mixing between two reservoirs (i.e. atmospheric and microbial sulfur). A similar scenario has been suggested to be responsible for the negative $\delta^{34}\text{S}$ values and positive $\Delta^{33}\text{S}$ values of pyrite in the upper Mount McRae shale in the Hamersley Basin, Western Australia (Kaufman et al., 2007). Alternatively, the low $\delta^{34}\text{S}$ value in this sample could arise during fractionation between S^{2-} in the melt and H_2S in a vapor phase (produced through metamorphic devolatilization) as documented for other samples from the Superior Craton (Bucholz et al., 2020).

The youngest sediment-derived granitoid of this study that shows S-MIF and oxygen isotopic signatures respectively implying an anoxic atmosphere and widely submerged continents (sample 18IM19) has a crystallization age of 2478 ± 18 Ma. The oldest sample (19GH11B) showing only S-MDF and O isotopic signatures indicating respectively an oxygenized

atmosphere and emergent continents yields a crystallization age of 2188 ± 20 Ma. The evolution of oxygen and sulfur isotopic signatures appear to be coupled in the samples of this study. However, the data is inconclusive for the ~ 300 Myr interval between the youngest S-MIF and the oldest S-MDF sample. The preserved rock record between 2.4 and 2.2 Ga is sparse (Condie et al., 2009; Spencer et al., 2018) making it challenging to fill this temporal gap. The lifespan of sedimentary basins ranges from <1 Myr for trench basins to >100 Myr for intracratonic basins (Woodcock, 2004). Hence, due to the lag time between sediment deposition and partial melting, the granitoids studied here only provide minimum ages for the secular changes in the oxygen and sulfur isotopic systems. Importantly however, this is inconsequential for the fact that the evolution of oxygen and sulfur isotopic signatures seems to be coupled in this sample set. If the evolution of sulfur and oxygen isotopic signatures in sediment-derived melts is truly coupled, this would provide strong evidence for a temporal, and potentially causal connection of the emergence of continents and atmospheric oxygenation.

According to Warke et al. (2020) atmospheric oxygenation preceded widespread, potentially global, glaciations. This conclusion is based on sedimentary formations on the Fennoscandian shield, in which the transition from S-MIF to S-MDF-bearing strata occurs below the diamictite member of the formations linked to the Makganyene glaciation (Warke et al., 2020). This temporal relationship between atmospheric oxygenation and widespread glaciations rules out models in which Proterozoic ice houses facilitated the invention of oxygenic photosynthesis (Kirschvink and Kopp, 2008), and hence, calls for an alternative driver for the rise of O₂. Numerical models demonstrate the strong influence of subaerial continental emergence on phosphorous fluxes to the oceans (Hao et al., 2020). Elevated, emerged continental crust and associated enhanced erosion would increase the supply of life-essential nutrients into the ocean, increasing that available for oxyphotobacteria (Campbell and Allen, 2008; Hao et al., 2020). It has been suggested that a similar mechanism involving the erosion of elevated continental crust has initiated the explosive radiation of animal-life during the Late Ediacaran to Early Cambrian periods (575-510 Ma; ‘Cambrian explosion’) (Squire et al., 2006). A flush of nutrients associated with enhanced erosion may have led to an increase in O₂ production and provided a favourable environment for the explosive diversification of life (Chen et al., 2015). Similarly, an increased

nutrient flux (e.g. phosphorous) to the oceans associated with the Paleoproterozoic subaerial emergence of continents may have fuelled a boost in oxygenic photosynthesis (either in terms of radiation or bioproductivity) (Cox et al., 2018). A shift in ocean nutrient availability from phosphorous to iron limiting may have resulted in ecological conditions favourable for oxygenic photoautotrophs over anoxygenic photoautotrophs (Jones et al., 2015; Ozaki et al., 2019). Furthermore, increased erosion and sediment supply from the elevated continents would facilitate the burial of organic carbon leading to diminished O₂ consumption (Campbell and Allen, 2008).

Potential causes of the Paleoproterozoic subaerial emergence of continents are a ~2.4-2.2 Ga tectono-magmatic slowdown (Condie et al., 2009; Spencer et al., 2018), or the effect of dynamic topography (Gurnis, 1988) during the ~2.45 Ga rifting of Superior (Bleeker, 2003). The proposed ~2.4-2.2 Ga lull in mantle activity and concomitant reduced plate-velocities (Spencer et al., 2018) and mid-ocean ridge activity (Eriksson and Condie, 2014) could have led to cooling and thickening of the oceanic lithosphere causing subsidence of the ocean floor and a drop in eustatic sea-level (Miller et al., 2005; Eriksson and Condie, 2014). Mantle upwelling during the ~2.45 Ga rifting of Superior (Bleeker, 2003) and associated dynamic topography would likely have led to continental uplift and high freeboard (Gurnis, 1988).

The implication of our study is that the subaerial emergence of continents constitutes a potential driver for ecological changes that fuelled oxygenic photosynthesis, ultimately leading to a change in redox state of the Earth's atmosphere and oceans.

4.5 References

- Baertschi, P., 1976, Absolute 18O content of standard mean ocean water: Earth and Planetary Science Letters, v. 31, p. 341–344, doi:10.1016/0012-821X(76)90115-1.
- Bekker, A., Barley, M.E., Fiorentini, M.L., Rouxel, O.J., Rumble, D., and Beresford, S.W., 2009, Atmospheric Sulfur in Archean Komatiïte-Hosted Nickel Deposits: Science, v. 326, p. 1086–1089, doi:10.1126/science.1177742.
- Bekker, A., and Holland, H.D., 2012, Oxygen overshoot and recovery during the early Paleoproterozoic: Earth and Planetary Science Letters, v. 317–318, p. 295–304, doi:10.1016/j.epsl.2011.12.012.

- Bindeman, I.N., Zakharov, D.O., Palandri, J., Greber, N.D., Dauphas, N., Retallack, G.J., Hofmann, A., Lackey, J.S., Bekker, A., and Data, E., 2018, Rapid emergence of subaerial landmasses and onset of a modern hydrologic cycle 2.5 billion years ago: *Nature*, v. 557, p. 545–548, doi:<https://doi.org/10.1038/s41586-018-0131-1>.
- Black, L.P. et al., 2004, Improved $^{206}\text{Pb}/^{238}\text{U}$ microprobe geochronology by the monitoring of a trace-element-related matrix effect; SHRIMP, ID-TIMS, ELA-ICP-MS and oxygen isotope documentation for a series of zircon standards: *Chemical Geology*, v. 205, p. 115–140, doi:[10.1016/j.chemgeo.2004.01.003](https://doi.org/10.1016/j.chemgeo.2004.01.003).
- Bleeker, W., 2003, The late Archean record: A puzzle in ca. 35 pieces: *Lithos*, v. 71, p. 99–134, doi:[10.1016/j.lithos.2003.07.003](https://doi.org/10.1016/j.lithos.2003.07.003).
- Breaks, F.W., Selway, J.B., and Tindle, A.G., 2005, Fertile Peraluminous Granites and Related Rare-Element Pegmatites, Superior Province of Ontario, in *Short Course Notes, Geological Association of Canada 17*, p. 87–125.
- Bucholz, C.E., Biasi, J.A., Beaudry, B.P., and Ono, S., 2020, Sulfur isotope behavior during metamorphism and anatexis of Archean sedimentary rocks: a case study from the Ghost Lake batholith, Ontario, Canada: *Earth and Planetary Science Letters*,
- Bucholz, C.E., and Spencer, C.J., 2019, Strongly peraluminous granites across the Archean-Proterozoic transition: *Journal of Petrology*, doi:[10.1093/petrology/egz033](https://doi.org/10.1093/petrology/egz033).
- Bucholz, C.E., Stolper, E.M., Eiler, J.M., and Breaks, F.W., 2018, A Comparison of Oxygen Fugacities of Strongly Peraluminous Granites across the Archean–Proterozoic Boundary: *Journal of Petrology*, v. 59, p. 2123–2156, doi:[10.1093/petrology/egy091](https://doi.org/10.1093/petrology/egy091).
- Campbell, I.H., and Allen, C.M., 2008, Formation of supercontinents linked to increases in atmospheric oxygen: *Nature Geoscience*, v. 1, p. 554–558, doi:[10.1038/ngeo259](https://doi.org/10.1038/ngeo259).
- Catling, D.C., Glein, C.R., Zahnle, K.J., and McKay, C.P., 2005, Why O₂ Is Required by Complex Life on Habitable Planets and the Concept of Planetary “Oxygenation Time”: *Astrobiology*, v. 5, p. 415–438, doi:[10.1089/ast.2005.5.415](https://doi.org/10.1089/ast.2005.5.415).
- Chappell, B.W., and White, A.J.R., 1992, I- and S-type granites in the Lachlan Fold Belt: *Earth and Environmental Science Transactions of the Royal Society of Edinburgh*, v. 83, p. 1–26, doi:[10.1017/S0263593300007720](https://doi.org/10.1017/S0263593300007720).
- Chen, X. et al., 2015, Rise to modern levels of ocean oxygenation coincided with the Cambrian radiation of animals: *Nature Communications*, v. 6, p. 7142, doi:[10.1038/ncomms8142](https://doi.org/10.1038/ncomms8142).
- Claesson, S., Bibikova, E., Bogdanova, S., and Skobelev, V., 2006, Archaean terranes, Palaeoproterozoic reworking and accretion in the Ukrainian Shield, East European Craton: *Geological Society, London, Memoirs*, v. 32, p. 645–654, doi:[10.1144/GSL.MEM.2006.32.01.38](https://doi.org/10.1144/GSL.MEM.2006.32.01.38).
- Claoue-Long, J.C., Compston, W., Roberts, J., and Fanning, C.M., 1995, Two Carboniferous

- ages: a comparison of SHRIMP zircon dating with conventional zircon ages and $^{40}\text{Ar}/^{39}\text{Ar}$ analysis, in Berggre, W.A., Kent, D. V, Aubrey, M.P., and Hardenbol, J. eds., Time Scales and Global Stratigraphic Correlation, Society for Sedimentary Geology, Special publication 54, p. 3–21.
- Condie, K.C., O'Neill, C., and Aster, R.C., 2009, Evidence and implications for a widespread magmatic shutdown for 250 My on Earth: Earth and Planetary Science Letters, v. 282, p. 294–298, doi:10.1016/j.epsl.2009.03.033.
- Corfu, F., Stott, G.M., and Breaks, F.W., 1995, U-Pb geochronology and evolution of the English River Subprovince, an Archean low P-high T metasedimentary belt in the Superior Province: Tectonics, v. 14, p. 1220–1233, doi:10.1029/95TC01452.
- Cox, G.M., Lyons, T.W., Mitchell, R.N., Hasterok, D., and Gard, M., 2018, Linking the rise of atmospheric oxygen to growth in the continental phosphorus inventory: Earth and Planetary Science Letters, v. 489, p. 28–36, doi:<https://doi.org/10.1016/j.epsl.2018.02.016>.
- Crowe, D.E., and Vaughan, R.G., 1996, Characterization and use of isotopically homogeneous standards for in situ laser microprobe analysis of $^{34}\text{S}/^{32}\text{S}$ ratios: American Mineralogist, v. 81, p. 187–193, doi:10.2138/am-1996-1-223.
- Dan, W., Li, X.-H., Wang, Q., Wang, X.-C., Liu, Y., and Wyman, D.A., 2014, Paleoproterozoic S-type granites in the Helanshan Complex, Khondalite Belt, North China Craton: Implications for rapid sediment recycling during slab break-off: Precambrian Research, v. 254, p. 59–72, doi:10.1016/j.precamres.2014.07.024.
- Ding, T., Valkiers, S., Kipphardt, H., De Bièvre, P., Taylor, P.D.P., Gonfiantini, R., and Krouse, R., 2001, Calibrated sulfur isotope abundance ratios of three IAEA sulfur isotope reference materials and V-CDT with a reassessment of the atomic weight of sulfur: Geochimica et Cosmochimica Acta, v. 65, p. 2433–2437, doi:10.1016/S0016-7037(01)00611-1.
- Ehlers, C., Lindroos, A., and Selonen, O., 1993, The late Svecofennian granite-migmatite zone of southern Finland-a belt of transpressive deformation and granite emplacement: Precambrian Research, v. 64, p. 295–309, doi:10.1016/0301-9268(93)90083-E.
- Eriksson, P.G., and Condie, K.C., 2014, Cratonic sedimentation regimes in the ca. 2450–2000Ma period: Relationship to a possible widespread magmatic slowdown on Earth? Gondwana Research, v. 25, p. 30–47, doi:10.1016/j.gr.2012.08.005.
- Farquhar, Bao, and Thiemens, 2000, Atmospheric influence of Earth's earliest sulfur cycle: Science (New York, NY), v. 289, p. 756–759, http://www.ncbi.nlm.nih.gov/entrez/query.fcgi?db=pubmed&cmd=Retrieve&am p;dopt=AbstractPlus&list_uids=10926533.
- Farquhar, J., Wing, B.A., McKeegan, K.D., Harris, J.W., Cartigny, P., and Thiemens, M.H.,

- 2002, Mass-Independent Sulfur of Inclusions in Diamond and Sulfur Recycling on Early Earth: *Science*, v. 298, p. 2369–2372, doi:10.1126/science.1078617.
- Flament, N., Coltice, N., and Rey, P.F., 2013, The evolution of the $^{87}\text{Sr}/^{86}\text{Sr}$ of marine carbonates does not constrain continental growth: *Precambrian Research*, v. 229, p. 177–188, doi:10.1016/j.precamres.2011.10.009.
- Frost, B.R., and Frost, C.D., 2008, A Geochemical Classification for Feldspathic Igneous Rocks: *Journal of Petrology*, v. 49, p. 1955–1969, doi:10.1093/petrology/egn054.
- Gumsley, A.P., Chamberlain, K.R., Bleeker, W., Söderlund, U., de Kock, M.O., Larsson, E.R., and Bekker, A., 2017, Timing and tempo of the Great Oxidation Event: *Proceedings of the National Academy of Sciences*, v. 114, p. 1811–1816, doi:10.1073/pnas.1608824114.
- Guo, Q. et al., 2009, Reconstructing Earth's surface oxidation across the Archean-Proterozoic transition: *Geology*, v. 37, p. 399–402, doi:10.1130/G25423A.1.
- Gurnis, M., 1988, Large-scale mantle convection and the aggregation and dispersal of supercontinents: *Nature*, v. 332, p. 695–699.
- Hao, J., Knoll, A.H., Huang, F., Hazen, R.M., and Daniel, I., 2020, Cycling phosphorus on the Archean Earth: Part I. Continental weathering and riverine transport of phosphorus: *Geochimica et Cosmochimica Acta*, v. 273, p. 70–84, doi:10.1016/j.gca.2020.01.027.
- Harada, M., Tajika, E., and Sekine, Y., 2015, Transition to an oxygen-rich atmosphere with an extensive overshoot triggered by the Paleoproterozoic snowball Earth: *Earth and Planetary Science Letters*, v. 419, p. 178–186, doi:10.1016/j.epsl.2015.03.005.
- Hoffman, P.F., 1988, United Plates of America, The Birth of a Craton: Early Proterozoic Assembly and Growth of Laurentia: *Annual Review of Earth and Planetary Sciences*, v. 16, p. 543–603, doi:10.1146/annurev.ea.16.050188.002551.
- Holland, H.D., 2002, Volcanic gases, black smokers, and the great oxidation event: *Geochimica et Cosmochimica Acta*, v. 66, p. 3811–3826, doi:10.1016/S0016-7037(02)00950-X.
- Hollis, J.A., Van Kranendonk, M.J., Cross, A.J., Kirkland, C.L., Armstrong, R.A., and Allen, C.M., 2014, Low $\delta^{18}\text{O}$ zircon grains in the Neoarchean Rum Jungle Complex, northern Australia: An indicator of emergent continental crust: *Lithosphere*, v. 6, p. 17–25, doi:10.1130/L296.1.
- Huhma, H., 1986, Sm-Nd, U-Pb, and Pb-Pb isotopic evidence for the origin of the early Proterozoic Svecokarelian cratons in Finland: *Geological Survey of Finland*, 48 p.
- Johnston, D.T., 2011, Multiple sulfur isotopes and the evolution of Earth's surface sulfur cycle: *Earth-Science Reviews*, v. 106, p. 161–183, doi:10.1016/j.earscirev.2011.02.003.
- Johnston, D.T., Farquhar, J., and Canfield, D.E., 2007, Sulfur isotope insights into microbial sulfate reduction: When microbes meet models: *Geochimica et Cosmochimica Acta*, v.

- 71, p. 3929–3947, doi:10.1016/j.gca.2007.05.008.
- Jones, C., Nomosatryo, S., Crowe, S.A., Bjerrum, C.J., and Canfield, D.E., 2015, Iron oxides, divalent cations, silica, and the early earth phosphorus crisis: *Geology*, v. 43, p. 135–138, doi:10.1130/G36044.1.
- Kaufman, A.J., Johnston, D.T., Farquhar, J., Masterson, A.L., Lyons, T.W., Bates, S., Anbar, A.D., Arnold, G.L., Garvin, J., and Buick, R., 2007, Late Archean Biospheric Oxygenation and Atmospheric Evolution: *Science*, v. 317, p. 1900–1903, doi:10.1126/science.1138700.
- Kirschvink, J.L., and Kopp, R.E., 2008, Palaeoproterozoic ice houses and the evolution of oxygen-mediating enzymes: the case for a late origin of photosystem II: *Philosophical Transactions of the Royal Society B: Biological Sciences*, v. 363, p. 2755–2765, doi:10.1098/rstb.2008.0024.
- Kump, L.R., 2008, The rise of atmospheric oxygen: *Nature*, v. 451, p. 277–278, doi:10.1038/nature06587.
- Kump, L.R., and Barley, M.E., 2007, Increased subaerial volcanism and the rise of atmospheric oxygen 2.5 billion years ago: *Nature*, v. 448, p. 1033–1036, doi:10.1038/nature06058.
- LaFlamme, C. et al., 2016, In situ multiple sulfur isotope analysis by SIMS of pyrite, chalcopyrite, pyrrhotite, and pentlandite to refine magmatic ore genetic models: *Chemical Geology*, v. 444, p. 1–15, doi:10.1016/j.chemgeo.2016.09.032.
- LaFlamme, C., Jamieson, J.W., Fiorentini, M.L., Thébaud, N., Caruso, S., and Selvaraja, V., 2018, Investigating sulfur pathways through the lithosphere by tracing mass independent fractionation of sulfur to the Lady Bountiful orogenic gold deposit, Yilgarn Craton: *Gondwana Research*, v. 58, p. 27–38, doi:10.1016/j.gr.2018.02.005.
- Li, X.-H. et al., 2010, Penglai Zircon Megacrysts: A Potential New Working Reference Material for Microbeam Determination of Hf-O Isotopes and U-Pb Age: *Geostandards and Geoanalytical Research*, v. 34, p. 117–134, doi:10.1111/j.1751-908X.2010.00036.x.
- Liebmann, J., Spencer, C.J., Kirkland, C.L., Bucholz, C.E., He, X., Santosh, M., Xia, X.-P., Martin, L., and Evans, N.J., 2020, Emergence of continents above sea-level influences composition of sediment melts: submitted to EPSL.,
- Lompo, M., 2009, Geodynamic evolution of the 2.25–2.0 Ga Palaeoproterozoic magmatic rocks in the Man-Leo Shield of the West African Craton. A model of subsidence of an oceanic plateau: *Geological Society, London, Special Publications*, v. 323, p. 231–254, doi:10.1144/SP323.11.
- Luo, G., Ono, S., Beukes, N.J., Wang, D.T., Xie, S., and Summons, R.E., 2016, Rapid oxygenation of Earth's atmosphere 2.33 billion years ago: *Science Advances*, v. 2, doi:10.1126/sciadv.1600134.
- Lyons, J.R., 2007, Mass-independent fractionation of sulfur isotopes by isotope-selective

photodissociation of SO₂: Geophysical Research Letters, v. 34, p. 1–5, doi:10.1029/2007GL031031.

Mikkola, P., Huhma, H., Heilimo, E., and Whitehouse, M., 2011, Archean crustal evolution of the Suomussalmi district as part of the Kianta Complex, Karelia: Constraints from geochemistry and isotopes of granitoids: Lithos, v. 125, p. 287–307, doi:10.1016/j.lithos.2011.02.012.

Miller, K.G., Kominz, M.A., Browning, J. V., Wright, J.D., Mountain, G.S., Katz, M.E., Sugarman, P.J., Cramer, B.S., Christie-Blick, N., and Pekar, S.F., 2005, The Phanerozoic Record of Global Sea-Level Change: Science, v. 310, p. 1293–1298, doi:10.1126/science.1116412.

Page, F.Z., Fu, B., Kita, N.T., Fournelle, J., Spicuzza, M.J., Schulze, D.J., Viljoen, F., Basei, M.A.S., and Valley, J.W., 2007, Zircons from kimberlite: New insights from oxygen isotopes , trace elements , and Ti in zircon thermometry: Geochimica et Cosmochimica Acta, v. 71, p. 3887–3903, doi:10.1016/j.gca.2007.04.031.

Paris, G., Adkins, J.F., Sessions, A.L., Webb, S.M., and Fischer, W.W., 2014, Neoarchean carbonate-associated sulfate records positive 33S anomalies: Science, v. 346, p. 739–741, doi:10.1126/science.1258211.

Parra-Avila, L.A., Baratoux, L., Eglinger, A., Fiorentini, M.L., and Block, S., 2019, The Eburnean magmatic evolution across the Baoulé-Mossi domain: Geodynamic implications for the West African Craton: Precambrian Research, v. 332, p. 105392, doi:10.1016/j.precamres.2019.105392.

Paton, C., Hellstrom, J., Paul, B., Woodhead, J., and Hergt, J., 2011, Iolite: Freeware for the visualisation and processing of mass spectrometric data: Journal of Analytical Atomic Spectrometry, v. 26, p. 2508, doi:10.1039/c1ja10172b.

Pavlov, A.A., and Kasting, J.F., 2002, Mass-Independent Fractionation of Sulfur-Isotopes in Archean Sediments: Strong Evidence for an Anoxic Archean Atmosphere: Astrobiology, v. 2.

Percival, J.A., 1989, A regional perspective of the Quetico metasedimentary belt, Superior Province, Canada: Canadian Journal of Earth Sciences, v. 26, p. 677–693, doi:10.1139/e89-058.

Percival, J.A., Sanborn-Barrie, M., Skulski, T., Stott, G.M., Helmstaedt, H., and White, D.J., 2006, Tectonic evolution of the western Superior Province from NATMAP and Lithoprobe studies: Canadian Journal of Earth Sciences, v. 43, p. 1085–1117, doi:10.1139/e06-062.

Pidgeon, R.T., Nemchin, A.A., and Whitehouse, M.J., 2017, The effect of weathering on U-Th-Pb and oxygen isotope systems of ancient zircons from the Jack Hills, Western Australia: Geochimica et Cosmochimica Acta, v. 197, p. 142–166, doi:10.1007/s11947-009-0181-3.

- Pufahl, P.K., and Hiatt, E.E., 2012, Oxygenation of the Earth's atmosphere–ocean system: A review of physical and chemical sedimentologic responses: *Marine and Petroleum Geology*, v. 32, p. 1–20, doi:10.1016/j.marpetgeo.2011.12.002.
- Reed, J.C., Bickford, M.E., Premo, W.R., Aleinikoff, J.N., and Pallister, J.S., 1987, Evolution of the Early Proterozoic Colorado province: Constraints from U-Pb geochronology: *Geology*, v. 15, p. 861, doi:10.1130/0091-7613(1987)15<861:EOTEP>2.0.CO;2.
- Rosing, M.T., and Frei, R., 2004, U-rich Archaean sea-floor sediments from Greenland – indications of >3700 Ma oxygenic photosynthesis: *Earth and Planetary Science Letters*, v. 217, p. 237–244, doi:10.1016/S0012-821X(03)00609-5.
- Savin, S.M., and Epstein, S., 1970, The oxygen and hydrogen isotope geochemistry of clay minerals: *Geochimica et Cosmochimica Acta*, v. 34, p. 25–42, doi:10.1016/0016-7037(70)90149-3.
- Schmitt, A.K., Magee Jr., C.W., Williams, I.S., Holden, P., Ireland, T.R., DiBugnara, D.L., and Bodorkos, S., 2019, Oxygen isotopic heterogeneity in the Temora-2 reference zircon; doi:10.11636/Record.2019.004.
- Sharp, Z.D., 1990, A laser-based microanalytical method for the in situ determination of oxygen isotope ratios of silicates and oxides: *Geochimica et Cosmochimica Acta*, v. 54, p. 1353–1357, doi:10.1016/0016-7037(90)90160-M.
- Spencer, C.J., Cawood, P.A., Hawkesworth, C.J., Raub, T.D., Prave, A.R., and Roberts, N.M.W., 2014, Proterozoic onset of crustal reworking and collisional tectonics: Reappraisal of the zircon oxygen isotope record: *Geology*, v. 42, p. 451–454, doi:10.1130/G35363.1.
- Spencer, C.J., Murphy, J.B., Kirkland, C.L., Liu, Y., and Mitchell, R.N., 2018, Was the supercontinent cycle activated by a Palaeoproterozoic tectono-magmatic lull? *Nature Geoscience*, v. 11, p. 97–101, doi:10.1038/s41561-017-0051-y.
- Spencer, C.J., Partin, C.A., Kirkland, C.L., Raub, T.D., Liebmann, J., and Stern, R.A., 2019, Paleoproterozoic increase in zircon $\delta^{18}\text{O}$ driven by rapid emergence of continental crust: *Geochimica et Cosmochimica Acta*, v. 257, p. 16–25, doi:10.1016/j.gca.2019.04.016.
- Squire, R., Campbell, I., Allen, C., and Wilson, C., 2006, Did the Transgondwanan Supermountain trigger the explosive radiation of animals on Earth? *Earth and Planetary Science Letters*, v. 250, p. 116–133, doi:10.1016/j.epsl.2006.07.032.
- Stacey, J.S., and Kramers, J.D., 1975, Approximation of terrestrial lead isotope evolution by a two-stage model: *Earth and Planetary Science Letters*, v. 26, p. 207–221, doi:10.1016/0012-821X(75)90088-6.
- Steiger, R.H., and Jäger, E., 1977, Subcommission on geochronology: Convention on the use of decay constants in geo- and cosmochronology: *Earth and Planetary Science Letters*, v.

36, p. 359–362, doi:10.1016/0012-821X(77)90060-7.

Stern, R.A., Bodorkos, S., Kamo, S.L., Hickman, A.H., and Corfu, F., 2009, Measurement of SIMS Instrumental Mass Fractionation of Pb Isotopes During Zircon Dating: Geostandards and Geoanalytical Research, v. 33, p. 145–168, doi:10.1111/j.1751-908X.2009.00023.x.

Taylor, H.P., 1980, The effects of assimilation of country rocks by magmas on $^{18}\text{O}/^{16}\text{O}$ and $^{87}\text{Sr}/^{86}\text{Sr}$ systematics in igneous rocks: Earth and Planetary Science Letters, v. 47, p. 243–254, doi:10.1016/0012-821X(80)90040-0.

Väisänen, M., Mänttäri, I., Kriegsman, L.M., and Hölttä, P., 2000, Tectonic setting of post-collisional magmatism in the Palaeoproterozoic Svecfennian Orogen, SW Finland: Lithos, v. 54, p. 63–81, doi:10.1016/S0024-4937(00)00018-9.

Valley, J.W. et al., 2005, 4.4 billion years of crustal maturation: Oxygen isotope ratios of magmatic zircon: Contributions to Mineralogy and Petrology, v. 150, p. 561–580, doi:10.1007/s00410-005-0025-8.

Valley, J.W., Bindeman, I.N., and Peck, W.H., 2003, Empirical calibration of oxygen isotope fractionation in zircon: *Geochimica et Cosmochimica Acta*, v. 67, p. 3257–3266, doi:10.1016/S0016-7037(03)00090-5.

Valley, J.W., Chiarenzelli, J.R., and McLelland, J.M., 1994, Oxygen isotope geochemistry of zircon: Earth and Planetary Science Letters, v. 126, p. 187–206, doi:10.1016/0012-821X(94)90106-6.

Valley, J.W., Kitchen, N., Kohn, M.J., Niendorf, C.R., and Spicuzza, M.J., 1995, UWG-2, a garnet standard for oxygen isotope ratios: Strategies for high precision and accuracy with laser heating: *Geochimica et Cosmochimica Acta*, v. 59, p. 5223–5231, doi:10.1016/0016-7037(95)00386-X.

Vielzeuf, D., 2005, Oxygen isotope heterogeneities and diffusion profile in composite metamorphic-magmatic garnets from the Pyrenees: *American Mineralogist*, v. 90, p. 463–472, doi:10.2138/am.2005.1576.

Ward, L.M., Kirschvink, J.L., and Fischer, W.W., 2016, Timescales of Oxygenation Following the Evolution of Oxygenic Photosynthesis: Origins of Life and Evolution of Biospheres, v. 46, p. 51–65, doi:10.1007/s11084-015-9460-3.

Warke, M.R., Di Rocco, T., Zerkle, A.L., Lepland, A., Prave, A.R., Martin, A.P., Ueno, Y., Condon, D.J., and Claire, M.W., 2020, The Great Oxidation Event preceded a Paleoproterozoic “snowball Earth”: *Proceedings of the National Academy of Sciences*, p. 202003090, doi:10.1073/pnas.2003090117.

Whitehouse, M.J., 2013, Multiple Sulfur Isotope Determination by SIMS: Evaluation of Reference Sulfides for $\Delta 33\text{ S}$ with Observations and a Case Study on the Determination

- of Δ 36 S: Geostandards and Geoanalytical Research, v. 37, p. 19–33, doi:10.1111/j.1751-908X.2012.00188.x.
- Wiedenbeck, M. et al., 2004, Further characterisation of the 91500 zircon crystal: Geostandards and Geoanalytical Research, v. 28, p. 9–39, doi:10.1111/j.1751-908X.2004.tb01041.x.
- Wingate, M.T.D., and Kirkland, C.L., 2015, Introduction to geochronology information released in 2015: Geological Survey of Western Australia, p. 5p.

Yang, Q., Xia, X., Zhang, W., Zhang, Y., Xiong, B., Xu, Y., Wang, Q., and Wei, G., 2018, An evaluation of precision and accuracy of SIMS oxygen isotope analysis: Solid Earth Sciences, v. 3, p. 81–86, doi:10.1016/j.sesci.2018.05.001.

Zhao, G., Wilde, S.A., Cawood, P.A., and Lu, L., 1999, Tectonothermal history of the basement rocks in the western zone of the North China Craton and its tectonic implications: Tectonophysics, v. 310, p. 37–53.

Zhao, G., and Zhai, M., 2013, Lithotectonic elements of Precambrian basement in the North China Craton: Review and tectonic implications: Gondwana Research, v. 23, p. 1207–1240, doi:10.1016/j.gr.2012.08.016.

4.6 Author contributions

JL, CJS, CLK, CEB designed the research or contributed to designing the research. JL, CJS, CEB, LS collected the samples. JL, CLK, CEB, XPX, LM, NK carried out the analyses. JL, CJS, CLK, CEB contributed to interpreting the results. JL wrote the manuscript. All authors provided comments on the manuscript.

Appendices

- A:** Supplementary information on geochronology, supplementary Figures A1-A8, and supplementary Tables A1-A4.
- B:** Supplementary Table B1 and B2, zircon SIMS and LA-ICPMS U-Pb data.
- C:** Supplementary Table C1, pyrite SIMS S isotope data.
- D:** Supplementary Table D1 and D2, zircon and garnet SIMS and LF O isotope data.

Appendix A

A1 Zircon U-Pb geochronology

In the following the interpretation of zircon U-Pb geochronological data is described in detail. With the exception of sample 15K-2, U-Pb geochronological data was obtained by SIMS

analysis. For sample 15K-2 U-Pb ages were obtained by LA-ICP-MS analysis. U-Pb ages are reported with 2σ uncertainty unless stated otherwise. Single spot results are given in supplementary Table B1 and B2. Tera Wasserburg diagrams are shown in Figure A1.

A1.1 Sample 17FIN02

Sample 17FIN02 is a migmatite with medium-grained, garnet-bearing leucosome. Zircon isolated from the leucosome is subhedral, purple in color, and up to 250 μm long. CL images reveal complex or oscillatory zoning, in some grains overgrown by a up to 20 μm thick, homogenous to weakly zoned, low CL response rim. A total of six single spot analyses was on six zircon grains was obtained for sample 17IN02. One analysis was omitted due to high common Pb content. Four of the remaining five analyses are located on zircon rims. They are concordant to normally discordant (1 to 15% discordant) and define a discordia with an upper intercept age of 1896 ± 26 Ma ($n=4$, MSWD=0.23) which is interpreted as the magmatic crystallization age of the leucosome. One analysis on an older zircon growth zone yields a $^{207}\text{Pb}/^{206}\text{Pb}^*$ age of 2756 ± 24 Ma (1σ), and is interpreted to date an inherited component.

A1.2 Sample 17FIN03B

Sample 17FIN03B is a migmatite with medium-grained, garnet-bearing leucosome. Zircon isolated from the leucosome is subhedral, brown in color, and up to 200 μm long. CL images reveal low CL response zircon cores overgrown by higher CL response rims with no to weak indication of oscillatory growth pattern. A total of eight single spot analyses on rims of eight zircon grains was obtained for sample 17FIN03B. Two analyses were omitted due to high common lead content ($n=2$) or due the spot being located on a crack in the zircon grain ($n=1$). The remaining five analyses are concordant ($\leq 3\%$ discordant). They yield a weighted mean $^{207}\text{Pb}/^{206}\text{Pb}^*$ age of 1824 ± 13 Ma ($n=5$, MSWD=0.67), which is interpreted as the magmatic crystallization age of the leucosome.

A1.3 Sample 17FIN05B

Sample 17FIN05B is a migmatite with coarse-grained, garnet-bearing leucosome. Zircon isolated from the leucosome is subhedral, brown in color, and up to 300 μm long. CL images reveal complex or blurred zircon growth patterns overgrown by homogenous to weakly zoned,

up to 40 μm thick, low CL response rims. In some cases the growth pattern of the core is truncated by the rims implying that the cores underwent physical abrasion before rim overgrowth. A total of eight single spot analyses on rims of eight zircon grains was obtained for sample 17FIN05B. Two analyses were omitted due to high common Pb content. All of the remaining six analyses are concordant (<9% discordant) and yield a weighted mean $^{207}\text{Pb}/^{206}\text{Pb}^*$ age of 1837 ± 9 Ma ($n=6$, MSWD=0.75) which is interpreted as the magmatic crystallization age of the leucosome.

A1.4 Sample 17FIN06

Sample 17FIN06 is a migmatite with medium-grained, garnet-bearing leucosome. Zircon isolated from the leucosome is subhedral, brown in color, and up to 500 μm long. CL images reveal two types of cores: type I with oscillatory zoning, and type II with low CL response, and homogenous. Zircon cores are overgrown by homogenous to weakly zoned, up to 30 μm thick rims. A total of eight single spot analyses on rims of eight zircon grains was obtained for sample 17FIN06. All of the analyses are concordant (<7% discordant) and yield a concordia age of 1815 ± 16 Ma ($n=8$, MSWD (of concordance and equivalence)=1.8) which is interpreted as the magmatic crystallization age of the leucosome.

A1.5 Sample 19GH9

Sample 19GH9 is a biotite-muscovite granite. Zircon isolated from this sample is euhedral, colorless, and up to 300 μm long. CL images reveal ubiquitous oscillatory zoning. A total of seven single spot analyses on five zircon grains was obtained for sample 19GH9. One analysis was omitted due to high common Pb content. The remaining analyses are concordant to normally discordant. Analyses that are <9% discordant yield a weighted mean $^{207}\text{Pb}/^{206}\text{Pb}^*$ age of 2183 ± 14 Ma ($n=5$, MSWD=0.2) which is interpreted as the magmatic crystallization age of the granite. One normally discordant analysis (12% discordant) is interpreted to reflect recent Pb loss and was omitted from the calculation of the crystallization age.

A1.6 Sample 19GH11B

Sample 19GH11B is a biotite-muscovite granite. Zircon isolated from this sample is euhedral, colorless, and up to 400 μm long. CL images reveal ubiquitous oscillatory zoning. A total of

seven single spot analyses on three zircon grains was obtained for sample 19GH11B. One analyses overlaps with a crack in the zircon grain and was therefore omitted. The remaining six analyses are concordant to normally discordant and define a discordia with an upper intercept age of 2188 ± 20 Ma ($n=6$, MSWD=1.5) which is interpreted as the magmatic crystallization age of the granite.

A1.7 Sample CO-17-8

Sample CO-17-8 is a biotite-muscovite granite. Zircon isolated from this sample is euhedral, colorless, and up to 250 μm long. CL images reveal ubiquitous oscillatory zoning. A total of six single spot analyses on rims of six zircon grains was obtained for sample CO-17-8. They are concordant to normally or reversely discordant. The four most concordant analyses ($\leq 11\%$ discordant) yield a weighted mean $^{207}\text{Pb}/^{206}\text{Pb}^*$ age of 1447 ± 50 Ma ($n=4$, MSWD=2.0) which is interpreted as the magmatic crystallization age of the granite. The remaining two discordant analyses are interpreted to reflect recent Pb loss. However, they do not define a meaningful discordia together with the other data (MSWD > 3) and are therefore not considered for the calculation of the crystallization age.

A1.8 Sample SP-16-2b

Sample SP-16-2b is a biotite-muscovite granite. Zircon isolated from this sample is subhedral to anhedral, brown in color, and up to 70 μm long. CL images reveal oscillatory zoning. A total of four single spot analyses on four zircon grains was obtained for sample SP-16-2b. One analysis was omitted due to a high common Pb content. The remaining three analyses are concordant to normally discordant and define a discordia with an upper intercept age of 2664 ± 45 Ma ($n=3$, MSWD=0.21) which is interpreted as the magmatic crystallization age of the granite.

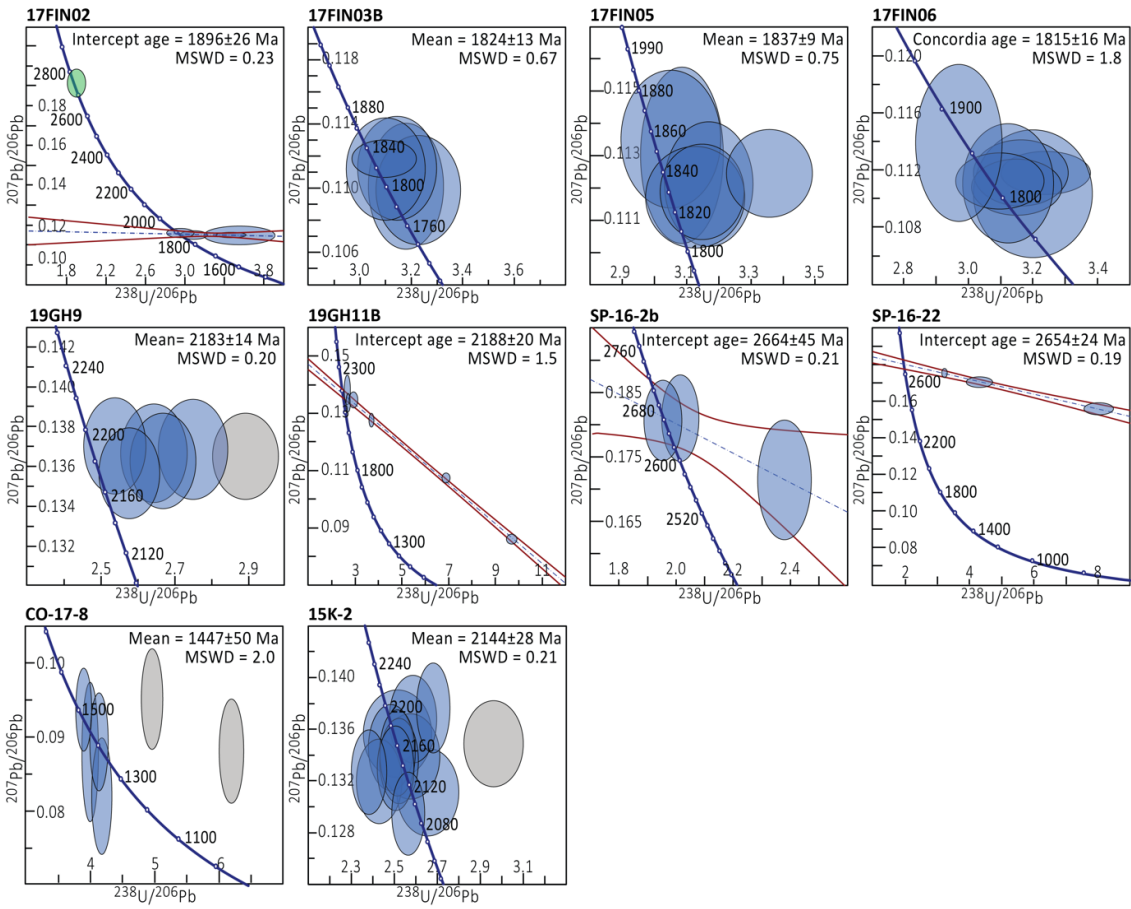
A1.9 Samples SP-16-22, SP-16-20a, and SP-16-34

Sample SP-16-22 is a biotite-muscovite granite. Zircon isolated from this sample is euhedral to subhedral, brown in color, and up to 200 μm long. CL images reveal ubiquitous oscillatory zoning. A total of four single spot analyses on three zircon grains was obtained for sample SP-16-22. One analysis was omitted due to a high common Pb content. The remaining three

analyses are normally discordant and define a discordia with an upper intercept age of 2654 ± 24 Ma ($n=3$, MSWD=0.19) which is interpreted as the magmatic crystallization age of the granite. Samples SP-16-20a, and SP-16-34 were collected from the same batholith as sample SP-16-22. Therefore all three samples likely have the same crystallization age of 2654 ± 24 Ma.

A1.10 Sample 15K-2

Sample 15K-2 is a biotite granite. Zircon isolated from this sample is subhedral, colorless, and up to $300 \mu\text{m}$ long. CL images reveal complex or blurred growth patterns in zircon cores and homogenous to oscillatory zoned rims. A total of 13 single spot analyses on 13 zircon grains was obtained for sample 15K-2. The analyses are concordant to normally or reversely discordant. Analyses that are less than 10% discordant yield a weighted mean $^{207}\text{Pb}/^{206}\text{Pb}$ age of 2144 ± 28 Ma ($n=12$, MSWD=0.21), which is interpreted as the magmatic crystallization age of the granite. One normally discordant analysis (13% discordant) is interpreted to reflect recent Pb loss and was omitted from the calculation of the crystallization age.



Supplementary Figure A1. Tera-Wasserburg diagrams. Data point error ellipses are shown at 2σ level.

Mean ages are weighted mean $^{207}\text{Pb}/^{206}\text{Pb}^*$ ages. MSWD of concordia age is that of concordance and equivalence. Single spot analyses interpreted as dating magmatic components are shown as blue ellipses, those dating inherited components are shown as green ellipses. Single spot analyses shown as grey ellipses were omitted from the calculation of the crystallization age (see supplementary section A1 for details).

A2 Geochronology of samples without zircon U-Pb data

A2.1 Samples 17FIN01, and 17FIN04A

Samples 17FIN01, and 17FIN04A are migmatites with medium-grained, garnet-bearing leucosome from the Turku area, Finland. In this area the crust was intruded by sediment-derived granites at ~ 1.85 Ga associated with high-temperature, low-pressure granulite facies metamorphism and migmatization (Huhma, 1986). We cite the age of 1850 Ma as the best estimate of the crystallization age of samples 17FIN01, and 17FIN04A. This is in accord with

the ages obtained for four other samples from this area, ranging from 1815 ± 16 Ma to 1896 ± 26 Ma (see supplementary section A.1 for details).

A2.2 Sample 19GH3

Samples 19GH3, 19GH9, and 19GH11B are granites from felsic intrusions in the Baoulé-Mossi domain, West African Craton. The emplacement of felsic intrusions across the Baoulé-Mossi domain is associated with the 2.2-1.8 Eburnean Orogeny (Lombo, 2009). Parra-Avila et al. (2017) suggested that the ~2.3-2.0 Ga felsic magmatism in the Baoulé-Mossi domain migrated westward at a rate of 35 km/Myr. Sample 19GH3 was collected ~30 km southeast of sample 19GH9, and ~ 50 km east of sample 19GH11B. Given the close proximity of these samples, we cite the ages of ~2.18 Ga obtained for samples 19GH9, and 19GH11B (see supplementary section A.1 for details) as the best estimate of the crystallization age of sample 19GH3.

A2.3 Sample SP-17-43

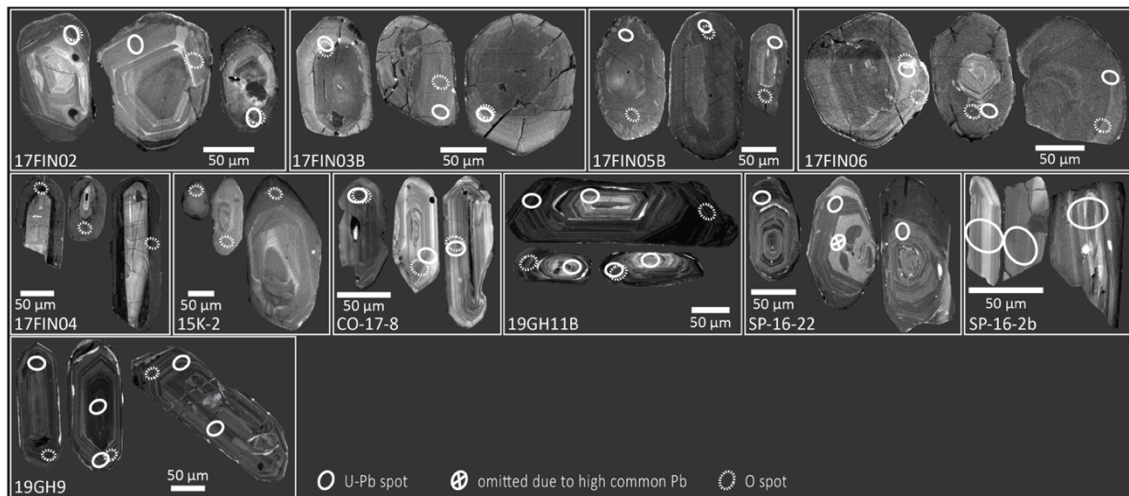
Sample SP-17-43 is a garnet-biotite-muscovite granite from the Wenasaga Lake batholith, Superior province. The Wenasaga Lake batholith belongs to a suite of strongly peraluminous granite plutons that intruded the metasedimentary English River Subprovince at ~2.7 Ga (Nitescu et al., 2006). These granite plutons are interpreted to be the result of the peak episode of a metamorphic event at 2691 Ma that resulted in migmatization and anatexis of the sediments from the English River Subprovince (Corfu et al., 1995). We cite the age of peak metamorphism at ~2.69 Ga (Corfu et al., 1995) as the best estimate for the crystallization age of sample SP-17-43.

A2.4 Sample SP-17-13

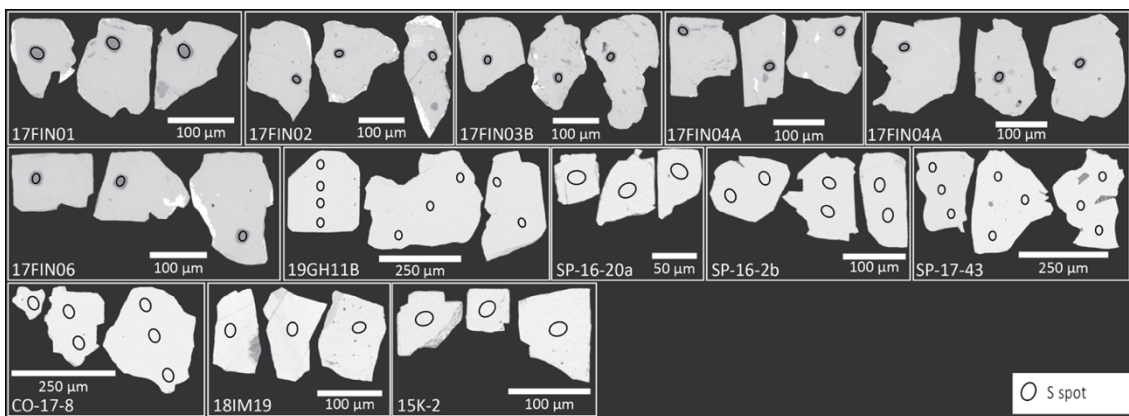
Sample SP-17-13 is a garnet-biotite granite from the Quetico belt, Superior province. From 2671 to 2652 Ma a major phase of felsic plutonism occurred in the metasedimentary Quetico belt (Percival, 1989). We therefore cite the age of 2660 ± 10 Ma as the best estimate of the crystallization age of sample SP-17-13.

A.2.5 Samples SP-17-33, SP-17-38, SP-17-82, SP-17-71, and SP-17-50

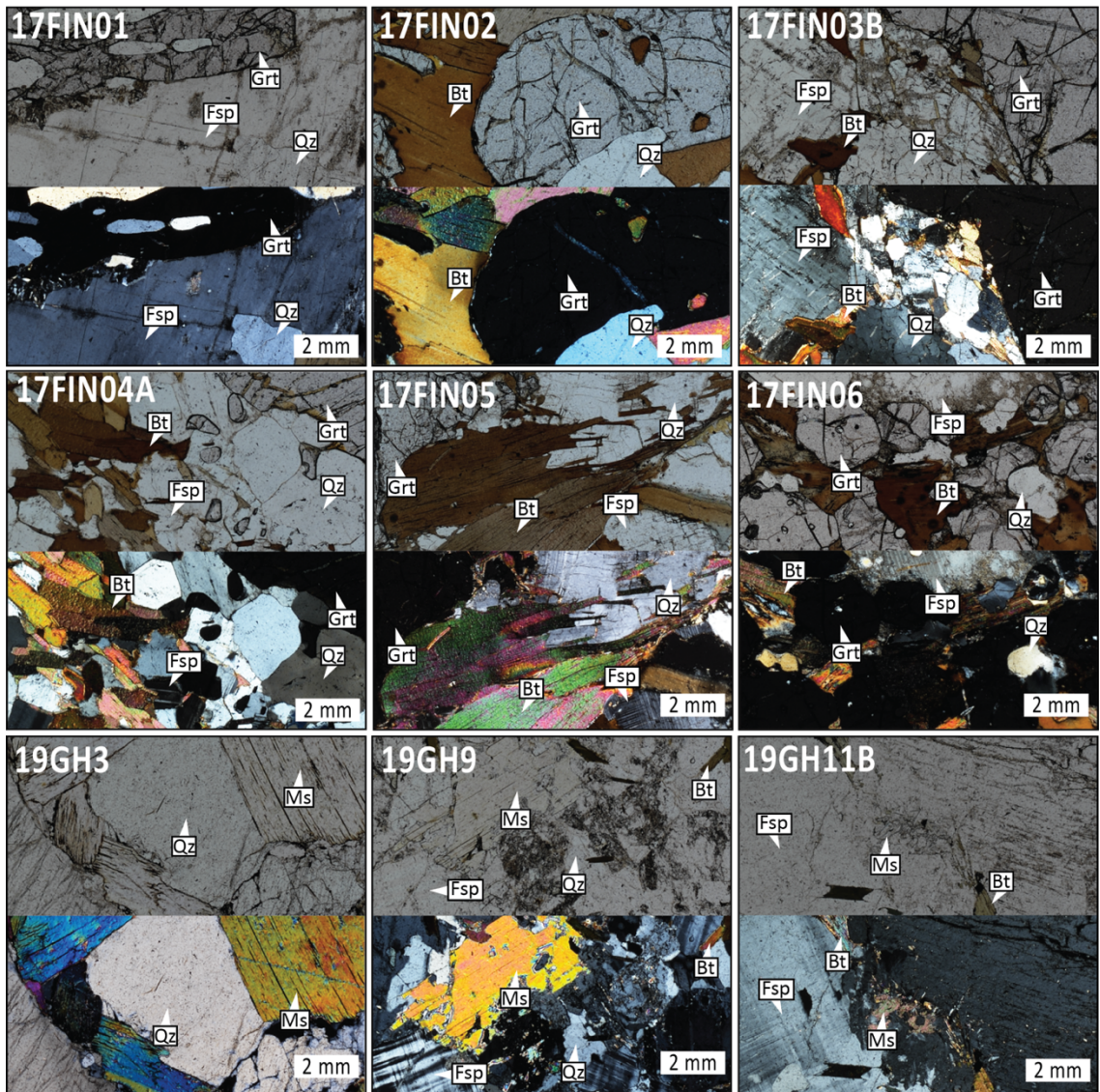
Samples SP-17-33, SP-17-38, SP-17-82, SP-17-71, and SP-17-50 are from various sediment-derived intrusions (Medicine Lake batholith, Treelined Lake Complex, Allison Lake batholith, and Sharpe Lake batholith) in the Superior Province. Neoarchean sediment-derived granites are common in the Superior Province (Breaks et al., 2005). Their emplacement has been linked to the collision of Archean tectonic blocks between \sim 2.7 and 2.6 Ga (Percival et al., 2006; Yang et al., 2019). We therefore cite \sim 2.65 Ga as the best estimate of the crystallization ages of samples SP-17-33, SP-17-38, SP-17-82, SP-17-71, and SP-17-50.



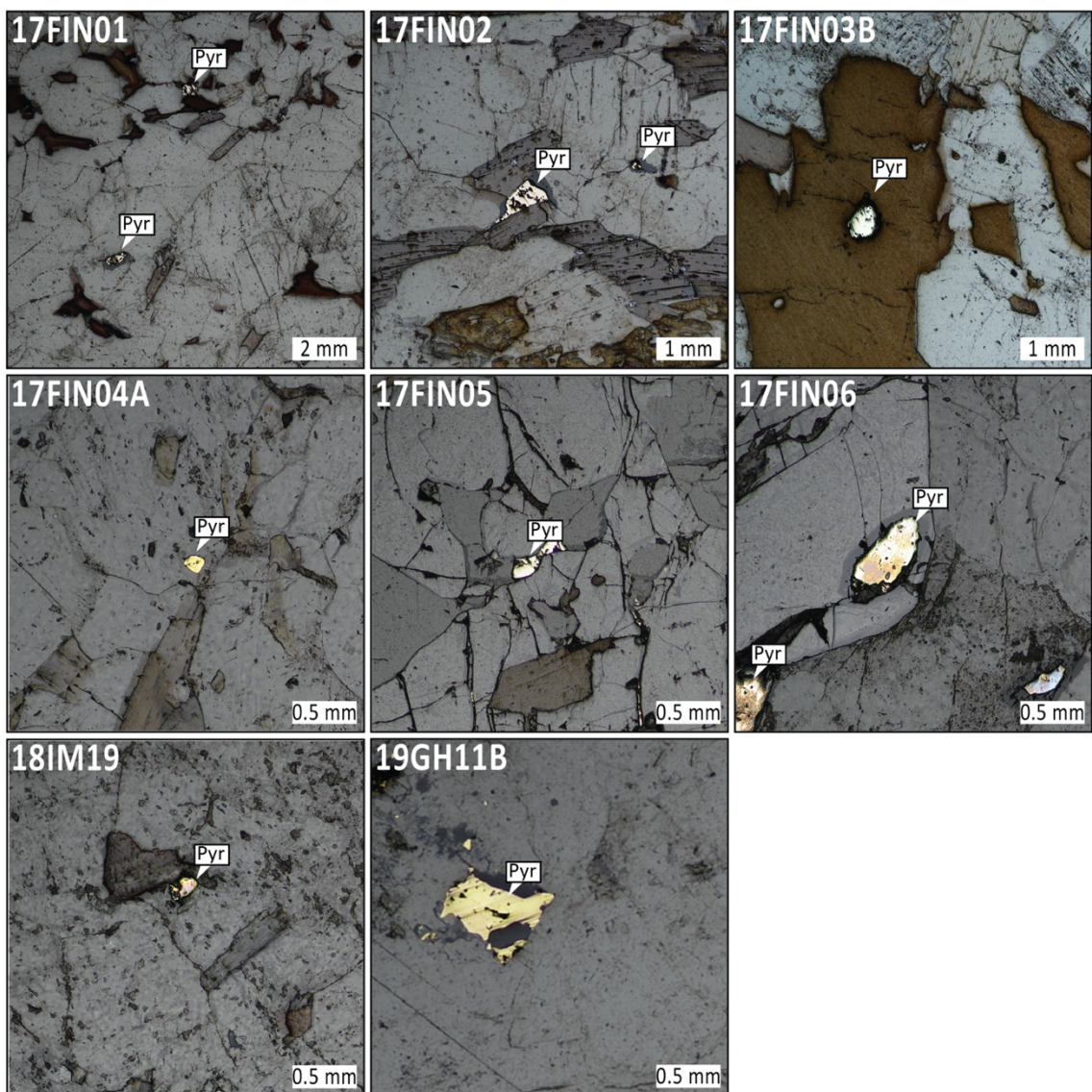
Supplementary Figure A2. Cathodoluminescence images of representative zircon grains with O and U-Pb spots marked.



Supplementary Figure A3. Back scatter electron images of representative pyrite grains with S spots marked.



Supplementary Figure A4. Thin section photomicrographs. Mineral abbreviations: Qz, quartz; Fsp, feldspar; Grt, garnet; Ms, muscovite; Bt, biotite.



Supplementary Figure A5. Reflected light photomicrographs showing the occurrence of pyrite (Pyr) in thin section.

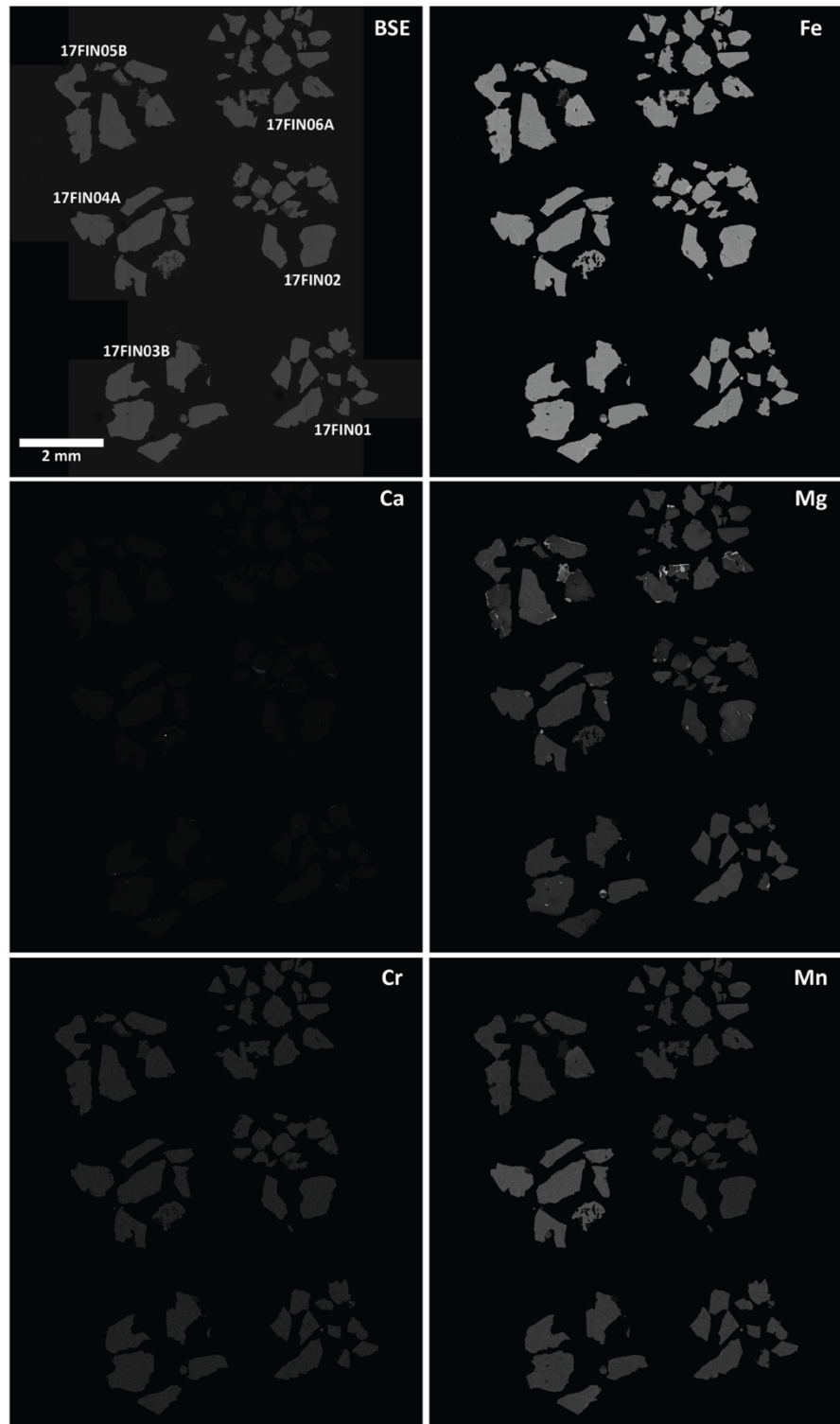


Figure A6. Backscatter electron image and element maps of garnet in samples from the Baltic Shield, East European Craton. Garnet grains are Fe-rich, but Ca-poor indicating almandine rich garnet.

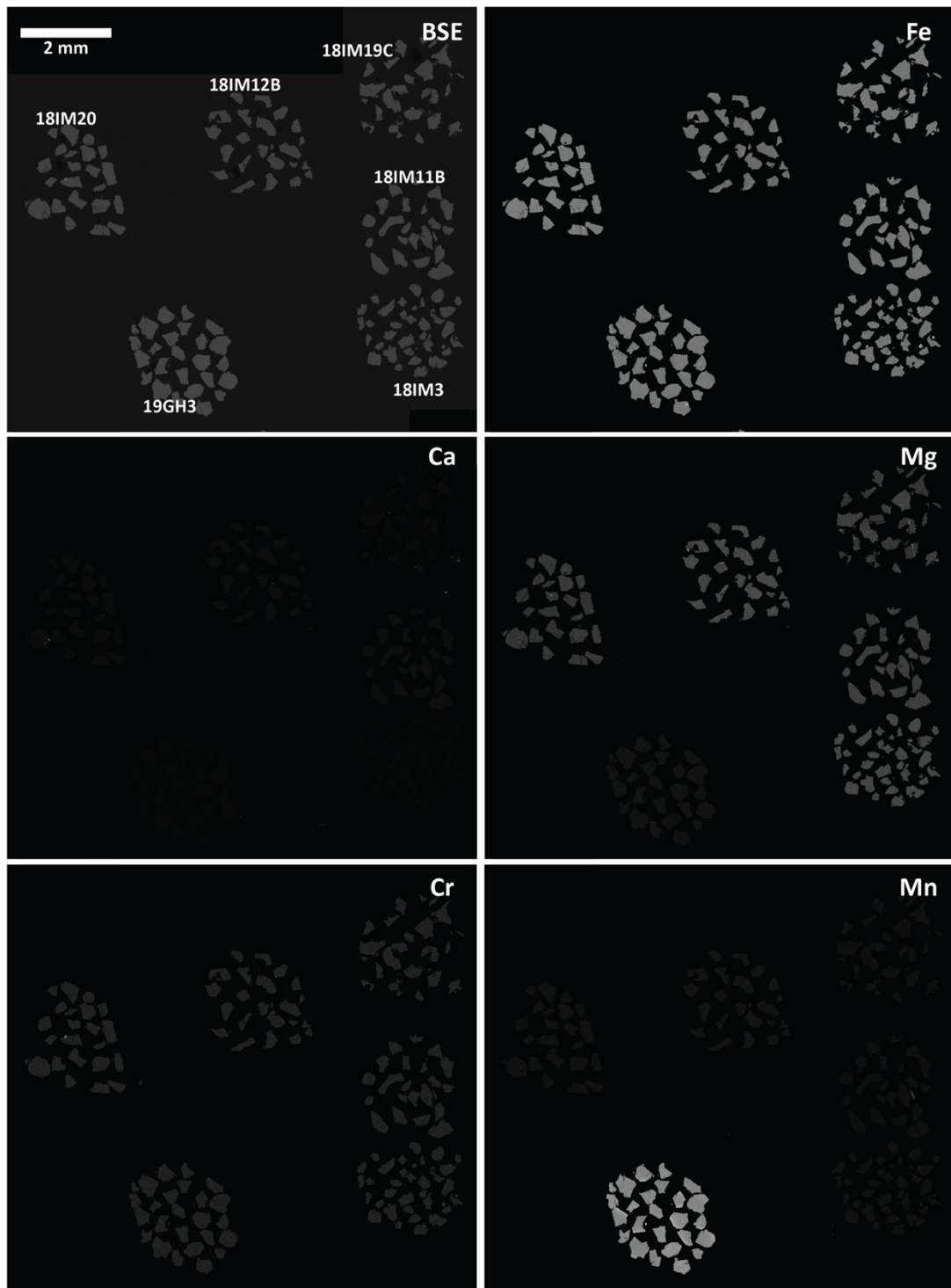
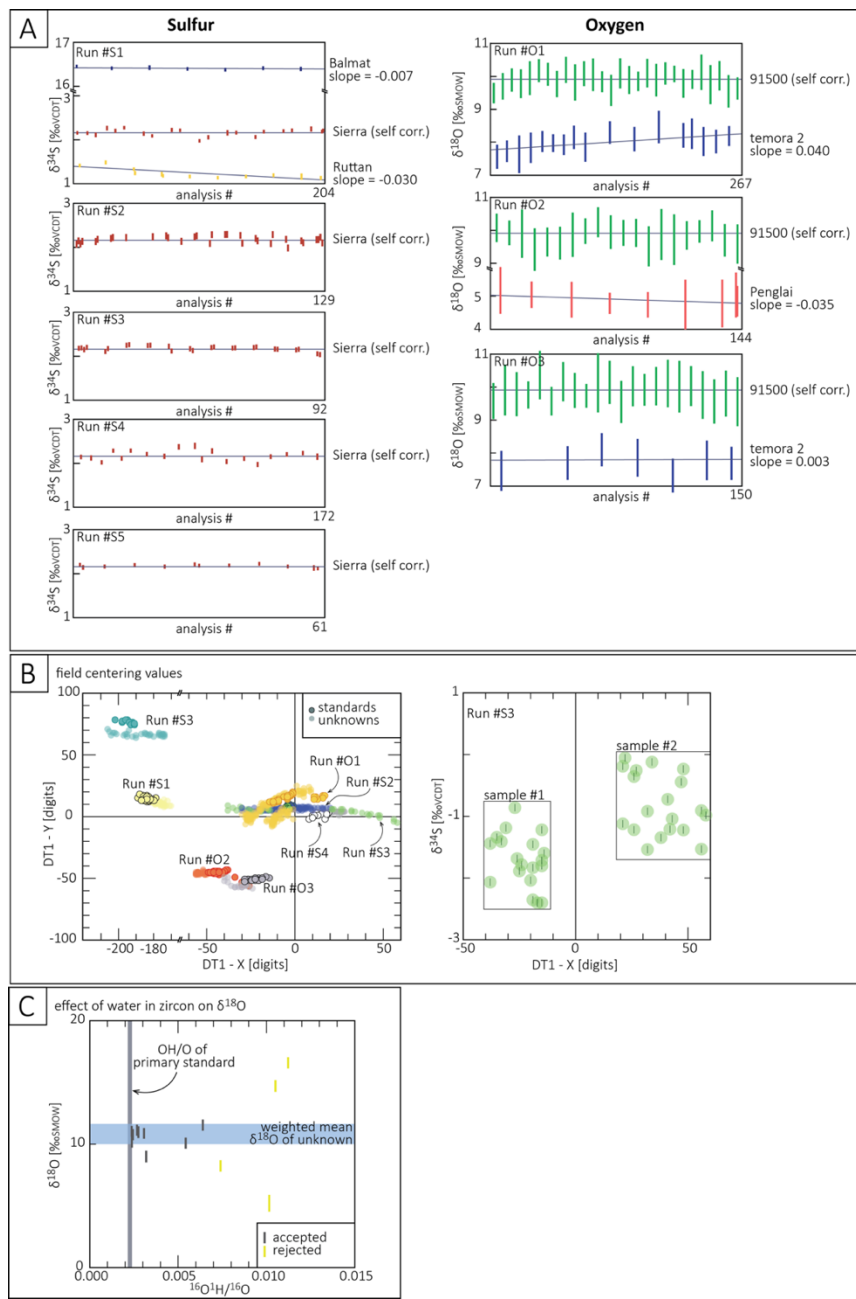


Figure A7. Backscatter electron image and element maps of garnet in samples from the North China and West African Cratons. Garnet grains are Fe-rich, but Ca-poor indicating almandine rich garnet.



Supplementary Figure A8. Sulfur and oxygen isotope data of standards and unknowns. **(A)** Corrected $\delta^{34}\text{S}$ and $\delta^{18}\text{O}$, respectively of standards over time show no significant drift. **(B)** Field centering values for standards and unknowns for each analytical run. Field centering (in X-direction) shows no correlation with measured isotopic composition, indicating that mount topography did not affect the analysis. **(C)** OH/O vs $\delta^{18}\text{O}$ plot. Measured $\delta^{18}\text{O}$ shifts with increasing zircon OH-content. Analyses with elevated OH/O (as compared to reference zircon) that yield distinctly lower or higher $\delta^{18}\text{O}$ values than those analyses with low OH/O are excluded from the calculation of the weighted mean $\delta^{18}\text{O}$ value.

U-Pb (SIMS)	calibration standard	uncertainty / reproducibility (1σ)			U concentration standard			secondary standard			
		# analyses	spot-to-spot	$^{238}\text{U}/^{206}\text{Pb}^*$	# analyses	# analyses	weighted mean age (Ma)	2σ	MSWD		
U-Pb1	temora-2	13	1.50%	0.54%	temora-2	6	91500	5	1078	1)	0.68
U-Pb2	91500	5	0.50%	0.80%	OGC	4	OGC	4	3452	2)	0.6
U-Pb3	91500	10	0.50%	0.61%	OGC	6	OGC	6	3470	2)	0.47

Table A1. U-Pb measurement results of zircon reference materials for SIMS analytical runs. ¹⁾ weighted mean $^{238}\text{U}/^{206}\text{Pb}^*$ age; ²⁾ weighted mean $^{207}\text{Pb}/^{206}\text{Pb}^*$ age.

U-Pb (LA-ICPMS)							
Secondary standard	# analyses	weighted mean $^{238}\text{U}/^{206}\text{Pb}$ age (Ma)	2σ	MSWD	Accepted age (Ma)	2σ	Reference
GJ1	16	601	2	0.73	601.2	0.4	Jackson et al. (2004)
Plešovice	15	338	1	1.3	337.13	0.37	Skáma et al. (2008)
91500	20	1062	2	1.3	1065	1	Wiedenbeck et al. (2004)

Table A2. U-Pb measurement results of secondary zircon reference materials for LA-ICPMS analytical run.

O isotopes session #	primary standard			secondary standard				
	# analyses	$\delta^{18}\text{O}$	2σ	# analyses	$\delta^{18}\text{O}$	2σ		
O1	91500	28	9.9	0.38	temora-2	17	8	0.48
O2	91500	20	9.9	0.41	Penghai	9	5	0.26
O3	91500	22	9.9	0.42	temora-2	7	7.8	0.42

Table A3. O isotope measurement results of zircon reference materials for SIMS analytical runs.

S isotopes			primary standard						secondary standards					
session #		# analyses	$\delta^{34}\text{S}$	2σ	$\Delta^{33}\text{S}$	2σ		# analyses	$\delta^{34}\text{S}$	2σ	$\Delta^{33}\text{S}$	2σ		
S1	Sierra	22	2.17	0.15	-0.03	0.05	Balmat	10	16.34	0.24	-0.03	0.08		
							Ruttan	10	1.24	0.25	-0.01	0.08		
S2	Sierra	18	2.17	0.13	-0.03	0.08	-	-	-	-	-	-	-	
S3	Sierra	26	2.17	0.11	-0.03	0.07	-	-	-	-	-	-	-	
S4	Sierra	23	2.17	0.31	-0.03	0.06	-	-	-	-	-	-	-	
S5	Sierra	13	2.17	0.07	-0.03	0.06	-	-	-	-	-	-	-	

Table A4. S isotope measurement results of pyrite reference materials for SIMS analytical runs.

A2 References

- Breaks, F.W., Selway, J.B., and Tindle, A.G., 2005, Fertile Peraluminous Granites and Related Rare-Element Pegmatites, Superior Province of Ontario, in Short Course Notes, Geological Association of Canada 17, p. 87–125.
- Corfu, F., Stott, G.M., and Breaks, F.W., 1995, U-Pb geochronology and evolution of the English River Subprovince, an Archean low P-high T metasedimentary belt in the Superior Province: Tectonics, v. 14, p. 1220–1233, doi:10.1029/95TC01452.
- Huhma, H., 1986, Sm-Nd, U-Pb, and Pb-Pb isotopic evidence for the origin of the early Proterozoic Svecokarelian crist in Finland: Geological Survey of Finland, 48 p.
- Jackson, S.E., Pearson, N.J., Griffin, W.L., and Belousova, E.A., 2004, The application of laser ablation-inductively coupled plasma-mass spectrometry to in situ U-Pb zircon geochronology: Chemical Geology, v. 211, p. 47–69, doi:10.1016/j.chemgeo.2004.06.017.
- Lompo, M., 2009, Geodynamic evolution of the 2.25-2.0 Ga Palaeoproterozoic magmatic rocks in the Man-Leo Shield of the West African Craton. A model of subsidence of an oceanic plateau: Geological Society, London, Special Publications, v. 323, p. 231–254, doi:10.1144/SP323.11.
- Nitescu, B., Cruden, A., and Bailey, R., 2006, Integrated potential-field and seismic constraints on the structure of the Archean metasedimentary English River belt, Western Superior craton, Canada: Precambrian Research, v. 144, p. 261–277, doi:10.1016/j.precamres.2005.11.008.
- Parra-Avila, L.A. et al., 2017, The geochronological evolution of the Paleoproterozoic Baoulé-Mossi domain of the Southern West African Craton: Precambrian Research, v. 300, p. 1–27, doi:10.1016/j.precamres.2017.07.036.
- Percival, J.A., 1989, A regional perspective of the Quetico metasedimentary belt, Superior Province, Canada: Canadian Journal of Earth Sciences, v. 26, p. 677–693, doi:10.1139/e89-058.

Percival, J.A., Sanborn-Barrie, M., Skulski, T., Stott, G.M., Helmstaedt, H., and White, D.J., 2006, Tectonic evolution of the western Superior Province from NATMAP and Lithoprobe studies: Canadian Journal of Earth Sciences, v. 43, p. 1085–1117, doi:10.1139/e06-062.

Sláma, J. et al., 2008, Plešovice zircon — A new natural reference material for U–Pb and Hf isotopic microanalysis: Chemical Geology, v. 249, p. 1–35, doi:10.1016/j.chemgeo.2007.11.005.

Wiedenbeck, M. et al., 2004, Further characterisation of the 91500 zircon crystal: Geostandards and Geoanalytical Research, v. 28, p. 9–39, doi:10.1111/j.1751-908X.2004.tb01041.x.

Yang, X.-M., Drayson, D., and Polat, A., 2019, S-type granites in the western Superior Province: a marker of Archean collision zones: Canadian Journal of Earth Sciences, v. 56, p. 1409–1436, doi:10.1139/cjes-2018-0056.

Appendix B

<i>Gp ID</i>	<i>Sample ID</i>	<i>Grain/spot</i>	^{238}U (ppm)	^{232}Th / ^{238}U (%)	δ^{204}	$^{238}\text{U}/^{206}\text{Pb}$	$^{207}\text{Pb}/^{206}\text{Pb}$	$^{238}\text{U}/^{206}\text{Pb}$	$^{207}\text{Pb}*/^{206}\text{Pb}*$	$^{238}\text{U}/^{206}\text{Pb}$	$^{207}\text{Pb}*/^{206}\text{Pb}*$	$^{238}\text{U}/^{206}\text{Pb}$	$^{207}\text{Pb}*/^{206}\text{Pb}*$	<i>Disc session #</i>	
						$\pm 1\sigma$	$\pm 1\sigma$	$\pm 1\sigma$	$\pm 1\sigma$	$\pm 1\sigma$	$\pm 1\sigma$	$\pm 1\sigma$	$\pm 1\sigma$		
1	17FIN02	17FIN02.2	2420	322	0.133	0.04	3.547	0.145	0.11553	0.00194	3.549	0.145	0.11525	0.00195	JL1
1	17FIN02	17FIN02.16	638	241	0.377	0.21	3.457	0.063	0.11712	0.00049	3.464	0.063	0.11551	0.00058	JL1
1	17FIN02	17FIN02.11	714	319	0.447	-0.03	3.089	0.056	0.11519	0.00088	3.088	0.056	0.11539	0.00088	JL1
1	17FIN02	17FIN02.9	653	76	0.116	0.05	2.950	0.056	0.11678	0.00100	2.951	0.056	0.11642	0.00101	JL1
X	17FIN02	17FIN02.13	332	168	0.507	0.05	1.903	0.038	0.19196	0.00280	1.904	0.038	0.19165	0.00280	JL1
D	17FIN02	17FIN02.18	591	53	0.090	1.58	2.931	0.055	0.14355	0.00123	2.978	0.056	0.13195	0.00214	JL1
1	17FIN03B	17FIN03B.8	287	22	0.078	0.07	3.222	0.067	0.11037	0.00136	3.224	0.067	0.10987	0.00139	JL1
1	17FIN03B	17FIN03B.19	489	23	0.047	0.09	3.175	0.059	0.11080	0.00159	3.177	0.060	0.11012	0.00161	JL1
1	17FIN03B	17FIN03B.4	354	31	0.088	0.25	3.134	0.062	0.11312	0.00124	3.142	0.062	0.11121	0.00132	JL1
1	17FIN03B	17FIN03B.23	337	27	0.080	0.09	3.095	0.062	0.11186	0.00127	3.098	0.062	0.11120	0.00130	JL1
1	17FIN03B	17FIN03B.5	2886	80	0.028	0.02	3.090	0.051	0.11196	0.00048	3.091	0.051	0.11184	0.00048	JL1
D	17FIN03B	17FIN03B.22	2255	64	0.028	0.59	4.162	0.067	0.11774	0.00057	4.187	0.068	0.11328	0.00081	JL1
D	17FIN03B	17FIN03B.3	533	36	0.067	2.91	3.084	0.058	0.14945	0.00449	3.176	0.067	0.12806	0.00087	JL1
D	17FIN03B	17FIN03B.14	517	28	0.054	0.19	3.492	0.066	0.11668	0.00109	3.499	0.066	0.11523	0.00114	JL1
1	17FIN05B	17FIN05B.11	1960	6	0.003	0.00	3.355	0.054	0.11243	0.00055	3.355	0.054	0.11245	0.00055	JL1
1	17FIN05B	17FIN05B.17	837	3	0.004	0.00	3.168	0.056	0.11212	0.00079	3.168	0.056	0.11212	0.00079	JL1
1	17FIN05B	17FIN05B.3	1561	7	0.005	0.03	3.146	0.053	0.11211	0.00060	3.147	0.053	0.11187	0.00060	JL1
1	17FIN05B	17FIN05B.5	1479	8	0.006	0.01	3.124	0.063	0.11180	0.00064	3.124	0.063	0.11172	0.00064	JL1
1	17FIN05B	17FIN05B.7	1527	9	0.006	0.02	3.084	0.053	0.11314	0.00111	3.084	0.053	0.11301	0.00111	JL1
1	17FIN05B	17FIN05B.10	784	4	0.005	0.06	3.047	0.064	0.11394	0.00086	3.049	0.064	0.11350	0.00087	JL1
D	17FIN05B	17FIN05B.1	496	67	0.135	0.20	2.938	0.055	0.12502	0.00098	2.944	0.055	0.12354	0.00103	JL1
D	17FIN05B	17FIN05B.4	898	7	0.008	1.10	3.215	0.057	0.12627	0.00263	3.251	0.058	0.11805	0.00289	JL1
I	17FIN06	17FIN06B.28	927	95	0.103	0.04	3.281	0.060	0.11286	0.00079	3.282	0.060	0.11257	0.00080	JL1
I	17FIN06	17FIN06B.14	1809	12	0.007	0.03	3.235	0.056	0.11198	0.00061	3.236	0.056	0.11177	0.00061	JL1
I	17FIN06	17FIN06B.18	603	67	0.111	0.02	3.197	0.075	0.11046	0.00182	3.197	0.075	0.11031	0.00182	JL1
I	17FIN06	17FIN06B.17	642	59	0.092	0.02	3.159	0.060	0.11196	0.00094	3.160	0.060	0.11178	0.00095	JL1
I	17FIN06	17FIN06B.15	925	119	0.128	0.02	3.147	0.057	0.11093	0.00080	3.148	0.057	0.11080	0.00081	JL1
I	17FIN06	17FIN06B.27	741	99	0.133	-0.03	3.122	0.058	0.11087	0.00170	3.121	0.058	0.11108	0.00170	JL1
I	17FIN06	17FIN06B.26	935	103	0.111	0.03	3.094	0.056	0.11146	0.00079	3.095	0.056	0.11121	0.00080	JL1
I	17FIN06	17FIN06B.19	1068	139	0.130	0.01	2.968	0.055	0.11396	0.00224	2.969	0.055	0.11390	0.00224	JL1
I	CO-17-8	CO-17-8.12.1	194	98	0.506	0.24	4.167	0.064	0.08387	0.31332	4.177	0.064	0.08199	0.00319	JL12
I	CO-17-8	CO-17-8.18.1	238	150	0.631	0.23	4.128	0.059	0.09104	0.26631	4.137	0.059	0.08927	0.00271	JL12
I	CO-17-8	CO-17-8.10.1	353	223	0.631	0.13	3.995	0.051	0.08895	0.38006	4.001	0.051	0.08790	0.00382	JL12

Table B1. SIMS zircon U-Pb single spot results. Group ID: I – magmatic, X – inherited, D – rejected.

<i>Gp</i>	<i>Sample</i>	<i>Grain/spot</i>	^{238}U	^{232}Th	f^{204}	$^{238}\text{U}/^{232}\text{Th}$	(ppm)	^{238}U	(ppm)	$\pm 1\sigma$	$^{238}\text{U}/^{232}\text{Th}$	f^{204}	$^{238}\text{U}/^{232}\text{Th}$	(ppm)	$\pm 1\sigma$	$^{207}\text{Pb}*/^{206}\text{Pb}$	$^{238}\text{U}/^{206}\text{Pb}$	$^{207}\text{Pb}*/^{206}\text{Pb}$	$^{238}\text{U}/^{206}\text{Pb}$	$^{207}\text{Pb}*/^{206}\text{Pb}$	$^{238}\text{U}/^{206}\text{Pb}$	$^{207}\text{Pb}*/^{206}\text{Pb}$	<i>Disc</i>	<i>session</i>	#	
<i>ID</i>	<i>ID</i>																									
1	CO-17-8	CO-17-8-8.1	329	213	0.647	0.00	3.895	0.051	0.09359	0.22831	3.895	0.051	0.09359	0.00228	1473	19	1500	37	1.8	JL12						
1	CO-17-8	CO-17-8-21.1	360	216	0.602	0.76	6.148	0.077	0.09398	0.23709	6.195	0.078	0.08806	0.00285	965	12	1384	45	30.3	JL12						
1	CO-17-8	CO-17-8-5.1	249	85	0.341	0.39	4.940	0.068	0.09800	0.27137	4.959	0.068	0.09503	0.00278	1184	16	1529	45	22.5	JL12						
1	SP-16-2b	SP-16-2B.9.1	193	199	1.030	0.64	2.363	0.038	0.17570	0.34781	2.378	0.038	0.17130	0.00380	2263	37	2570	57	12.0	JL12						
1	SP-16-2b	SP-16-2B.6.1	289	530	1.143	1.83	1.977	0.026	0.19335	0.23568	2.014	0.027	0.18088	0.00275	2599	35	2661	40	2.3	JL12						
1	SP-16-2b	SP-16-2B.8.1	257	464	1.810	0.13	1.951	0.027	0.18139	0.25251	1.953	0.027	0.18052	0.00254	2665	37	2558	37	-0.3	JL12						
D	SP-16-2b	SP-16-2B.4.1	389	200	0.513	3.80	1.023	0.042	0.19741	0.29534	1.064	0.044	0.17111	0.00390	4272	176	2568	58	-66.3	JL12						
1	SP-16-22	SP-16-22-11.1	805	272	0.338	0.77	7.939	0.184	0.16119	0.09376	8.000	0.186	0.15576	0.00134	759	18	2410	21	68.5	JL13						
1	SP-16-22	SP-16-22-22.2	607	100	0.165	0.44	4.276	0.165	0.17319	0.08697	4.295	0.166	0.17016	0.00117	1349	52	2559	18	47.3	JL13						
1	SP-16-22	SP-16-22-5.2	894	123	0.137	1.07	3.179	0.035	0.18266	0.06764	3.213	0.036	0.17527	0.00105	1747	20	2609	16	33.0	JL13						
D	SP-16-22	SP-16-22-2.1	917	260	0.283	1.69	5.779	2.193	0.18055	9.17931	5.878	2.231	0.16882	0.009343	1013	384	2546	1409	60.2	JL13						
I	19GH11B	GH11B.11.1	2203	11	0.005	0.13	9.689	0.093	0.08691	0.05649	9.701	0.094	0.08587	0.00069	632	6	1335	11	52.6	JL13						
I	19GH11B	GH11B.10.1	1711	6	0.003	0.09	6.878	0.068	0.10794	0.06183	6.884	0.068	0.10727	0.00073	874	9	1753	12	50.1	JL13						
I	19GH11B	GH11B.16.1	493	156	0.316	0.19	3.674	0.046	0.12889	0.09289	3.681	0.046	0.12753	0.00096	1549	20	2064	16	24.9	JL13						
I	19GH11B	GH11B.16.2	149	85	0.574	0.49	2.642	0.048	0.14164	0.15350	2.655	0.049	0.13808	0.00218	2060	38	2203	35	6.5	JL13						
I	19GH11B	GH11B.20.1	302	112	0.370	0.21	2.915	0.074	0.13608	0.10969	2.921	0.074	0.13458	0.00114	1898	48	2159	18	12.1	JL13						
I	19GH11B	GH11B.11.2	259	72	0.279	0.06	2.689	0.042	0.13417	0.13059	2.691	0.042	0.13373	0.00132	2037	32	2148	21	5.1	JL13						
D	19GH11B	GH11.6.2	967	55	0.057	0.21	7.637	0.155	0.11944	0.07597	7.654	0.155	0.11786	0.00093	792	16	1924	15	58.9	JL13						
I	19GH9	GH9-6.1	468	191	0.408	0.11	2.886	0.037	0.13727	0.08652	2.889	0.037	0.13650	0.00088	1916	24	2183	14	12.2	JL13						
I	19GH9	GH9-5.1	374	189	0.507	0.20	2.742	0.038	0.13830	0.09865	2.748	0.038	0.13683	0.00102	2001	28	2187	16	8.5	JL13						
I	19GH9	GH9-2.1	380	129	0.340	0.12	2.663	0.036	0.13712	0.09591	2.666	0.036	0.13627	0.00098	2053	28	2180	16	5.8	JL13						
I	19GH9	GH9-14.2	294	96	0.325	0.03	2.640	0.037	0.13690	0.09961	2.641	0.037	0.13665	0.00100	2070	29	2185	16	5.3	JL13						
I	19GH9	GH9-15.1	396	137	0.348	0.14	2.571	0.034	0.13670	0.09047	2.575	0.034	0.13567	0.00093	2115	28	2173	15	2.6	JL13						
I	19GH9	GH9-15.2	339	77	0.227	0.02	2.535	0.034	0.13715	0.09844	2.555	0.034	0.13700	0.00099	2143	29	2190	16	2.1	JL13						
D	19GH9	GH9-14.1	703	803	1.143	0.52	4.569	0.052	0.14095	0.08661	4.593	0.053	0.13718	0.00118	1270	15	2192	19	42.1	JL13						

Table B1. Continued.

<i>G_{IP}</i>	Sample	Grain/ <i>spot</i>	<i>238</i> U	<i>232</i> Th	<i>238</i> U/ <i>206</i> Pb	<i>207</i> Pb/ <i>206</i> Pb	<i>207</i> Pb/ <i>235</i> U	<i>208</i> Pb/ <i>232</i> Th	<i>235</i> U/ <i>207</i> Pb	<i>208</i> Pb/ <i>232</i> Th	<i>238</i> U/ <i>206</i> Pb	<i>207</i> Pb/ <i>206</i> Pb	<i>Disc</i>
<i>ID</i>	<i>ID</i>		(ppm)	(ppm)	±1 σ	±1 σ	±1 σ	date (Ma) ±1 σ	date (Ma) ±1 σ	date (Ma) ±1 σ	date (Ma) ±1 σ	(%)	
D	15K-2	15K-2-1	624	153	2.959	0.06	0.135	0.001	6.260	0.118	0.126	0.004	2011
1	15K-2	15K-2-2	328	111	2.380	0.03	0.133	0.001	7.590	0.122	0.124	0.002	2183
1	15K-2	15K-2-3	660	124	2.571	0.06	0.134	0.001	7.140	0.153	0.115	0.002	2127
1	15K-2	15K-2-4	779	200	2.520	0.04	0.134	0.001	7.260	0.108	0.112	0.002	2148
1	15K-2	15K-2-5	579	197	2.481	0.04	0.135	0.001	7.430	0.129	0.121	0.003	2169
1	15K-2	15K-2-6	620	158	2.653	0.06	0.131	0.001	6.770	0.147	0.099	0.003	2079
1	15K-2	15K-2-8	450	117	2.427	0.04	0.132	0.001	7.440	0.137	0.125	0.003	2164
1	15K-2	15K-2-10	1020	329	2.513	0.07	0.136	0.001	7.370	0.199	0.130	0.004	2154
1	15K-2	15K-2-11	950	282	2.513	0.03	0.134	0.001	7.300	0.101	0.115	0.002	2148
1	15K-2	15K-2-12	469	83	2.584	0.04	0.137	0.001	7.230	0.123	0.162	0.005	2139
1	15K-2	15K-2-15	328	83	2.562	0.03	0.129	0.001	6.920	0.085	0.113	0.002	2101
1	15K-2	15K-2-16	566	171	2.503	0.03	0.133	0.001	7.210	0.094	0.123	0.002	2138
1	15K-2	15K-2-17	973	235	2.678	0.03	0.138	0.001	7.010	0.086	0.133	0.003	2112

Table B2. LA-ICPMS zircon U-Pb single spot results. Group ID: I – magmatic, D – rejected.

Appendix C

<i>Sample ID</i>	<i>Spot ID</i>	$\delta^{34}S$ ‰	2σ (abs.)	$\delta^{33}S$ ‰	2σ (abs.)	$\Delta^{33}S$ ‰	1σ (abs.)	# S run	rejected
CO-17-8	CO-17-8@1	3.43	0.05	1.71	0.09	-0.05	0.04	#S1	
CO-17-8	CO-17-8@2	3.21	0.05	1.65	0.12	0.00	0.05	#S1	
CO-17-8	CO-17-8@3	3.48	0.05	1.78	0.11	-0.01	0.05	#S1	
CO-17-8	CO-17-8@4	3.14	0.04	1.63	0.09	0.02	0.04	#S1	
CO-17-8	CO-17-8@5	3.31	0.05	1.69	0.15	-0.01	0.07	#S1	
CO-17-8	CO-17-8@6	3.35	0.04	1.69	0.11	-0.04	0.05	#S1	
SP-16-20a	SP-16-20A@02	0.80	0.06	0.55	0.11	0.15	0.05	#S1	
SP-16-20a	SP-16-20A@03	0.64	0.06	0.47	0.09	0.14	0.04	#S1	
SP-16-20a	SP-16-20A@04	0.60	0.04	0.42	0.10	0.11	0.04	#S1	
SP-16-20a	SP-16-20A@05	0.48	0.04	0.39	0.09	0.14	0.04	#S1	
SP-16-20a	SP-16-20A@06	0.52	0.05	0.43	0.11	0.16	0.05	#S1	
SP-16-20a	SP-16-20A@08	0.56	0.04	0.48	0.09	0.19	0.04	#S1	
SP-16-20a	SP-16-20A@1	0.96	0.06	0.60	0.09	0.10	0.04	#S1	
SP-16-20a	SP-16-20A@10	1.01	0.05	0.67	0.10	0.15	0.04	#S1	
SP-16-20a	SP-16-20A@11	0.07	0.04	0.16	0.10	0.13	0.04	#S1	
SP-16-20a	SP-16-20A@12	0.50	0.05	0.41	0.13	0.16	0.06	#S1	
SP-16-20a	SP-16-20A@14	0.93	0.04	0.62	0.11	0.14	0.05	#S1	
SP-16-20a	SP-16-20A@15	0.53	0.05	0.35	0.11	0.08	0.05	#S1	
SP-16-20a	SP-16-20A@16	1.00	0.05	0.59	0.10	0.07	0.04	#S1	
SP-16-20a	SP-16-20A@18	0.32	0.04	0.27	0.10	0.11	0.04	#S1	
SP-16-20a	SP-16-20A@19	0.33	0.05	0.32	0.09	0.14	0.04	#S1	
SP-16-20a	SP-16-20A@17	0.41	0.04	0.12	0.11	-0.09	0.05	#S1	
SP-16-20a	SP-16-20A@13	9.02	0.04	4.54	0.09	-0.09	0.04	#S1	X
SP-16-20a	SP-16-20A@09	3.81	0.06	1.95	0.10	-0.01	0.04	#S1	X
SP-16-20a	SP-16-20A@07	3.37	0.05	1.69	0.09	-0.04	0.04	#S1	X
SP-16-2b	SP-16-2B@02	1.67	0.04	1.02	0.11	0.16	0.05	#S1	
SP-16-2b	SP-16-2B@03	1.86	0.05	1.10	0.09	0.14	0.04	#S1	
SP-16-2b	SP-16-2B@04	2.08	0.04	1.31	0.09	0.24	0.04	#S1	
SP-16-2b	SP-16-2B@05	1.84	0.04	1.13	0.10	0.18	0.04	#S1	
SP-16-2b	SP-16-2B@06	1.78	0.06	1.10	0.10	0.18	0.04	#S1	
SP-16-2b	SP-16-2B@07	1.82	0.05	1.12	0.10	0.18	0.04	#S1	
SP-16-2b	SP-16-2B@08	1.44	0.05	0.91	0.11	0.17	0.05	#S1	
SP-16-2b	SP-16-2B@09	2.17	0.04	1.32	0.11	0.21	0.05	#S1	
SP-16-2b	SP-16-2B@1	1.41	0.06	0.91	0.12	0.18	0.06	#S1	
SP-16-2b	SP-16-2B@10	1.71	0.06	1.05	0.11	0.17	0.05	#S1	
SP-16-2b	SP-16-2B@11	1.94	0.04	1.15	0.09	0.15	0.04	#S1	
SP-16-2b	SP-16-2B@12	1.16	0.05	0.75	0.11	0.16	0.05	#S1	
SP-16-2b	SP-16-2B@13	2.21	0.06	1.32	0.09	0.18	0.04	#S1	
SP-16-2b	SP-16-2B@14	3.98	0.04	2.08	0.11	0.03	0.05	#S1	X
SP-16-2b	SP-16-2B@15	3.88	0.04	1.99	0.09	-0.01	0.04	#S1	X
SP-17-43	SP-17-43@02	-13.18	0.04	-6.66	0.12	0.14	0.05	#S1	
SP-17-43	SP-17-43@03	-13.16	0.07	-6.66	0.12	0.14	0.05	#S1	
SP-17-43	SP-17-43@04	-15.22	0.13	-7.78	0.15	0.09	0.08	#S1	
SP-17-43	SP-17-43@05	-13.26	0.07	-6.70	0.12	0.16	0.05	#S1	
SP-17-43	SP-17-43@06	-13.58	0.04	-6.86	0.11	0.16	0.05	#S1	
SP-17-43	SP-17-43@07	-13.06	0.05	-6.56	0.10	0.19	0.04	#S1	

Table C1. SIMS pyrite sulfur single spot results. X marks rejected analyses with $\delta^{34}S$ outside of 2σ .

<i>Sample ID</i>	<i>Spot ID</i>	$\delta^{34}S$ ‰	2σ (abs.)	$\delta^{33}S$ ‰	2σ (abs.)	$\Delta^{33}S$ ‰	1σ (abs.)	# S run	rejected
SP-17-43	SP-17-43@08	-13.10	0.04	-6.62	0.13	0.15	0.06	#S1	
SP-17-43	SP-17-43@09	-13.37	0.07	-6.77	0.10	0.14	0.04	#S1	
SP-17-43	SP-17-43@1	-13.12	0.05	-6.64	0.10	0.14	0.04	#S1	
SP-17-43	SP-17-43@10	-13.35	0.05	-6.74	0.10	0.16	0.05	#S1	
SP-17-43	SP-17-43@11	-13.24	0.07	-6.66	0.11	0.18	0.05	#S1	
SP-17-43	SP-17-43@12	-13.28	0.06	-6.71	0.10	0.15	0.04	#S1	
SP-17-43	SP-17-43@13	-13.48	0.04	-6.80	0.10	0.17	0.04	#S1	
SP-17-43	SP-17-43@14	-13.46	0.07	-6.82	0.11	0.13	0.05	#S1	
SP-17-43	SP-17-43@15	-13.57	0.04	-6.87	0.10	0.14	0.05	#S1	
SP-17-43	SP-17-43@16	-13.40	0.04	-6.76	0.11	0.17	0.05	#S1	
SP-17-43	SP-17-43@17	-13.70	0.04	-6.90	0.10	0.18	0.04	#S1	
SP-17-43	SP-17-43@18	-13.18	0.05	-6.64	0.10	0.18	0.04	#S1	
SP-17-43	SP-17-43@19	-13.26	0.05	-6.65	0.10	0.20	0.04	#S1	
SP-17-43	SP-17-43@20	-13.27	0.05	-6.71	0.10	0.15	0.04	#S1	
SP-17-43	SP-17-43@21	-12.11	0.05	-6.10	0.12	0.15	0.05	#S1	
SP-17-43	SP-17-43@22	-11.85	0.04	-6.00	0.10	0.12	0.04	#S1	
SP-17-43	SP-17-43@23	-12.08	0.05	-5.98	0.10	0.25	0.04	#S1	
15K-2	15K-2@1	9.05	0.04	4.65	0.10	-0.01	0.05	#S5	
15K-2	15K-2@10	10.24	0.07	5.19	0.10	-0.08	0.05	#S5	
15K-2	15K-2@11	9.44	0.05	4.84	0.11	-0.01	0.06	#S5	
15K-2	15K-2@12	10.19	0.04	5.23	0.10	-0.01	0.05	#S5	
15K-2	15K-2@13	10.15	0.05	5.17	0.10	-0.04	0.05	#S5	
15K-2	15K-2@14	10.24	0.04	5.22	0.10	-0.03	0.05	#S5	
15K-2	15K-2@15	10.11	0.05	5.17	0.10	-0.03	0.05	#S5	
15K-2	15K-2@16	9.77	0.06	4.96	0.10	-0.06	0.05	#S5	
15K-2	15K-2@17	10.04	0.04	5.13	0.10	-0.03	0.05	#S5	
15K-2	15K-2@18	10.15	0.04	5.20	0.10	-0.01	0.05	#S5	
15K-2	15K-2@19	9.98	0.06	5.11	0.10	-0.02	0.05	#S5	
15K-2	15K-2@2	8.52	0.04	4.31	0.10	-0.06	0.05	#S5	
15K-2	15K-2@20	9.93	0.05	4.99	0.10	-0.11	0.05	#S5	
15K-2	15K-2@21	10.06	0.04	5.09	0.11	-0.08	0.05	#S5	
15K-2	15K-2@22	8.45	0.05	4.26	0.11	-0.08	0.06	#S5	X
15K-2	15K-2@23	9.93	0.07	5.11	0.10	0.00	0.05	#S5	
15K-2	15K-2@24	9.35	0.04	4.77	0.13	-0.04	0.06	#S5	
15K-2	15K-2@25	9.87	0.06	4.98	0.12	-0.09	0.06	#S5	
15K-2	15K-2@26	10.06	0.04	5.14	0.13	-0.03	0.07	#S5	
15K-2	15K-2@27	8.61	0.05	4.39	0.12	-0.03	0.06	#S5	
15K-2	15K-2@28	10.09	0.04	5.12	0.14	-0.07	0.07	#S5	
15K-2	15K-2@29	8.27	0.04	4.17	0.12	-0.09	0.06	#S5	X
15K-2	15K-2@30	9.08	0.06	4.58	0.10	-0.09	0.05	#S5	
15K-2	15K-2@32	9.24	0.04	4.73	0.10	-0.02	0.05	#S5	
15K-2	15K-2@4	9.36	0.04	4.79	0.10	-0.02	0.05	#S5	
15K-2	15K-2@5	10.09	0.05	5.15	0.11	-0.04	0.06	#S5	
15K-2	15K-2@6	10.15	0.04	5.17	0.11	-0.04	0.06	#S5	
15K-2	15K-2@7	10.00	0.05	5.14	0.10	0.00	0.05	#S5	
15K-2	15K-2@8	9.57	0.05	4.87	0.10	-0.05	0.05	#S5	

Table C1. Continued.

<i>Sample</i>	<i>Spot</i>	$\delta^{34}S$	2σ	$\delta^{33}S$	2σ	$\Delta^{33}S$	1σ	# S run	rejected
<i>ID</i>	<i>ID</i>	%	(abs.)	%	(abs.)	%	(abs.)		
15K-2	15K-2@9	9.32	0.04	4.75	0.10	-0.03	0.05	#S5	
17FIN01	17FIN01D@01	1.70	0.04	0.87	0.09	-0.01	0.04	#S2	
17FIN01	17FIN01D@02	2.13	0.04	1.16	0.08	0.07	0.04	#S2	
17FIN01	17FIN01D@03	2.39	0.05	1.26	0.08	0.03	0.04	#S2	
17FIN01	17FIN01D@04	2.17	0.04	1.13	0.10	0.02	0.05	#S2	
17FIN01	17FIN01D@05	1.70	0.04	0.83	0.09	-0.04	0.04	#S2	
17FIN01	17FIN01D@06	1.93	0.04	0.98	0.09	-0.01	0.04	#S2	
17FIN01	17FIN01D@07	1.25	0.04	0.69	0.11	0.05	0.05	#S2	
17FIN01	17FIN01D@08	2.09	0.04	1.05	0.11	-0.03	0.05	#S2	
17FIN01	17FIN01D@09	1.70	0.04	0.88	0.09	0.01	0.04	#S2	
17FIN01	17FIN01D@10	1.81	0.04	0.98	0.09	0.05	0.04	#S2	
17FIN01	17FIN01D@11	1.08	0.04	0.58	0.10	0.03	0.05	#S2	
17FIN01	17FIN01D@12	1.20	0.04	0.59	0.10	-0.02	0.04	#S2	
17FIN01	17FIN01D@13	1.05	0.04	0.49	0.11	-0.05	0.05	#S2	
17FIN01	17FIN01D@14	0.75	0.04	0.35	0.10	-0.04	0.05	#S2	
17FIN01	17FIN01D@15	1.74	0.04	0.81	0.08	-0.09	0.04	#S2	
17FIN01	17FIN01D@16	1.56	0.04	0.85	0.08	0.05	0.04	#S2	
17FIN01	17FIN01D@17	1.34	0.04	0.66	0.10	-0.04	0.05	#S2	
17FIN01	17FIN01D@18	2.22	0.04	1.08	0.10	-0.06	0.05	#S2	
17FIN01	17FIN01D@19	0.95	0.04	0.47	0.09	-0.02	0.04	#S2	
17FIN01	17FIN01D@20	2.01	0.04	1.03	0.09	-0.01	0.04	#S2	
17FIN01	17FIN01D@21	1.39	0.04	0.69	0.12	-0.03	0.06	#S2	
17FIN01	17FIN01D@22	0.99	0.04	0.46	0.09	-0.05	0.04	#S2	
17FIN01	17FIN01D@23	1.26	0.04	0.63	0.09	-0.01	0.04	#S2	
17FIN01	17FIN01D@24	2.42	0.05	1.25	0.11	0.01	0.05	#S2	
17FIN01	17FIN01D@25	1.13	0.05	0.63	0.09	0.05	0.04	#S2	
17FIN01	17FIN01D@26	1.91	0.04	0.97	0.10	-0.01	0.05	#S2	
17FIN01	17FIN01D@27	1.22	0.04	0.67	0.10	0.04	0.05	#S2	
17FIN01	17FIN01D@28	1.51	0.05	0.73	0.09	-0.04	0.04	#S2	
17FIN01	17FIN01D@29	0.60	0.05	0.26	0.11	-0.05	0.05	#S2	
17FIN01	17FIN01D@30	1.14	0.04	0.52	0.10	-0.06	0.05	#S2	
17FIN02	17FIN02@02	-0.77	0.05	-0.42	0.10	-0.02	0.05	#S2	
17FIN02	17FIN02@03	-0.27	0.04	-0.12	0.11	0.02	0.05	#S2	
17FIN02	17FIN02@04	-1.19	0.05	-0.64	0.09	-0.02	0.04	#S2	
17FIN02	17FIN02@05	-0.70	0.05	-0.39	0.09	-0.03	0.04	#S2	
17FIN02	17FIN02@06	-0.91	0.04	-0.47	0.08	0.00	0.04	#S2	
17FIN02	17FIN02@07	-0.88	0.06	-0.52	0.11	-0.06	0.05	#S2	
17FIN02	17FIN02@08	-1.67	0.05	-0.93	0.10	-0.07	0.05	#S2	
17FIN02	17FIN02@09	-0.64	0.04	-0.33	0.08	0.00	0.04	#S2	
17FIN02	17FIN02@1	-1.89	0.17	-1.01	0.13	-0.04	0.07	#S2	
17FIN02	17FIN02@10	-0.32	0.04	-0.19	0.10	-0.03	0.05	#S2	
17FIN02	17FIN02@11	-0.40	0.04	-0.20	0.10	0.00	0.05	#S2	
17FIN02	17FIN02@12	-0.90	0.05	-0.49	0.09	-0.02	0.04	#S2	
17FIN02	17FIN02@13	-1.35	0.04	-0.77	0.09	-0.08	0.04	#S2	
17FIN02	17FIN02@14	-1.31	0.05	-0.71	0.10	-0.04	0.05	#S2	
17FIN02	17FIN02@15	-0.66	0.04	-0.40	0.11	-0.06	0.05	#S2	

Table C1. Continued.

<i>Sample</i>	<i>Spot</i>	$\delta^{34}S$	2σ	$\delta^{33}S$	2σ	$\Delta^{33}S$	1σ	# S run	rejected
<i>ID</i>	<i>ID</i>	%	(abs.)	%	(abs.)	%	(abs.)		
17FIN02	17FIN02@16	-0.53	0.04	-0.31	0.09	-0.04	0.04	#S2	
17FIN02	17FIN02@17	-0.71	0.04	-0.31	0.13	0.05	0.06	#S2	
17FIN02	17FIN02@18	-1.15	0.04	-0.56	0.08	0.04	0.04	#S2	
17FIN02	17FIN02@19	-1.16	0.04	-0.57	0.08	0.03	0.04	#S2	
17FIN02	17FIN02@20	-1.67	0.19	-0.88	0.13	-0.01	0.08	#S2	
17FIN02	17FIN02@21	-0.79	0.04	-0.38	0.11	0.02	0.05	#S2	
17FIN03B	17FIN03B@02	0.21	0.04	0.16	0.09	0.05	0.04	#S2	
17FIN03B	17FIN03B@03	-1.12	0.13	-0.54	0.09	0.03	0.05	#S2	
17FIN03B	17FIN03B@04	0.07	0.05	0.01	0.11	-0.02	0.05	#S2	
17FIN03B	17FIN03B@05	-1.56	0.05	-0.79	0.09	0.01	0.04	#S2	X
17FIN03B	17FIN03B@06	0.41	0.04	0.16	0.09	-0.06	0.04	#S2	
17FIN03B	17FIN03B@07	0.49	0.04	0.29	0.11	0.04	0.05	#S2	
17FIN03B	17FIN03B@08	-1.89	0.04	-0.90	0.11	0.07	0.05	#S2	X
17FIN03B	17FIN03B@09	-0.49	0.04	-0.24	0.11	0.01	0.05	#S2	
17FIN03B	17FIN03B@1	-0.50	0.05	-0.23	0.09	0.03	0.04	#S2	
17FIN03B	17FIN03B@10	0.39	0.04	0.24	0.09	0.03	0.04	#S2	
17FIN03B	17FIN03B@11	0.13	0.04	0.03	0.11	-0.03	0.05	#S2	
17FIN03B	17FIN03B@12	-0.57	0.04	-0.34	0.09	-0.05	0.04	#S2	
17FIN03B	17FIN03B@13	-0.45	0.04	-0.21	0.12	0.02	0.06	#S2	
17FIN03B	17FIN03B@14	-0.57	0.04	-0.33	0.09	-0.03	0.04	#S2	
17FIN03B	17FIN03B@15	-0.19	0.04	-0.06	0.11	0.03	0.05	#S2	
17FIN03B	17FIN03B@16	0.08	0.04	0.06	0.10	0.02	0.05	#S2	
17FIN03B	17FIN03B@17	-0.40	0.05	-0.18	0.09	0.03	0.04	#S2	
17FIN03B	17FIN03B@18	-0.80	0.04	-0.39	0.09	0.02	0.04	#S2	
17FIN03B	17FIN03B@19	-0.17	0.04	-0.13	0.09	-0.04	0.04	#S2	
17FIN03B	17FIN03B@20	0.05	0.04	-0.02	0.11	-0.05	0.05	#S2	
17FIN03B	17FIN03B@21	0.59	0.04	0.31	0.09	0.01	0.04	#S2	
17FIN03B	17FIN03B@22	-0.04	0.04	-0.02	0.09	0.00	0.04	#S2	
17FIN03B	17FIN03B@23	-0.07	0.05	-0.06	0.09	-0.02	0.04	#S2	
17FIN03B	17FIN03B@24	-0.89	0.04	-0.39	0.12	0.07	0.06	#S2	
17FIN03B	17FIN03B@25	0.05	0.04	0.09	0.10	0.06	0.05	#S2	
17FIN03B	17FIN03B@26	0.15	0.04	0.16	0.11	0.08	0.05	#S2	
17FIN03B	17FIN03B@27	-0.52	0.04	-0.24	0.11	0.03	0.05	#S2	
17FIN03B	17FIN03B@28	-0.47	0.04	-0.24	0.09	0.00	0.04	#S2	
17FIN03B	17FIN03B@29	-0.49	0.04	-0.28	0.09	-0.03	0.04	#S2	
17FIN04A	17FIN04A@02	-0.41	0.04	-0.23	0.11	-0.01	0.05	#S2	
17FIN04A	17FIN04A@03	0.78	0.04	0.40	0.11	-0.01	0.05	#S2	
17FIN04A	17FIN04A@04	2.12	0.04	1.03	0.09	-0.06	0.04	#S2	
17FIN04A	17FIN04A@05	0.05	0.05	-0.01	0.09	-0.03	0.04	#S2	
17FIN04A	17FIN04A@06	0.23	0.04	0.12	0.10	0.00	0.05	#S2	
17FIN04A	17FIN04A@07	0.81	0.04	0.43	0.09	0.02	0.04	#S2	
17FIN04A	17FIN04A@08	0.23	0.05	0.14	0.10	0.02	0.05	#S2	
17FIN04A	17FIN04A@09	1.87	0.04	1.00	0.09	0.03	0.04	#S2	
17FIN04A	17FIN04A@1	0.49	0.04	0.31	0.11	0.05	0.05	#S2	
17FIN04A	17FIN04A@10	0.94	0.04	0.49	0.09	0.00	0.04	#S2	
17FIN04A	17FIN04A@11	0.93	0.04	0.53	0.09	0.06	0.04	#S2	

Table C1. Continued.

<i>Sample</i>	<i>Spot</i>	$\delta^{34}S$	2σ	$\delta^{33}S$	2σ	$\Delta^{33}S$	1σ	# S run	rejected
<i>ID</i>	<i>ID</i>	%	(abs.)	%	(abs.)	%	(abs.)		
17FIN04A	17FIN04A@12	0.54	0.04	0.27	0.12	-0.01	0.06	0.06	#S2
17FIN04A	17FIN04A@13	1.26	0.04	0.66	0.09	0.01	0.04	0.04	#S2
17FIN04A	17FIN04A@14	-0.20	0.04	-0.10	0.09	0.01	0.04	0.04	#S2
17FIN04A	17FIN04A@15	-0.12	0.04	-0.01	0.09	0.06	0.04	0.04	#S2
17FIN04A	17FIN04A@16	1.70	0.04	0.88	0.09	0.00	0.04	0.04	#S2
17FIN04A	17FIN04A@17	-0.13	0.04	-0.04	0.10	0.02	0.05	0.05	#S2
17FIN04A	17FIN04A@18	1.22	0.04	0.63	0.09	0.00	0.04	0.04	#S2
17FIN04A	17FIN04A@19	1.21	0.04	0.58	0.11	-0.05	0.05	0.05	#S2
17FIN04A	17FIN04A@20	1.71	0.04	0.91	0.09	0.03	0.04	0.04	#S2
17FIN04A	17FIN04A@21	0.26	0.04	0.17	0.09	0.03	0.04	0.04	#S2
17FIN04A	17FIN04A@22	0.00	0.13	0.01	0.10	0.01	0.06	0.06	#S2
17FIN04A	17FIN04A@23	1.50	0.04	0.79	0.09	0.02	0.04	0.04	#S2
17FIN04A	17FIN04A@24	1.29	0.04	0.66	0.10	0.00	0.05	0.05	#S2
17FIN04A	17FIN04A@25	1.27	0.04	0.69	0.09	0.04	0.04	0.04	#S2
17FIN04A	17FIN04A@26	0.12	0.04	0.02	0.10	-0.04	0.05	0.05	#S2
17FIN04A	17FIN04A@27	0.80	0.04	0.39	0.09	-0.03	0.04	0.04	#S2
17FIN04A	17FIN04A@28	1.81	0.04	0.95	0.11	0.02	0.05	0.05	#S2
17FIN04A	17FIN04A@29	1.39	0.04	0.79	0.10	0.08	0.05	0.05	#S2
17FIN04A	17FIN04A@30	0.70	0.04	0.38	0.09	0.02	0.04	0.04	#S2
17FIN05B	17FIN05B@02	1.75	0.04	0.94	0.09	0.03	0.04	0.04	#S2
17FIN05B	17FIN05B@03	1.66	0.04	0.91	0.09	0.05	0.04	0.04	#S2
17FIN05B	17FIN05B@04	1.20	0.04	0.63	0.10	0.01	0.05	0.05	#S2
17FIN05B	17FIN05B@05	1.34	0.06	0.65	0.13	-0.04	0.06	0.06	#S2
17FIN05B	17FIN05B@06	1.48	0.04	0.70	0.10	-0.06	0.05	0.05	#S2
17FIN05B	17FIN05B@07	1.33	0.04	0.59	0.09	-0.09	0.04	0.04	#S2
17FIN05B	17FIN05B@08	1.35	0.04	0.66	0.08	-0.03	0.04	0.04	#S2
17FIN05B	17FIN05B@09	1.74	0.04	0.88	0.09	-0.02	0.04	0.04	#S2
17FIN05B	17FIN05B@1	2.01	0.05	1.01	0.09	-0.02	0.04	0.04	#S2
17FIN05B	17FIN05B@10	1.84	0.04	0.97	0.09	0.02	0.04	0.04	#S2
17FIN05B	17FIN05B@11	1.84	0.04	0.96	0.09	0.01	0.04	0.04	#S2
17FIN05B	17FIN05B@12	1.94	0.04	0.96	0.11	-0.03	0.05	0.05	#S2
17FIN05B	17FIN05B@13	1.31	0.04	0.65	0.10	-0.03	0.05	0.05	#S2
17FIN05B	17FIN05B@14	1.61	0.04	0.83	0.09	0.00	0.04	0.04	#S2
17FIN05B	17FIN05B@15	2.12	0.04	1.04	0.10	-0.05	0.05	0.05	#S2
17FIN05B	17FIN05B@16	1.46	0.04	0.76	0.08	0.01	0.04	0.04	#S2
17FIN05B	17FIN05B@17	1.50	0.04	0.76	0.11	-0.01	0.05	0.05	#S2
17FIN05B	17FIN05B@18	2.00	0.04	1.03	0.11	-0.01	0.05	0.05	#S2
17FIN05B	17FIN05B@19	1.64	0.04	0.86	0.10	0.02	0.05	0.05	#S2
17FIN05B	17FIN05B@20	1.67	0.04	0.80	0.10	-0.05	0.05	0.05	#S2
17FIN05B	17FIN05B@21	1.15	0.04	0.57	0.09	-0.02	0.04	0.04	#S2
17FIN05B	17FIN05B@22	1.77	0.04	0.87	0.12	-0.04	0.06	0.06	#S2
17FIN05B	17FIN05B@23	1.47	0.04	0.77	0.11	0.01	0.05	0.05	#S2
17FIN05B	17FIN05B@24	1.15	0.04	0.62	0.09	0.03	0.04	0.04	#S2
17FIN05B	17FIN05B@25	1.71	0.04	0.91	0.12	0.03	0.06	0.06	#S2
17FIN05B	17FIN05B@26	1.94	0.04	1.02	0.10	0.02	0.05	0.05	#S2
17FIN05B	17FIN05B@27	1.67	0.04	0.86	0.09	0.00	0.04	0.04	#S2

Table C1. Continued.

<i>Sample</i>	<i>Spot</i>	$\delta^{34}S$	2σ	$\delta^{33}S$	2σ	$\Delta^{33}S$	1σ	# S run	rejected
<i>ID</i>	<i>ID</i>	%	(abs.)	%	(abs.)	%	(abs.)		
17FIN05B	17FIN05B@28	1.19	0.04	0.59	0.08	-0.02	0.04	#S2	
17FIN05B	17FIN05B@29	1.83	0.04	0.94	0.10	0.00	0.05	#S2	
17FIN05B	17FIN05B@30	1.57	0.04	0.79	0.10	-0.02	0.05	#S2	
17FIN06	17FIN06A@02	1.17	0.04	0.60	0.08	0.00	0.04	#S2	
17FIN06	17FIN06A@03	0.87	0.04	0.49	0.09	0.05	0.04	#S2	
17FIN06	17FIN06A@04	1.44	0.04	0.72	0.09	-0.02	0.04	#S2	
17FIN06	17FIN06A@05	1.32	0.04	0.65	0.10	-0.03	0.05	#S2	
17FIN06	17FIN06A@06	1.02	0.04	0.50	0.08	-0.02	0.04	#S2	
17FIN06	17FIN06A@07	1.28	0.04	0.73	0.09	0.07	0.04	#S2	
17FIN06	17FIN06A@08	0.07	0.04	0.07	0.10	0.03	0.05	#S2	
17FIN06	17FIN06A@09	0.85	0.04	0.43	0.10	-0.01	0.05	#S2	
17FIN06	17FIN06A@1	-0.64	0.20	-0.31	0.15	0.02	0.09	#S2	
17FIN06	17FIN06A@10	1.27	0.04	0.63	0.08	-0.02	0.04	#S2	
17FIN06	17FIN06A@11	1.58	0.04	0.83	0.08	0.02	0.04	#S2	
17FIN06	17FIN06A@12	2.19	0.04	1.16	0.09	0.03	0.04	#S2	
17FIN06	17FIN06A@13	1.85	0.04	0.98	0.10	0.03	0.05	#S2	
17FIN06	17FIN06A@14	1.25	0.04	0.60	0.10	-0.05	0.05	#S2	
17FIN06	17FIN06A@15	0.78	0.04	0.44	0.09	0.04	0.04	#S2	
17FIN06	17FIN06A@16	0.93	0.06	0.47	0.12	-0.01	0.06	#S2	
17FIN06	17FIN06A@17	0.23	0.04	0.15	0.08	0.03	0.04	#S2	
17FIN06	17FIN06A@18	1.34	0.04	0.69	0.10	0.00	0.05	#S2	
17FIN06	17FIN06A@19	1.05	0.05	0.61	0.10	0.07	0.05	#S2	
17FIN06	17FIN06A@20	1.45	0.04	0.74	0.10	-0.01	0.05	#S2	
17FIN06	17FIN06A@21	1.91	0.04	0.98	0.09	0.00	0.04	#S2	
17FIN06	17FIN06A@22	0.20	0.07	0.04	0.09	-0.06	0.05	#S2	
17FIN06	17FIN06A@23	0.91	0.04	0.45	0.09	-0.02	0.04	#S2	
17FIN06	17FIN06A@24	1.29	0.04	0.60	0.11	-0.06	0.05	#S2	
17FIN06	17FIN06A@25	0.36	0.07	0.22	0.11	0.03	0.05	#S2	
17FIN06	17FIN06A@26	2.18	0.04	1.15	0.08	0.02	0.04	#S2	
17FIN06	17FIN06A@27	1.87	0.04	0.92	0.08	-0.04	0.04	#S2	
17FIN06	17FIN06A@28	0.83	0.04	0.36	0.10	-0.06	0.05	#S2	
17FIN06	17FIN06A@29	1.27	0.04	0.63	0.10	-0.02	0.05	#S2	
17FIN06	17FIN06A@30	1.27	0.04	0.61	0.11	-0.04	0.05	#S2	
17FIN06	17FIN06B@02	1.69	0.04	0.88	0.10	0.01	0.05	#S2	
17FIN06	17FIN06B@03	1.95	0.04	0.95	0.11	-0.05	0.05	#S2	
17FIN06	17FIN06B@04	1.09	0.04	0.61	0.09	0.05	0.04	#S2	
17FIN06	17FIN06B@05	1.57	0.04	0.78	0.09	-0.03	0.04	#S2	
17FIN06	17FIN06B@06	2.22	0.04	1.13	0.08	-0.01	0.04	#S2	
17FIN06	17FIN06B@07	1.97	0.04	1.02	0.09	0.00	0.04	#S2	
17FIN06	17FIN06B@08	2.58	0.04	1.32	0.09	-0.01	0.04	#S2	
17FIN06	17FIN06B@09	2.24	0.04	1.16	0.13	0.01	0.06	#S2	
17FIN06	17FIN06B@1	1.98	0.04	0.97	0.10	-0.05	0.05	#S2	
17FIN06	17FIN06B@10	1.68	0.04	0.87	0.12	0.00	0.06	#S2	
17FIN06	17FIN06B@11	2.60	0.04	1.40	0.09	0.06	0.04	#S2	
17FIN06	17FIN06B@12	1.67	0.04	0.88	0.09	0.02	0.04	#S2	
17FIN06	17FIN06B@13	2.09	0.04	1.04	0.08	-0.03	0.04	#S2	

Table C1. Continued.

<i>Sample</i> <i>ID</i>	<i>Spot</i> <i>ID</i>	$\delta^{34}S$ ‰	2σ (abs.)	$\delta^{33}S$ ‰	2σ (abs.)	$\Delta^{33}S$ ‰	1σ (abs.)	# S run	rejected
17FIN06	17FIN06B@14	0.96	0.04	0.48	0.09	-0.01	0.04	#S2	
17FIN06	17FIN06B@15	2.31	0.04	1.14	0.12	-0.05	0.06	#S2	
17FIN06	17FIN06B@16	1.52	0.04	0.72	0.08	-0.06	0.04	#S2	
17FIN06	17FIN06B@17	1.54	0.04	0.83	0.09	0.04	0.04	#S2	
17FIN06	17FIN06B@18	1.54	0.04	0.85	0.09	0.05	0.04	#S2	
17FIN06	17FIN06B@19	2.02	0.04	1.00	0.09	-0.04	0.04	#S2	
17FIN06	17FIN06B@20	2.72	0.04	1.42	0.09	0.02	0.04	#S2	
17FIN06	17FIN06B@21	1.78	0.04	0.93	0.11	0.02	0.05	#S2	
17FIN06	17FIN06B@22	2.16	0.04	1.10	0.11	-0.01	0.05	#S2	
17FIN06	17FIN06B@23	1.80	0.04	0.95	0.11	0.03	0.06	#S2	
17FIN06	17FIN06B@24	1.78	0.04	0.98	0.11	0.07	0.05	#S2	
17FIN06	17FIN06B@25	1.69	0.04	0.84	0.09	-0.03	0.04	#S2	
17FIN06	17FIN06B@26	3.25	0.04	1.71	0.09	0.04	0.04	#S2	
17FIN06	17FIN06B@27	1.49	0.04	0.73	0.09	-0.04	0.04	#S2	
17FIN06	17FIN06B@28	1.37	0.04	0.67	0.11	-0.04	0.05	#S2	
17FIN06	17FIN06B@29	1.63	0.04	0.85	0.09	0.01	0.04	#S2	
17FIN06	17FIN06B@30	1.10	0.04	0.48	0.10	-0.09	0.05	#S2	
18IM19	18IM19c@1	-1.60	0.06	-1.09	0.03	-0.27	0.04	#S3	
18IM19	18IM19c@10	-2.35	0.06	-1.43	0.03	-0.22	0.04	#S3	
18IM19	18IM19c@11	-1.78	0.06	-1.14	0.03	-0.22	0.04	#S3	
18IM19	18IM19c@12	-1.89	0.06	-1.20	0.03	-0.23	0.04	#S3	
18IM19	18IM19c@13	-1.68	0.06	-1.10	0.03	-0.23	0.05	#S3	
18IM19	18IM19c@14	-0.86	0.06	-0.70	0.04	-0.25	0.05	#S3	
18IM19	18IM19c@15	-1.19	0.06	-0.89	0.03	-0.28	0.04	#S3	
18IM19	18IM19c@16	-2.07	0.06	-1.26	0.04	-0.19	0.05	#S3	
18IM19	18IM19c@17	-1.34	0.06	-0.97	0.03	-0.28	0.04	#S3	
18IM19	18IM19c@18	-1.41	0.06	-0.98	0.03	-0.26	0.04	#S3	
18IM19	18IM19c@19	-1.44	0.06	-0.93	0.03	-0.19	0.04	#S3	
18IM19	18IM19c@2	-1.80	0.06	-1.25	0.04	-0.33	0.05	#S3	
18IM19	18IM19c@3	-2.40	0.06	-1.52	0.04	-0.29	0.05	#S3	
18IM19	18IM19c@4	-1.22	0.06	-0.87	0.03	-0.24	0.04	#S3	
18IM19	18IM19c@5	-1.71	0.06	-1.18	0.03	-0.30	0.05	#S3	
18IM19	18IM19c@6	-2.40	0.06	-1.43	0.03	-0.20	0.04	#S3	
18IM19	18IM19c@7	-2.04	0.06	-1.36	0.03	-0.31	0.04	#S3	
18IM19	18IM19c@8	-1.83	0.06	-1.15	0.03	-0.21	0.04	#S3	
18IM19	18IM19c@9	-1.45	0.06	-1.04	0.03	-0.29	0.04	#S3	
18IM19	18IM19e@1	-1.12	0.06	-0.90	0.03	-0.33	0.04	#S3	
18IM19	18IM19e@10	-0.73	0.06	-0.63	0.03	-0.26	0.04	#S3	
18IM19	18IM19e@11	-1.21	0.06	-0.99	0.03	-0.37	0.04	#S3	
18IM19	18IM19e@12	-1.35	0.06	-0.99	0.03	-0.30	0.04	#S3	
18IM19	18IM19e@13	-1.04	0.06	-0.88	0.03	-0.35	0.04	#S3	
18IM19	18IM19e@14	-0.23	0.06	-0.49	0.04	-0.37	0.05	#S3	
18IM19	18IM19e@15	-1.22	0.06	-0.99	0.03	-0.36	0.04	#S3	
18IM19	18IM19e@16	-0.44	0.06	-0.46	0.03	-0.23	0.05	#S3	
18IM19	18IM19e@17	-0.91	0.06	-0.82	0.03	-0.35	0.04	#S3	
18IM19	18IM19e@18	-0.98	0.06	-0.92	0.04	-0.42	0.05	#S3	

Table C1. Continued.

<i>Sample ID</i>	<i>Spot ID</i>	$\delta^{34}S$ ‰	2σ (abs.)	$\delta^{33}S$ ‰	2σ (abs.)	$\Delta^{33}S$ ‰	1σ (abs.)	# S run	rejected
18IM19	18IM19e@19	-1.53	0.06	-1.19	0.04	-0.40	0.05	#S3	
18IM19	18IM19e@2	-0.19	0.06	-0.40	0.04	-0.31	0.05	#S3	
18IM19	18IM19e@3	-0.05	0.06	-0.32	0.04	-0.29	0.05	#S3	
18IM19	18IM19e@4	-0.26	0.06	-0.51	0.04	-0.37	0.05	#S3	
18IM19	18IM19e@5	-0.36	0.06	-0.50	0.03	-0.32	0.04	#S3	
18IM19	18IM19e@6	-1.22	0.06	-0.94	0.03	-0.31	0.05	#S3	
18IM19	18IM19e@7	-1.54	0.06	-1.16	0.03	-0.37	0.04	#S3	
18IM19	18IM19e@8	-0.92	0.06	-0.80	0.03	-0.32	0.04	#S3	
18IM19	18IM19e@9	-0.12	0.06	-0.38	0.03	-0.32	0.05	#S3	
19GH11B	19GH11B@02	-3.99	0.06	-2.14	0.12	-0.09	0.05	#S4	
19GH11B	19GH11B@03	-4.09	0.05	-2.14	0.14	-0.04	0.06	#S4	
19GH11B	19GH11B@04	-2.57	0.06	-1.37	0.11	-0.05	0.04	#S4	
19GH11B	19GH11B@05	-1.92	0.06	-1.03	0.11	-0.04	0.04	#S4	
19GH11B	19GH11B@06	-4.55	0.05	-2.30	0.11	0.04	0.04	#S4	
19GH11B	19GH11B@07	-4.53	0.05	-2.35	0.13	-0.02	0.05	#S4	
19GH11B	19GH11B@1	-4.82	0.06	-2.49	0.13	0.00	0.06	#S4	
19GH11B	19GH11B@12	-2.53	0.05	-1.36	0.12	-0.06	0.05	#S4	
19GH11B	19GH11B@13	-3.86	0.05	-2.10	0.15	-0.11	0.07	#S4	
19GH11B	19GH11B@14	-4.18	0.05	-2.21	0.11	-0.06	0.04	#S4	
19GH11B	19GH11B@15	-4.39	0.05	-2.32	0.14	-0.05	0.06	#S4	
19GH11B	19GH11B@16	-4.20	0.05	-2.27	0.11	-0.10	0.04	#S4	
19GH11B	19GH11B@17	-3.97	0.05	-2.11	0.11	-0.06	0.04	#S4	
19GH11B	19GH11B@18	-3.54	0.05	-1.86	0.11	-0.04	0.04	#S4	
19GH11B	19GH11B@19	-3.47	0.06	-1.79	0.11	-0.01	0.04	#S4	
19GH11B	19GH11B@20	-3.55	0.05	-1.90	0.12	-0.07	0.05	#S4	
19GH11B	19GH11B@22	-3.11	0.05	-1.62	0.11	-0.02	0.04	#S4	
19GH11B	19GH11B@23	-3.15	0.05	-1.65	0.11	-0.02	0.04	#S4	
19GH11B	19GH11B@24	-3.35	0.06	-1.75	0.12	-0.03	0.05	#S4	
19GH11B	19GH11B@25	-3.28	0.05	-1.76	0.14	-0.07	0.06	#S4	
19GH11B	19GH11B@21	-0.60	0.05	-0.36	0.14	-0.05	0.06	#S4	X

Table C1. Continued.

Appendix D

<i>Sample ID</i>	<i>Grain ID</i>	$\delta^{18}\text{O}$ ‰	2σ (abs.)	$^{16}\text{O}^{1}\text{H}/^{16}\text{O}$	1σ (abs.)	# O run	comments
17FIN02	17FIN02.02	10.92	0.65	-	-	#O1	
17FIN02	17FIN02.04	6.86	0.57	-	-	#O1	
17FIN02	17FIN02.05	9.93	0.52	-	-	#O1	
17FIN02	17FIN02.06	8.72	0.52	-	-	#O1	
17FIN02	17FIN02.07	6.09	0.39	-	-	#O1	
17FIN02	17FIN02.08	9.76	0.35	-	-	#O1	
17FIN02	17FIN02.09	9.82	0.44	-	-	#O1	
17FIN02	17FIN02.1	9.09	0.49	-	-	#O1	
17FIN02	17FIN02.10	9.96	0.39	-	-	#O1	
17FIN02	17FIN02.11	8.74	0.44	-	-	#O1	
17FIN02	17FIN02.12	9.35	0.43	-	-	#O1	
17FIN02	17FIN02.13	11.08	0.31	-	-	#O1	
17FIN02	17FIN02.14	6.76	0.38	-	-	#O1	
17FIN02	17FIN02.15	7.36	0.41	-	-	#O1	
17FIN02	17FIN02.16	7.86	0.39	-	-	#O1	
17FIN02	17FIN02.17	6.10	0.52	-	-	#O1	
17FIN02	17FIN02.18	10.09	0.37	-	-	#O1	
17FIN02	17FIN02.19	9.00	0.51	-	-	#O1	
17FIN02	17FIN02.20	10.61	0.31	-	-	#O1	
17FIN02	17FIN02.21	10.63	0.30	-	-	#O1	
17FIN02	17FIN02.22	6.48	0.38	-	-	#O1	
17FIN02	17FIN02.23	8.83	0.61	-	-	#O1	
17FIN02	17FIN02.24	11.33	0.36	-	-	#O1	
17FIN02	17FIN02.26	8.61	0.42	-	-	#O1	
17FIN02	17FIN02.27	8.10	0.44	-	-	#O1	
17FIN02	17FIN02.28	7.86	0.40	-	-	#O1	
17FIN02	17FIN02.29	6.41	0.26	-	-	#O1	
17FIN02	17FIN02.03	13.93	0.59	-	-	#O1	X: outside of 2σ
17FIN02	17FIN02.25	14.62	0.46	-	-	#O1	X: outside of 2σ
17FIN02	17FIN02.30	15.80	0.43	-	-	#O1	X: outside of 2σ
17FIN03B	17FIN03B.02	9.47	0.30	-	-	#O1	
17FIN03B	17FIN03B.03	9.49	0.44	-	-	#O1	
17FIN03B	17FIN03B.04	9.20	0.41	-	-	#O1	
17FIN03B	17FIN03B.05	9.13	0.33	-	-	#O1	
17FIN03B	17FIN03B.06	9.58	0.48	-	-	#O1	
17FIN03B	17FIN03B.07	9.28	0.37	-	-	#O1	
17FIN03B	17FIN03B.08	9.32	0.41	-	-	#O1	
17FIN03B	17FIN03B.09	9.12	0.47	-	-	#O1	
17FIN03B	17FIN03B.1	8.48	0.47	-	-	#O1	
17FIN03B	17FIN03B.10	9.54	0.25	-	-	#O1	
17FIN03B	17FIN03B.11	9.42	0.31	-	-	#O1	
17FIN03B	17FIN03B.12	8.80	0.36	-	-	#O1	
17FIN03B	17FIN03B.13	10.02	0.40	-	-	#O1	
17FIN03B	17FIN03B.14	8.46	0.72	-	-	#O1	
17FIN03B	17FIN03B.16	10.29	0.31	-	-	#O1	
17FIN03B	17FIN03B.17	9.72	0.44	-	-	#O1	

Table D1. SIMS zircon oxygen single spot results. X marks rejected analyses.

<i>Sample ID</i>	<i>Grain ID</i>	$\delta^{18}\text{O}$ ‰	2σ (abs.)	$^{16}\text{O}^1\text{H}/^{16}\text{O}$	1σ (abs.)	# O run	comments
17FIN03B	17FIN03B.18	7.84	0.31	-	-	#O1	
17FIN03B	17FIN03B.19	9.50	0.25	-	-	#O1	
17FIN03B	17FIN03B.20	9.25	0.62	-	-	#O1	
17FIN03B	17FIN03B.21	8.22	0.25	-	-	#O1	
17FIN03B	17FIN03B.22	9.53	0.45	-	-	#O1	
17FIN03B	17FIN03B.23	9.83	0.33	-	-	#O1	
17FIN03B	17FIN03B.24	9.85	0.36	-	-	#O1	
17FIN03B	17FIN03B.25	8.81	0.36	-	-	#O1	
17FIN03B	17FIN03B.27	9.32	0.40	-	-	#O1	
17FIN03B	17FIN03B.28	9.52	0.29	-	-	#O1	
17FIN03B	17FIN03B.29	9.62	0.44	-	-	#O1	
17FIN03B	17FIN03B.30	10.35	0.44	-	-	#O1	
17FIN03B	17FIN03B.15	7.78	0.46	-	-	#O1	X: outside of 2σ
17FIN03B	17FIN03B.26	13.45	0.49	-	-	#O1	X: outside of 2σ
17FIN04A	17FIN04A.02	7.63	0.60	-	-	#O1	
17FIN04A	17FIN04A.03	10.96	0.52	-	-	#O1	
17FIN04A	17FIN04A.04	13.35	0.66	-	-	#O1	
17FIN04A	17FIN04A.05	8.84	0.36	-	-	#O1	
17FIN04A	17FIN04A.06	11.17	0.58	-	-	#O1	
17FIN04A	17FIN04A.07	8.32	0.44	-	-	#O1	
17FIN04A	17FIN04A.08	8.79	0.48	-	-	#O1	
17FIN04A	17FIN04A.09	13.00	0.31	-	-	#O1	
17FIN04A	17FIN04A.1	10.66	0.33	-	-	#O1	
17FIN04A	17FIN04A.10	9.67	0.51	-	-	#O1	
17FIN04A	17FIN04A.12	13.19	0.34	-	-	#O1	
17FIN04A	17FIN04A.13	10.16	0.49	-	-	#O1	
17FIN04A	17FIN04A.14	8.97	0.42	-	-	#O1	
17FIN04A	17FIN04A.15	8.66	0.47	-	-	#O1	
17FIN04A	17FIN04A.16	10.58	0.43	-	-	#O1	
17FIN04A	17FIN04A.17	8.63	0.28	-	-	#O1	
17FIN04A	17FIN04A.18	9.50	0.43	-	-	#O1	
17FIN04A	17FIN04A.19	10.14	0.44	-	-	#O1	
17FIN04A	17FIN04A.20	12.76	0.60	-	-	#O1	
17FIN04A	17FIN04A.22	11.87	0.44	-	-	#O1	
17FIN04A	17FIN04A.23	8.49	0.42	-	-	#O1	
17FIN04A	17FIN04A.24	12.99	0.44	-	-	#O1	
17FIN04A	17FIN04A.25	10.35	0.45	-	-	#O1	
17FIN04A	17FIN04A.26	10.49	0.37	-	-	#O1	
17FIN04A	17FIN04A.27	6.48	0.55	-	-	#O1	X: outside of 2σ
17FIN04A	17FIN04A.11	5.48	0.38	-	-	#O1	X: outside of 2σ
17FIN04A	17FIN04A.21	14.46	0.40	-	-	#O1	X: outside of 2σ
17FIN05B	17FIN05B.02	9.89	0.25	-	-	#O1	
17FIN05B	17FIN05B.03	10.43	0.27	-	-	#O1	
17FIN05B	17FIN05B.04	9.82	0.36	-	-	#O1	
17FIN05B	17FIN05B.05	10.34	0.33	-	-	#O1	
17FIN05B	17FIN05B.06	10.71	0.51	-	-	#O1	

Table D1. Continued.

<i>Sample ID</i>	<i>Grain ID</i>	$\delta^{18}\text{O}$ ‰	2σ (abs.)	$^{16}\text{O}^1\text{H}/^{16}\text{O}$	1σ (abs.)	# O run	comments
17FIN05B	17FIN05B.07	10.42	0.36	-	-	#O1	
17FIN05B	17FIN05B.1	10.87	0.57	-	-	#O1	
17FIN05B	17FIN05B.10	10.67	0.52	-	-	#O1	
17FIN05B	17FIN05B.11	10.35	0.26	-	-	#O1	
17FIN05B	17FIN05B.12	10.33	0.33	-	-	#O1	
17FIN05B	17FIN05B.13	10.81	0.61	-	-	#O1	
17FIN05B	17FIN05B.14	11.36	0.40	-	-	#O1	
17FIN05B	17FIN05B.15	10.77	0.43	-	-	#O1	
17FIN05B	17FIN05B.16	10.51	0.48	-	-	#O1	
17FIN05B	17FIN05B.17	10.48	0.49	-	-	#O1	
17FIN05B	17FIN05B.18	10.89	0.35	-	-	#O1	
17FIN05B	17FIN05B.20	10.68	0.51	-	-	#O1	
17FIN05B	17FIN05B.21	11.15	0.49	-	-	#O1	
17FIN05B	17FIN05B.08	8.93	0.46	-	-	#O1	X: outside of 2σ
17FIN05B	17FIN05B.09	11.72	0.46	-	-	#O1	X: outside of 2σ
17FIN05B	17FIN05B.19	12.41	0.50	-	-	#O1	X: outside of 2σ
17FIN06	17FIN06A.02	10.54	0.42	-	-	#O1	
17FIN06	17FIN06A.03	10.50	0.44	-	-	#O1	
17FIN06	17FIN06A.04	10.84	0.35	-	-	#O1	
17FIN06	17FIN06A.05	8.97	0.38	-	-	#O1	
17FIN06	17FIN06A.06	9.98	0.41	-	-	#O1	
17FIN06	17FIN06A.07	11.17	0.47	-	-	#O1	
17FIN06	17FIN06A.08	10.58	0.37	-	-	#O1	
17FIN06	17FIN06A.09	10.86	0.37	-	-	#O1	
17FIN06	17FIN06A.1	10.48	0.55	-	-	#O1	
17FIN06	17FIN06A.10	10.09	0.48	-	-	#O1	
17FIN06	17FIN06A.11	10.47	0.46	-	-	#O1	
17FIN06	17FIN06A.12	9.16	0.45	-	-	#O1	
17FIN06	17FIN06A.14	10.46	0.38	-	-	#O1	
17FIN06	17FIN06A.15	9.47	0.40	-	-	#O1	
17FIN06	17FIN06A.17	10.34	0.58	-	-	#O1	
17FIN06	17FIN06A.19	11.02	0.42	-	-	#O1	
17FIN06	17FIN06A.20	12.68	0.47	-	-	#O1	
17FIN06	17FIN06A.21	11.08	0.25	-	-	#O1	
17FIN06	17FIN06A.22	11.22	0.59	-	-	#O1	
17FIN06	17FIN06A.23	10.12	0.25	-	-	#O1	
17FIN06	17FIN06A.24	12.31	0.26	-	-	#O1	
17FIN06	17FIN06A.26	10.28	0.34	-	-	#O1	
17FIN06	17FIN06A.27	11.26	0.26	-	-	#O1	
17FIN06	17FIN06A.28	10.04	0.49	-	-	#O1	
17FIN06	17FIN06A.30	10.55	0.44	-	-	#O1	
17FIN06	17FIN06A.13	8.59	0.43	-	-	#O1	X: outside of 2σ
17FIN06	17FIN06A.16	12.76	0.34	-	-	#O1	X: outside of 2σ
17FIN06	17FIN06A.18	7.27	0.51	-	-	#O1	X: outside of 2σ
17FIN06	17FIN06A.25	7.17	0.50	-	-	#O1	X: outside of 2σ
17FIN06	17FIN06A.29	6.87	0.52	-	-	#O1	X: outside of 2σ

Table D1. Continued.

<i>Sample ID</i>	<i>Grain ID</i>	$\delta^{18}\text{O}$ ‰	2σ (abs.)	$^{16}\text{O}^1\text{H}/^{16}\text{O}$	1σ (abs.)	# O run	comments
17FIN06	FIN06B.01	9.97	0.45	-	-	#O1	
17FIN06	FIN06B.03	10.02	0.27	-	-	#O1	
17FIN06	FIN06B.04	10.18	0.27	-	-	#O1	
17FIN06	FIN06B.05	10.73	0.40	-	-	#O1	
17FIN06	FIN06B.06	10.90	0.38	-	-	#O1	
17FIN06	FIN06B.07	9.87	0.33	-	-	#O1	
17FIN06	FIN06B.08	10.39	0.46	-	-	#O1	
17FIN06	FIN06B.09	10.17	0.36	-	-	#O1	
17FIN06	FIN06B.11	9.87	0.34	-	-	#O1	
17FIN06	FIN06B.12	10.70	0.28	-	-	#O1	
17FIN06	FIN06B.13	9.58	0.52	-	-	#O1	
17FIN06	FIN06B.15	10.60	0.35	-	-	#O1	
17FIN06	FIN06B.16	10.11	0.38	-	-	#O1	
17FIN06	FIN06B.17	10.28	0.32	-	-	#O1	
17FIN06	FIN06B.18	10.01	0.34	-	-	#O1	
17FIN06	FIN06B.19	9.83	0.32	-	-	#O1	
17FIN06	FIN06B.2	10.43	0.34	-	-	#O1	
17FIN06	FIN06B.20	10.24	0.36	-	-	#O1	
17FIN06	FIN06B.21	10.05	0.45	-	-	#O1	
17FIN06	FIN06B.23	9.96	0.49	-	-	#O1	
17FIN06	FIN06B.24	10.27	0.64	-	-	#O1	
17FIN06	FIN06B.25	10.09	0.46	-	-	#O1	
17FIN06	FIN06B.26	10.13	0.31	-	-	#O1	
17FIN06	FIN06B.27	10.44	0.32	-	-	#O1	
17FIN06	FIN06B.28	10.18	0.41	-	-	#O1	
17FIN06	FIN06B.30	10.08	0.47	-	-	#O1	
17FIN06	FIN06B.14	9.24	0.47	-	-	#O1	X: outside of 2σ
17FIN06	FIN06B.29	11.15	0.36	-	-	#O1	X: outside of 2σ
17FIN06	FIN06B.22	7.88	0.31	-	-	#O1	X: outside of 2σ
17FIN06	FIN06B.10	15.08	0.55	-	-	#O1	X: outside of 2σ
15K-2	15K-2.1	8.88	0.51	0.0099	1.39E-05	#O2	
15K-2	15K-2.10	9.24	0.59	0.0114	6.30E-06	#O2	
15K-2	15K-2.12	8.97	0.62	0.0065	8.79E-06	#O2	
15K-2	15K-2.15	8.57	0.75	0.0073	8.82E-06	#O2	
15K-2	15K-2.16	9.18	0.61	0.0072	6.63E-05	#O2	
15K-2	15K-2.17	8.14	0.59	0.0065	5.63E-06	#O2	
15K-2	15K-2.4	8.61	0.57	0.0082	2.52E-06	#O2	
15K-2	15K-2.5	8.86	0.37	0.0080	7.45E-06	#O2	
15K-2	15K-2.6	8.54	0.70	0.0085	2.80E-05	#O2	
15K-2	15K-2.7	9.57	0.34	0.0094	2.20E-05	#O2	
15K-2	15K-2.8	8.95	0.47	0.0056	1.02E-05	#O2	
15K-2	15K-2.9	8.35	0.41	0.0083	6.60E-06	#O2	
15K-2	15K-2.3	7.48	0.51	0.0086	6.04E-06	#O2	X: outside of 2σ
15K-2	15K-2.11	11.48	0.44	0.0222	3.04E-05	#O2	X: high OH
CO-17-8	CO-17-8.02	8.64	0.73	0.0059	1.34E-03	#O2	
CO-17-8	CO-17-8.04	8.89	0.58	0.0056	1.08E-03	#O2	

Table D1. Continued.

<i>Sample ID</i>	<i>Grain ID</i>	$\delta^{18}\text{O}$ ‰	2σ (abs.)	$^{16}\text{O}^1\text{H}/^{16}\text{O}$	1σ (abs.)	# O run	comments
CO-17-8	CO-17-8.05	8.38	0.82	0.0058	1.22E-03	#O2	
CO-17-8	CO-17-8.11	8.29	0.70	0.0055	4.68E-04	#O2	
CO-17-8	CO-17-8.12	8.91	0.53	0.0055	6.54E-04	#O2	
CO-17-8	CO-17-8.13	8.73	0.79	0.0057	9.80E-04	#O2	
CO-17-8	CO-17-8.18	9.15	0.68	0.0056	2.44E-03	#O2	
CO-17-8	CO-17-8.1.2	7.93	0.49	0.0054	6.15E-04	#O2	
CO-17-8	CO-17-8.11.2	8.87	0.68	0.0055	8.38E-04	#O2	
CO-17-8	CO-17-8.03	7.65	0.64	0.0075	6.00E-04	#O2	X: high OH
CO-17-8	CO-17-8.06	6.50	0.72	0.0085	7.69E-04	#O2	X: high OH
CO-17-8	CO-17-8.07	7.95	0.52	0.0072	6.77E-04	#O2	X: high OH
CO-17-8	CO-17-8.08	7.46	0.73	0.0074	1.60E-03	#O2	X: high OH
CO-17-8	CO-17-8.09	5.21	0.47	0.0110	2.86E-04	#O2	X: high OH
CO-17-8	CO-17-8.1	7.40	0.60	0.0077	3.76E-04	#O2	X: high OH
CO-17-8	CO-17-8.10	4.21	0.64	0.0122	4.55E-04	#O2	X: high OH
CO-17-8	CO-17-8.15	7.88	0.57	0.0068	3.30E-04	#O2	X: high OH
CO-17-8	CO-17-8.16	7.25	0.63	0.0078	5.67E-04	#O2	X: high OH
CO-17-8	CO-17-8.12.2	7.71	0.54	0.0067	4.52E-04	#O2	X: high OH
CO-17-8	CO-17-8.5.2	6.59	0.54	0.0081	3.14E-04	#O2	X: high OH
CO-17-8	CO-17-8.6.2	5.65	0.61	0.0065	2.82E-04	#O2	X: high OH
19GH11B	19GH11B.10.2	5.63	0.83	0.0054	1.95889E-05	#O3	
19GH11B	19GH11B.11.2	5.71	0.54	0.0055	2.53486E-05	#O3	
19GH11B	19GH11B.3.2	5.56	0.69	0.0058	3.87323E-05	#O3	
19GH11B	19GH11B.5.2	5.59	0.57	0.0050	2.05226E-05	#O3	
19GH11B	19GH11B.9.2	5.02	0.66	0.0051	1.94497E-05	#O3	
19GH11B	19GH11B.16	4.58	0.66	0.0053	3.40522E-05	#O3	
19GH11B	19GH11B.20	5.21	0.75	0.0054	3.83186E-05	#O3	
19GH11B	19GH11B.21	3.23	0.63	0.0090	3.21491E-05	#O3	X: high OH
19GH11B	19GH11B.22	3.37	0.73	0.0088	4.46579E-05	#O3	X: high OH
19GH11B	19GH11B.23	2.61	0.83	0.0116	1.58777E-05	#O3	X: high OH
19GH11B	19GH11B.12.2	4.78	0.62	0.0067	6.83006E-05	#O3	X: high OH
19GH11B	19GH11B.8.2	2.27	0.49	0.0118	2.73538E-05	#O3	X: high OH
19GH11B	19GH11B.03	2.85	0.65	0.0113	5.19422E-05	#O3	X: high OH
19GH11B	19GH11B.04	2.19	0.60	0.0103	2.45E-05	#O3	X: high OH
19GH11B	19GH11B.05	3.52	0.55	0.0076	4.03E-05	#O3	X: high OH
19GH11B	19GH11B.06	2.55	0.70	0.0131	4.20E-05	#O3	X: high OH
19GH11B	19GH11B.07	1.78	0.45	0.0109	3.30E-05	#O3	X: high OH
19GH11B	19GH11B.08	3.17	0.68	0.0125	3.02E-05	#O3	X: high OH
19GH11B	19GH11B.09	1.35	0.59	0.0115	1.42E-05	#O3	X: high OH
19GH11B	19GH11B.10	4.30	0.60	0.0080	1.49E-05	#O3	X: high OH
19GH11B	19GH11B.11	3.77	0.60	0.0127	3.99E-05	#O3	X: high OH
19GH11B	19GH11B.12	4.12	0.61	0.0099	3.42E-05	#O3	X: high OH
19GH11B	19GH11B.14	2.69	0.56	0.0134	2.74E-05	#O3	X: high OH
19GH11B	19GH11B.15	2.97	0.84	0.0104	3.59E-05	#O3	X: high OH
19GH11B	19GH11B.18	2.32	0.60	0.0111	7.61E-06	#O3	X: high OH
19GH11B	19GH11B.2	3.84	0.47	0.0123	4.52E-05	#O3	X: high OH
19GH9	19GH9.1.2	5.00	0.52	0.0062	2.85E-05	#O3	

Table D1. Continued.

<i>Sample ID</i>	<i>Grain ID</i>	$\delta^{18}\text{O}$ ‰	2σ (abs.)	$^{16}\text{O}^1\text{H}/^{16}\text{O}$	1σ (abs.)	# O run	comments
19GH9	19GH9.14.2	4.75	0.65	0.0054	2.57E-05	#O3	
19GH9	19GH9.15.2	4.65	0.50	0.0054	1.83E-05	#O3	
19GH9	19GH9.2.2	5.40	0.53	0.0055	1.88E-05	#O3	
19GH9	19GH9.3.3	4.85	0.62	0.0045	3.12E-05	#O3	
19GH9	19GH9.6.2	5.34	0.70	0.0047	4.29E-05	#O3	
19GH9	19GH9.10	4.44	0.50	0.0068	1.14E-05	#O3	
19GH9	19GH9.11	4.35	0.69	0.0055	2.76E-05	#O3	
19GH9	19GH9.13	5.39	0.73	0.0068	1.31E-05	#O3	
19GH9	19GH9.14	4.77	0.69	0.0066	4.36E-05	#O3	
19GH9	19GH9.15	4.75	0.69	0.0046	3.55E-05	#O3	
19GH9	19GH9.17	5.70	0.58	0.0068	5.58E-05	#O3	
19GH9	19GH9.2	5.20	0.65	0.0050	3.01E-05	#O3	
19GH9	19GH9.3	4.73	0.53	0.0067	7.15E-05	#O3	
19GH9	19GH9.4	5.71	0.59	0.0055	1.73E-05	#O3	
19GH9	19GH9.5	4.78	0.71	0.0065	6.97E-05	#O3	
19GH9	19GH9.7	4.76	0.47	0.0064	4.93E-05	#O3	
19GH9	19GH9.9	4.54	0.42	0.0051	3.26E-05	#O3	
19GH9	19GH9.1	3.23	0.61	0.0094	5.01E-05	#O3	X: high OH
19GH9	19GH9.16	2.23	0.78	0.0096	1.60E-05	#O3	X: high OH
19GH9	19GH9.18	4.28	0.68	0.0075	8.86E-05	#O3	X: high OH
19GH9	19GH9.6	3.68	0.78	0.0071	3.60E-05	#O3	X: high OH

Table D1. Continued.

<i>Sample</i>	<i>aliquot</i>	$\delta^{18}\text{O}$	2σ	<i>sample weight</i>	<i>yield (actual)</i>	<i>yield (calculated assuming almandine, T=21°C)</i>
<i>ID</i>		<i>%o</i>	<i>(abs.)</i>	<i>mg</i>	<i>Torr</i>	<i>Torr</i>
17FIN01	A	10.46	0.04	1.81	36.58	33.35
17FIN01	B	10.31	0.05	1.77	35.04	32.62
17FIN02	A	9.78	0.04	1.68	23.95	30.96
17FIN02	B	9.95	0.03	1.63	31.09	30.04
17FIN03B	A	9.73	0.08	1.75	22.58	32.25
17FIN03B	B	9.37	0.04	1.84	37.33	33.91
17FIN04A	A	10.04	0.02	1.64	31.58	30.22
17FIN04A	B	9.97	0.06	1.73	33.50	31.88
17FIN05B	A	10.27	0.04	1.87	37.41	34.46
17FIN05B	B	10.34	0.06	1.77	30.06	32.62
17FIN06	A	10.32	0.06	1.69	34.70	31.14
17FIN06	B	10.24	0.05	1.75	33.68	32.25
18IM11B	A	10.83	0.05	1.61	29.54	29.67
18IM11B	B	10.73	0.03	1.77	26.76	32.62
18IM12B	A	10.03	0.04	1.81	29.5	33.35
18IM12B	B	10.08	0.05	1.71	31.75	31.51
18IM19C	A	7.61	0.04	1.83	34.37	33.72
18IM19C	B	7.32	0.07	1.82	35.31	33.54
18IM20	A	7.22	0.09	1.67	20.18	30.77
18IM20	B	7.22	0.05	1.78	27.63	32.80
18IM3	A	11.50	0.03	1.67	36.91	30.77
18IM3	B	11.54	0.02	1.78	32.27	32.80
19GH3	A	9.70	0.07	1.65	32.52	30.41
19GH3	B	9.73	0.04	1.79	34.00	32.98
SP-16-34	A	7.97	0.04	1.76	24.62	32.43
SP-16-34	B	8.04	0.07	1.59	29.46	29.30
SP-17-13	A	7.12	0.04	1.88	35.26	34.64
SP-17-13	B	7.19	0.05	1.71	33.60	31.51
SP-17-33	A	7.82	0.02	1.80	13.20	33.17
SP-17-33	B	7.91	0.05	1.77	34.90	32.62
SP-17-38	A	6.92	0.03	1.71	35.43	31.51
SP-17-38	B	6.93	0.01	1.75	33.60	32.25
SP-17-43	A	7.07	0.06	1.72	32.30	31.70
SP-17-43	B	7.06	0.03	1.78	34.61	32.80
SP-17-50	A	7.57	0.06	1.63	30.18	30.04
SP-17-50	B	7.52	0.08	1.80	31.96	33.17
SP-17-71	A	6.94	0.04	1.68	31.82	30.96
SP-17-71	B	6.88	0.06	1.74	31.91	32.06
SP-17-82	A	6.02	0.05	1.73	31.83	31.88
SP-17-82	B	6.11	0.05	1.68	32.45	30.96

Table D2. Laser fluorination garnet O isotope single aliquot results. Note that low actual yields (compared to calculated yields) are likely the result of single garnet grains jumping out of the sample holder during laser fluorination.

EFFECT OF WATER ON $\delta^{18}\text{O}$ IN ZIRCON

This chapter is submitted for publication as:

Liebmann, J., Spencer, C.J., Kirkland, C.K., Xia, X.P., and Bourdet, J. Effect of water on $\delta^{18}\text{O}$ in zircon. *Submitted to Chemical Geology*.

Abstract

The mineral zircon is stable across a wide range of temperature and pressure conditions, and the most widely used geochronometer in felsic rocks. The oxygen isotope ratio recorded by zircon crystals is a sensitive tracer for crustal recycling in magmatic rocks and is a commonly used tool to address zircon petrogenetic questions (e.g. in studies on the evolution of geodynamics and continents). However, secondary processes (i.e. water uptake facilitated by radiation damage) can alter the oxygen isotopic composition of zircon. We present in-situ oxygen isotopic and $^{16}\text{O}^{1\text{H}}/^{16}\text{O}$ data of natural zircon samples in combination with zircon trace element concentrations, and parameters that quantify crystal damage (i.e. Raman spectral parameters and alpha dose). In agreement with previous studies, our results demonstrate that the uptake of water into the zircon crystal structure strongly influences its recorded oxygen isotope ratio. Two distinct secondary processes are recorded that lead to shifting of zircon $\delta^{18}\text{O}$ values towards isotopically heavier and lighter values, respectively. A local charge balance process where the interaction of radiation-damaged zircon with meteoric water leads to lower $\delta^{18}\text{O}$ values with increasing $^{16}\text{O}^{1\text{H}}/^{16}\text{O}$ and broadening of zircon Raman bands; and, in contrast, an equilibrium fractionation process between zircon and percolating water leading to higher $\delta^{18}\text{O}$ values with increasing $^{16}\text{O}^{1\text{H}}/^{16}\text{O}$. The disturbance of the oxygen isotopic system in zircon can be assessed through monitoring zircon $^{16}\text{O}^{1\text{H}}/^{16}\text{O}$; a parameter that is highly sensitive to

the influx of water into radiation-damaged areas of the zircon grain, providing a powerful tool to access the validity of primary $\delta^{18}\text{O}$ signatures.

5.1. Introduction

Zircon (ZrSiO_4) is a common accessory mineral in felsic rocks and stable across a wide range of pressure and temperature conditions. As oxygen diffusion is slow in crystalline grains, zircon often preserves a record of the primary magmatic oxygen signature (Bindeman et al., 2018; Valley et al., 2003), which is a sensitive tracer for intracrustal recycling (Eiler, 2001; J. W. Valley et al., 2005). Also, zircon is the prime U-Pb geochronometer and preserver of primary Hf isotopic and trace element signatures, allowing for a correlation of oxygen isotope ratio, age, and constraints on the genesis of the zircon host rock (Valley, 2003). Due to these characteristics, zircon oxygen isotope geochemistry has found widespread usage in numerous geologic studies, including investigations on the evolution of geodynamics, continental growth and destruction rates, and continental freeboard (Kirkland et al., 2010; Spencer et al., 2017; J W Valley et al., 2005; Valley et al., 2002; Van Kranendonk and Kirkland, 2013). Whilst normally considered anhydrous zircon can contain significant H_2O (Nasdala, 2001). Previous studies have indicated up to 0.2 wt.% water in fully crystalline zircon grains (De Hoog et al., 2014; Trail et al., 2011) and up to 16.6 wt.% in metamict grains (Coleman and Erd, 1961; Nasdala, 2001). Importantly, secondary-ion mass spectrometry (SIMS) studies of zircon demonstrate a correlation between zircon water content and oxygen isotope composition, suggesting that the uptake of water influences the zircon oxygen isotope ratio (Pidgeon et al., 2017, 2013; Wang et al., 2014). Water can be incorporated into the zircon crystal lattice through both primary (i.e. crystallization from a hydrous melt) (De Hoog et al., 2014; Trail et al., 2011) and secondary processes (i.e. as an indirect result of metamictization; the accumulation of structural damage in the zircon crystal lattice as a result of alpha decay of ^{238}U , ^{235}U , and ^{232}Th , which can substitute for Zr^{4+}) (Woodhead et al., 1991). In both cases (primary and secondary uptake of water) water is incorporated into the zircon structure to maintain charge balance (De Hoog et al., 2014; Geisler et al., 2002; Trail et al., 2011).

To study the effect of OH-uptake on the recorded oxygen isotope ratio in zircon, we analysed $\delta^{18}\text{O}$ and relative OH-content of natural zircon samples. Furthermore, the interpretation of zircon oxygen isotopic and $^{16}\text{O}^{1\text{H}}/^{16}\text{O}$ data in combination with zircon trace element concentrations, Raman spectral parameters, and alpha dose allow constraints on the mechanism leading to the incorporation of water into zircon grains. This study concludes with recommendations for assessing potential disturbance of the zircon oxygen isotopic system, which may be of critical relevance to the validity of geological interpretations of such data sets.

5.2. Materials & Methods

5.2.1 Sample context

Samples used in this study to elucidate the mechanism of water uptake into zircon include igneous zircon isolated from Paleoproterozoic granitoids from various localities in the North China Craton, and the West African Craton (Table 5.1). In addition, the effectiveness of a $^{16}\text{O}^{1\text{H}}/^{16}\text{O}$ filter for $\delta^{18}\text{O}$ zircon data is tested for thirteen igneous basement and detrital zircon samples from the Luliang Complex, North China Craton.

Sample ID	Locality	Latitude	Longitude	Lithology	Age $\pm 2\sigma$ Ma	Reference
18IM3	North China Craton	40.848	113.921	Grt granite	1917 ± 70	1
18IM11B	North China Craton	40.604	112.500	Grt granitoid	1901 ± 17	1
18IM12B	North China Craton	40.839	112.565	Grt granitoid	1929 ± 29	1
18IM21C	North China Craton	40.698	109.721	Grt granitoid	1855 ± 16	1
17ZAN05	North China Craton	37.247	114.100	migmatite	2795 ± 10	this study
19GH1	West African Craton	-0.536	5.496	granite	2150 ± 22	this study
19GH9	West African Craton	-1.377	5.340	Bt Ms granite	2183 ± 12	2
19GH11B	West African Craton	-1.609	5.140	Bt Ms granite	2188 ± 20	2

Table 5.1. List of igneous zircon samples, including location, lithology, and magmatic crystallization age. 1 Liebmann et al. (submitted to *Terra Nova*); 2 Liebmann et al. (submitted to *Geochim. Cosmochim. Acta*).

5.2.2 Methods

Igneous rock samples were prepared by removal of weathered surfaces using a rock saw. The remaining material was washed in water and disaggregated by high voltage pulse power fragmentation using the SelFrag facility of the John de Laeter Centre, Curtin University, Western Australia. Igneous and detrital zircon crystals were extracted using standard separation

techniques (Jasper Canyon shaking table, Frantz magnetic separation, heavy liquids [lithium heteropolytungstates, and diiodomethane]). Zircon grains from igneous samples were hand-picked, whereas for the detrital samples the heavy fraction (predominantly consisting of zircon) was poured into a ‘dump mount’. The resulting zircon crystals were mounted in epoxy resin and polished to approximately half grain thickness to expose an interior cross section through the individual crystals. Grains were mounted within 5 mm radius from the centre of a 25 mm diameter epoxy resin disk for SIMS analysis. The polished mounts were cleaned in an ultrasonic bath in multiple steps using isopropanol, ethanol, soap solution, and deionized water. Subsequently, the mounts were dried in an oven for ~24 hrs at 60°C. A 40 nm gold coat was applied to the mount surface. To reveal internal growth structures, cathodoluminescence (CL) images of zircon grains were taken (Figure 5.1) prior to SIMS analysis using a Tescan MIRA3 field emission scanning electron microscope at the John de Laeter Centre.

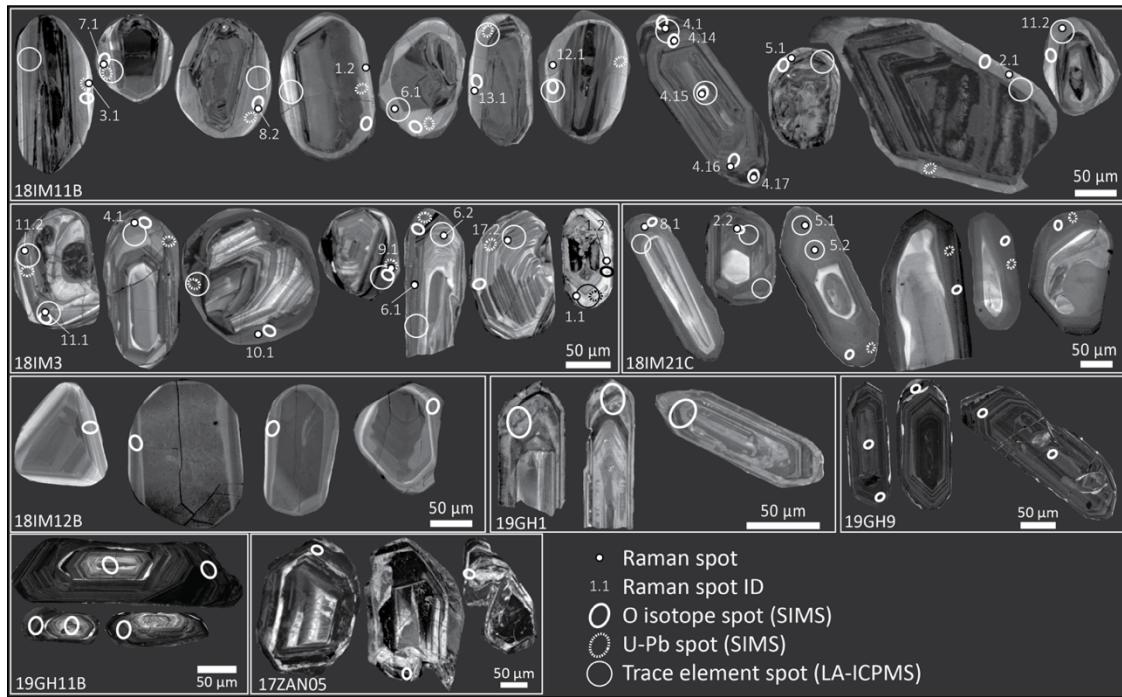


Figure 5.1. CL images of representative zircon grains.

SIMS analysis of zircon oxygen isotopic composition and $^{16}\text{O}^1\text{H}/^{16}\text{O}$

Oxygen isotope and OH analyses were conducted on a CAMECA IMS 1280 secondary ion mass spectrometer (SIMS) at the Centre for Microscopy, Characterisation, and Analysis (CMCA) at the University of Western Australia and a CAMECA IMS 1280-HR SIMS at the Guangzhou Institute of Geochemistry (GIG), Chinese Academy of Sciences, China. Analytical methods have been described in detail by Yang et al. (2018). A Cs^+ primary ion beam was accelerated at 10 keV with an intensity of 2–3 nA. The spot diameter was \sim 10–15 μm . Prior to analysis, each site was pre-sputtered for 30–35 s to remove the Au-coat in a \sim 20 μm^2 area. Secondary optics were centred automatically before each analysis. The ^{18}O and ^{16}O ions were detected simultaneously by two faraday cups. Oxygen isotope compositions are reported in the conventional delta notation; expressed as $\delta^{18}\text{O}$, reflecting the permil deviation in the isotope ratio of the sample ($^{18}\text{O}/^{16}\text{O}$) relative to average seawater (VSMOW; Baertschi, 1976). Instrumental mass fractionation and drift were determined through repetitive analyses of zircon standard 91500 ($\delta^{18}\text{O} = 9.9 \pm 0.6\text{\textperthousand}$) (Wiedenbeck et al., 2004). Zircon reference material Temora-2 ($\delta^{18}\text{O} = 8.2 \pm 0.03\text{\textperthousand}$) (Black et al., 2004) was used as a secondary reference to monitor the quality of the applied corrections. The analysis of the secondary standard Temora-2 yielded $\delta^{18}\text{O}$ of $7.93 \pm 0.39\text{\textperthousand}$, $7.88 \pm 0.38\text{\textperthousand}$, $7.78 \pm 0.42\text{\textperthousand}$, 7.92 ± 0.33 (2σ) consistent with the accepted value (but see Schmitt et al. (2019) for a discussion of oxygen isotopic heterogeneity in different batches of Temora-2). The analysis of the primary standard indicates a precision of $0.4\text{\textperthousand}$ (2σ) or better. Zircon OH-content was determined qualitatively as counts of $^{16}\text{O}^1\text{H}$ divided by counts of ^{16}O and is reported as $^{16}\text{O}^1\text{H}/^{16}\text{O}$. Measured zircon $^{16}\text{O}^1\text{H}/^{16}\text{O}$ ratios are interpreted in comparison to the mean $^{16}\text{O}^1\text{H}/^{16}\text{O}$ of the mount-specific primary standard 91500. The $^{16}\text{O}^1\text{H}/^{16}\text{O}$ of the primary crystalline standard is dominantly a function of the background $^{16}\text{O}^1\text{H}/^{16}\text{O}$ signal of each analytical run. The intensity of $^{16}\text{O}^1\text{H}/^{16}\text{O}$ background is predominantly controlled by the pressure in the source chamber, and hence, affected by the degassing of the epoxy mounts (Pidgeon et al., 2017). Epoxy mounts were held under vacuum for at least three days before analysis and results are reported as a delta function between session-specific crystalline reference material and unknown on the same epoxy mount. Where necessary a drift correction for measured $^{16}\text{O}^1\text{H}/^{16}\text{O}$ was applied to correct for slight variations

in the chamber pressure over time. The mean measured $^{16}\text{O}^{1}\text{H}/^{16}\text{O}$ ratios of reference zircon 91500 were $(2.27\pm0.28)*10^{-3}$, $(1.95\pm0.22)*10^{-3}$, $(4.73\pm0.63)*10^{-3}$, and $(0.56\pm0.02)*10^{-3}$, respectively. Data of reference materials is summarized in supplementary Table A3 for each analytical run.

LA-ICPMS zircon trace element analysis

Three samples (18IM11B, 18IM3, and 18IM21C) were selected for zircon trace element analysis via laser ablation inductively coupled plasma mass spectrometry (LA-ICPMS) using a Resonetics RESOlution M50-A excimer laser coupled with an Agilent 7700s quadrupole at the John de Laeter Centre, Curtin University, Western Australia. Following two cleaning pulses and a 15–20 s period of background analysis, samples were spot ablated for 30 s at a 7 Hz repetition rate using a 33 μm beam. The sample cell was flushed by ultrahigh purity He and N₂. Measured isotopes include ^{29}Si , ^{31}P , ^{43}Ca , ^{57}Fe , ^{89}Y , ^{91}Zr , ^{139}La , ^{140}Ce , ^{141}Pr , ^{146}Nd , ^{147}Sm , ^{153}Eu , ^{157}Gd , ^{159}Tb , ^{163}Dy , ^{165}Ho , ^{166}Er , ^{169}Tm , ^{172}Yb , ^{175}Lu , ^{238}U , and ^{232}Th . Glass reference material NIST 612 (Pearce et al., 1997) was used for calibration with ^{29}Si as internal reference isotope (assuming 14.76 wt% Si in zircon) for all elements except ^{238}U and ^{232}Th . The measured trace element concentrations in glass reference material NIST 610 (Pearce et al., 1997) reproduced the accepted values within 4% and 17 ppm (except ^{57}Fe : 66% and 300 ppm, ^{43}Ca : 0.1% and 63 ppm). Concentrations of ^{238}U and ^{232}Th were calibrated based on zircon reference material GJ-1 (Liu et al., 2010) with ^{91}Zr as internal reference isotope (assuming 43.14 wt% Zr in zircon). The measured concentrations of ^{238}U and ^{232}Th in zircon reference material 91500 (Wiedenbeck et al., 2004) reproduced the accepted values within 5%, and 2 ppm for ^{232}Th , and 30%, and 30 ppm for ^{238}U . Measured concentrations of raw data were reduced using Iolite (Paton et al., 2011). Results of trace element analysis are provided in supplementary Table A2.

Determination of alpha dose

Measurement of U-Th-Pb isotopic concentrations was conducted following O isotopic analysis. Magmatic crystallization ages are from Liebmann et al. (submitted to Terra Nova). Based on zircon ^{238}U , ^{235}U , and ^{232}Th concentrations, and the magmatic crystallization age the alpha dose (α -decay events/mg) can be calculated as follows (Holland and Gottfried, 1955):

$$D_\alpha = 8N_1[\exp(\lambda_1 t) - 1] + 7N_2[\exp(\lambda_2 t) - 1] + 6N_3[\exp(\lambda_3 t) - 1] \quad (1)$$

Where D_α is the accumulated dose in α -decay events/mg; N_1 , N_2 , and N_3 are the present numbers of ^{238}U , ^{235}U , and ^{232}Th , respectively, in atoms/mg; λ_1 , λ_2 , and λ_3 are the decay constants of ^{238}U , ^{235}U , and ^{232}Th in years $^{-1}$, and t is the crystallization age of the zircon (or more specifically, the age assumed from which crystal damage is recorded and not annealed).

Raman spectroscopy

Three samples (18IM3, 18IM11B, 18IM21C) were selected for Raman spectroscopic analysis. Raman analysis was carried out using a Horiba LabRAM HR Evolution Raman spectrometer with a Synapse Visible detector at CSIRO, Australian Resources Research Centre, Kensington, Western Australia. A 600 grooves/mm grating was used for the analysis. Incident radiation with a wavelength of 532 nm was produced by a 100 nW Laser Quantum Torus continuous wave single frequency diode laser. During analysis, the laser was focused to a width of about 0.72 μm with a 100x objective, the numeric aperture of the objective was 0.90, and the beam was aimed perpendicular to the sample. The spectral resolution was 5 cm^{-1} . Raman spots were located within the same internal zircon growth zone (as revealed by CL images) as O isotopic and OH analyses. Fityk (Wojdyl, 2010) was used for the analysis of the acquired Raman spectra. A Lorentzian function was used for peak fitting. The measured full width at half maximum (FWHM) was corrected for the Gaussian apparatus function following the mathematical correction described by Nasdala et al. (2001). This mathematical correction yields reliable results for FWHM larger than two times the spectral resolution (Nasdala et al., 2001).

5.3. Results

5.3.1 Zircon $\delta^{18}\text{O}$ and $^{16}\text{O}^{1}\text{H}/^{16}\text{O}$

Igneous zircon grains with $^{16}\text{O}^{1}\text{H}/^{16}\text{O}$ ratios within 30% of the average $^{16}\text{O}^{1}\text{H}/^{16}\text{O}$ ratio of the crystalline reference material yield relatively homogenous $\delta^{18}\text{O}$ values with 2σ errors ranging from 0.51‰ (sample 18IM21C, $n=20$) to 1.50‰ (sample 18IM3, $n=3$). With increasing $^{16}\text{O}^{1}\text{H}/^{16}\text{O}$ ratio the measured $\delta^{18}\text{O}$ values move away from those obtained for grains with $^{16}\text{O}^{1}\text{H}/^{16}\text{O}$ ratio close to the crystalline reference material ($\leq 30\%$ deviation). This shift in

measured $\delta^{18}\text{O}$ value occurs towards isotopically lighter values, or both lighter and heavier values (Figure 5.2), resulting in an increase in overall scatter in $\delta^{18}\text{O}$ (Figure 5.3). The $^{16}\text{O}^1\text{H}/^{16}\text{O}$ ‘threshold’ above which measured $\delta^{18}\text{O}$ significantly shift (i.e. leading to an increase in 2σ of overall $\delta^{18}\text{O}$ by the factor of 1.5 or higher) is between 30% and 100% deviation from the crystalline reference (Figure 5.3). For comparison, analyses of zircon reference materials 91500 and Temora-2 collected during five analytical runs at two different laboratories yield homogenous $\delta^{18}\text{O}$ (91500, self-corrected: $2\sigma=0.46\text{\textperthousand}$, $n=149$; Temora-2: $2\sigma=0.41\text{\textperthousand}$, $n=79$) (Figure 5.2), and $^{16}\text{O}^1\text{H}/^{16}\text{O}$ values within 16% deviation from the average of the mount-specific crystalline reference for 91500 (self-corrected) and within 100% for Temora-2. Results of single spot O isotopic and $^{16}\text{O}^1\text{H}/^{16}\text{O}$ data is given in supplementary Table A1.

5.3.2 Raman spectra

The most intense Raman bands of zircon are the bands at 1008 cm^{-1} assigned to $\nu_3(\text{SiO}_4)$ (antisymmetric stretching mode), at 975 cm^{-1} assigned to $\nu_1(\text{SiO}_4)$ (symmetric stretching mode), at 439 cm^{-1} assigned to $\nu_2(\text{SiO}_4)$ (symmetric bending mode), and at 356 cm^{-1} assigned to $\nu_4(\text{SiO}_4)$ (antisymmetric bending mode) or an external lattice mode (Dawson et al., 1971; Nasdala, 2003; Syme et al., 1977). All four of these Raman bands are present in the spectra of all but one of the analysed zircon crystals (Figure 5.4). Furthermore, all but one zircon crystal show a Raman band at $\sim 3420\text{ cm}^{-1}$ (Figure 5.4), which may be caused by OH in the crystal structure or molecular H_2O (Bell et al., 2004; Trail et al., 2011). The FWHM of the $\nu_3(\text{SiO}_4)$ Raman band at $\sim 1000\text{ cm}^{-1}$ correlates positively with $^{16}\text{O}^1\text{H}/^{16}\text{O}$ (Figure 5.5). Zircon grains with $^{16}\text{O}^1\text{H}/^{16}\text{O}$ deviating less than 30% from the crystalline reference show $\nu_3(\text{SiO}_4)$ Raman bands with FWHM $<17\text{ cm}^{-1}$. With increasing $^{16}\text{O}^1\text{H}/^{16}\text{O}$ the $\nu_3(\text{SiO}_4)$ Raman band broadens with FWHM up to 27 cm^{-1} . No correlation was observed between $^{16}\text{O}^1\text{H}/^{16}\text{O}$ and FWHM of the Raman band at $\sim 3420\text{ cm}^{-1}$. A summary of Raman spectral parameters is given in Supplementary Table A1.

5.3.3 Zircon trace element concentrations

Zircon of this study show chondrite-normalized trace element pattern typical for igneous zircon (Belousova et al., 2002) with an enrichment in the heavy rare earth elements (HREE; Figure 5.6). With increasing water content zircon from sample 18IM11B becomes more enriched in

rare earth elements (REE; Figure 5.6), and the concentration of non-formula elements, such as Ca and Fe, increases (Figure 5.7). In addition, four high $^{16}\text{O}^{\text{H}}/\text{O}$ zircon grains of sample 18IM11B show a positive Eu anomaly ($\text{Eu}/\text{Eu}^*=1.28-1.71$). In contrast, zircon from sample 18IM3 does not show a clear correlation of REE or non-formula element concentrations with

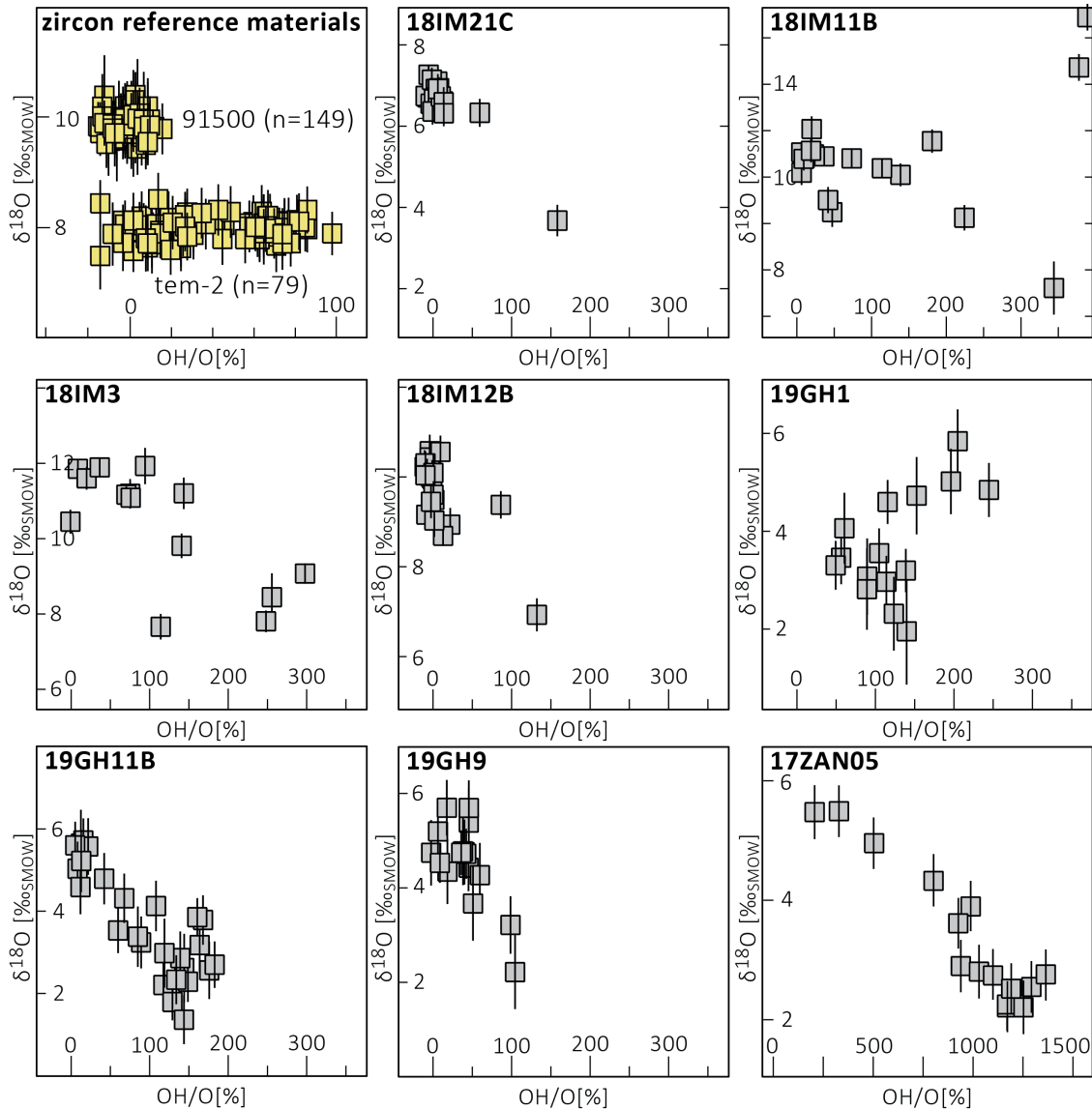


Figure 5.2. $\delta^{18}\text{O}$ vs. $^{16}\text{O}^{\text{H}}/\text{O}$ (% deviation from crystalline reference) plots for zircon reference materials and unknowns. Data of zircon reference materials is compiled from five analytical runs in two different laboratories. Zircon reference materials show homogenous $\delta^{18}\text{O}$ and $^{16}\text{O}^{\text{H}}/\text{O}$ values. In contrast, unknowns show a spread in $\delta^{18}\text{O}$ values, often correlated to increased $^{16}\text{O}^{\text{H}}/\text{O}$ values.

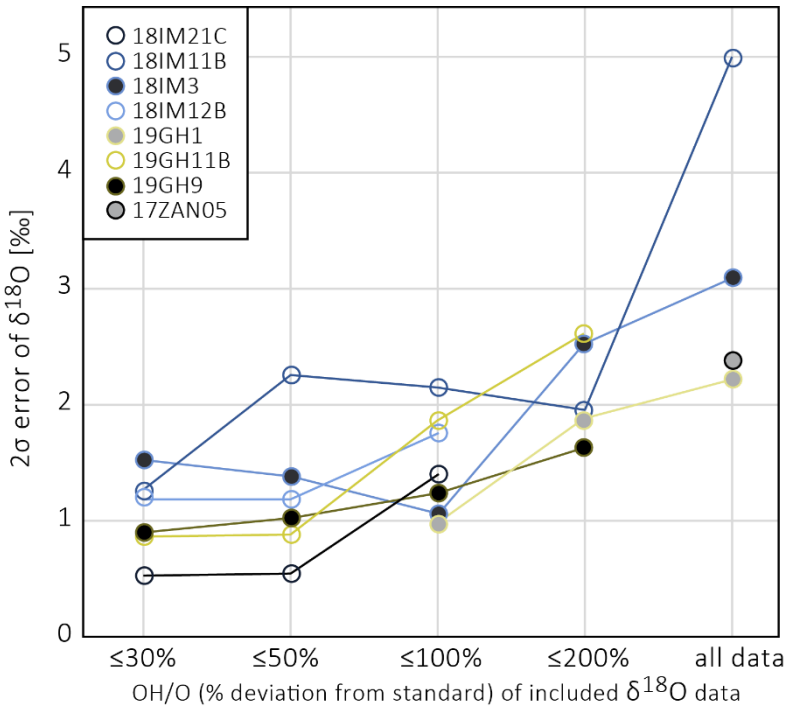


Figure 5.3. Two sigma error of mean δ¹⁸O value vs. ¹⁶O¹H/¹⁶O ratio of included data for igneous zircon populations.

increasing zircon water content (Figures 5.6 and 5.7). Out of 26 analyzed zircon grains 21 show an excess of REE+Y over P (Figure 5.8). The absolute excess of zircon Y+REE over P shows a positive correlation with ¹⁶O¹H/¹⁶O (Figure 5.8). Zircon trace element concentrations are provided in supplementary Table A2.

5.3.4 Alpha dose

Alpha doses of the analysed zircon grains calculated based on the crystallization ages provided in Table 5.1 range from 0.9×10^{-15} to 12.0×10^{-15} α-decay events/mg and show a positive correlation with zircon ¹⁶O¹H/¹⁶O (Figure 5.5). According to the classification of Murakami et al., (1991) the majority of zircon crystals (17 out of 26) analysed in this study are stage I zircon, characterized by alpha doses $< 3 \times 10^{-15}$ α-decay events/mg with minor crystal damage dominated by the accumulation of isolated point defects. Eight zircon crystals yield alpha doses

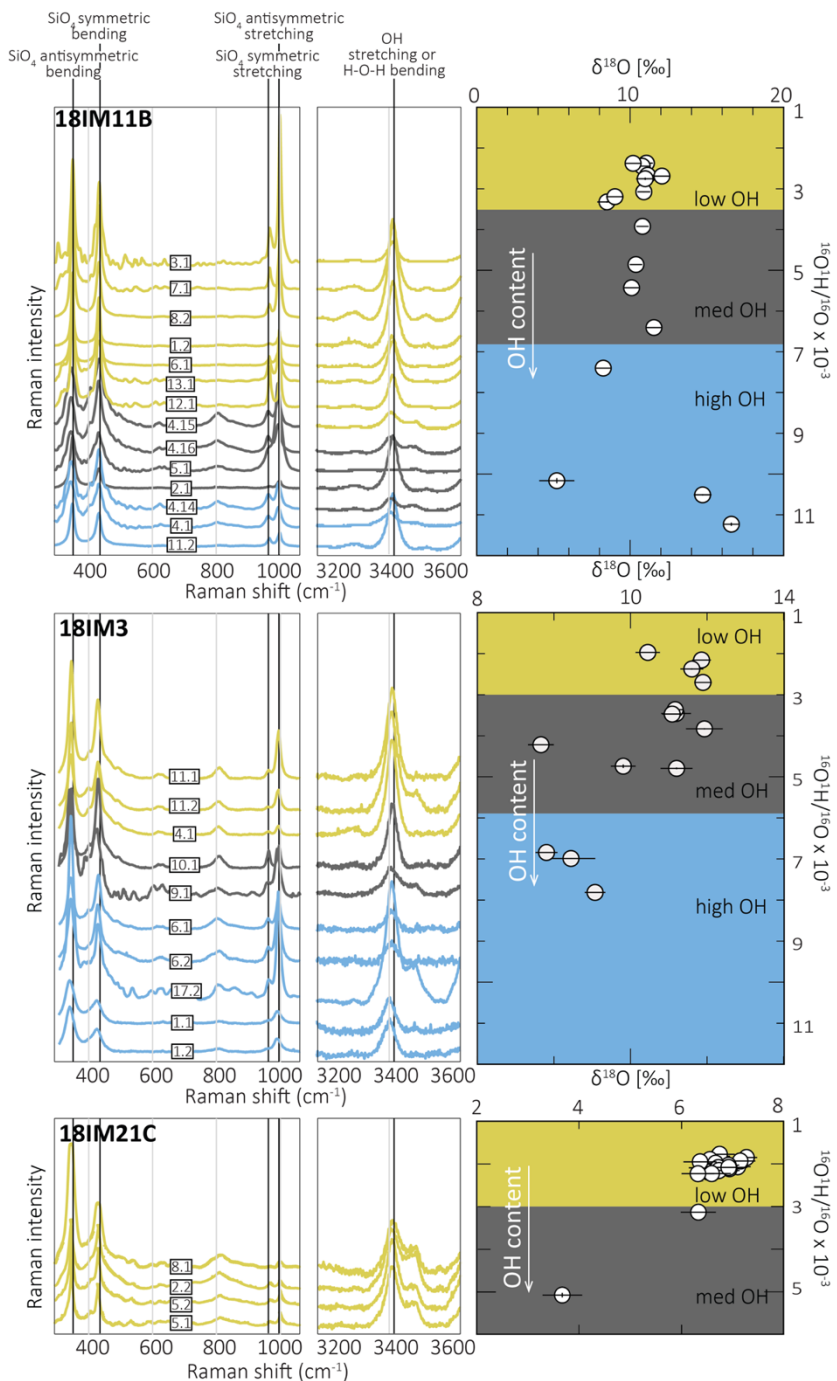


Figure 5.4. Raman spectra and $\delta^{18}\text{O}$ vs. $^{16}\text{O}^{1\text{H}}/^{16}\text{O}$ plots of three samples, color-coded by OH-content (low: $^{16}\text{O}^{1\text{H}}/^{16}\text{O}$ within 50% of crystalline reference, medium: within 200%, high: $\geq 200\%$ deviation). Numbers attached to Raman spectra indicate grain/spot ID (see supplementary Table A1).

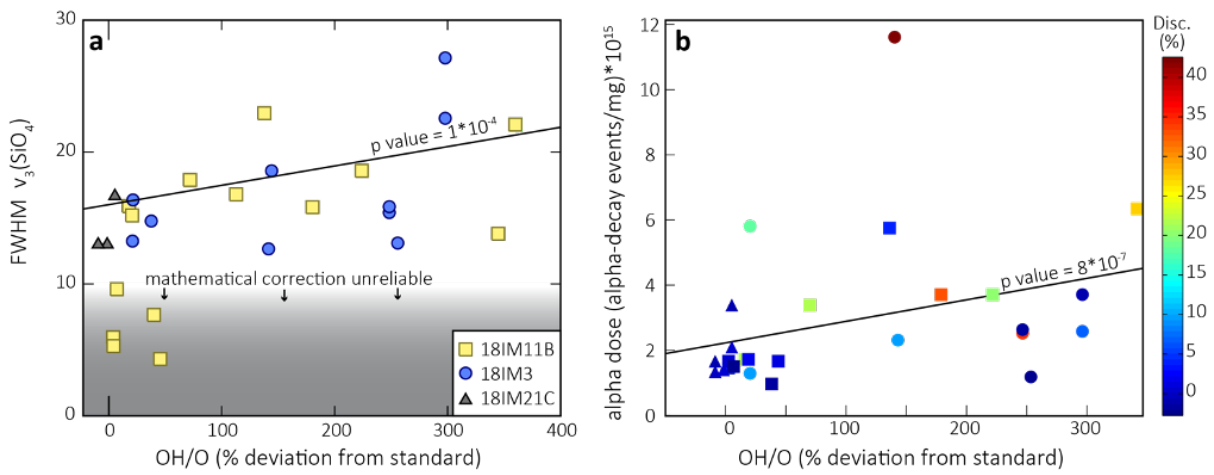


Figure 5.5. Zircon water content ($^{16}\text{O}^{1\text{H}}/^{16}\text{O}$) vs. measurement parameters for crystal damage. Symbol legend in (a) applies to both parts of the figure. Error bars at 2σ level are smaller than the symbols. **(a)** Zircon water content vs. FWHM of the $v_3\text{SiO}_4$ Raman band ($\sim 1000 \text{ cm}^{-1}$). With increasing OH-content the $v_3\text{SiO}_4$ Raman band broadens indicating that the incorporation of water is related to the accumulation of crystal defects. Note that the mathematical correction of FWHM is unreliable for FWHM values smaller than two times the spectral resolution (grey area in the diagram). Therefore, FWHM values $\leq 10 \text{ cm}^{-1}$ have been excluded from the regression. **(b)** Zircon water content ($^{16}\text{O}^{1\text{H}}/^{16}\text{O}$) vs. alpha dose color-coded by discordance of $^{207}\text{Pb}/^{206}\text{Pb}^*$ and $^{238}\text{U}/^{206}\text{Pb}^*$ ages. Zircon water content shows an overall increase with increasing alpha dose.

between 3×10^{-15} and 8×10^{-15} α -decay events/mg, which classifies them as stage II zircon characterized by crystalline regions with point defect and amorphous tracks (Murakami et al., 1991). One grain shows an alpha dose of 12×10^{-15} α -decay events/mg, and hence, is classified as stage III zircon (metamictization is pervasive, Murakami et al., 1991). Note that alpha dose calculated based on crystallization age represents the maximum amount of radiation damage that might be present in a zircon grain. Thermal annealing of zircon after the closure of the U-Pb system leads to an overestimation of alpha dose, as in this case, the crystallization age of the zircon grain does not reflect the period of damage accumulation (Nasdala et al., 2001). The samples studied here show a positive correlation of alpha dose and FWHM of the $v_3(\text{SiO}_4)$ Raman band (Figure 5.9). Comparison of our data to the calibration line (FWHM $v_3(\text{SiO}_4)$ vs. alpha dose) of un-annealed zircon from Nasdala et al. (2001) (Figure 5.9) suggests that the radiation damage as indicated by alpha dose calculated based on the magmatic crystallization

age is likely overestimated in all samples. Therefore, the stages after Murakami et al., (1991) quoted above reflect the highest possible stage of metamictization in these zircon grains.

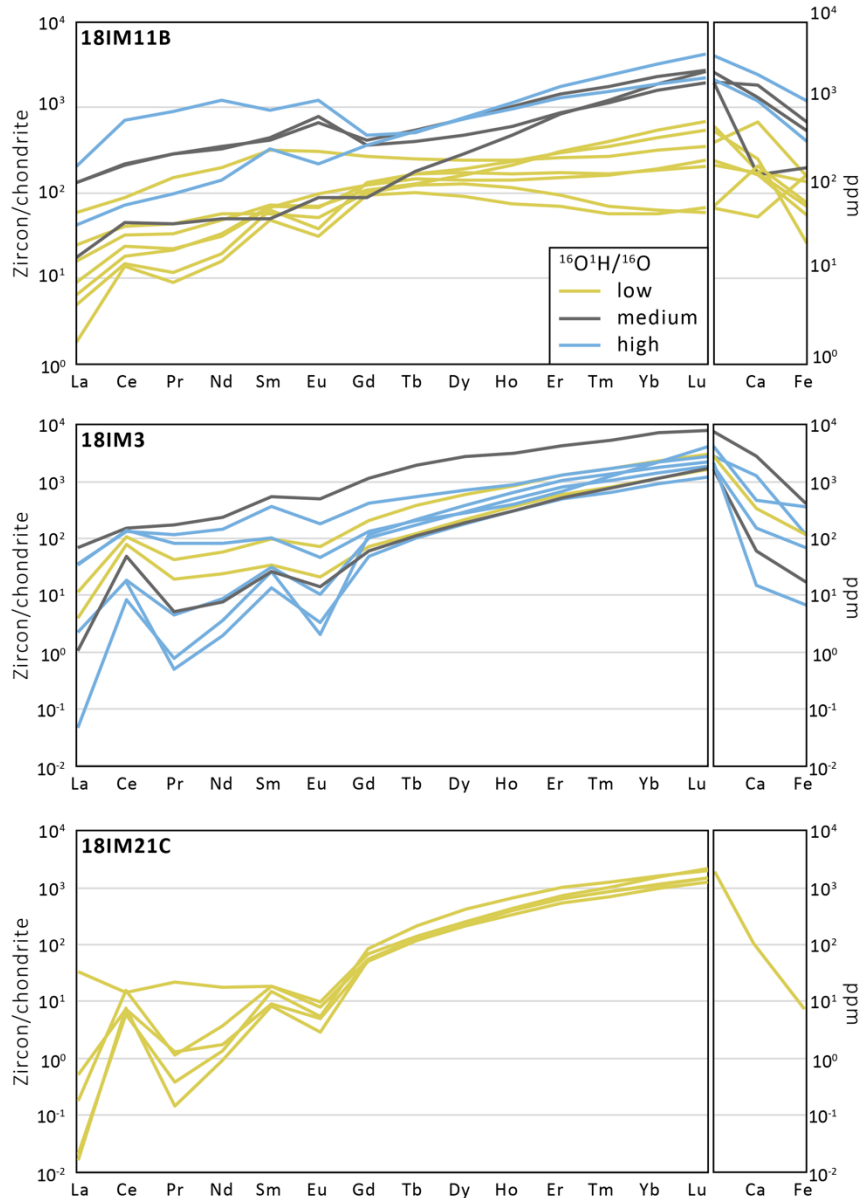


Figure 5.6. Chondrite-normalized REE pattern and Ca and Fe concentrations (not normalized) of zircon from samples 18IM11B, 18IM3, and 18IM21C color-coded by OH-content (low: $^{16}\text{O}^{1\text{H}}/^{16}\text{O}$ within 50% of crystalline reference, medium: within 200%, high: $\geq 200\%$ deviation). Chondrite values are from (Sun and McDonough, 1989). Note that zero values are not shown.

5.4. Discussion

5.4.1. Water uptake in zircon through primary and secondary processes

Common elevation of zircon $^{16}\text{O}^1\text{H}/^{16}\text{O}$ compared to the crystalline reference and the presence of a Raman band at $\sim 3420 \text{ cm}^{-1}$ indicate the presence of water in the zircon crystals of this study. No agreement has been reached upon the question of whether water in zircon is present exclusively in the form of OH^- , or as a combination of both OH^- , and molecular H_2O (Nasdala, 2001; Woodhead et al., 1991). SIMS analysis measures water as OH^- , whereas H_2O will not be recognised. However, water present as H_2O will likely be ionized to OH^- during SIMS analysis, and hence, detected as OH^- (Pidgeon et al., 2013). The Raman band at $\sim 3420 \text{ cm}^{-1}$ observed in all but one Raman spectrum may be caused by OH^- in the crystal structure or by molecular H_2O (Bell et al., 2004; Trail et al., 2011).

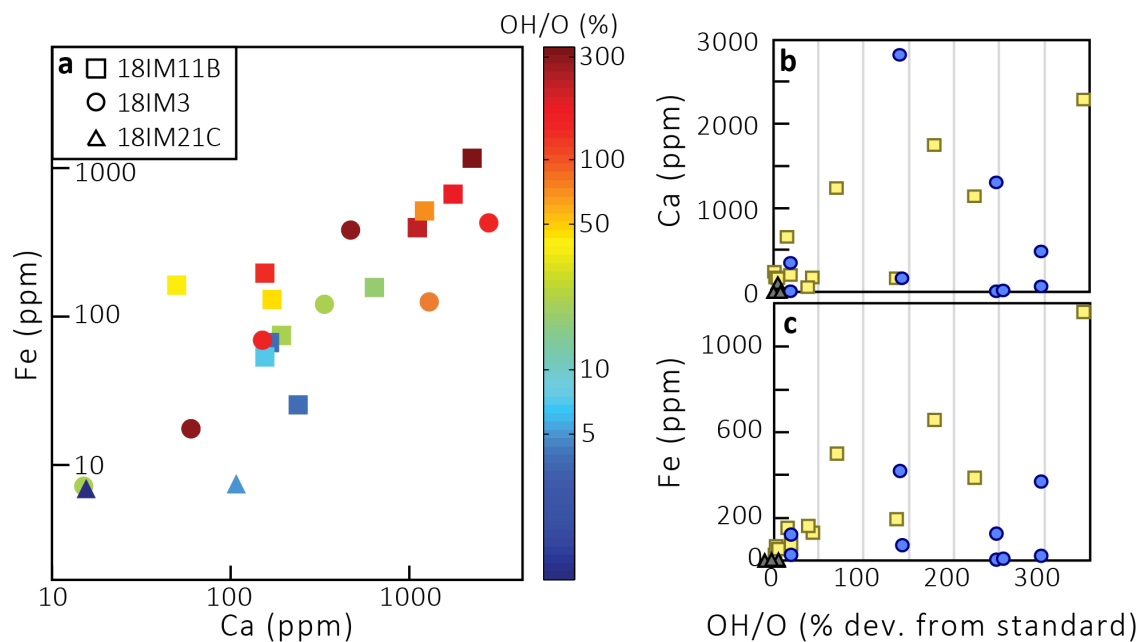


Figure 5.7. (a) Zircon Ca and Fe concentration color-coded by water content ($^{16}\text{O}^1\text{H}/^{16}\text{O}$ from crystalline reference). Note that zero values are not shown. **(b)** Zircon Ca and **(c)** Fe concentrations vs. zircon water content ($^{16}\text{O}^1\text{H}/^{16}\text{O}$ % deviation from crystalline reference).

The correlation of FWHM of the $\nu_3(\text{SiO}_4)$ Raman band and $^{16}\text{O}^1\text{H}/^{16}\text{O}$ suggests that the uptake of water in the samples studied here is predominantly the result of metamictization. Leaching experiments have shown that the interaction of metamict zircon with hydrothermal solutions

leads to loss of Si, U, Th, and Pb, whereas Al, Ca, and water infiltrate the zircon structure to maintain charge balance (Geisler et al., 2002). An increasing degree of metamictization of zircon results in a decrease in Raman intensity and a line-broadening of Raman modes (Ming et al., 2000). Furthermore, it has been suggested that the broadening of the $\nu_3(\text{SiO}_4)$ band is the Raman spectral parameter that is most sensitive to metamictization (Nasdala et al., 2001). A positive correlation of alpha dose and zircon $^{16}\text{O}^1\text{H}/^{16}\text{O}$ (Figure 5.5) shown by samples 18IM11B and 18IM3 further supports that the accumulation of radiation damage facilitated the uptake of water in these samples. Sample 18IM21C does not show a correlation between alpha dose and $^{16}\text{O}^1\text{H}/^{16}\text{O}$, which is not surprising given that the zircon of this sample is generally low in $^{16}\text{O}^1\text{H}/^{16}\text{O}$. Previous studies report increasing REE content, and the incorporation of non-formula elements correlated with the accumulation of radiation damage in zircon (Horie et al., 2006; Wang et al., 2014). Increasing concentrations of non-formula elements (Ca, and Fe) and REE in sample 18IM11B (Figures 5.6 and 5.7) with increasing zircon $^{16}\text{O}^1\text{H}/^{16}\text{O}$ supports that the uptake of water in these zircon grains is linked to metamictization. Four high $\delta^{18}\text{O}$ zircon grains of sample 18IM11B show a positive Eu anomaly ($\text{Eu/Eu}^*=1.28-1.71$) which has been observed in metamict zircon previously (Horie et al., 2006). Sample 18IM3 shows no clear correlation of zircon water content and REE or non-formula element concentrations. Hence, in this sample the accumulation of radiation damage and concomitant uptake of water was not accompanied by incorporation of REE and non-formula elements in zircon.

The presence of the Raman band at $\sim 3400 \text{ cm}^{-1}$ (assigned to OH-stretching, or H-O-H bending; Bell et al., 2004; Trail et al., 2011) in Raman spectra of zircon grains with low $^{16}\text{O}^1\text{H}/^{16}\text{O}$ (within 50% of the crystalline reference), and small $\nu_3(\text{SiO}_4)$ FWHM implies that small amounts of water in these grains may have been incorporated through primary processes during crystallization of zircon. Previous studies show that fully crystalline zircon can contain up to 0.2 wt% water (De Hoog et al., 2014; Trail et al., 2011). The mechanisms that have been suggested for primary OH⁻ incorporation into zircon are hydrogrossular-type substitution of SiO₄ tetrahedrons [$4(\text{OH})^- \leftrightarrow (\text{SiO}_4)^4-$] (Trail et al., 2011), and charge balance substitution [$\text{H}^+ + \text{REE}^{3+} \leftrightarrow \text{Zr}^{4+}$] (De Hoog et al., 2014). As hydrogrossular-type substitution requires a Si vacancy, it should be more likely to occur in rocks with low silica activities (De Hoog et al.,

2014), as is the case for zircon from a kimberlite reported by Bell et al. (2004). However, samples 18IM3, 18IM11B, and 18IM21C have whole-rock SiO₂ concentrations of 62 to 82 wt% (Table 5.2). Hence, charge balance substitution associated with Y³⁺+REE³⁺ taking the place of Zr⁴⁺ in the crystal lattice (De Hoog et al., 2014) seems to be the more likely mechanism responsible for the primary uptake of water in the zircon samples of this study. This is supported by the excess of Y³⁺+REE³⁺ over P⁵⁺ in these zircon grains (Figure 5.8), indicating that Y³⁺+REE³⁺ are only partially charge balanced P⁵⁺ (De Hoog et al., 2014). The presence of primary OH in the zircon structure may facilitate the metamictization of zircon, and associated uptake of secondary water (Caruba et al., 1985). This is supported by our data that indicate a positive correlation between excess of zircon Y³⁺+REE³⁺ over P⁵⁺ and ¹⁶O¹H/¹⁶O (Figure 5.8).

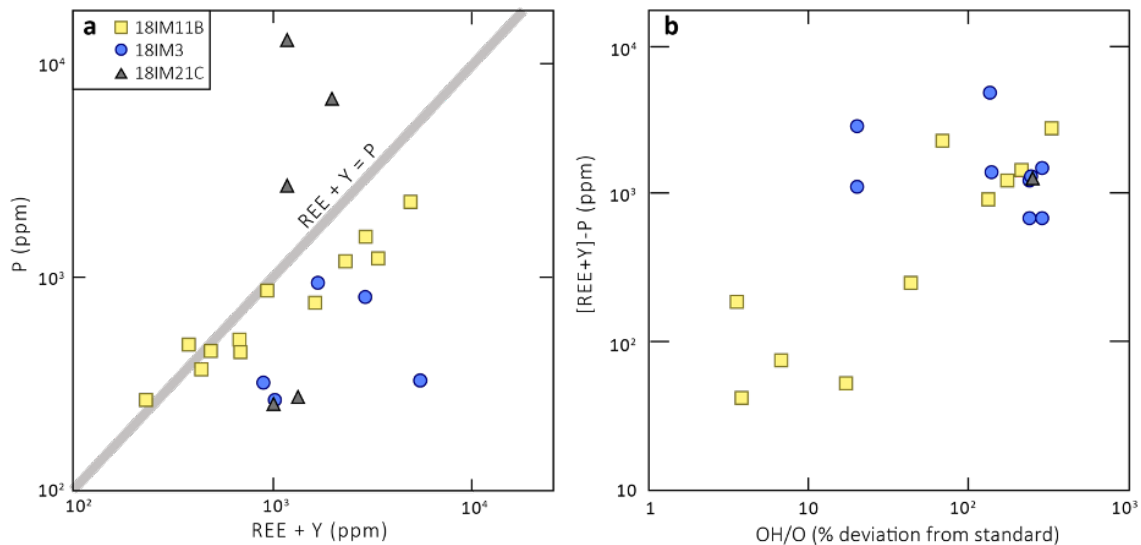


Figure 5.8. (a) Zircon REE+Y and P concentration. P⁵⁺ partially charge-balances REE³⁺ and Y³⁺ replacing Zr⁴⁺ in the zircon crystal lattice. An excess of REE³⁺ and Y³⁺ over P⁵⁺ may lead to the incorporation of water through a charge balance substitution [H⁺ + REE³⁺ ↔ Zr⁴⁺] (De Hoog et al., 2014). (b) Excess of zircon Y³⁺+REE³⁺ over P⁵⁺ vs. ¹⁶O¹H/¹⁶O. The presence of primary OH in the zircon structure may facilitate the metamictization of zircon, and associated uptake of secondary water (Caruba et al., 1985).

major element concentrations (reported as oxide wt%)	sample ID		
	18IM11B	18IM21C	18IM3
SiO₂	61.93	81.84	77.57
TiO₂	1.06	0.04	0.37
Al₂O₃	18.04	8.75	10.88
Fe₂O₃	6.58	2.84	3.01
MgO	2.18	0.65	0.87
CaO	2.88	1.11	1.03
Na₂O	2.80	2.19	2.23
K₂O	3.58	0.76	2.72
P₂O₅	0.07	0.18	0.05
MnO	0.06	0.18	0.05
LOI	0.22	0.93	0.68
Total	99.38	99.48	99.45

Table 5.2. Whole rock major element concentrations. Data is from Liebmann et al. (submitted to Terra Nova).

5.4.2. The effect of water uptake on zircon δ¹⁸O

The water content of zircon strongly influences the recorded δ¹⁸O values (Figure 5.2) and may lead to heterogenous δ¹⁸O values in igneous zircon populations (Figure 5.3). All igneous zircon samples of this study show a trend towards lower δ¹⁸O values with increasing ¹⁶O¹H/¹⁶O content. Two samples (18IM11B, and 19GH1) show an additional trend towards higher δ¹⁸O values with increasing ¹⁶O¹H/¹⁶O. This observation is in accord with previous studies that reported shifts to isotopically heavier and lighter values associated with post-crystallization alteration of zircon (e.g. Van Kranendonk et al., 2015; Pidgeon et al., 2017). Fractionation of zircon oxygen isotopes in opposite directions with increasing ¹⁶O¹H/¹⁶O implies that multiple processes affect δ¹⁸O during interaction of water with metamict zircon. Zircon formed in magmatic environments typically exhibits δ¹⁸O values ranging from 5-10‰ (e.g. Eiler, 2001). Meteoric waters, in contrast, have δ¹⁸O values below ~0‰, as they are generally depleted in ¹⁸O compared to seawater (Dansgaard, 1964). Thus, the influx of meteoric water into metamict parts of zircon grains to maintain local charge balance, shifts zircon δ¹⁸O towards isotopically lighter values (Pidgeon et al., 2017). The reverse trend of increasing zircon δ¹⁸O values with increasing ¹⁶O¹H/¹⁶O can be rationalised as the result of equilibrium fractionation of oxygen isotopes between percolating water and zircon (Pidgeon et al., 2017). Equilibrium fractionation

between two phases leads to enrichment of the heavy isotope (^{18}O in this case) in the phase with higher bond strength (Young et al., 2002). The magnitude of equilibrium fractionation is strongly temperature-dependent, and can be large for water and crystalline silicates or amorphous silica phases (i.e. resulting in several 10‰ difference in $\delta^{18}\text{O}$ values of the equilibrated phases; e.g. Clayton et al., 1972; Kita et al., 1985). Hence, the exchange of oxygen isotopes between zircon and percolating water leads to enrichment of ^{18}O in zircon, whereas ^{16}O is preferably released into solution, resulting in an increase in zircon $\delta^{18}\text{O}$ (Pidgeon et al., 2017). The fact that all igneous samples show a decreasing zircon $\delta^{18}\text{O}$ trend with increasing $^{16}\text{O}^{1\text{H}}/^{16}\text{O}$, in contrast to only two samples additionally showing an increasing trend may be related to different reaction rates for the two alteration mechanisms: Namely, relatively rapid influx of water into zircon, and relatively slow exchange of oxygen isotopes between water and zircon (Pidgeon et al., 2017).

The shift towards isotopically heavier and lighter $\delta^{18}\text{O}$ values related to uptake of water into metamict zircon is also evident from the detrital and igneous zircon data shown in Figure 5.10. The application of a $^{16}\text{O}^{1\text{H}}/^{16}\text{O}$ filter reduces the scatter in $\delta^{18}\text{O}$ values, and reveals distinct peaks that would otherwise be masked by $\delta^{18}\text{O}$ data from zircon grains affected by water uptake. In the case of the detrital zircon data shown in Figure 5.10a, neglection of a $^{16}\text{O}^{1\text{H}}/^{16}\text{O}$ filter leads to a significant overestimation of supracrustal component (indicated by high $\delta^{18}\text{O}$ values > 6‰; e.g. Eiler, 2001) in the parent melts of the detrital zircon. The igneous zircon data shown in Figure 5.10b shows a tail towards low $\delta^{18}\text{O}$ zircon if no $^{16}\text{O}^{1\text{H}}/^{16}\text{O}$ filter is applied, leading to reduced precision when estimating the primary oxygen isotopic composition of the parent magma. In contrast, the application of a $^{16}\text{O}^{1\text{H}}/^{16}\text{O}$ reveals distinct peaks in $\delta^{18}\text{O}$ values indicating that both detrital and igneous zircon are predominantly derived from melts in equilibrium with the mantle with $\delta^{18}\text{O} \sim 5\text{--}6\text{\textperthousand}$ (Eiler, 2001).

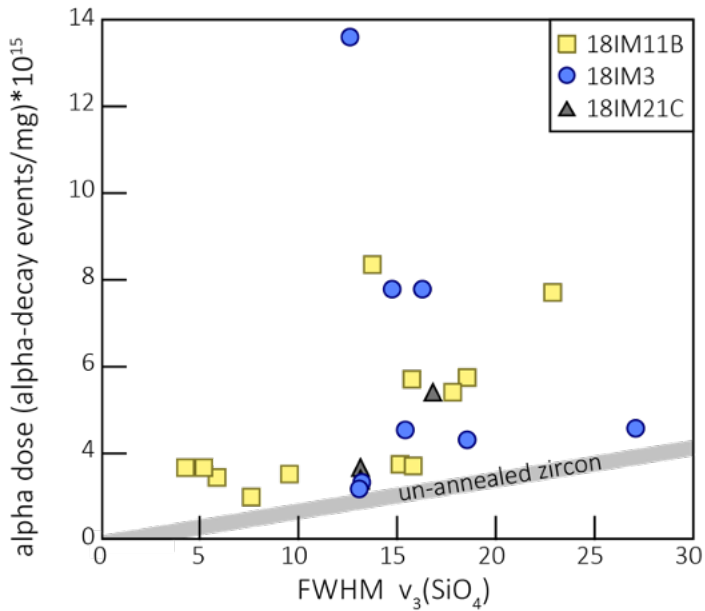


Figure 5.9. FWHM of the $v_3(\text{SiO}_4)$ Raman band vs. alpha dose. Both parameters are commonly used to quantify radiation damage in zircon (e.g. Murakami et al., 1991; Nasdala et al., 2001). Grey bar marks calibration line of zircon with nearly complete storage of radiation damage ('un-annealed zircon') after Nasdala et al. (2001).

5.4.3. Assessing disturbance of the zircon O isotopic system

Alpha dose and Raman spectroscopic parameters are commonly used to quantify metamictization of zircon (e.g. Murakami et al., 1991; Nasdala et al., 2001). It is therefore not surprising the samples studied here show a positive correlation of alpha dose, and FWHM of the $v_3(\text{SiO}_4)$ Raman band (Figure 5.9). However, radiation-induced structural damage can be healed through annealing (Geisler et al., 2001). As demonstrated by comparison of our data to the calibration line of un-annealed zircon from Nasdala et al. (2001) (Figure 5.9) the radiation damage as indicated by alpha dose calculated based on the magmatic crystallization age is likely overestimated in the samples of this study. While alpha dose, and Raman spectroscopic parameters can be useful as first order assessments of metamictization for zircon unaffected by annealing, these parameters are not nearly as sensitive as zircon $^{18}\text{O} / ^{16}\text{O}$ to detect disturbance of the zircon O isotopic system related to the accumulation of radiation damage. Our results demonstrate a significant shift in recorded $\delta^{18}\text{O}$ value in zircon with $^{18}\text{O} / ^{16}\text{O}$ 30% to 100% elevated to the crystalline reference (Figures 5.2 and 5.3). It should be noted, that these values

do not represent fixed cut-off values, as the background signal, and hence $^{16}\text{O}^1\text{H}/^{16}\text{O}$ of the crystalline reference, is strongly dependent on the pressure in the SIMS source chamber. Allowing longer degassing time for the epoxy mounts will lower the background signal and, hence, increase the sensitivity of $^{16}\text{O}^1\text{H}/^{16}\text{O}$. A novel sample preparation technique that utilizes alloy instead of epoxy mounts has been introduced to further reduce the signal of background water during SIMS analysis (Zhang et al., 2018). This method enables quantitative measurement of zircon water content by SIMS analysis (Xia et al., 2019). For epoxy grain mounts that allow qualitative monitoring of zircon $^{16}\text{O}^1\text{H}/^{16}\text{O}$ it is recommended to assess each analytical run individually, and to determine a session specific cut-off value for $^{16}\text{O}^1\text{H}/^{16}\text{O}$ filtering (i.e. $^{16}\text{O}^1\text{H}/^{16}\text{O}$ ‘threshold’ above which the overall scatter of $\delta^{18}\text{O}$ values increases significantly, Figure 5.3). A correlation of $\delta^{18}\text{O}$ value and $^{16}\text{O}^1\text{H}/^{16}\text{O}$ (as shown for the igneous and detrital zircon samples in Figures 5.2 and 5.10) is an indication that the oxygen isotope ratio recorded by zircon is affected by secondary uptake of water, and therefore should not be interpreted as primary.

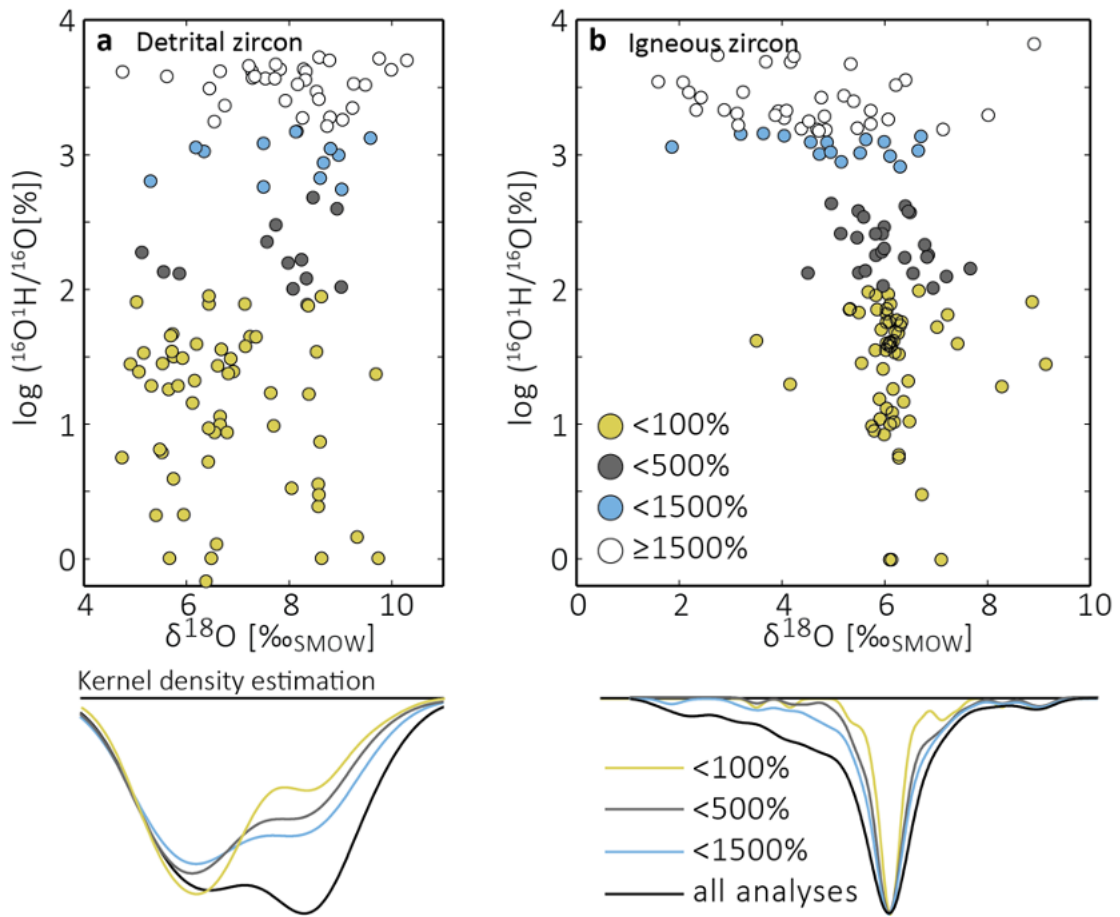


Figure 5.10. Zircon water content ($^{16}\text{O}^1\text{H}/^{16}\text{O}$) vs. $\delta^{18}\text{O}$ of (A) detrital and (B) igneous zircon from the Luliang complex, North China Craton. With increasing water content $\delta^{18}\text{O}$ values shift towards isotopically heavier or lighter values resulting in increasing scatter of $\delta^{18}\text{O}$. The application of a $^{16}\text{O}^1\text{H}/^{16}\text{O}$ filter (i.e. exclusion of high $^{16}\text{O}^1\text{H}/^{16}\text{O}$ zircon) indicates that detrital zircon (shown in A) and igneous zircon (shown in B) is predominantly derived from melts in equilibrium with the mantle with $\delta^{18}\text{O} \sim 5\text{--}6\text{\textperthousand}$. The inclusion of all data (i.e. no $^{16}\text{O}^1\text{H}/^{16}\text{O}$ filter is applied) leads to a significant overestimation of supracrustal component (indicated by high $\delta^{18}\text{O}$ values $> 6\text{\textperthousand}$) in the parent melts of the detrital zircon. In contrast, inclusion of all igneous zircon samples shown in B leads to a tail of low $\delta^{18}\text{O}$ zircon due to hydrothermal alteration. Legend in (B) refers to zircon water content (reported as percent deviation of zircon $^{16}\text{O}^1\text{H}/^{16}\text{O}$ to the crystalline reference) and applies to both parts of the figure.

5.5. Concluding remarks

Our results confirm that the uptake of water associated with the accumulation of radiation damage in zircon can strongly affect the recorded $\delta^{18}\text{O}$ values as indicated by previous studies

(Pidgeon et al., 2017, 2013; Wang et al., 2014). Furthermore, our results demonstrate that zircon $^{16}\text{O}^{1\text{H}}/^{16}\text{O}$ is a sensitive parameter to assess disturbance of the O isotopic system in zircon. As $^{16}\text{O}^{1\text{H}}/^{16}\text{O}$ can be measured simultaneously to $^{18}\text{O}/^{16}\text{O}$ during SIMS analysis, monitoring zircon water content provides a practicable tool to distinguish primary from secondary oxygen isotopic signatures in zircon. It is therefore recommended to interpret zircon $\delta^{18}\text{O}$ in tandem with $^{16}\text{O}^{1\text{H}}/^{16}\text{O}$, especially for samples with heterogenous zircon $\delta^{18}\text{O}$ values, and detrital zircon data.

5.6 References

- Baertschi, P., 1976, Absolute ^{18}O content of standard mean ocean water: Earth and Planetary Science Letters, v. 31, p. 341–344, doi:10.1016/0012-821X(76)90115-1.
- Bell, D.R., Rossman, G.R., and Morre, R.O., 2004, Abundance and Partitioning of OH in a High-pressure Magmatic System: Megacrysts from the Monastery Kimberlite, South Africa: Journal of Petrology, v. 45, p. 1539–1564, doi:10.1093/petrology/egh015.
- Belousova, E., Griffin, W., O'Reilly, S.Y., and Fisher, N., 2002, Igneous zircon: trace element composition as an indicator of source rock type: Contributions to Mineralogy and Petrology, v. 143, p. 602–622, doi:10.1007/s00410-002-0364-7.
- Bindeman, I.N., Schmitt, A.K., Lundstrom, C.C., and Hervig, R.L., 2018, Stability of Zircon and Its Isotopic Ratios in High-Temperature Fluids: Long-Term (4 months) Isotope Exchange Experiment at 850°C and 50 MPa: Frontiers in Earth Science, v. 6, doi:10.3389/feart.2018.00059.
- Black, L.P. et al., 2004, Improved $^{206}\text{Pb}/^{238}\text{U}$ microprobe geochronology by the monitoring of a trace-element-related matrix effect; SHRIMP, ID-TIMS, ELA-ICP-MS and oxygen isotope documentation for a series of zircon standards: Chemical Geology, v. 205, p. 115–140, doi:10.1016/j.chemgeo.2004.01.003.
- Caruba, R., Baumer, A., Ganteaume, M., and Iacconi, P., 1985, An experimental study of hydroxyl groups and water in synthetic and natural zircons: a model of the metamict state: American Mineralogist, v. 70, p. 1224–1231.
- Clayton, R.N., O'Neil, J.R., and Mayeda, T.K., 1972, Oxygen isotope exchange between quartz and water: Journal of Geophysical Research, v. 77, p. 3057–3067, doi:10.1029/JB077i017p03057.
- Coleman, R.G., and Erd, R.C., 1961, Hydrozircon from the wind river formation, Wyoming: Journal of Research of the US Geological Survey, v. 256, p. 297–300.
- Dansgaard, W., 1964, Stable isotopes in precipitation: Tellus, v. 16, p. 436–468, doi:10.3402/tellusa.v16i4.8993.

- Dawson, P., Hargreave, M.M., and Wilkinson, G.R., 1971, The vibrational spectrum of zircon (ZrSiO_4): *Journal of Physics C: Solid State Physics*, v. 4, p. 240.
- Eiler, J.M., 2001, Oxygen Isotope Variations of Basaltic Lavas and Upper Mantle Rocks, *in* Valley, J.W. and Cole, D.R. eds., Stable Isotope Geochemistry. Reviews in Mineralogy and Geochemistry, Mineralogical Society of America/Geochemical Society, Washington, DC, p. 319–364.
- Geisler, T., Pidgeon, R.T., van Bronswijk, W., and Kurtz, R., 2002, Transport of uranium, thorium, and lead in metamict zircon under low-temperature hydrothermal conditions: *Chemical Geology*, v. 191, p. 141–154, doi:10.1016/S0009-2541(02)00153-5.
- Geisler, T., Pidgeon, R.T., van Bronswijk, W., and Pleysier, R., 2001, Kinetics of thermal recovery and recrystallization of partially metamict zircon: a Raman spectroscopic study: *European Journal of Mineralogy*, v. 13, p. 1163–1176, doi:10.1127/0935-1221/2001/0013-1163.
- Holland, H.D., and Gottfried, D., 1955, The effect of nuclear radiation on the structure of zircon: *Acta Crystallographica*, v. 8, p. 291–300, doi:10.1107/S0365110X55000947.
- De Hoog, J.C.M., Lissenberg, C.J., Brooker, R.A., Hinton, R., Trail, D., and Hellebrand, E., 2014, Hydrogen incorporation and charge balance in natural zircon: *Geochimica et Cosmochimica Acta*, v. 141, p. 472–486, doi:10.1016/j.gca.2014.06.033.
- Horie, K., Hidaka, H., and Gauthier-Lafaye, F., 2006, Elemental distribution in zircon: Alteration and radiation-damage effects: *Physics and Chemistry of the Earth, Parts A/B/C*, v. 31, p. 587–592, doi:10.1016/j.pce.2006.01.001.
- Kirkland, C.L., Whitehouse, M.J., Pease, V., and Van Kranendonk, M., 2010, Oxygen isotopes in detrital zircons: Insight into crustal recycling during the evolution of the Greenland Shield: *Lithosphere*, v. 2, p. 3–12, doi:10.1130/L80.1.
- Kita, I., Taguchi, S., and Matsubaya, O., 1985, Oxygen isotope fractionation between amorphous silica and water at 34–93°C: *Nature*, v. 314, p. 83–84, doi:10.1038/314083a0.
- Van Kranendonk, M.J., and Kirkland, C.L., 2013, Orogenic climax of Earth: The 1.2-1.1 Ga Grenvillian superevent: *Geology*, v. 41, p. 735–738, doi:10.1130/G34243.1.
- Van Kranendonk, M.J., Kirkland, C.L., and Cliff, J., 2015, Oxygen isotopes in Pilbara Craton zircons support a global increase in crustal recycling at 3.2Ga: *Lithos*, v. 228–229, p. 90–98, doi:10.1016/j.lithos.2015.04.011.
- Liebmann, J., Spencer, C.J., Kirkland, C.L., Bucholz, C.E., He, X., Santosh, M., Xia, X.-P., Martin, L., and Evans, N.J., 2020a, Emergence of continents above sea-level influences composition of sediment melts: submitted to *Terra Nova*.
- Liebmann, J., Spencer, C.J., Kirkland, C.L., Bucholz, C.E., Xia, X.-P., Martin, L., Kitchen, N., and Shumlyansky, L., 2020b, Coupling of the atmosphere and sediment melts across the

Archean-Proterozoic transition: Communications Earth & Environment, doi:10.21203/rs.3.rs-55162/v1.

Ming, Z., Salje, E.K.H., Farnan, I., Graeme-Barber, A., Daniel, P., Ewing, R.C., Clark, A.M., and Leroux, H., 2000, Metamictization of zircon: Raman spectroscopic study: Journal of Physics: Condensed Matter, v. 12, p. 1915–1925.

Murakami, T., Chakoumakos, B.C., Ewing, R.C., Lumpkin, G.R., and Weber, W.J., 1991, Alpha-decay event damage in zircon: American Mineralogist, v. 76.

Nasdala, L., 2003, Spectroscopic methods applied to zircon: Reviews in Mineralogy and Geochemistry, v. 53, p. 427–467, doi:10.2113/0530427.

Nasdala, 2001, The incorporation of hydroxyl groups and molecular water in natural zircon (ZrSiO₄): American Journal of Science, v. 301, p. 831–857, doi:10.2475/ajs.301.10.831.

Nasdala, L., Wenzel, M., Vavra, G., Irmer, G., Wenzel, T., and Kober, B., 2001, Metamictisation of natural zircon: Accumulation versus thermal annealing of radioactivity-induced damage: Contributions to Mineralogy and Petrology, v. 141, p. 125–144, doi:10.1007/s004100000235.

Paton, C., Hellstrom, J., Paul, B., Woodhead, J., and Hergt, J., 2011, Iolite: Freeware for the visualisation and processing of mass spectrometric data: Journal of Analytical Atomic Spectrometry, v. 26, p. 2508, doi:10.1039/c1ja10172b.

Pearce, N.J.G., Perkins, W.T., Westgate, J.A., Gorton, M.P., Jackson, S.E., Neal, C.R., and Chenery, S.P., 1997, A Compilation of New and Published Major and Trace Element Data for NIST SRM 610 and NIST SRM 612 Glass Reference Materials: Geostandards and Geoanalytical Research, v. 21, p. 115–144, doi:10.1111/j.1751-908X.1997.tb00538.x.

Pidgeon, R.T., Nemchin, A.A., and Cliff, J., 2013, Interaction of weathering solutions with oxygen and U–Pb isotopic systems of radiation-damaged zircon from an Archean granite, Darling Range Batholith, Western Australia: Contributions to Mineralogy and Petrology, v. 166, p. 511–523, doi:10.1007/s00410-013-0888-z.

Pidgeon, R.T., Nemchin, A.A., and Whitehouse, M.J., 2017, The effect of weathering on U-Th–Pb and oxygen isotope systems of ancient zircons from the Jack Hills, Western Australia: Geochimica et Cosmochimica Acta, v. 197, p. 142–166, doi:10.1007/s11947-009-0181-3.

Schmitt, A.K., Magee Jr., C.W., Williams, I.S., Holden, P., Ireland, T.R., DiBugnara, D.L., and Bodorkos, S., 2019, Oxygen isotopic heterogeneity in the Temora-2 reference zircon;, doi:10.11636/Record.2019.004.

Spencer, C.J., Roberts, N.M.W., and Santosh, M., 2017, Growth, destruction, and preservation of Earth's continental crust: Earth-Science Reviews, v. 172, p. 87–106, doi:10.1016/j.earscirev.2017.07.013.

Sun, S. -s., and McDonough, W.F., 1989, Chemical and isotopic systematics of oceanic basalts:

- implications for mantle composition and processes: Geological Society, London, Special Publications, v. 42, p. 313–345, doi:10.1144/GSL.SP.1989.042.01.19.
- Syme, R.W.G., Lockwood, D.J., and Kerr, H.J., 1977, Raman spectrum of synthetic zircon (ZrSiO_4) and thorite (ThSiO_4): Journal of Physics C: Solid State Physics, v. 10, p. 1335–1348, doi:10.1088/0022-3719/10/8/036.
- Trail, D., Thomas, J.B., and Watson, E.B., 2011, The incorporation of hydroxyl into zircon: American Mineralogist, v. 96, p. 60–67, doi:10.2138/am.2011.3506.
- Valley, J.W. et al., 2005a, 4.4 billion years of crustal maturation: Oxygen isotope ratios of magmatic zircon: Contributions to Mineralogy and Petrology, v. 150, p. 561–580, doi:10.1007/s00410-005-0025-8.
- Valley, J.W. et al., 2005b, 4.4 billion years of crustal maturation: Oxygen isotope ratios of magmatic zircon: Contributions to Mineralogy and Petrology, v. 150, p. 561–580, doi:10.1007/s00410-005-0025-8.
- Valley, J.W., 2003, Oxygen Isotopes in Zircon: Reviews in Mineralogy and Geochemistry, v. 53, p. 343–385, doi:10.2113/0530343.
- Valley, J.W., Bindeman, I.N., and Peck, W.H., 2003, Empirical calibration of oxygen isotope fractionation in zircon: Geochimica et Cosmochimica Acta, v. 67, p. 3257–3266, doi:10.1016/S0016-7037(03)00090-5.
- Valley, J.W., Peck, W.H., King, E.M., and Wilde, S.A., 2002, A cool early Earth: Geology, v. 30, p. 351, doi:10.1130/0091-7613(2002)030<0351:ACEE>2.0.CO;2.
- Wang, X.-L., Coble, M.A., Valley, J.W., Shu, X.-J., Kitajima, K., Spicuzza, M.J., and Sun, T., 2014, Influence of radiation damage on Late Jurassic zircon from southern China: Evidence from in situ measurements of oxygen isotopes, laser Raman, U–Pb ages, and trace elements: Chemical Geology, v. 389, p. 122–136, doi:10.1016/j.chemgeo.2014.09.013.
- Wiedenbeck, M. et al., 2004, Further characterisation of the 91500 zircon crystal: Geostandards and Geoanalytical Research, v. 28, p. 9–39, doi:10.1111/j.1751-908X.2004.tb01041.x.
- Wojdyr, M., 2010, Fityk: a general-purpose peak fitting program: Journal of Applied Crystallography, v. 43, p. 1126–1128, doi:10.1107/S0021889810030499.
- Woodhead, J.A., Rossman, G.R., and Thomas, A.P., 1991, Hydrous species in zircon: American Mineralogist, v. 76, p. 1533–1546.
- Xia, X.-P., Cui, Z.-X., Li, W., Zhang, W.-F., Yang, Q., Hui, H., and Lai, C.-K., 2019, Zircon water content: reference material development and simultaneous measurement of oxygen isotopes by SIMS: Journal of Analytical Atomic Spectrometry, v. 34, p. 1088–1097, doi:10.1039/C9JA00073A.

Yang, Q., Xia, X., Zhang, W., Zhang, Y., Xiong, B., Xu, Y., Wang, Q., and Wei, G., 2018, An evaluation of precision and accuracy of SIMS oxygen isotope analysis: Solid Earth Sciences, v. 3, p. 81–86, doi:10.1016/j.sesci.2018.05.001.

Young, E.D., Galy, A., and Nagahara, H., 2002, Kinetic and equilibrium mass-dependent isotope fractionation laws in nature and their geochemical and cosmochemical significance: *Geochimica et Cosmochimica Acta*, v. 66, p. 1095–1104, doi:10.1016/S0016-7037(01)00832-8.

Zhang, W., Xia, X., Zhang, Y., Peng, T., and Yang, Q., 2018, A novel sample preparation method for ultra-high vacuum (UHV) secondary ion mass spectrometry (SIMS) analysis: *Journal of Analytical Atomic Spectrometry*, v. 33, p. 1559–1563, doi:10.1039/C8JA00087E.

5.7 Author contributions

JL, CJS, CLK designed the research or contributed to designing the research. JL, XX, JB carried out the analyses. JL wrote the manuscript. All authors contributed to interpreting the data, and provided comments on the manuscript.

Appendices

Supplementary Table A1: Single spot zircon O, U-Pb, and Raman data.

Supplementary Table A2: Zircon trace element data.

Supplementary Table A3: Oxygen isotopic and $^{16}\text{O}^1\text{H}/^{16}\text{O}$ data of reference materials for SIMS analytical runs.

Appendix A

sample ID	grain/spot ID	#O run	$\delta^{18}\text{O}$ (‰)	${}^{16}\text{O} / {}^{18}\text{O}$	${}^{16}\text{O} {}^{1\text{H}} / {}^{16}\text{O}$	1σ	${}^{16}\text{O} {}^{1\text{H}} / {}^{16}\text{O}$ deviation from background (average OH/O reference zircon)	${}^{16}\text{O} {}^{1\text{H}} / {}^{16}\text{O}$ background (‰)	${}^{238}\text{U}$ (ppm)	${}^{226}\text{Th}$ (ppm)	Disc. (%)	Ref. O isotope data
18IM1B	18IM1B.02	1	11.54	0.45	6.40E-03	2.23E-05	2.27E-03	182	3.67E+15	468	60	32.9
18IM1B	18IM1B.03	1	11.05	0.43	2.37E-03	7.34E-06	2.27E-03	4	1.42E+15	172	66	4.0
18IM1B	18IM1B.04	1	14.71	0.47	1.05E-02	7.60E-06	2.27E-03	363				
18IM1B	18IM1B.05	1	10.08	0.45	5.43E-03	1.97E-05	2.27E-03	139	5.68E+15	713	148	3.7
18IM1B	18IM1B.06	1	10.97	0.47	2.75E-03	1.90E-05	2.27E-03	21	1.70E+15	211	57	2.1
18IM1B	18IM1B.07	1	10.18	0.46	2.38E-03	7.84E-06	2.27E-03	5	1.63E+15	194	98	0.4
18IM1B	18IM1B.08	1	10.77	0.45	2.44E-03	4.14E-06	2.27E-03	8	1.48E+15	178	79	-2.8
18IM1B	18IM1B.09	1	10.88	0.43	3.07E-03	8.99E-06	2.27E-03	36				
18IM1B	18IM1B.1	1	12.07	0.55	2.69E-03	9.66E-06	2.27E-03	19	1.68E+15	205	75	21.5
18IM1B	18IM1B.10	1	11.13	0.45	2.67E-03	2.13E-06	2.27E-03	18				
18IM1B	18IM1B.11	1	5.21	0.68	1.02E-02	5.86E-05	2.27E-03	348	6.31E+15	812	67	27.6
18IM1B	18IM1B.12	1	8.49	0.63	3.32E-03	1.77E-05	2.27E-03	46	1.63E+15	192	108	1.2
18IM1B	18IM1B.13	1	9.00	0.47	3.19E-03	1.24E-05	2.27E-03	41	9.38E+14	106	85	-1.8
18IM1B	18IM1B.17	1	16.59	0.45	1.12E-02	9.66E-06	2.27E-03	395				
18IM1B	18IM1B.4-14	1	8.24	0.46	7.40E-03	1.09E-05	2.27E-03	226	3.69E+15	469	66	20.1
18IM1B	18IM1B.4-15	1	10.80	0.40	3.92E-03	1.18E-05	2.27E-03	73	3.35E+15	385	262	21.9
18IM1B	18IM1B.4-16	1	10.38	0.41	4.86E-03	5.96E-06	2.27E-03	114				
18IM3	18IM3.07	2	11.82	0.40	2.16E-03	3.02E-06	1.95E-03	11				
18IM3	18IM3.08	2	11.15	0.43	3.46E-03	8.58E-06	1.95E-03	78				
18IM3	18IM3.09	2	11.16	0.43	4.79E-03	1.31E-05	1.95E-03	146	2.27E+15	273	101	9.9
18IM3	18IM3.1	2	9.03	0.40	7.82E-03	2.43E-06	1.95E-03	302	2.54E+15	312	83	6.8
18IM3	18IM3.10	2	9.77	0.41	4.74E-03	2.33E-05	1.95E-03	144	1.16E+16	1389	536	42.6
18IM3	18IM3.11	2	11.56	0.41	2.37E-03	9.37E-06	1.95E-03	22	1.22E+15	143	111	9.4
18IM3	18IM3.11	2	11.56	0.41	2.37E-03	9.37E-06	1.95E-03	22	5.75E+15	717	134	17.9
18IM3	18IM3.12	2	11.13	0.40	3.36E-03	2.23E-05	1.95E-03	73				
18IM3	18IM3.13	2	7.61	0.42	4.22E-03	7.92E-06	1.95E-03	117				
18IM3	18IM3.14	2	11.05	0.40	3.47E-03	1.70E-06	1.95E-03	78				
18IM3	18IM3.15	2	11.89	0.45	3.83E-03	9.08E-06	1.95E-03	97				
18IM3	18IM3.16	2	10.41	0.41	1.97E-03	2.87E-06	1.95E-03	1				
18IM3	18IM3.17	2	8.40	0.50	6.99E-03	6.69E-06	1.95E-03	259	1.13E+15	127	96	-2.2
18IM3	18IM3.4	2	11.85	0.40	2.70E-03	2.46E-06	1.95E-03	39	3.69E+15	463	69	-1.1
18IM3	18IM3.6	2	7.76	0.41	6.84E-03	5.69E-06	1.95E-03	252	2.51E+15	313	57	34.4

Table A1.1. SIMS zircon O isotopes, and U-Th-Pb data. 1 Liebmann et al., submitted to Terra Nova.

sample ID	grain/spot ID	#O mm	$\delta^{18}\text{O}$ (‰ SMOW)	background			OH/O (average OH/O reference zircon)	deviation from background (%)	alpha dose (ppm)	^{238}U (ppm)	^{232}Th (ppm)	Disc. (%)	Ref. O isotope data
				2σ	$^{16}\text{O}^{1\text{H}}/\text{O}^{16}$	1σ							
18IM3	18IM3.6	2	7.76	0.41	6.84E-03	5.69E-06	1.95E-03	252	2.57E+15	324	46	-2.0	1
18IM21C	18IM21C.02	2	7.04	0.40	2.07E-03	5.07E-06	1.95E-03	6	3.40E+15	431	134	-1.3	1
18IM21C	18IM21C.02	2	7.04	0.40	2.07E-03	5.07E-06	1.95E-03	6	2.10E+15	259	123	0.7	1
18IM21C	18IM21C.03	2	6.66	0.40	1.82E-03	4.45E-06	1.95E-03	-6					1
18IM21C	18IM21C.04	2	7.21	0.39	1.85E-03	1.57E-06	1.95E-03	-5					1
18IM21C	18IM21C.05	2	6.69	0.41	1.78E-03	5.12E-06	1.95E-03	-9	1.37E+15	155	148	-0.3	1
18IM21C	18IM21C.05	2	6.69	0.41	1.78E-03	5.12E-06	1.95E-03	-9	1.68E+15	186	198	-1.0	1
18IM21C	18IM21C.06	2	6.52	0.41	2.12E-03	1.67E-06	1.95E-03	9					1
18IM21C	18IM21C.07	2	6.55	0.39	2.21E-03	4.38E-06	1.95E-03	14					1
18IM21C	18IM21C.08	2	7.09	0.41	1.93E-03	3.04E-06	1.95E-03	-1	1.39E+15	167	101	0.7	1
18IM21C	18IM21C.09	2	6.50	0.39	1.90E-03	7.70E-07	1.95E-03	-2					1
18IM21C	18IM21C.1	2	6.37	0.40	2.09E-03	1.82E-06	1.95E-03	8					1
18IM21C	18IM21C.10	2	6.86	0.39	2.03E-03	3.43E-06	1.95E-03	4					1
18IM21C	18IM21C.11	2	6.65	0.41	2.06E-03	3.56E-06	1.95E-03	6					1
18IM21C	18IM21C.12	2	6.61	0.41	1.98E-03	2.51E-06	1.95E-03	2					1
18IM21C	18IM21C.13	2	3.61	0.42	5.08E-03	2.62E-05	1.95E-03	161					1
18IM21C	18IM21C.14	2	6.48	0.42	2.20E-03	5.55E-06	1.95E-03	13					1
18IM21C	18IM21C.15	2	6.88	0.40	2.11E-03	2.11E-06	1.95E-03	9					1
18IM21C	18IM21C.16	2	6.66	0.41	2.09E-03	3.70E-06	1.95E-03	7					1
18IM21C	18IM21C.17	2	6.31	0.41	1.95E-03	4.66E-06	1.95E-03	0					1
18IM21C	18IM21C.18	2	6.68	0.43	2.16E-03	1.96E-06	1.95E-03	11					1
18IM21C	18IM21C.19	2	6.87	0.42	2.08E-03	2.41E-06	1.95E-03	7					1
18IM21C	18IM21C.20	2	6.53	0.42	2.23E-03	1.45E-06	1.95E-03	15					1
18IM21C	18IM21C.21	2	6.27	0.42	3.13E-03	3.03E-06	1.95E-03	61					1
18IM21C	18IM21C.22	2	6.27	0.41	2.23E-03	4.53E-06	1.95E-03	15					1
19GH11B	19GH11B.core.10	3	5.63	0.83	5.35E-03	1.96E-05	4.73E-03	13					1
19GH11B	19GH11B.core.11	3	5.71	0.54	5.50E-03	2.53E-05	4.73E-03	16					1
19GH11B	19GH11B.core.3	3	5.56	0.69	5.79E-03	3.87E-05	4.73E-03	22					1
19GH11B	19GH11B.core.5	3	5.59	0.57	5.01E-03	2.05E-05	4.73E-03	6					1
19GH11B	19GH11B.core.9	3	5.02	0.66	5.15E-03	1.94E-05	4.73E-03	9					1
19GH11B	19GH11B.16	3	4.58	0.66	5.32E-03	3.41E-05	4.73E-03	12					1
19GH11B	19GH11B.20	3	5.21	0.75	5.37E-03	3.83E-05	4.73E-03	13					1

Table A1.1. Continued.

sample ID	grain/spot ID	#O min	$\delta^{18}\text{O}$ (‰)	2σ	${}^{16}\text{O}{}^{1\text{H}}/{}^{16}\text{O}$	1σ	OH/O (average OH/O reference zircon)	background	${}^{16}\text{O}{}^{1\text{H}}/{}^{16}\text{O}$ deviation from background (‰)
	SMOW								
19GH11B	19GH11B.21	3	3.23	0.63	8.97E-03	3.21E-05	4.73E-03	90	
19GH11B	19GH11B.22	3	3.37	0.73	8.77E-03	4.47E-05	4.73E-03	85	
19GH11B	19GH11B.23	3	2.61	0.83	1.16E-02	1.59E-05	4.73E-03	144	
19GH11B	19GH11B.core.12	3	4.78	0.62	6.75E-03	6.83E-05	4.73E-03	43	
19GH11B	19GH11B.core.8	3	2.27	0.49	1.18E-02	2.74E-05	4.73E-03	149	
19GH11B	19GH11B.03	3	2.85	0.65	1.13E-02	5.19E-05	4.73E-03	139	
19GH11B	19GH11B.04	3	2.19	0.60	1.03E-02	2.45E-05	4.73E-03	118	
19GH11B	19GH11B.05	3	3.52	0.55	7.59E-03	4.03E-05	4.73E-03	60	
19GH11B	19GH11B.06	3	2.55	0.70	1.31E-02	4.20E-05	4.73E-03	176	
19GH11B	19GH11B.07	3	1.78	0.45	1.09E-02	3.30E-05	4.73E-03	129	
19GH11B	19GH11B.08	3	3.17	0.68	1.25E-02	3.02E-05	4.73E-03	164	
19GH11B	19GH11B.09	3	1.35	0.59	1.15E-02	1.42E-05	4.73E-03	144	
19GH11B	19GH11B.10	3	4.30	0.60	7.96E-03	1.49E-05	4.73E-03	68	
19GH11B	19GH11B.11	3	3.77	0.60	1.27E-02	3.99E-05	4.73E-03		
19GH11B	19GH11B.12	3	4.12	0.61	9.87E-03	3.42E-05	4.73E-03		
19GH11B	19GH11B.14	3	2.69	0.56	1.34E-02	2.74E-05	4.73E-03		
19GH11B	19GH11B.15	3	2.97	0.84	1.04E-02	3.59E-05	4.73E-03		
19GH11B	19GH11B.18	3	2.32	0.60	1.11E-02	7.61E-06	4.73E-03		
19GH11B	19GH11B.2	3	3.84	0.47	1.23E-02	4.52E-05	4.73E-03		
17ZAN05	ZAN05A.1	4	2.52	0.43	7.44E-03	2.32E-06	5.56E-04	1238	
17ZAN05	ZAN05A.2	4	2.55	0.43	8.00E-03	3.46E-06	5.56E-04	1340	
17ZAN05	ZAN05A.4	4	5.48	0.45	1.90E-03	5.89E-06	5.56E-04	241	
17ZAN05	ZAN05A.5	4	2.75	0.43	8.41E-03	1.12E-05	5.56E-04	1413	
17ZAN05	ZAN05A.6	4	2.21	0.45	7.78E-03	1.04E-05	5.56E-04	1300	
17ZAN05	ZAN05A.7	4	4.33	0.44	5.25E-03	6.41E-06	5.56E-04	844	
17ZAN05	ZAN05A.8	4	3.90	0.42	6.29E-03	4.96E-06	5.56E-04	1032	
17ZAN05	ZAN05A.9	4	2.22	0.43	7.33E-03	5.54E-06	5.56E-04	1218	
17ZAN05	ZAN05A.10	4	2.76	0.42	6.92E-03	2.19E-06	5.56E-04	1145	
17ZAN05	ZAN05A.11	4	2.81	0.45	6.53E-03	1.48E-06	5.56E-04	1074	
17ZAN05	ZAN05A.12	4	4.96	0.43	3.56E-03	1.22E-05	5.56E-04	541	
17ZAN05	ZAN05A.13	4	5.49	0.43	2.58E-03	1.71E-05	5.56E-04	364	
17ZAN05	ZAN05A.14	4	3.62	0.42	5.94E-03	5.58E-06	5.56E-04	969	

Table A1.1. Continued.

sample ID	grain/spot ID	#O min	$\delta^{18}\text{O}$ (‰)	2σ	${}^{16}\text{O}{}^{1\text{H}}/{}^{16}\text{O}$	1σ	OH/O (average OH/O reference zircon)	background	${}^{16}\text{O}{}^{1\text{H}}/{}^{16}\text{O}$ deviation from background (‰)
ZAN05	ZAN05A.15	4	2.90	0.44	6.02E-03	1.27E-05	5.56E-04	982	
ZAN05	ZAN05A.16	4	2.26	0.43	7.32E-03	3.32E-06	5.56E-04	1217	
19GH1	19GH1.1	3	3.46	0.54	7.33E-03	3.43E-05	4.73E-03	55	
19GH1	19GH1.11	3	3.30	0.50	7.00E-03	2.55E-05	4.73E-03	48	
19GH1	19GH1.14	3	4.60	0.45	1.01E-02	3.42E-05	4.73E-03	114	
19GH1	19GH1.15	3	3.07	0.78	8.90E-03	3.45E-05	4.73E-03	88	
19GH1	19GH1.16	3	2.82	0.83	8.89E-03	2.17E-05	4.73E-03	88	
19GH1	19GH1.18	3	1.95	1.09	1.13E-02	1.55E-05	4.73E-03	139	
19GH1	19GH1.19	3	3.20	0.44	1.12E-02	6.12E-06	4.73E-03	138	
19GH1	19GH1.2	3	5.84	0.65	1.44E-02	6.19E-05	4.73E-03	204	
19GH1	19GH1.20	3	3.55	0.51	9.63E-03	1.67E-05	4.73E-03	103	
19GH1	19GH1.22	3	4.84	0.55	1.63E-02	3.49E-05	4.73E-03	244	
19GH1	19GH1.4	3	4.73	0.79	1.19E-02	3.69E-05	4.73E-03	151	
19GH1	19GH1.5	3	2.97	0.53	1.01E-02	1.16E-05	4.73E-03	113	
19GH1	19GH1.6	3	5.02	0.67	1.40E-02	4.50E-05	4.73E-03	195	
19GH1	19GH1.7	3	4.06	0.73	7.52E-03	2.78E-05	4.73E-03	59	
19GH1	19GH1.8	3	2.31	0.75	1.05E-02	1.82E-05	4.73E-03	122	
19GH9	19GH9.1	3	3.23	0.61	9.36E-03	5.01E-05	4.73E-03	98	
19GH9	19GH9.1.2	3	5.00	0.52	6.24E-03	2.85E-05	4.73E-03	32	
19GH9	19GH9.10	3	4.44	0.50	6.82E-03	1.14E-05	4.73E-03	44	
19GH9	19GH9.11	3	4.35	0.69	5.54E-03	2.76E-05	4.73E-03	17	
19GH9	19GH9.13	3	5.39	0.73	6.83E-03	1.31E-05	4.73E-03	44	
19GH9	19GH9.14	3	4.77	0.69	6.57E-03	4.36E-05	4.73E-03	39	
19GH9	19GH9.14.2	3	4.75	0.65	5.37E-03	2.57E-05	4.73E-03	14	
19GH9	19GH9.15	3	4.75	0.69	4.56E-03	3.55E-05	4.73E-03	4	
19GH9	19GH9.15.2	3	4.65	0.50	5.44E-03	1.83E-05	4.73E-03	15	
19GH9	19GH9.16	3	2.23	0.78	9.63E-03	1.60E-05	4.73E-03	103	
19GH9	19GH9.17	3	5.70	0.58	6.83E-03	5.58E-05	4.73E-03	44	
19GH9	19GH9.18	3	4.28	0.68	7.50E-03	8.86E-05	4.73E-03	59	
19GH9	19GH9.2	3	5.20	0.65	4.97E-03	3.01E-05	4.73E-03	5	
19GH9	19GH9.22	3	5.40	0.53	5.55E-03	1.88E-05	4.73E-03	17	
19GH9	19GH9.3	3	4.73	0.53	6.68E-03	7.15E-05	4.73E-03	41	

Table A1.1. Continued.

sample ID	grain/spot ID	#O min	$\delta^{18}\text{O}$ (‰)	2 σ	${}^{16}\text{O}{}^{1\text{H}}/{}^{16}\text{O}$	1 σ	OH/O (average OH/O reference zircon)	background	${}^{16}\text{O}{}^{1\text{H}}/{}^{16}\text{O}$ deviation from background (‰)
	19GH9	19GH9.3.3	3	4.85	0.62	4.49E-03	3.12E-05	4.73E-03	-5
	19GH9	19GH9.4	3	5.71	0.59	5.50E-03	1.73E-05	4.73E-03	16
	19GH9	19GH9.5	3	4.78	0.71	6.48E-03	6.97E-05	4.73E-03	37
	19GH9	19GH9.6	3	3.68	0.78	7.09E-03	3.60E-05	4.73E-03	50
	19GH9	19GH9.6.2	3	5.34	0.70	4.74E-03	4.29E-05	4.73E-03	0
	19GH9	19GH9.7	3	4.76	0.47	6.38E-03	4.93E-05	4.73E-03	35
	19GH9	19GH9.9	3	4.54	0.42	5.09E-03	3.26E-05	4.73E-03	7
	18IM12B.02	1	8.93	0.42	2.79E-03	3.97E-06	2.27E-03	23	
	18IM12B	18IM12B.03	1	6.92	0.41	5.31E-03	8.88E-06	2.27E-03	134
	18IM12B	18IM12B.04	1	10.57	0.42	2.19E-03	1.58E-05	2.27E-03	-3
	18IM12B	18IM12B.05	1	10.43	0.41	2.19E-03	6.26E-06	2.27E-03	-4
	18IM12B	18IM12B.06	1	10.21	0.42	2.04E-03	3.48E-06	2.27E-03	-10
	18IM12B	18IM12B.07	1	9.48	0.42	2.32E-03	5.85E-06	2.27E-03	2
	18IM12B	18IM12B.08	1	10.55	0.41	2.50E-03	2.55E-06	2.27E-03	10
	18IM12B	18IM12B.09	1	10.00	0.42	2.21E-03	4.65E-06	2.27E-03	-3
	18IM12B	18IM12B.1	1	10.29	0.40	2.07E-03	3.76E-06	2.27E-03	-9
	18IM12B	18IM12B.10	1	10.03	0.41	2.11E-03	4.46E-06	2.27E-03	-7
	18IM12B	18IM12B.11	1	9.95	0.43	2.26E-03	5.42E-06	2.27E-03	0
	18IM12B	18IM12B.12	1	10.08	0.43	2.30E-03	4.71E-06	2.27E-03	1
	18IM12B	18IM12B.13	1	10.03	0.40	2.06E-03	3.65E-06	2.27E-03	-9
	18IM12B	18IM12B.14	1	9.60	0.40	2.30E-03	2.18E-06	2.27E-03	1
	18IM12B	18IM12B.15	1	9.37	0.40	4.26E-03	1.52E-05	2.27E-03	88
	18IM12B	18IM12B.16	1	8.68	0.39	2.58E-03	1.34E-06	2.27E-03	14
	18IM12B	18IM12B.17	1	9.15	0.39	2.09E-03	2.68E-06	2.27E-03	-8
	18IM12B	18IM12B.18	1	9.02	0.41	2.32E-03	3.88E-06	2.27E-03	2
	18IM12B	18IM12B.19	1	9.44	0.41	2.23E-03	2.33E-06	2.27E-03	-2
DZ1	O_CS16-DZ1@1	5	5.13	0.43	5.36E-04	4.24E-04	1.84E-04	192	
DZ1	O_CS16-DZ1@2	5	6.63	0.42	2.05E-04	1.95E-04	1.84E-04	11	
DZ1	O_CS16-DZ1@3	5	9.71	0.44	1.78E-04	2.10E-04	1.84E-04	-3	
DZ1	O_CS16-DZ1@4	5	7.50	0.44	1.25E-03	6.26E-04	1.84E-04	579	
DZ1	O_CS16-DZ1@5	5	6.46	0.46	1.80E-04	2.17E-04	1.84E-04	-2	
DZ1	O_CS16-DZ1@6	5	6.40	0.41	1.93E-04	1.12E-04	1.84E-04	5	

Table A1.1. Continued.

sample ID	grain/spot ID	#O min	$\delta^{18}\text{O}$ (‰ SMOW)	${}^{16}\text{O}{}^{1\text{H}}/{}^{16}\text{O}$	${}^{1\sigma}$	OH/O (average OH/O reference zircon)	background ${}^{16}\text{O}{}^{1\text{H}}/{}^{16}\text{O}$ deviation from background (‰)	
DZ1	O_CS16-DZ1@07	5	6.17	0.43	2.55E-04	1.41E-04	1.84E-04	39
DZ1	O_CS16-DZ1@08	5	6.59	0.42	2.33E-04	2.99E-04	1.84E-04	27
DZ1	O_CS16-DZ1@09	5	6.57	0.46	1.86E-04	1.98E-04	1.84E-04	1
DZ1	O_CS16-DZ1@10	5	8.54	0.46	1.90E-04	2.59E-04	1.84E-04	4
DZ1	O_CS16-DZ1@11	5	6.35	0.47	2.13E-03	2.52E-03	1.84E-04	1061
DZ1	O_CS16-DZ1@12	5	6.18	0.46	2.26E-03	4.69E-04	1.84E-04	1132
DZ1	O_CS16-DZ1@13	5	5.50	0.46	1.95E-04	2.85E-04	1.84E-04	6
DZ1	O_CS16-DZ1@14	5	9.30	0.42	1.86E-04	2.24E-04	1.84E-04	1
DZ1	O_CS16-DZ1@15	5	5.73	0.42	2.41E-04	2.35E-04	1.84E-04	31
DZ1	O_CS16-DZ1@16	5	7.22	0.44	2.65E-04	2.19E-04	1.84E-04	44
DZ1	O_CS16-DZ1@17	5	5.65	0.45	1.82E-04	2.38E-04	1.84E-04	-1
DZ1	O_CS16-DZ1@18	5	6.63	0.45	2.02E-04	2.20E-04	1.84E-04	10
DZ1	O_CS16-DZ1@19	5	5.56	0.47	4.38E-04	1.41E-04	1.84E-04	138
DZ1	O_CS16-DZ1@20	5	5.90	0.44	2.40E-04	1.84E-04	1.84E-04	31
DZ1	O_CS16-DZ1@21	5	6.65	0.50	2.49E-04	2.05E-04	1.84E-04	36
DZ1	O_CS16-DZ1@22	5	5.70	0.50	2.68E-04	3.67E-05	1.84E-04	46
DZ1	O_CS16-DZ1@23	5	5.72	0.44	1.91E-04	2.37E-04	1.84E-04	4
DZ1	O_CS16-DZ1@24	5	4.89	0.45	2.34E-04	2.16E-04	1.84E-04	28
DZ1	O_CS16-DZ1@25	5	6.89	0.48	2.28E-04	2.21E-04	1.84E-04	24
DZ1	O_CS16-DZ1@26	5	5.63	0.43	2.17E-04	1.10E-04	1.84E-04	18
DZ1	O_CS16-DZ1@27	5	8.51	0.46	2.47E-04	2.22E-04	1.84E-04	34
DZ1	O_CS16-DZ1@28	5	6.84	0.46	2.39E-04	1.77E-04	1.84E-04	30
DZ1	O_CS16-DZ1@29	5	5.82	0.43	2.19E-04	2.51E-04	1.84E-04	19
DZ1	O_CS16-DZ1@30	5	7.62	0.46	2.15E-04	2.28E-04	1.84E-04	17
DZ1	O_CS16-DZ1@31	5	6.09	0.40	2.10E-04	1.44E-04	1.84E-04	14
DZ1	O_CS16-DZ1@32	5	8.61	0.46	1.84E-04	1.36E-04	1.84E-04	0
DZ1	O_CS16-DZ1@33	5	4.72	0.45	1.94E-04	2.04E-04	1.84E-04	6
DZ1	O_CS16-DZ1@34	5	7.12	0.42	3.25E-04	8.15E-05	1.84E-04	77
DZ1	O_CS16-DZ1@35	5	8.54	0.39	1.88E-04	2.81E-04	1.84E-04	2
DZ1	O_CS16-DZ1@36	5	6.52	0.48	2.00E-04	2.07E-04	1.84E-04	9
DZ1	O_CS16-DZ1@37	5	5.38	0.43	1.88E-04	2.20E-04	1.84E-04	2
DZ1	O_CS16-DZ1@38	5	6.79	0.43	2.27E-04	1.05E-04	1.84E-04	23

Table A1.1. Continued.

sample ID	grain/spot ID	#O mm	$\delta^{18}\text{O}$ (‰)	2σ	${}^{16}\text{O}{}^{1\text{H}}/{}^{16}\text{O}$	1σ	OH/O (average OH/O reference zircon)	background	${}^{16}\text{O}{}^{1\text{H}}/{}^{16}\text{O}$ deviation from background (‰)
DZ1	O_CS16-DZ1@39	5	5.51	0.46	2.35E-04	2.60E-04	1.84E-04	28	
DZ1	O_CS16-DZ1@40	5	6.36	0.41	1.85E-04	2.15E-04	1.84E-04	1	
DZ1	O_CS16-DZ1@41	5	5.92	0.45	1.88E-04	2.31E-04	1.84E-04	2	
DZ1	O_CS16-DZ1@42	5	5.15	0.42	2.45E-04	2.11E-04	1.84E-04	33	
DZ1	O_CS16-DZ1@43	5	5.01	0.44	3.30E-04	3.85E-04	1.84E-04	80	
DZ1	O_CS16-DZ1@44	5	8.02	0.43	1.90E-04	1.54E-04	1.84E-04	3	
DZ1	O_CS16-DZ1@45	5	5.67	0.42	2.66E-04	3.96E-04	1.84E-04	45	
DZ1	O_CS16-DZ1@46	5	5.46	0.44	1.96E-04	2.06E-04	1.84E-04	6	
DZ1	O_CS16-DZ1@47	5	5.06	0.41	2.28E-04	3.15E-04	1.84E-04	24	
DZ1	O_CS16-DZ1@48	5	7.33	0.43	2.64E-04	1.27E-04	1.84E-04	44	
DZ1	O_CS16-DZ1@49	5	5.30	0.44	2.19E-04	1.55E-04	1.84E-04	19	
DZ1	O_CS16-DZ1@50	5	6.14	0.42	2.22E-04	1.85E-04	1.84E-04	21	
DZ1	O_CS16-DZ1@51	5	8.56	0.43	1.89E-04	1.43E-04	1.84E-04	3	
DZ1	O_CS16-DZ1@52	5	8.58	0.46	1.97E-04	2.13E-04	1.84E-04	7	
DZ1	O_CS16-DZ1@53	5	6.77	0.46	2.00E-04	2.07E-04	1.84E-04	9	
DZ1	O_CS16-DZ1@54	5	6.42	0.47	3.26E-04	1.62E-04	1.84E-04	77	
DZ1	O_CS16-DZ1@55	5	6.41	0.47	2.01E-04	1.09E-04	1.84E-04	9	
DZ2	O_CS16-DZZ2@01	5	7.75	0.43	7.49E-04	9.58E-04	1.84E-04	307	
DZ2	O_CS16-DZZ2@02	5	7.28	0.41	7.77E-03	1.31E-02	1.84E-04	4126	
DZ2	O_CS16-DZZ2@03	5	8.32	0.51	3.24E-04	1.68E-04	1.84E-04	76	
DZ2	O_CS16-DZZ2@04	5	6.55	0.45	3.39E-03	6.37E-03	1.84E-04	1746	
DZ2	O_CS16-DZZ2@05	5	8.29	0.53	8.05E-03	4.94E-03	1.84E-04	4277	
DZ2	O_CS16-DZZ2@06	5	8.34	0.45	4.10E-04	1.45E-03	1.84E-04	123	
DZ2	O_CS16-DZZ2@07	5	9.59	0.47	2.64E-03	1.67E-03	1.84E-04	1336	
DZ2	O_CS16-DZZ2@08	5	7.50	0.43	2.41E-03	3.06E-03	1.84E-04	1209	
DZ2	O_CS16-DZZ2@09	5	7.67	0.44	2.01E-04	1.96E-04	1.84E-04	10	
DZ2	O_CS16-DZZ2@10	5	5.87	0.52	4.31E-04	4.14E-04	1.84E-04	134	
DZ2	O_CS16-DZZ2@11	5	9.50	0.44	2.98E-03	8.28E-04	1.84E-04	1522	
DZ2	O_CS16-DZZ2@12	5	8.67	0.43	1.78E-03	1.04E-03	1.84E-04	867	
DZ2	O_CS16-DZZ2@13	5	8.24	0.48	4.96E-04	1.14E-04	1.84E-04	170	
DZ2	O_CS16-DZZ2@14	5	6.66	0.44	7.76E-03	5.90E-03	1.84E-04	4121	
DZ2	O_CS16-DZZ2@15	5	5.69	0.45	2.47E-04	2.40E-04	1.84E-04	34	

Table A1.1. Continued.

sample ID	grain/spot ID	#O min	$\delta^{18}\text{O}$ (‰)	2σ	${}^{16}\text{O}^1\text{H}/{}^{16}\text{O}$	1σ	OH/O (average OH/O reference zircon)	background	${}^{16}\text{O}^1\text{H}/{}^{16}\text{O}$ deviation from background (‰)
	O_CS16-DZ2@16	5	9.66	0.51	2.27E-04	3.17E-04	1.84E-04	23	
DZ2	O_CS16-DZ2@17	5	8.34	0.47	7.71E-03	1.82E-03	1.84E-04	4095	
DZ2	O_CS16-DZ2@18	5	6.75	0.49	4.39E-03	1.35E-02	1.84E-04	2290	
DZ2	O_CS16-DZ2@19	5	8.55	0.50	5.53E-03	2.01E-02	1.84E-04	2909	
DZ2	O_CS16-DZ2@20	5	7.29	0.55	6.94E-03	2.66E-04	1.84E-04	3678	
DZ2	O_CS16-DZ2@21	5	7.58	0.49	6.07E-04	2.58E-04	1.84E-04	231	
DZ2	O_CS16-DZ2@22	5	7.84	0.46	8.05E-03	2.80E-03	1.84E-04	4278	
DZ2	O_CS16-DZ2@23	5	8.15	0.47	2.92E-03	4.72E-03	1.84E-04	1491	
DZ2	O_CS16-DZ2@24	5	7.23	0.44	8.47E-03	6.91E-03	1.84E-04	4510	
DZ2	O_CS16-DZ2@25	5	8.60	0.53	9.77E-03	2.15E-03	1.84E-04	5218	
DZ2	O_CS16-DZ2@26	5	9.76	0.51	9.62E-03	3.41E-03	1.84E-04	5135	
DZ2	O_CS16-DZ2@27	5	4.77	0.47	7.68E-03	6.18E-04	1.84E-04	4079	
DZ2	O_CS16-DZ2@28	5	8.35	0.51	3.21E-04	1.45E-04	1.84E-04	75	
DZ2	O_CS16-DZ2@29	5	5.31	0.52	1.35E-03	6.63E-04	1.84E-04	635	
DZ2	O_CS16-DZ2@30	5	8.96	0.49	2.01E-03	6.08E-04	1.84E-04	994	
DZ2	O_CS16-DZ2@31	5	10.00	0.44	7.95E-03	3.54E-03	1.84E-04	4224	
DZ2	O_CS16-DZ2@32	5	8.26	0.46	3.58E-03	5.38E-03	1.84E-04	1849	
DZ2	O_CS16-DZ2@33	5	8.81	0.58	3.63E-03	2.02E-03	1.84E-04	1875	
DZ2	O_CS16-DZ2@34	5	8.08	0.43	3.73E-04	1.91E-04	1.84E-04	103	
DZ2	O_CS16-DZ2@35	5	8.75	0.59	3.13E-03	4.87E-03	1.84E-04	1605	
DZ2	O_CS16-DZ2@36	5	7.55	0.55	6.86E-03	3.01E-03	1.84E-04	3630	
DZ2	O_CS16-DZ2@37	5	8.13	0.45	2.90E-03	4.62E-03	1.84E-04	1479	
DZ2	O_CS16-DZ2@38	5	7.34	0.43	7.11E-03	4.14E-03	1.84E-04	3771	
DZ2	O_CS16-DZ2@39	5	7.13	0.47	2.53E-04	1.97E-04	1.84E-04	37	
DZ2	O_CS16-DZ2@40	5	8.93	0.50	9.32E-04	3.42E-03	1.84E-04	407	
DZ2	O_CS16-DZ2@41	5	5.63	0.45	7.09E-03	4.06E-03	1.84E-04	3760	
DZ2	O_CS16-DZ2@42	5	9.24	0.39	4.24E-03	1.28E-02	1.84E-04	2207	
DZ2	O_CS16-DZ2@43	5	10.32	0.45	9.41E-03	2.60E-03	1.84E-04	5021	
DZ2	O_CS16-DZ2@44	5	9.27	0.44	6.32E-03	3.18E-03	1.84E-04	3338	
DZ2	O_CS16-DZ2@45	5	7.98	0.47	4.79E-04	1.03E-04	1.84E-04	160	
DZ2	O_CS16-DZ2@46	5	9.02	0.48	3.80E-04	2.17E-04	1.84E-04	107	
DZ2	O_CS16-DZ2@47	5	8.32	0.44	6.75E-03	5.29E-03	1.84E-04	3572	

Table A1.1. Continued.

sample ID	grain/spot ID	#O min	$\delta^{18}\text{O}$ (‰)	2 σ	${}^{16}\text{O}{}^{1\text{H}}/{}^{16}\text{O}$	1 σ	OH/O (average OH/O reference zircon)	background	${}^{16}\text{O}{}^{1\text{H}}/{}^{16}\text{O}$ deviation from background (‰)
			SMMOW)						
DZ2	O_CS16-DZ2@48	5	8.46	0.47	1.09E-03	6.01E-04	1.84E-04	492	
DZ2	O_CS16-DZ2@49	5	8.18	0.46	6.21E-03	7.30E-04	1.84E-04	3279	
DZ2	O_CS16-DZ2@50	5	12.65	0.43	5.78E-04	2.31E-04	1.84E-04	215	
DZ2	O_CS16-DZ2@51	5	8.81	0.46	2.23E-03	2.16E-03	1.84E-04	1111	
DZ2	O_CS16-DZ2@52	5	7.73	0.45	6.87E-03	1.95E-03	1.84E-04	3638	
DZ2	O_CS16-DZ2@53	5	8.59	0.53	4.89E-03	8.53E-04	1.84E-04	2561	
DZ2	O_CS16-DZ2@54	5	8.80	0.46	9.35E-03	2.04E-03	1.84E-04	4987	
DZ2	O_CS16-DZ2@55	5	7.75	0.48	8.65E-03	1.88E-03	1.84E-04	4606	
DZ2	O_CS16-DZ2@56	5	7.93	0.44	4.77E-03	7.50E-03	1.84E-04	2494	
DZ2	O_CS16-DZ2@57	5	8.60	0.50	3.45E-04	1.95E-04	1.84E-04	88	
DZ2	O_CS16-DZ2@58	5	9.04	0.48	3.50E-03	4.84E-03	1.84E-04	1803	
DZ2	O_CS16-DZ2@59	5	8.61	0.47	1.41E-03	3.93E-03	1.84E-04	667	
DZ2	O_CS16-DZ2@60	5	8.36	0.41	2.14E-04	2.30E-04	1.84E-04	17	
DZ2	O_CS16-DZ2@61	5	9.02	0.45	1.20E-03	3.27E-03	1.84E-04	552	
DZ2	O_CS16-DZ2@62	5	6.46	0.41	5.81E-03	1.44E-03	1.84E-04	3061	
DZ2	O_CS16-DZ2@63	5	6.42	0.47	3.46E-04	2.77E-04	1.84E-04	89	
DZ2	O_CS16-DZ2@64	5	9.49	0.45	6.18E-03	9.34E-04	1.84E-04	3264	
CS16-14	O_CS16-14@001	5	6.11	0.47	3.28E-04	8.72E-04	1.84E-04	79	
CS16-14	O_CS16-14@10	5	5.49	0.48	4.32E-04	1.90E-04	1.84E-04	135	
CS16-14	O_CS16-14@11	5	6.17	0.43	2.61E-04	1.30E-04	1.84E-04	42	
CS16-14	O_CS16-14@12	5	6.40	0.42	5.05E-04	7.20E-04	1.84E-04	175	
CS16-14	O_CS16-14@13	5	5.99	0.43	7.27E-04	1.17E-04	1.84E-04	295	
CS16-14	O_CS16-14@14	5	6.71	0.51	2.72E-03	8.31E-03	1.84E-04	1380	
CS16-14	O_CS16-14@15	5	6.39	0.44	6.77E-03	1.26E-03	1.84E-04	3584	
CS16-14	O_CS16-14@16	5	6.04	0.39	2.90E-04	7.56E-05	1.84E-04	58	
CS16-14	O_CS16-14@17	5	6.37	0.47	2.11E-04	1.45E-04	1.84E-04	15	
CS16-14	O_CS16-14@2	5	5.83	0.43	5.16E-04	9.81E-04	1.84E-04	181	
CS16-14	O_CS16-14@3	5	6.12	0.41	2.54E-04	1.25E-04	1.84E-04	38	
CS16-14	O_CS16-14@4	5	6.73	0.42	1.89E-04	4.24E-05	1.84E-04	3	
CS16-14	O_CS16-14@5	5	5.80	0.46	2.00E-04	1.03E-04	1.84E-04	9	
CS16-14	O_CS16-14@6	5	6.27	0.47	2.72E-04	1.43E-04	1.84E-04	48	
CS16-14	O_CS16-14@7	5	6.19	0.40	2.03E-04	1.23E-04	1.84E-04	11	

Table A1.1. Continued.

sample ID	grain/spot ID	#O min	$\delta^{18}\text{O}$ (‰)	2σ	${}^{16}\text{O}{}^{1\text{H}}/{}^{16}\text{O}$	1σ	OH/O (average OH/O reference zircon)	background	${}^{16}\text{O}{}^{1\text{H}}/{}^{16}\text{O}$ deviation from background (‰)
CS16-14	O_CS16-14@8	5	7.21	0.43	4.17E-04	1.94E-04	1.84E-04	127	
CS16-14	O_CS16-14@9	5	6.16	0.45	2.18E-04	1.04E-04	1.84E-04	19	
CS16-15	O_CS16-15@001	5	6.28	0.47	2.45E-04	2.93E-04	1.84E-04	33	
CS16-15	O_CS16-15@10	5	6.21	0.40	2.74E-04	1.90E-04	1.84E-04	49	
CS16-15	O_CS16-15@11	5	6.85	0.48	5.19E-04	3.60E-04	1.84E-04	182	
CS16-15	O_CS16-15@12	5	6.50	0.46	8.81E-04	6.94E-04	1.84E-04	379	
CS16-15	O_CS16-15@13	5	5.93	0.42	2.77E-04	1.64E-04	1.84E-04	51	
CS16-15	O_CS16-15@14	5	6.40	0.48	9.55E-04	1.13E-03	1.84E-04	420	
CS16-15	O_CS16-15@15	5	4.15	0.44	9.17E-03	1.50E-03	1.84E-04	4889	
CS16-15	O_CS16-15@16	5	6.15	0.43	2.06E-04	1.27E-04	1.84E-04	12	
CS16-15	O_CS16-15@17	5	6.46	0.49	2.23E-04	9.09E-05	1.84E-04	21	
CS16-15	O_CS16-15@18	5	6.12	0.43	2.60E-04	1.76E-04	1.84E-04	41	
CS16-15	O_CS16-15@2	5	6.83	0.44	5.07E-04	5.68E-04	1.84E-04	176	
CS16-15	O_CS16-15@3	5	6.28	0.42	1.95E-04	9.04E-05	1.84E-04	6	
CS16-15	O_CS16-15@4	5	6.03	0.46	2.50E-04	1.13E-04	1.84E-04	36	
CS16-15	O_CS16-15@5	5	6.19	0.43	2.47E-04	3.76E-04	1.84E-04	34	
CS16-15	O_CS16-15@6	5	6.10	0.43	1.86E-04	1.24E-04	1.84E-04	1	
CS16-15	O_CS16-15@7	5	6.07	0.42	2.55E-04	4.35E-04	1.84E-04	39	
CS16-15	O_CS16-15@8	5	6.04	0.44	3.17E-04	8.64E-05	1.84E-04	72	
CS16-15	O_CS16-15@9	5	6.24	0.45	2.95E-04	1.52E-04	1.84E-04	60	
CS16-16	O_CS16-16@001	5	7.22	0.45	3.04E-04	3.63E-04	1.84E-04	65	
CS16-16	O_CS16-16@2	5	6.20	0.45	6.24E-03	5.59E-03	1.84E-04	3295	
CS16-16	O_CS16-16@3	5	4.16	0.42	2.21E-04	4.97E-04	1.84E-04	20	
CS16-16	O_CS16-16@4	5	5.82	0.45	2.50E-04	7.82E-05	1.84E-04	36	
CS16-16	O_CS16-16@5	5	6.66	0.42	3.65E-04	2.58E-04	1.84E-04	99	
CS16-16	O_CS16-16@6	5	12.69	0.53	2.26E-04	5.58E-05	1.84E-04	23	
CS16-16	O_CS16-16@7	5	5.68	0.44	3.62E-04	9.59E-05	1.84E-04	97	
CS16-16	O_CS16-16@8	5	6.05	0.50	3.55E-03	2.54E-03	1.84E-04	1829	
CS16-16	O_CS16-16@9	5	7.99	0.45	3.82E-03	4.96E-03	1.84E-04	1976	
CS16-16	O_CS16-16@10	5	6.11	0.44	2.00E-03	2.48E-03	1.84E-04	986	
CS16-16	O_CS16-16@11	5	7.11	0.53	3.03E-03	1.82E-03	1.84E-04	1551	
CS16-16	O_CS16-16@12	5	7.42	0.47	2.57E-04	2.39E-04	1.84E-04	40	

Table A1.1. Continued.

sample ID	grain/spot ID	#O mm	$\delta^{18}\text{O}$ (‰)	2σ	${}^{16}\text{O}{}^{1\text{H}}/{}^{16}\text{O}$	1σ	OH/O (average OH/O reference zircon)	background	${}^{16}\text{O}{}^{1\text{H}}/{}^{16}\text{O}$ deviation from background (‰)
CS16-22	O_CS16-22@4	5	2.85	0.42	4.15E-03	6.64E-04	1.84E-04	2160	
CS16-22	O_CS16-22@5	5	2.06	0.44	6.54E-03	8.47E-04	1.84E-04	3460	
CS16-22	O_CS16-22@6	5	1.58	0.44	6.59E-03	3.13E-03	1.84E-04	3485	
CS16-22	O_CS16-22@7	5	5.95	0.44	6.64E-04	5.32E-04	1.84E-04	261	
CS16-22	O_CS16-22@8	5	4.83	0.50	2.99E-03	2.93E-04	1.84E-04	1527	
CS16-22	O_CS16-22@9	5	4.66	0.42	3.03E-03	1.27E-03	1.84E-04	1550	
CS16-23	O_CS16-23@02	5	6.09	0.48	2.58E-04	2.66E-04	1.84E-04	41	
CS16-23	O_CS16-23@03	5	5.32	0.46	3.11E-04	8.37E-05	1.84E-04	72	
CS16-23	O_CS16-23@04	5	5.15	0.44	6.69E-04	6.35E-04	1.84E-04	264	
CS16-23	O_CS16-23@05	5	5.47	0.44	6.33E-04	2.19E-04	1.84E-04	245	
CS16-23	O_CS16-23@06	5	5.49	0.42	8.97E-04	2.37E-04	1.84E-04	388	
CS16-23	O_CS16-23@07	5	5.97	0.43	3.82E-04	1.98E-04	1.84E-04	108	
CS16-23	O_CS16-23@08	5	5.71	0.52	3.28E-03	4.12E-04	1.84E-04	1687	
CS16-23	O_CS16-23@09	5	5.33	0.47	3.17E-04	1.35E-04	1.84E-04	72	
CS16-23	O_CS16-23@1	5	5.62	0.44	4.40E-04	5.98E-04	1.84E-04	140	
CS16-23	O_CS16-23@10	5	6.09	0.47	2.91E-04	2.20E-04	1.84E-04	58	
CS16-23	O_CS16-23@11	5	5.90	0.39	2.13E-04	1.97E-04	1.84E-04	16	
CS16-23	O_CS16-23@12	5	4.74	0.45	5.07E-03	3.89E-03	1.84E-04	2659	
CS16-24	O_CS16-24@001	5	6.56	0.46	4.29E-04	2.46E-04	1.84E-04	133	
CS16-24	O_CS16-24@10	5	2.31	0.42	4.15E-03	1.32E-03	1.84E-04	2157	
CS16-24	O_CS16-24@11	5	2.17	0.44	5.55E-03	1.14E-03	1.84E-04	2921	
CS16-24	O_CS16-24@12	5	4.88	0.50	2.49E-03	1.65E-03	1.84E-04	1255	
CS16-24	O_CS16-24@13	5	6.30	0.43	1.70E-03	5.25E-03	1.84E-04	825	
CS16-24	O_CS16-24@14	5	4.81	0.46	3.73E-03	2.76E-03	1.84E-04	1932	
CS16-24	O_CS16-24@15	5	4.56	0.45	2.49E-03	1.25E-03	1.84E-04	1255	
CS16-24	O_CS16-24@2	5	1.86	0.43	2.31E-03	1.62E-03	1.84E-04	1157	
CS16-24	O_CS16-24@3	5	5.59	0.45	8.26E-04	1.05E-03	1.84E-04	349	
CS16-24	O_CS16-24@4	5	5.83	0.47	6.65E-04	3.55E-04	1.84E-04	262	
CS16-24	O_CS16-24@5	5	5.55	0.43	2.37E-04	1.03E-04	1.84E-04	29	
CS16-24	O_CS16-24@6	5	5.19	0.48	5.24E-03	1.28E-03	1.84E-04	2754	
CS16-24	O_CS16-24@7	5	4.07	0.48	4.11E-03	4.57E-03	1.84E-04	2134	
CS16-24	O_CS16-24@8	5	3.64	0.41	2.85E-03	6.06E-04	1.84E-04	1451	

Table A1.1. Continued.

sample ID	grain/spot ID	#O run	$\delta^{18}\text{O}$ (‰)	SMOW	2σ	$^{16}\text{O}^{\text{H}}/\text{O}$	1σ	(average OH/O background zircon) (%)	$^{16}\text{O}^{\text{H}}/\text{O}$ deviation from background OH/O background (%)
CS16-24	O_CS16-24@09	5	5.16	0.46	1.84E-03	5.61E-04	1.84E-04	899	
CS16-25	O_CS16-25@001	5	4.51	0.45	4.30E-04	8.08E-05	1.84E-04	134	
CS16-25	O_CS16-25@02	5	4.73	0.43	2.06E-03	5.88E-04	1.84E-04	1020	
CS16-25	O_CS16-25@03	5	4.35	0.46	3.05E-03	8.20E-04	1.84E-04	1562	
CS16-25	O_CS16-25@04	5	4.95	0.46	2.13E-03	4.71E-04	1.84E-04	1059	
CS16-25	O_CS16-25@05	5	5.63	0.45	2.59E-03	1.11E-03	1.84E-04	1311	
CS16-33	O_CS16-33@001	5	5.38	0.49	4.78E-03	3.50E-03	1.84E-04	2502	
CS16-33	O_CS16-33@02	5	4.96	0.48	9.92E-04	9.96E-04	1.84E-04	439	
CS16-33	O_CS16-33@03	5	3.67	0.51	9.24E-03	9.61E-04	1.84E-04	4925	
CS16-33	O_CS16-33@04	5	5.52	0.46	2.11E-03	9.40E-03	1.84E-04	1048	
CS16-33	O_CS16-33@05	5	6.65	0.40	2.18E-03	6.41E-03	1.84E-04	1086	
CS16-34	O_CS16-34@001	5	2.40	0.45	5.09E-03	3.65E-03	1.84E-04	2668	
CS16-34	O_CS16-34@02	5	5.32	0.47	8.88E-03	7.90E-03	1.84E-04	4733	
CS16-34	O_CS16-34@03	5	6.48	0.48	2.03E-04	7.18E-05	1.84E-04	11	
CS16-34	O_CS16-34@04	5	3.14	0.43	3.24E-03	1.77E-03	1.84E-04	1661	
CS16-34	O_CS16-34@05	5	3.20	0.45	2.83E-03	1.24E-03	1.84E-04	1442	
CS16-34	O_CS16-34@06	5	4.51	0.42	3.46E-03	4.80E-03	1.84E-04	1784	
CS16-34	O_CS16-34@07	5	2.73	0.43	1.03E-02	2.28E-03	1.84E-04	5515	
CS16-34	O_CS16-34@08	5	6.28	0.44	1.94E-04	1.11E-04	1.84E-04	6	
CS16-34	O_CS16-34@09	5	6.14	0.41	1.85E-04	2.76E-04	1.84E-04	0	
CS16-34	O_CS16-34@10	5	6.00	0.43	5.58E-04	8.15E-04	1.84E-04	204	
CS16-34	O_CS16-34@11	5	7.67	0.47	4.49E-04	2.29E-04	1.84E-04	144	
CS16-34	O_CS16-34@12	5	4.21	0.40	1.01E-02	2.65E-03	1.84E-04	5372	
CS16-34	O_CS16-34@13	5	8.89	0.47	1.24E-02	2.97E-03	1.84E-04	6632	
CS16-34	O_CS16-34@14	5	4.70	0.43	2.95E-03	1.72E-03	1.84E-04	1506	
CS16-34	O_CS16-34@15	5	5.99	0.41	2.51E-03	8.18E-04	1.84E-04	1264	
91500	91500.39	4	9.78	0.44	5.45E-04	9.80E-07	5.56E-04	-2	
91500	91500.38	4	9.84	0.42	5.49E-04	1.01E-06	5.56E-04	-1	
91500	91500.35	4	9.58	0.43	5.50E-04	9.80E-07	5.56E-04	-1	
91500	91500.37	4	9.96	0.46	5.50E-04	7.62E-07	5.56E-04	-1	
91500	91500.34	4	9.92	0.44	5.50E-04	1.06E-06	5.56E-04	-1	

Table A1.1. Continued.

sample ID	grain/spot ID	#O run	$\delta^{18}\text{O}$ (‰)	2σ	${}^{16}\text{O}^{\text{H}}/{}^{16}\text{O}$	1σ	(average OH/O background zircon)	${}^{16}\text{O}^{\text{H}}/\text{O}$ deviation from background
		SMOW					reference zircon (%)	
91500	91500.36	4	10.19	0.45	5.50E-04	8.38E-07	5.56E-04	-1
91500	91500.3	4	9.97	0.44	5.52E-04	1.00E-06	5.56E-04	-1
91500	91500.33	4	9.86	0.45	5.52E-04	7.85E-07	5.56E-04	-1
91500	91500.29	4	9.86	0.43	5.53E-04	9.25E-07	5.56E-04	0
91500	91500.28	4	9.86	0.45	5.54E-04	9.71E-07	5.56E-04	0
91500	91500.27	4	9.58	0.44	5.56E-04	1.04E-06	5.56E-04	0
91500	91500.26	4	10.14	0.43	5.57E-04	9.27E-07	5.56E-04	0
91500	91500.25	4	9.72	0.44	5.58E-04	8.41E-07	5.56E-04	0
91500	91500.23	4	9.65	0.42	5.59E-04	9.67E-07	5.56E-04	1
91500	91500.09	4	9.66	0.44	5.60E-04	9.47E-07	5.56E-04	1
91500	91500.31	4	9.99	0.42	5.61E-04	9.01E-07	5.56E-04	1
91500	91500.18	4	9.84	0.43	5.61E-04	1.25E-06	5.56E-04	1
91500	91500.24	4	10.07	0.44	5.63E-04	8.84E-07	5.56E-04	1
91500	91500.17	4	9.67	0.45	5.64E-04	1.01E-06	5.56E-04	1
91500	91500.12	4	9.94	0.44	5.66E-04	1.03E-06	5.56E-04	2
91500	91500.15	4	9.73	0.44	5.66E-04	1.01E-06	5.56E-04	2
91500	91500.16	4	9.91	0.44	5.67E-04	1.09E-06	5.56E-04	2
91500	91500.11	4	10.22	0.43	5.67E-04	9.71E-07	5.56E-04	2
91500	91500.21	4	9.68	0.43	5.68E-04	1.09E-06	5.56E-04	2
91500	91500.01	4	10.01	0.42	5.68E-04	1.04E-06	5.56E-04	2
91500	91500.19	4	10.03	0.45	5.68E-04	1.08E-06	5.56E-04	2
91500	91500.13	4	9.79	0.42	5.68E-04	9.91E-07	5.56E-04	2
91500	91500.02	4	9.90	0.43	5.69E-04	1.01E-06	5.56E-04	2
temora 2	TEM2.06	4	7.88	0.43	6.16E-04	7.97E-07	5.56E-04	11
temora 2	TEM2.05	4	7.71	0.44	6.19E-04	9.17E-07	5.56E-04	11
temora 2	TEM2.02	4	7.98	0.44	7.26E-04	7.98E-07	5.56E-04	31
temora 2	TEM2.03	4	7.86	0.44	7.28E-04	9.14E-07	5.56E-04	31
91500	91500.8	2	9.82	0.33	1.74E-03	1.24E-05	1.97E-03	-12
91500	91500.19	2	9.95	0.37	1.85E-03	1.13E-05	1.97E-03	-6
91500	91500.18	2	9.76	0.33	1.85E-03	9.50E-06	1.97E-03	-6
91500	91500.15	2	9.84	0.24	1.86E-03	1.45E-05	1.97E-03	-6
91500	91500.12	2	9.82	0.22	1.89E-03	1.00E-05	1.97E-03	-4

Table A1.1. Continued.

sample ID	grain/spot ID	#O run	$\delta^{18}\text{O}$ (‰)	2σ	$^{16}\text{O}^{\text{H}}/\text{H}_2\text{O}$	1σ	background OH/O (average OH/O reference zircon)	$^{16}\text{O}^{\text{H}}/\text{H}_2\text{O}$ deviation from background (‰)
91500	91500.1	2	10.02	0.25	1.89E-03	1.46E-05	1.97E-03	-4
91500	91500.17	2	9.97	0.27	1.90E-03	1.58E-05	1.97E-03	-4
temora 2	TEM2.2	2	8.11	0.29	1.91E-03	1.25E-05	1.97E-03	-3
91500	91500.13	2	9.80	0.36	1.92E-03	1.92E-05	1.97E-03	-3
91500	91500.11	2	9.92	0.37	1.92E-03	1.30E-05	1.97E-03	-2
91500	91500.16	2	9.89	0.38	1.94E-03	1.89E-05	1.97E-03	-1
91500	91500.2	2	9.86	0.34	1.95E-03	1.36E-05	1.97E-03	-1
91500	91500.14	2	9.96	0.25	1.96E-03	1.76E-05	1.97E-03	-1
91500	91500.5	2	9.97	0.33	2.00E-03	1.15E-05	1.97E-03	2
91500	91500.21	2	9.81	0.35	2.00E-03	1.69E-05	1.97E-03	2
temora 2	TEM2.5	2	7.85	0.33	2.00E-03	6.13E-06	1.97E-03	2
91500	91500.2	2	10.01	0.35	2.03E-03	1.01E-05	1.97E-03	3
91500	91500.22	2	9.83	0.21	2.05E-03	1.46E-05	1.97E-03	4
91500	91500.23	2	9.86	0.41	2.05E-03	8.04E-06	1.97E-03	4
91500	91500.4	2	9.87	0.24	2.07E-03	2.83E-06	1.97E-03	5
temora 2	TEM2.3	2	8.09	0.34	2.07E-03	1.26E-05	1.97E-03	5
temora 2	TEM2.4	2	7.82	0.22	2.08E-03	8.34E-06	1.97E-03	6
91500	91500.24	2	10.02	0.32	2.09E-03	1.30E-05	1.97E-03	6
temora 2	TEM2.1	2	8.08	0.35	2.10E-03	3.70E-06	1.97E-03	7
temora 2	TEM2.6	2	7.63	0.22	2.15E-03	6.59E-06	1.97E-03	9
91500	91500.3	2	9.81	0.33	2.20E-03	1.04E-05	1.97E-03	12
91500	91500.3	1	9.94	0.24	2.08E-03	1.40E-06	2.27E-03	-8
91500	91500.14	1	9.88	0.29	2.12E-03	1.46E-06	2.27E-03	-7
91500	91500.5	1	10.02	0.34	2.13E-03	2.89E-06	2.27E-03	-6
91500	91500.6	1	9.92	0.32	2.14E-03	2.09E-06	2.27E-03	-6
91500	91500.2	1	9.80	0.33	2.18E-03	9.84E-07	2.27E-03	-4
91500	91500.11	1	10.00	0.51	2.30E-03	6.43E-06	2.27E-03	2
91500	91500.1	1	9.93	0.52	2.32E-03	8.58E-06	2.27E-03	2

Table A1.1. Continued.

sample ID	grain/spot ID	#O run	$\delta^{18}\text{O}$ (‰)	$\delta^{18}\text{O}$ SMOW	2σ	${}^{16}\text{O}\text{H/}{}^{16}\text{O}$	1σ	(average OH/O reference zircon)	background OH/O deviation from background (‰)	${}^{16}\text{O}\text{H/}{}^{16}\text{O}$
temora_2	TEM2.3	1	7.56	0.38	2.32E-03	8.12E-07	2.27E-03	2	2	
91500	91500.7	1	9.89	0.41	2.35E-03	3.30E-06	2.27E-03	4	4	
91500	TEM2.4	1	7.97	0.44	2.40E-03	7.29E-06	2.27E-03	6	6	
91500	91500.8	1	9.79	0.53	2.42E-03	2.45E-06	2.27E-03	6	6	
91500	TEM2.6	1	7.89	0.48	2.47E-03	3.27E-06	2.27E-03	9	9	
91500	91500.9	1	9.88	0.39	2.51E-03	4.55E-06	2.27E-03	10	10	
temora_2	TEM2.5	1	7.69	0.53	2.51E-03	3.50E-06	2.27E-03	11	11	
91500	91500@1	3	10.01	0.53	4.60E-03	2.81E-05	4.73E-03	-3	-3	
91500	91500@10	3	10.14	0.90	4.94E-03	1.43E-05	4.73E-03	4	4	
91500	91500@11	3	10.16	0.65	4.91E-03	1.17E-05	4.73E-03	4	4	
91500	91500@12	3	9.56	0.64	4.25E-03	3.40E-05	4.73E-03	-10	-10	
91500	91500@13	3	10.04	0.61	4.51E-03	2.14E-05	4.73E-03	-5	-5	
91500	91500@14	3	9.93	0.48	4.68E-03	3.73E-05	4.73E-03	-1	-1	
91500	91500@15	3	10.04	0.58	4.92E-03	2.33E-05	4.73E-03	4	4	
91500	91500@16	3	10.12	0.72	4.83E-03	2.10E-05	4.73E-03	2	2	
91500	91500@17	3	10.03	0.78	5.07E-03	2.22E-05	4.73E-03	7	7	
91500	91500@19	3	10.04	0.61	4.74E-03	2.68E-05	4.73E-03	0	0	
91500	91500@22	3	9.59	0.55	5.10E-03	2.19E-05	4.73E-03	8	8	
91500	91500@20	3	9.77	0.72	4.78E-03	2.79E-05	4.73E-03	1	1	
91500	91500@21	3	9.58	0.67	4.81E-03	2.51E-05	4.73E-03	2	2	
91500	91500@22	3	9.82	0.70	4.84E-03	2.60E-05	4.73E-03	2	2	
91500	91500@23	3	9.57	0.74	4.45E-03	4.13E-05	4.73E-03	-6	-6	
91500	91500@25	3	9.78	0.41	4.91E-03	1.29E-05	4.73E-03	4	4	
91500	91500@3	3	9.92	0.77	5.15E-03	2.06E-05	4.73E-03	9	9	
91500	91500@4	3	9.80	0.67	4.21E-03	2.67E-05	4.73E-03	-11	-11	
91500	91500@5	3	10.38	0.73	4.15E-03	3.72E-05	4.73E-03	-12	-12	
91500	91500@6	3	9.59	0.43	4.85E-03	2.49E-05	4.73E-03	3	3	
91500	91500@7	3	10.18	0.59	4.11E-03	3.00E-05	4.73E-03	-13	-13	
91500	91500@8	3	9.91	0.53	5.04E-03	1.49E-05	4.73E-03	7	7	
91500	91500@9	3	9.75	0.36	5.01E-03	2.16E-05	4.73E-03	6	6	
temora_2	TEM2@1	3	7.47	0.61	4.07E-03	3.94E-05	4.73E-03	-14	-14	
temora_3	TEM2@2	3	8.43	0.42	4.07E-03	4.03E-05	4.73E-03	-14	-14	

Table A1.1. Continued.

sample ID	grain/spot ID	#O run	$\delta^{18}\text{O}$ (‰)	2σ	$^{16}\text{O}^{1\text{H}}/\text{^{16}\text{O}}$	1σ	(average OH/O background zircon)	$^{16}\text{O}\text{OH}/\text{^{16}\text{O}}$ deviation from background OH/O background (%)
temora 4	TEM2@3	3	7.71	0.51	4.57E-03	3.26E-05	4.73E-03	-3
temora 5	TEM2@4	3	8.12	0.50	4.83E-03	2.67E-05	4.73E-03	2
temora 6	TEM2@5	3	7.87	0.57	4.34E-03	3.56E-05	4.73E-03	-8
temora 7	TEM2@7	3	7.79	0.60	5.11E-03	2.93E-05	4.73E-03	8
temora 8	TEM2@8	3	7.70	0.50	5.14E-03	2.72E-05	4.73E-03	9
91500	O_CS240417_915@01	5	9.82	0.44	1.56E-04	1.06E-04	1.84E-04	-15
91500	O_CS240417_915@02	5	9.70	0.41	1.59E-04	7.74E-05	1.84E-04	-14
91500	O_CS240417_915@10	5	9.94	0.43	1.75E-04	1.11E-04	1.84E-04	-5
91500	O_CS240417_915@11	5	10.08	0.47	1.80E-04	5.57E-05	1.84E-04	-2
91500	O_CS240417_915@12	5	9.94	0.40	1.78E-04	7.71E-05	1.84E-04	-3
91500	O_CS240417_915@13	5	9.74	0.42	1.81E-04	5.38E-05	1.84E-04	-2
91500	O_CS240417_915@14	5	9.89	0.46	1.84E-04	6.08E-05	1.84E-04	0
91500	O_CS240417_915@15	5	9.72	0.40	1.81E-04	5.92E-05	1.84E-04	-2
91500	O_CS240417_915@16	5	9.72	0.48	1.80E-04	6.64E-05	1.84E-04	-2
91500	O_CS240417_915@17	5	9.83	0.40	1.78E-04	7.29E-05	1.84E-04	-3
91500	O_CS240417_915@20	5	9.87	0.49	1.74E-04	8.52E-05	1.84E-04	-5
91500	O_CS240417_915@21	5	9.85	0.47	1.78E-04	8.58E-05	1.84E-04	-3
91500	O_CS240417_915@22	5	10.18	0.42	1.80E-04	9.09E-05	1.84E-04	-2
91500	O_CS240417_915@23	5	9.76	0.44	1.82E-04	8.71E-05	1.84E-04	-1
91500	O_CS240417_915@24	5	9.42	0.47	1.90E-04	8.39E-05	1.84E-04	4
91500	O_CS240417_915@25	5	10.14	0.50	1.86E-04	8.66E-05	1.84E-04	1
91500	O_CS240417_915@26	5	9.98	0.49	1.93E-04	8.70E-05	1.84E-04	5
91500	O_CS240417_915@27	5	10.39	0.42	1.90E-04	1.54E-04	1.84E-04	3
91500	O_CS240417_915@28	5	9.63	0.52	1.94E-04	5.32E-05	1.84E-04	6
91500	O_CS240417_915@29	5	10.03	0.52	1.84E-04	8.06E-05	1.84E-04	0
91500	O_CS240417_915@33	5	9.82	0.44	1.58E-04	8.46E-05	1.84E-04	-14
91500	O_CS240417_915@30	5	10.30	0.49	1.90E-04	6.10E-05	1.84E-04	3
91500	O_CS240417_915@31	5	9.91	0.51	1.86E-04	9.40E-05	1.84E-04	1
91500	O_CS240417_915@32	5	9.74	0.48	1.82E-04	1.24E-04	1.84E-04	-1
91500	O_CS240417_915@33	5	9.68	0.43	1.86E-04	6.10E-05	1.84E-04	1
91500	O_CS240417_915@34	5	9.83	0.46	1.90E-04	1.03E-04	1.84E-04	4
91500	O_CS240417_915@35	5	9.96	0.40	1.95E-04	6.45E-05	1.84E-04	6

Table A1.1. Continued.

sample ID	grain/spot ID	#O run	$\delta^{18}\text{O}$ (‰)	2 σ	${}^{16}\text{O}^{\text{H}}/{}^{16}\text{O}$	1 σ	background OH/O (average OH/O reference zircon)	${}^{16}\text{O}^{\text{H}}/\text{O}$ deviation from background (‰)
		SMOW						
91500	O_CS240417_915@36	5	9.78	0.47	1.93E-04	8.75E-05	1.84E-04	5
91500	O_CS240417_915@37	5	9.74	0.51	1.98E-04	5.68E-05	1.84E-04	8
91500	O_CS240417_915@38	5	9.79	0.48	2.00E-04	6.67E-05	1.84E-04	9
91500	O_CS240417_915@38-2	5	9.89	0.47	1.74E-04	1.76E-04	1.84E-04	-5
91500	O_CS240417_915@38-3	5	9.94	0.47	1.76E-04	1.64E-04	1.84E-04	-4
91500	O_CS240417_915@38-4	5	9.64	0.43	1.72E-04	2.30E-04	1.84E-04	-6
91500	O_CS240417_915@44	5	10.00	0.47	1.60E-04	6.17E-05	1.84E-04	-13
91500	O_CS240417_915@40	5	9.99	0.43	1.76E-04	2.00E-04	1.84E-04	-4
91500	O_CS240417_915@42	5	9.60	0.50	1.72E-04	2.28E-04	1.84E-04	-7
91500	O_CS240417_915@43	5	9.96	0.42	1.77E-04	1.36E-04	1.84E-04	-4
91500	O_CS240417_915@44	5	9.96	0.46	1.79E-04	6.80E-05	1.84E-04	-3
91500	O_CS240417_915@45	5	9.81	0.45	1.71E-04	1.63E-04	1.84E-04	-7
91500	O_CS240417_915@46	5	9.69	0.46	1.78E-04	1.76E-04	1.84E-04	-3
91500	O_CS240417_915@47	5	9.94	0.48	1.85E-04	1.01E-04	1.84E-04	1
91500	O_CS240417_915@48	5	9.97	0.47	1.81E-04	1.15E-04	1.84E-04	-2
91500	O_CS240417_915@49	5	9.77	0.46	1.82E-04	1.48E-04	1.84E-04	-1
91500	O_CS240417_915@5	5	9.51	0.44	1.63E-04	8.19E-05	1.84E-04	-11
91500	O_CS240417_915@50	5	10.04	0.43	1.91E-04	9.02E-05	1.84E-04	4
91500	O_CS240417_915@51	5	9.83	0.47	1.87E-04	2.25E-04	1.84E-04	2
91500	O_CS240417_915@52	5	10.03	0.44	1.88E-04	2.20E-04	1.84E-04	2
91500	O_CS240417_915@53	5	10.18	0.45	2.00E-04	6.55E-05	1.84E-04	9
91500	O_CS240417_915@55	5	9.96	0.46	1.93E-04	2.05E-04	1.84E-04	5
91500	O_CS240417_915@56	5	9.94	0.42	2.02E-04	2.09E-04	1.84E-04	10
91500	O_CS240417_915@57	5	9.78	0.55	2.00E-04	1.15E-04	1.84E-04	9
91500	O_CS240417_915@58	5	9.88	0.52	1.97E-04	2.09E-04	1.84E-04	7
91500	O_CS240417_915@59	5	10.05	0.47	1.93E-04	2.10E-04	1.84E-04	5
91500	O_CS240417_915@66	5	9.88	0.41	1.61E-04	8.35E-05	1.84E-04	-12
91500	O_CS240417_915@60	5	9.96	0.48	1.91E-04	2.31E-04	1.84E-04	4
91500	O_CS240417_915@61	5	9.94	0.50	1.96E-04	1.64E-04	1.84E-04	7
91500	O_CS240417_915@62	5	9.49	0.43	1.99E-04	1.62E-04	1.84E-04	8
91500	O_CS240417_915@63	5	9.78	0.45	2.00E-04	1.82E-04	1.84E-04	9
91500	O_CS240417_915@64	5	9.81	0.49	1.96E-04	9.09E-05	1.84E-04	7

Table A1.1. Continued.

sample ID	grain/spot ID	#O run	$\delta^{18}\text{O}$ (‰)	2σ	$^{16}\text{O}^{\text{H}}/\text{H}_2\text{O}$	1σ	background OH/O (average OH/O reference zircon)	$^{16}\text{O}^{\text{H}}/\text{H}_2\text{O}$ deviation from background (‰)
			SMOW					
91500	O_CS240417_915@65	5	9.78	0.46	2.12E-04	7.77E-05	1.84E-04	16
91500	O_CS240417_915@66	5	9.84	0.46	2.03E-04	2.12E-04	1.84E-04	10
91500	O_CS240417_915@67	5	9.54	0.42	2.00E-04	9.40E-05	1.84E-04	9
91500	O_CS240417_915@7	5	9.86	0.43	1.69E-04	5.40E-05	1.84E-04	-8
91500	O_CS240417_915@8	5	9.78	0.44	1.69E-04	9.47E-05	1.84E-04	-8
91500	O_CS240417_915@9	5	9.70	0.46	1.72E-04	9.73E-05	1.84E-04	-7
temora 2	O_CS240417_rem@1	5	8.19	0.46	1.95E-04	8.48E-05	1.84E-04	6
temora 2	O_CS240417_rem@10	5	7.96	0.42	3.41E-04	7.05E-05	1.84E-04	86
temora 2	O_CS240417_rem@11	5	8.17	0.43	3.09E-04	1.00E-04	1.84E-04	68
temora 2	O_CS240417_rem@12	5	8.09	0.48	2.94E-04	4.18E-05	1.84E-04	60
temora 2	O_CS240417_rem@13	5	8.06	0.41	2.90E-04	1.35E-04	1.84E-04	58
temora 2	O_CS240417_rem@14	5	8.08	0.42	3.03E-04	6.39E-05	1.84E-04	65
temora 2	O_CS240417_rem@15	5	8.10	0.42	3.22E-04	1.10E-04	1.84E-04	75
temora 2	O_CS240417_rem@16	5	8.15	0.45	3.04E-04	4.89E-05	1.84E-04	65
temora 2	O_CS240417_rem@17	5	7.85	0.46	2.99E-04	6.40E-05	1.84E-04	63
temora 2	O_CS240417_rem@18	5	8.01	0.50	2.33E-04	7.11E-05	1.84E-04	27
temora 2	O_CS240417_rem@19	5	8.00	0.45	2.15E-04	8.36E-05	1.84E-04	17
temora 2	O_CS240417_rem@20	5	8.03	0.42	1.92E-04	9.05E-05	1.84E-04	5
temora 2	O_CS240417_rem@21	5	7.62	0.42	2.29E-04	7.45E-05	1.84E-04	25
temora 2	O_CS240417_rem@22	5	8.04	0.44	2.68E-04	9.21E-05	1.84E-04	46
temora 2	O_CS240417_rem@23	5	7.66	0.48	3.14E-04	1.20E-04	1.84E-04	71
temora 2	O_CS240417_rem@24	5	8.01	0.46	2.90E-04	1.58E-04	1.84E-04	58
temora 2	O_CS240417_rem@25	5	8.27	0.48	3.01E-04	1.16E-04	1.84E-04	64
temora 2	O_CS240417_rem@26	5	8.06	0.52	3.03E-04	1.10E-04	1.84E-04	65
temora 2	O_CS240417_rem@27	5	8.09	0.44	3.25E-04	1.03E-04	1.84E-04	77
temora 2	O_CS240417_rem@28	5	7.82	0.51	3.03E-04	1.11E-04	1.84E-04	65
temora 2	O_CS240417_rem@29	5	7.82	0.54	2.30E-04	7.49E-05	1.84E-04	67
temora 2	O_CS240417_rem@30	5	7.78	0.47	2.66E-04	1.16E-04	1.84E-04	45
temora 2	O_CS240417_rem@31	5	8.27	0.47	2.74E-04	8.86E-05	1.84E-04	49
temora 2	O_CS240417_rem@32	5	7.82	0.47	2.08E-04	5.09E-05	1.84E-04	13

Table A1.1. Continued.

sample ID	grain/spot ID	#O run	$\delta^{18}\text{O}$ (‰)	SMOW	2σ	$^{16}\text{O}^{1\text{H}}/^{16}\text{O}$	1σ	background OH/O (average OH/O reference zircon)	$^{16}\text{O}^{1\text{H}}/\text{O}$ deviation from background (%)
temora 2	O_CS240417_rem@36	5	7.93	0.44	2.12E-04	7.51E-05	1.84E-04	1.84E-04	1.5
temora 2	O_CS240417_rem@37	5	8.50	0.48	2.09E-04	1.25E-04	1.84E-04	1.84E-04	14
temora 2	O_CS240417_rem@38	5	8.04	0.44	1.81E-04	6.22E-05	1.84E-04	1.84E-04	-2
temora 2	O_CS240417_rem@39	5	8.01	0.42	3.06E-04	1.27E-04	1.84E-04	1.84E-04	67
temora 2	O_CS240417_rem@44	5	7.93	0.46	2.32E-04	1.14E-04	1.84E-04	1.84E-04	26
temora 2	O_CS240417_rem@40	5	7.91	0.46	2.98E-04	7.63E-05	1.84E-04	1.84E-04	62
temora 2	O_CS240417_rem@41	5	7.78	0.42	3.00E-04	1.68E-04	1.84E-04	1.84E-04	63
temora 2	O_CS240417_rem@42	5	7.89	0.44	3.03E-04	1.13E-04	1.84E-04	1.84E-04	65
temora 2	O_CS240417_rem@43	5	7.98	0.51	3.22E-04	1.58E-04	1.84E-04	1.84E-04	75
temora 2	O_CS240417_rem@44	5	8.12	0.46	3.32E-04	2.01E-04	1.84E-04	1.84E-04	81
temora 2	O_CS240417_rem@45	5	8.26	0.43	2.35E-04	1.39E-04	1.84E-04	1.84E-04	28
temora 2	O_CS240417_rem@46	5	8.21	0.42	2.34E-04	1.65E-04	1.84E-04	1.84E-04	27
temora 2	O_CS240417_rem@47	5	8.05	0.46	2.51E-04	1.55E-04	1.84E-04	1.84E-04	37
temora 2	O_CS240417_rem@49	5	8.31	0.47	2.64E-04	1.41E-04	1.84E-04	1.84E-04	43
temora 2	O_CS240417_rem@55	5	7.88	0.45	2.12E-04	8.97E-05	1.84E-04	1.84E-04	15
temora 2	O_CS240417_rem@50	5	8.25	0.46	2.48E-04	2.49E-04	1.84E-04	1.84E-04	35
temora 2	O_CS240417_rem@53	5	7.88	0.46	3.12E-04	7.22E-05	1.84E-04	1.84E-04	70
temora 2	O_CS240417_rem@54	5	7.97	0.42	3.04E-04	1.18E-04	1.84E-04	1.84E-04	66
temora 2	O_CS240417_rem@55	5	7.99	0.44	3.39E-04	1.69E-04	1.84E-04	1.84E-04	85
temora 2	O_CS240417_rem@56	5	8.31	0.43	3.41E-04	1.11E-04	1.84E-04	1.84E-04	86
temora 2	O_CS240417_rem@57	5	7.71	0.42	3.27E-04	9.21E-05	1.84E-04	1.84E-04	78
temora 2	O_CS240417_rem@58	5	7.70	0.47	3.20E-04	7.27E-05	1.84E-04	1.84E-04	74
temora 2	O_CS240417_rem@59	5	8.10	0.51	3.34E-04	9.46E-05	1.84E-04	1.84E-04	82
temora 2	O_CS240417_rem@66	5	7.58	0.45	2.20E-04	4.91E-05	1.84E-04	1.84E-04	20
temora 2	O_CS240417_rem@60	5	7.88	0.39	3.63E-04	1.17E-04	1.84E-04	1.84E-04	98
temora 2	O_CS240417_rem@61	5	8.08	0.48	2.23E-04	1.34E-04	1.84E-04	1.84E-04	21
temora 2	O_CS240417_rem@62	5	8.00	0.45	2.33E-04	1.78E-04	1.84E-04	1.84E-04	27
temora 2	O_CS240417_rem@63	5	7.83	0.43	2.36E-04	1.48E-04	1.84E-04	1.84E-04	28
temora 2	O_CS240417_rem@7	5	7.78	0.44	2.86E-04	1.22E-04	1.84E-04	1.84E-04	56
temora 2	O_CS240417_rem@8	5	8.00	0.44	2.96E-04	1.46E-04	1.84E-04	1.84E-04	61
temora 2	O_CS240417_rem@9	5	7.87	0.47	3.20E-04	7.03E-05	1.84E-04	1.84E-04	74

Table A1.1. Continued.

sample ID	Raman grain/spot ID	OH/H-O-H Raman band ($\sim 3420 \text{ cm}^{-1}$)			$\nu_3(\text{SiO}_4)$ Raman band ($\sim 1000 \text{ cm}^{-1}$)		
		FWHM (uncorr.)	FWHM (corr.)	peak centre intensity (cts) (cm^{-1})	FWHM (uncorr.) (cts)	FWHM (corr.) (cm^{-1})	peak centre intensity (cts)
18IM11B	18IM11B-2.1	31.96	31.17	3412	3056	17.31	15.80
18IM11B	18IM11B-3.1	43.85	43.28	3411	1496	9.23	5.93
18IM11B	18IM11B-4.1	79.43	79.11	3403	1590	23.17	22.06
18IM11B	18IM11B-5.1	-	-	-	-	24	22.93
18IM11B	18IM11B-6.1	33.06	32.29	3409	1700	16.75	15.18
18IM11B	18IM11B-7.1	38	37.34	3412	4389	8.82	5.27
18IM11B	18IM11B-8.2	29.3572	28.49	3411	5682	11.91	9.58
18IM11B	18IM11B-1.2	30.74	29.92	3412	3703	17.38	15.88
18IM11B	18IM11B-11.2	32.18	31.39	3410	3464	15.5	13.79
18IM11B	18IM11B-12.1	38.01	37.35	3411	2265	8.27	4.29
18IM11B	18IM11B-13.1	41.69	41.09	3411	2812	10.4	7.63
18IM11B	18IM11B-4.14	78.52	78.20	3405	1611	19.86	18.56
18IM11B	18IM11B-4.15	86.75	86.46	3406	1856	19.22	17.87
18IM11B	18IM11B-4.16	76.69	76.36	3405	1997	18.2	16.77
18IM3	18IM3-9.1	85.24	84.95	3406	743	19.86	18.56
18IM3	18IM3-1.1	45.53	44.98	3400	483	28.03	27.12
18IM3	18IM3-1.2	47.87	47.34	3402	536	23.65	22.57
18IM3	18IM3-10.1	31.88	31.09	3411	827	14.48	12.64
18IM3	18IM3-11.1	33.34	32.58	3410	1148	15	13.23
18IM3	18IM3-11.2	36.85	36.17	3407	1207	17.81	16.35
18IM3	18IM3-17.2	62.36	61.96	3409	2460	14.89	13.10
18IM3	18IM3-4.1	41.76	41.16	3409	1444	16.36	14.75
18IM3	18IM3-6.1	55.17	54.71	3407	336	17.01	15.47
18IM3	18IM3-6.2	59.63	59.21	3405	318	17.35	15.84
18IM21C	18IM21C-2.2	24.03	22.97	3409	611	18.2	16.77
18IM21C	18IM21C-5.1	44.15	43.58	3409	582	14.89	13.10
18IM21C	18IM21C-5.2	39.25	38.61	3409	671	14.89	13.10
18IM21C	18IM21C-8.1	43.14	42.56	3412	511	14.89	13.10

Table A1.2. Raman spectroscopy results.

sample ID	LA-ICPMS analysis ID	grain/spot ID	P	Ca	Fe	Y	Zircon trace element concentrations (ppm)										Lu	Y	Σ REE+Y			
							La	Ce	Pr	Nd	Sm	Eu	Gd	Tb	Dy	Ho						
18IM11B	1.d	1.2	890	646	151	1830	14	55	14	91	49	18	56	9	62	13	43	7	53	9	1830	2322
18IM11B	10.d	11.1, 11.2	2274	2284	1158	136	48	436	84	573	143	70	97	19	194	64	288	60	543	106	136	2862
18IM11B	11.d	12.1, 12.2	451	170	126	217	4	19	3	23	11	4	22	5	41	12	51	10	91	17	217	531
18IM11B	12.d	13.1, 13.2	262	50	157	899	0	9	1	8	7	2	19	4	23	4	11	1	10	2	899	1000
18IM11B	2.d	2.1	1206	1744	655	2237	32	133	27	154	67	45	74	15	122	34	142	29	267	50	2237	3426
18IM11B	3.d	3.1, 3.2	512	238	25	448	2	11	2	15	11	4	26	6	49	13	49	9	76	14	448	735
18IM11B	4.d	4.1, 4.14	1556	1131	382	382	10	43	9	65	49	13	74	19	186	54	214	39	321	57	382	1535
18IM11B	5.d	4.15	1186	1232	498	307	31	129	27	163	62	38	85	20	186	58	236	44	383	69	307	1838
18IM11B	6.d	5.1, 5.2	760	155	189	252	4	28	4	23	8	5	18	7	74	27	138	31	320	65	252	1002
18IM11B	7.d	6.1, 6.2	494	194	72	1883	6	25	4	26	9	3	21	5	33	6	16	2	11	2	1883	2050
18IM11B	8.d	7.1	453	165	66	1210	1	9	1	9	10	2	27	6	43	9	29	4	31	5	1210	1397
18IM11B	9.d	8.2	371	155	52	409	2	15	2	14	10	6	25	6	36	8	25	4	33	6	409	601
18IM3	1.d	1.1	954	476	368	1493	8	83	8	39	15	3	27	8	70	23	114	32	383	107	1493	2413
18IM3	2.d	2.1	269	59	17	1119	0	29	0	4	4	1	13	4	48	17	87	20	195	43	1119	1583
18IM3	3.d	6.1	821	1293	123	817	8	81	11	69	57	10	84	20	181	51	214	43	386	72	817	2106
18IM3	4.d	6.2	322	0	0	5163	0	10	0	1	2	0	10	4	46	18	84	17	154	31	5163	5539
18IM3	5.d	9.1	0	153	69	538	1	11	0	4	5	1	21	6	75	28	131	27	240	48	538	1135
18IM3	6.d	10.1	0	2814	413	1651	16	94	16	109	84	29	233	74	703	181	702	140	1265	201	1651	5497
18IM3	7.d	11.1	0	26	800	1	48	2	11	5	1	15	5	55	20	98	21	198	42	800	1322	
18IM3	8.d	11.2	0	337	119	576	3	65	4	27	15	4	43	14	150	49	215	44	398	76	576	1681
18IM3	9.d	17.2	0	15	7	626	0	5	0	2	4	0	23	8	99	37	172	34	299	58	626	1367
18IM21C	1.d	2.1	12797	0	0	699	8	9	2	8	3	0	12	5	61	23	105	22	192	38	699	1186
18IM21C	2.d	2.2	6843	105	7	1279	0	4	0	1	2	0	18	8	106	38	170	33	277	50	1279	1986
18IM21C	3.d	5.1	2691	0	1	719	0	5	0	0	1	0	10	4	54	19	89	18	163	32	610	1184
18IM21C	4.d	5.2	255	0	0	610	0	5	0	1	1	0	10	4	54	19	89	18	163	32	610	1007
18IM21C	5.d	8.1	278	0	5	758	0	10	0	2	3	1	14	5	64	24	120	26	262	55	758	1345

Table A2. LA-ICPMS zircon trace element data

primary standard (91500)						secondary standard (temora-2)					
# O run	# analyses	$\delta^{18}\text{O}$	2σ	$^{16}\text{O}^1\text{H}/^{16}\text{O}$	2σ	# analyses	$\delta^{18}\text{O}$	2σ	$^{16}\text{O}^1\text{H}/^{16}\text{O}$	2σ	
1	13	9.9	0.23	0.00227	0.00028	7	7.88	0.38	0.00237	0.00022	
2	21	9.9	0.38	0.00195	0.00022	6	7.93	0.39	0.00205	0.00017	
3	22	9.9	0.42	0.00473	0.00063	7	7.78	0.42	0.00468	0.00086	
4	37	9.9	0.40	0.00056	0.00002	5	7.92	0.33	0.00067	0.00011	
5	65	9.9	0.36	0.00018	0.00002	57	8.00	0.37	0.00028	0.00009	

Table A3. O isotope measurement results of zircon reference materials for SIMS analytical runs.

CONCLUSIONS:

MODELS AND QUESTIONS CONCERNING THE COEVOLUTION OF LITHOSPHERE, ATMOSPHERE, AND BIOSPHERE AT THE ARCHEAN- PROTEROZOIC TRANSITION

6.1 Widespread emergence of continents above sea-level at ~2.4 Ga

The results of the research presented in this thesis suggest that subaerial continental area increased significantly at ~2.4 Ga (hereafter referred to as widespread continental emergence), which led to 1) an increase in subaerial eruptions of continental large igneous provinces (see Chapter 3), and 2) enhanced erosion, and changes in subaerial weathering pattern, associated with a change in the oxygen isotope composition of sediments (Bindeman et al., 2018), and sediment-melts (see Chapter 2). The widespread emergence of continents above sea-level at 2.4 Ga is supported by a pervasive erosional event at <2.42 Ga on six cratonic terranes (including Superior Province, Hearne Domain, Fennoscandian Shield, São Francisco, Pilbara, and Kaapvaal cratons) that has been interpreted to reflect a relatively rapid global sea-level drop (Eriksson and Condie, 2014). Broadly overlapping, an increase in seawater $^{87}\text{Sr}/^{86}\text{Sr}$ ratio occurs between 2.7 and 2.4 Ga, suggesting enhanced crustal erosive run-off, and increased continental influence on ocean chemistry (Flament et al., 2013; Chapter 3 of this thesis).

The widespread emergence of continents is temporally associated with a ~2.4-2.2 Ga tectono-magmatic slowdown (Condie et al., 2009; Spencer et al., 2018). This proposed lull in mantle activity, and concomitant reduced plate-velocities (Spencer et al., 2018), and mid-ocean ridge activity (Eriksson and Condie, 2014) may have led to cooling and thickening of the oceanic

lithosphere, causing rapid subsidence of the ocean floor and a drop in eustatic sea-level (Miller et al., 2005; Eriksson and Condie, 2014). Another possible geodynamic driver for the increase in freeboard at \sim 2.4 Ga is mantle upwelling during the \sim 2.45 Ga rifting of Superior (Bleeker, 2003) and associated dynamic topography causing continental uplift (Gurnis, 1988).

6.1.1 Validity of geochemical signatures used to constrain continental emergence

The oxygen isotope ratio recorded by zircon is a sensitive tracer for crustal recycling in magmatic rocks and is a commonly used tool to address zircon petrogenetic questions (e.g. in studies on the evolution of freeboard as presented in chapter 2). However, secondary processes (i.e. water uptake facilitated by radiation damage) can alter the oxygen isotopic composition of zircon; in agreement with previous studies (e.g. Wang et al., 2014; Pidgeon et al., 2017) the results of chapter 5 confirm that the uptake of water into the zircon crystal structure strongly influences its recorded oxygen isotope ratio. Furthermore, the results of chapter 5 demonstrate that the disturbance of the oxygen isotopic system in zircon can be assessed through monitoring zircon $^{16}\text{O}^1\text{H}/^{16}\text{O}$; a parameter that is highly sensitive to the influx of water into radiation-damaged areas of the zircon grain, providing a powerful tool to access the validity of primary $\delta^{18}\text{O}$ signatures. Hence, the oxygen isotope ratio of zircon provides a reliable record of primary magmatic signatures, if interpreted in tandem with zircon $^{16}\text{O}^1\text{H}/^{16}\text{O}$ (as is the case for the data presented in this thesis).

6.2 A coevolution of atmosphere and lithosphere?

The pyrite-bearing pre-GOE granitoids presented in Chapter 4 record the recycling of anoxic atmospheric sulfur isotopic signatures (i.e. S-MIF signatures) into the igneous rock record. In contrast, the post-GOE counterparts of these granitoids exclusively show S-MDF signatures. The disappearance of S-MIF signatures (recorded by pyrite) is coupled with an increase in $\delta^{18}\text{O}$ (recorded by zircon and garnet) in these samples (see Chapter 4). The attenuation of mass-independent fractionation of sulfur isotopes has been attributed to the development of an ozone shield related to the rise of atmospheric oxygen (Farquhar et al., 2000; Johnston, 2011). Chapter 2 argues that the Paleoproterozoic increase in average zircon $\delta^{18}\text{O}$ is related to the widespread emergence of continents above sea-level. Thus, the coupled behavior of sulfur and

oxygen isotopic signatures in the granitoids of this thesis support a temporal, and potentially causal link between the widespread emergence of continents, and the increase in atmospheric oxygen level (Figure 6.1).

6.3 Continental emergence as a potential driver of atmospheric oxygenation

The widespread subaerial emergence of continents constitutes a potential driver for the rise in atmospheric oxygen as increased subaerial land area may lead to decreased O₂ consumption through a shift towards less reducing volcanic gases associated with diminished submarine volcanism (Kump and Barley, 2007; Gaillard et al., 2011). In addition, increased subaerial weathering of felsic material enhances CO₂ consumption (Lowe and Tice, 2004). Furthermore, a flush of life-essential nutrients (e.g. phosphorous, and iron) from newly emergent continental crust into oceans may have supported primary production of O₂ through photosynthetic activity (Campbell and Allen, 2008). Numerical models demonstrate a strong influence of emergent continental land area on phosphorous flux into the ocean (Hao et al., 2020). A mechanism involving the erosion of elevated continental crust has been suggested to have initiated the explosive radiation of animal-life during the Late Ediacaran to Early Cambrian periods (575-510 Ma; ‘Cambrian explosion’) (Squire et al., 2006). It has been proposed that the amalgamation of supercontinent Gondwana and associated extensive mountain building and erosion led to an enormous flush of nutrients into the ocean (Squire et al., 2006; Campbell and Allen, 2008). The increase of essential nutrients available for marine bioproductivity may have led to an increase in O₂ production and provided a favourable environment for the explosive diversification of life (Chen et al., 2015). Similarly, a flush of nutrients to the oceans associated with the Paleoproterozoic subaerial emergence of continents may have fuelled oxygenic photosynthesis (either in terms of radiation or bioproductivity) (Cox et al., 2018). A shift in ocean nutrient availability from phosphorous to iron limiting could have supported O₂ production by providing an environment favourable for oxygenic photoautotrophs over anoxygenic photoautotrophs (Jones et al., 2015). Furthermore, increased erosion and sediment supply from the elevated continents may facilitate the burial of organic carbon reducing the overall sink for O₂ (Campbell and Allen, 2008).

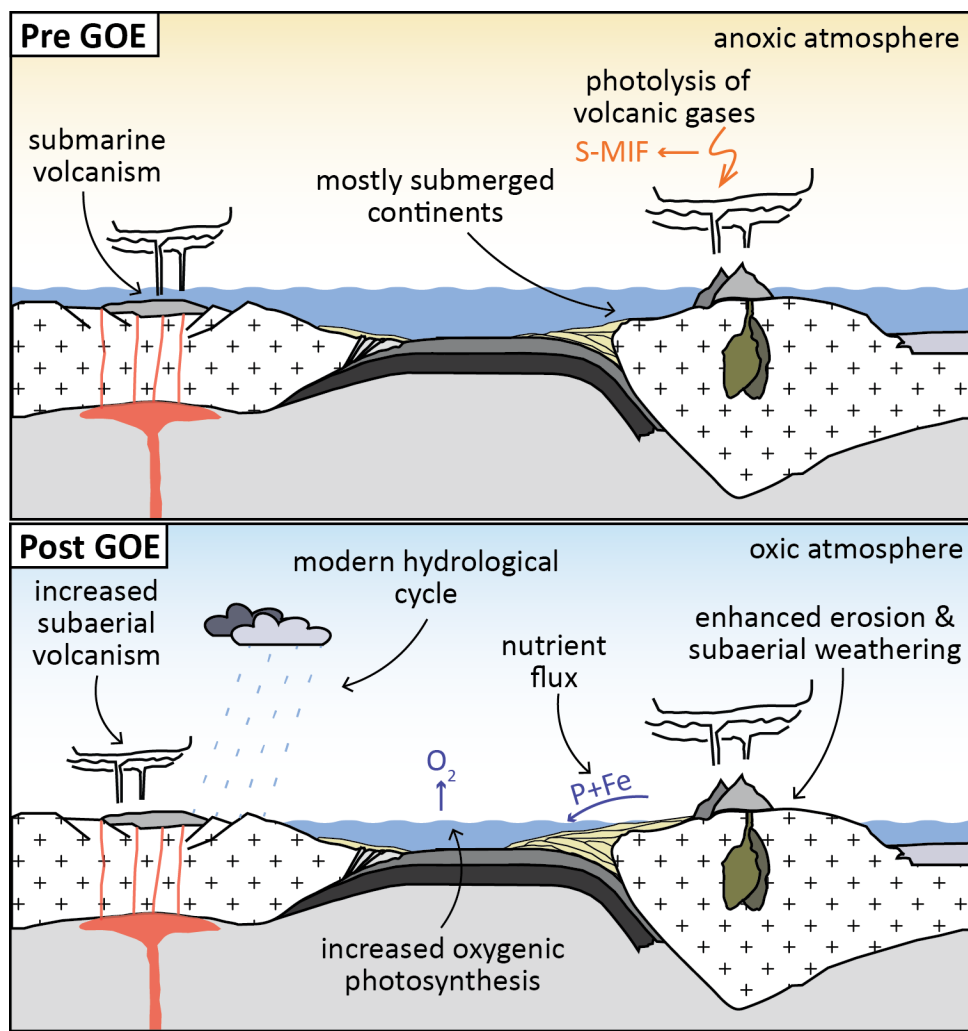


Figure 6.1. Illustration of a possible model for the coevolution of lithosphere, atmosphere, and biosphere at the Archean Proterozoic transition. The upper part of the figure shows the Archean Earth with mostly submerged continents, extensive submarine volcanism emitting strongly reducing volcanic gases (Kump and Barley, 2007; Gaillard et al., 2011), and mass independent fractionation of sulfur isotopes under an anoxic atmosphere (Johnston, 2011). In contrast, the bottom part of the Figure shows Earth after the widespread emergence of continents at ~2.4 Ga with a modern hydrological cycle (Bindeman et al., 2018), and enhanced erosion and subaerial weathering leading to the generation of high $\delta^{18}\text{O}$ sediments and sediment melts. Diminished submarine volcanism is associated with a change in the redox state of volcanic gases (Gaillard et al., 2011), and decreased O_2 consumption. A flush of nutrients from the emergent continental crust into the ocean fuels photosynthetic activity leading to enhanced production of O_2 , and ultimately, the oxygenation of the atmosphere.

6.4 Limitations and avenues for future work

The evolution of oxygen and sulfur isotopic signatures appear to be coupled in the set of sediment-derived granitoids studied in this thesis. As discussed in section 6.2 and in chapter 3 of this thesis, coevolution of sulfur and oxygen isotopic signatures provides strong evidence for a temporal and potentially causal connection of the emergence of continents and atmospheric oxygenation. Important to note, the youngest sediment-derived granitoid of this study that shows S-MIF signatures generated under an anoxic atmosphere has a crystallization age of 2478 ± 18 Ma; the oldest sample with S-MDF signatures has a crystallization age of 2188 ± 20 Ma. Therefore, the data presented here is inconclusive for the ~ 300 Myr interval between the youngest S-MIF and the oldest S-MDF sample. The preserved igneous rock record between 2.4 and 2.2 Ga is sparse due to diminished magmatic activity (Condie et al., 2009; Spencer et al., 2018) making it challenging to fill this temporal gap. Further work is required to find and investigate a more continuous record of the isotopic proxies for atmospheric oxygen level and freeboard used in this thesis. A recent effort to compile a comprehensive data set of triple oxygen isotopic signatures to unravel the evolution of hydrosphere and continental weathering pattern uses the combined records of siliciclastic sediments and sediment-derived melts (Bindeman, 2020). Similarly, future work could combine the igneous and sedimentary record to test the hypothesis of a coupled behavior of sulfur and oxygen isotopic signatures to further advance our understanding of the link between lithosphere, atmosphere, and biosphere across the Archean Proterozoic transition.

6.5 Epilogue: Implications for the search of inhabited worlds

The evolution of the atmosphere of a terrestrial planet (rocky planet, primarily composed of silicates and metals) is controlled by the interaction with the planet's interior over geologic time (Foley and Driscoll, 2016). This thesis presents a model that draws specific links between the emergence of continents above sea-level (potentially initiated through processes at the core-mantle boundary), atmospheric composition, and bioproductivity. This 'whole planet coupling' between a planet's surface and interior potentially explains why planets with similar bulk composition, size, and distance from their host star take drastically different evolutionary paths

(e.g. the Earth-Venus dichotomy, see Chapter 1) many of which are detrimental for life (Foley and Driscoll, 2016).



Figure 6.2. Artist's concept of Kepler-186f, the first validated Earth-size planet to orbit a star in the habitable zone about 500 light-years from Earth in the constellation Cygnus (Quintana et al., 2014). Image credits: NASA Ames/SETI institute/JPL-Caltech.

Life uses chemical reactions to extract, store, and release energy (e.g. Krissansen-Totton et al., 2018). This process produces waste gases that modify the composition of a planet's atmosphere (Krissansen-Totton et al., 2018). Detecting such 'biosignature gases' in thermochemical disequilibrium with the planetary atmosphere is one of the aims of the James Webb Space Telescope due to launch in 2021 (Deming et al., 2009). The dominant biosignature gas on Earth is O₂ (Figure 6.3) produced by plants and photosynthetic bacteria (Turnbull et al., 2006). Other biogenic waste gases on Earth, e.g. CO₂, are not unique to life as they can be produced abiotically. Therefore, determining a catalogue of diagnostic criteria, including both features of the atmosphere and planetary interior (Seager, 2013; Shahar et al., 2019; Spaargaren et al., 2020), is an important step towards finding extraterrestrial life (e.g. on exoplanets like Kepler-186f, Figure 6.2). Understanding atmosphere-interior coupling on Earth will increase our future chances of discovering other habitable and inhabited worlds.

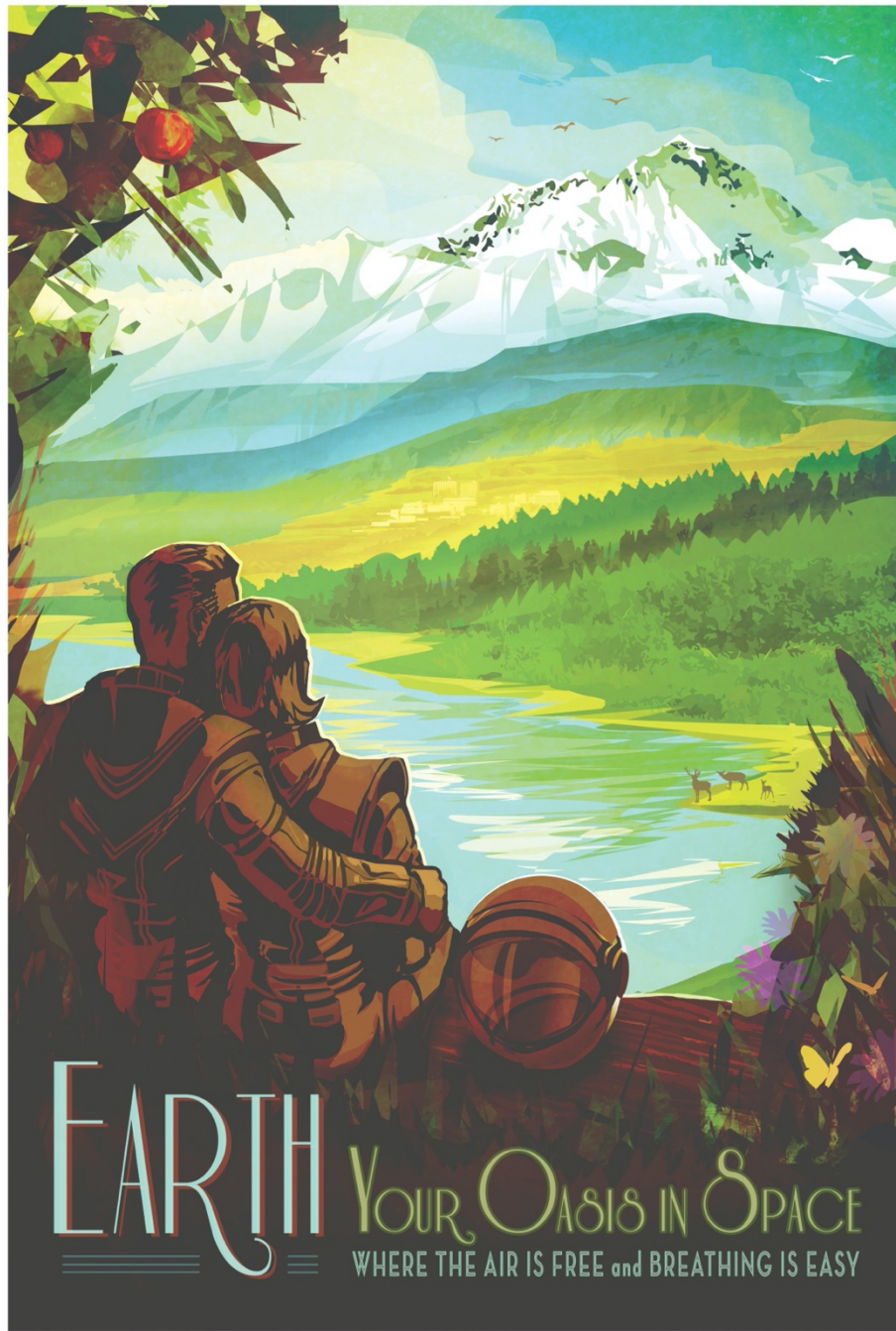


Figure 6.3. “There is no place like home. Warm, wet and with an atmosphere that’s just right, Earth is the only place we know of with life – and lots of it”. This poster is from the “Visions of the Future” poster series created by The Studio, a creative team of visual strategists at the Jet Propulsion Laboratory, California Institute of Technology. Courtesy NASA/JPL-Caltech.

6.6 References

- Bindeman, I.N., 2020, Triple oxygen isotopes in evolving continental crust, granites, and clastic sediments: Reviews in mineralogy and geochemistry, v. 86, doi:10.2138/rmg.2020.86.X.
- Bindeman, I.N., Zakharov, D.O., Palandri, J., Greber, N.D., Dauphas, N., Retallack, G.J., Hofmann, A., Lackey, J.S., Bekker, A., and Data, E., 2018, Rapid emergence of subaerial landmasses and onset of a modern hydrologic cycle 2.5 billion years ago: Nature, v. 557, p. 545–548, doi:<https://doi.org/10.1038/s41586-018-0131-1>.
- Bleeker, W., 2003, The late Archean record: A puzzle in ca. 35 pieces: Lithos, v. 71, p. 99–134, doi:10.1016/j.lithos.2003.07.003.
- Campbell, I.H., and Allen, C.M., 2008, Formation of supercontinents linked to increases in atmospheric oxygen: Nature Geoscience, v. 1, p. 554–558, doi:10.1038/ngeo259.
- Condie, K.C., O'Neill, C., and Aster, R.C., 2009, Evidence and implications for a widespread magmatic shutdown for 250 My on Earth: Earth and Planetary Science Letters, v. 282, p. 294–298, doi:10.1016/j.epsl.2009.03.033.
- Cox, G.M., Lyons, T.W., Mitchell, R.N., Hasterok, D., and Gard, M., 2018, Linking the rise of atmospheric oxygen to growth in the continental phosphorus inventory: Earth and Planetary Science Letters, v. 489, p. 28–36, doi:<https://doi.org/10.1016/j.epsl.2018.02.016>.
- Deming, D. et al., 2009, Discovery and Characterization of Transiting Super Earths Using an All-Sky Transit Survey and Follow-up by the James Webb Space Telescope: Publications of the Astronomical Society of the Pacific, v. 121, p. 952–967, doi:10.1086/605913.
- Eriksson, P.G., and Condie, K.C., 2014, Cratonic sedimentation regimes in the ca. 2450–2000Ma period: Relationship to a possible widespread magmatic slowdown on Earth? Gondwana Research, v. 25, p. 30–47, doi:10.1016/j.gr.2012.08.005.
- Farquhar, Bao, and Thiemens, 2000, Atmospheric influence of Earth's earliest sulfur cycle: Science (New York, NY), v. 289, p. 756–759, http://www.ncbi.nlm.nih.gov/entrez/query.fcgi?db=pubmed&cmd=Retrieve&am;p;dopt=AbstractPlus&list_uids=10926533.
- Flament, N., Coltice, N., and Rey, P.F., 2013, The evolution of the $^{87}\text{Sr}/^{86}\text{Sr}$ of marine carbonates does not constrain continental growth: Precambrian Research, v. 229, p. 177–188, doi:10.1016/j.precamres.2011.10.009.
- Foley, B.J., and Driscoll, P.E., 2016, Whole planet coupling between climate, mantle, and core: Implications for rocky planet evolution: Geochemistry, Geophysics, Geosystems, v. 17, p. 1885–1914, doi:10.1002/2015GC006210.
- Gaillard, F., Scaillet, B., and Arndt, N.T., 2011, Atmospheric oxygenation caused by a change in volcanic degassing pressure: Nature, v. 478, p. 229–232, doi:10.1038/nature10460.

- Gurnis, M., 1988, Large-scale mantle convection and the aggregation and dispersal of supercontinents: *Nature*, v. 332, p. 695–699.
- Johnston, D.T., 2011, Multiple sulfur isotopes and the evolution of Earth's surface sulfur cycle: *Earth-Science Reviews*, v. 106, p. 161–183, doi:10.1016/j.earscirev.2011.02.003.
- Jones, C., Nomosatryo, S., Crowe, S.A., Bjerrum, C.J., and Canfield, D.E., 2015, Iron oxides, divalent cations, silica, and the early earth phosphorus crisis: *Geology*, v. 43, p. 135–138, doi:10.1130/G36044.1.
- Krissansen-Totton, J., Olson, S., and Catling, D.C., 2018, Disequilibrium biosignatures over Earth history and implications for detecting exoplanet life: *Science Advances*, v. 4, p. eaao5747, doi:10.1126/sciadv.aao5747.
- Kump, L.R., and Barley, M.E., 2007, Increased subaerial volcanism and the rise of atmospheric oxygen 2.5 billion years ago: *Nature*, v. 448, p. 1033–1036, doi:10.1038/nature06058.
- Lowe, D.R., and Tice, M.M., 2004, Geologic evidence for Archean atmospheric and climatic evolution: Fluctuating levels of CO₂, CH₄, and O₂ with an overriding tectonic control: *Geology*, v. 32, p. 493–496, doi:10.1130/G20342.1.
- Pidgeon, R.T., Nemchin, A.A., and Whitehouse, M.J., 2017, The effect of weathering on U-Th-Pb and oxygen isotope systems of ancient zircons from the Jack Hills, Western Australia: *Geochimica et Cosmochimica Acta*, v. 197, p. 142–166, doi:10.1007/s11947-009-0181-3.
- Quintana, E. V. et al., 2014, An Earth-Sized Planet in the Habitable Zone of a Cool Star: *Science*, v. 344, p. 277–280, doi:10.1126/science.1249403.
- Seager, S., 2013, Exoplanet Habitability: *Science*, v. 340, p. 577–581, doi:10.1126/science.1232226.
- Shahar, A., Driscoll, P., Weinberger, A., and Cody, G., 2019, What makes a planet habitable? *Science*, v. 364, p. 434–435, doi:10.1126/science.aaw4326.
- Spaargaren, R.J., Ballmer, M.D., Bower, D.J., Dorn, C., and Tackley, P.J., 2020, The influence of bulk composition on long-term interior-atmosphere evolution of terrestrial exoplanets: *Astronomy & Astrophysics*, <http://arxiv.org/abs/2007.09021>.
- Spencer, C.J., Murphy, J.B., Kirkland, C.L., Liu, Y., and Mitchell, R.N., 2018, Was the supercontinent cycle activated by a Palaeoproterozoic tectono-magmatic lull? *Nature Geoscience*, v. 11, p. 97–101, doi:10.1038/s41561-017-0051-y.
- Squire, R., Campbell, I., Allen, C., and Wilson, C., 2006, Did the Transgondwanan Supermountain trigger the explosive radiation of animals on Earth? *Earth and Planetary Science Letters*, v. 250, p. 116–133, doi:10.1016/j.epsl.2006.07.032.
- Turnbull, M.C., Traub, W.A., Jucks, K.W., Woolf, N.J., Meyer, M.R., Gorlova, N., Skrutskie, M.F., and Wilson, J.C., 2006, Spectrum of a Habitable World: Earthshine in the Near-

Infrared: The Astrophysical Journal, v. 644, p. 551–559, doi:10.1086/503322.

Wang, X.-L., Coble, M.A., Valley, J.W., Shu, X.-J., Kitajima, K., Spicuzza, M.J., and Sun, T., 2014, Influence of radiation damage on Late Jurassic zircon from southern China: Evidence from in situ measurements of oxygen isotopes, laser Raman, U–Pb ages, and trace elements: Chemical Geology, v. 389, p. 122–136, doi:10.1016/j.chemgeo.2014.09.013.